Wideband Integrated Lens Antennas for Terahertz Deep Space Investigation

Yurduseven, Ozan

DOI
10.4233/uuid:f30b8bca-173f-4a13-b545-e18e137c9fc6

Publication date
2016

Document Version
Final published version

Citation (APA)
Yurduseven, O. (2016). *Wideband Integrated Lens Antennas for Terahertz Deep Space Investigation*. [Dissertation (TU Delft), Delft University of Technology]. https://doi.org/10.4233/uuid:f30b8bca-173f-4a13-b545-e18e137c9fc6

Wideband Integrated Lens Antennas for Terahertz Deep Space Investigation

Ph.D. Thesis

Ozan Yurduseven

Wideband Integrated Lens Antennas for Terahertz Deep Space Investigation

PROEFSCHRIFT

ter verkrijging van de graad van doctor
aan de Technische Universiteit Delft,
op gezag van de Rector Magnificus Prof. ir. K. C. A. M. Luyben,
voorzitter van het College van Promoties,
in het openbaar te verdedigen op
woensdag 6 Juli om 10.00 uur

door

Ozan Yurduseven

geboren te Istanbul, Turkije.

This dissertation has been approved by the:

Promotor:	Prof. Dr. A. Neto
Copromotor:	Dr. N. Llombart Juan

Composition of the doctoral committee:

Rector Magnificus
Prof. Dr. A. Neto, promotor
Dr. N. Llombart Juan, copromotor

Independent members:

Prof. dr. ir. T.M. Klapwijk	Delft University of Technology, The Netherlands
Prof. C. Craeye	Université Catholique de Louvain (UCL), Belgium
Prof. J.R. Costa	Instituto Universitário de Lisboa (ISCTE), Portugal
Dr. J.F. Johansson	RUAG Space, Sweden
Dr. M. van der Vorst	ESA-ESTEC, The Netherlands

Substitute member:

Prof. dr. L. de Vreede	Delft University of Technology, The Netherlands

The work presented in this thesis has been performed at TU Delft and financed by the European Research Council starting grants ERC-2011-StG Grant AAATSI 278794.

Keywords: Leaky slots, connected arrays, dielectric lens antennas, wide-band antennas, dual-polarization, focal plane arrays, terahertz astronomy.

Front cover background image credit: ESA / NASA
The pictures of the antennas on the front cover are taken from SRON
Back cover image credit: Multiwavelength images of M31, via the Planck mission team; ESA / NASA

Summary

Wideband Integrated Lens Antennas for Terahertz Deep Space Investigation

The Terahertz (THz) band is the portion of the spectrum that covers a frequency range from 300 GHz to 3 THz. The potential of this band has been proven for numerous type of applications including medical imaging, non-destructive testing, space observation, spectroscopy and security screening, thanks to its good compromise between the spatial resolution and penetration. Most of these applications demand for high spatial and range resolution of the images, as well as fast acquisition time. To fulfill such requirements, focal plane arrays (FPAs) need to comprise a large number of elements and be able to operate over broad bandwidths. Moreover, fabrication of the FPAs with thousands of antenna elements becomes a real issue at such frequencies due to the fabrications constraints and immense manufacturing costs.

This doctoral thesis consists of two parts: Part I focuses on the design of the lens antennas using a multiple feed per lens scenario, specifically aiming at imaging for security and the telecommunication systems as potential applications. The aim of the study is to design integrated lens antennas to achieve frequency stable radiation characteristics either to obtain an efficient reflector illumination or to be used directly as an imager over a wideband operation, typically more than one octave. In the literature, double slot antennas have been widely proposed as an efficient lens feeder, yet they are able to operate within a very narrow bandwidth, in the order of $10 - 15\%$. Due to its wideband characteristics connected array of leaky slot antenna concept has been used as a lens feeder. Depending on the application type, two different approaches have been implemented to achieve frequency independent lens radiation: A coherently fed connected leaky slot array based design with a traditional extended hemi-spherical lens for phased array antenna applications and an integrated double shell lens based design where each source element is associated to an independent beam for telecommunication and security systems.

Part II of the thesis focuses on a single feed per lens scenario, specifically aiming at Ter-

ahertz (THz) astronomy applications. Such applications mostly require antennas consist of multi-pixels with large operational bandwidths. Many of the sub-mm wave instruments done for this kind of applications are envisioned to have large format focal plane arrays (FPA) that are based on single beam per feed and tight sampling and are coupled to reflector systems with large F/D ratios. Future satellite based, astronomic THz radiometers will be most likely based on cryogenically cooled detectors to reach the highest sensitivities, will consist of tens of thousands receivers to provide a broad field of view and could address simultaneously a broad portion of the THz band. Several type of reflector feeds have been proposed in the literature including the Vivaldi antennas, horn antennas and the eleven antennas. These antennas, however, are typically optimized to maximize the reflector illumination efficiencies as a single reflector feed. As a result, they suffer from the feed taper efficiency which is crucial to characterize the total system performance for tightly packed FPAs. No need to mention about the feasibility issues when it comes to the fabrication of the thousands of array elements with the manufacturing techniques available nowadays in sub-mm band. Integrated lens antennas, on the other hand, are widely used in sub-mm band since they allow the integration of the antenna and the detector on the same chip. Space instruments based on cryogenic power detectors often use focal plane arrays based on dielectric lenses. In the literature, the most commonly used lens feed is a double slot antenna, which typically operates in a bandwidth much less than one octave and with single polarization. Sinuous and spiral antennas have been also proposed as wideband lens antenna solutions. However, the fabrication of the feeding lines integrated to the antenna becomes challenging at sub-mm band since they have to be extremely tiny in order not to disturb the radiated fields. To overcome these issues, we propose a highly efficient, dual-polarized wideband leaky lens antenna design that can be integrated to planar feeding lines on the same chip. To our knowledge, the proposed design is the only practical wideband dual polarized antenna solution presently available at sub-mm wave frequencies which lends itself as an extremely useful alternative for next generation sub-mm wave space astronomical instruments.

Samenvatting

Breedband Geïntegreerde Lens Antennes voor Terahertz Ruimte Onderzoek

De Terahertz (THz) band is dat gedeelte van het spectrum dat de frequenties van 300 GHz tot 3 THz bestrijkt. Het potentieel van deze band is bewezen voor talrijke toepassingen waarbij te denken valt aan medische beeldvorming, niet-destructief onderzoek, ruimteonderzoek, spectroscopie en veiligheidscontroles. Het potentieel ligt in de balans tussen resolutie en de penetratie van sommige objecten. De meeste van deze toepassingen vereisen een hoge ruimtelijke resolutie en een snelle acquisitietijd. Om aan dergelijke eisen te kunnen voldoen moeten antennestelsels die het brandvlak bestrijken (FPAs; English: Focal Plane Arrays) bestaan uit een groot aantal elementen. Daarnaast moeten ze over een brede frequentieband kunnen opereren. De fabricage van FPA's wordt bovendien een echt knelpunt op THz frequenties vanwege de beperkingen in het fabricageproces en daardoor ook immense productiekosten.

Dit proefschrift bestaat uit twee delen. Deel I richt zich op het ontwerp van lensantennes waarbij gebruik gemaakt wordt van meerdere sensoren per lens. Dit deel richt zich vooral op de potentiele applicaties met betrekking tot veiligheidscontroles en telecommunicatiesystemen. Het doel van deze studie is om geïntegreerde lensantennes te ontwerpen met een frequentie-stabiel radiatiepatroon. Deze stabiliteit is nodig om de reflector efficiënt te kunnen belichten ofwel om direct als een camera te gebruiken die operationeel is over een brede frequentieband, vaak meer dan een octaaf. In de literatuur zijn dubbele-sleufantennes vaak aangedragen als efficiënte lens-belichters. Deze antennes hebben echter een smalle bandbreedte welke in de orde is van 10-15%. Een verbonden stelsel van doorlatende sleufantennes wordt daarom gebruikt als lens-belichting vanwege de breedband eigenschappen. Afhankelijk van de toepassing zijn twee verschillende strategieën geïmplementeerd om de lens onafhankelijk van de frequentie te belichten. Voor fase gestuurde antenne toepassingen wordt een traditioneel verlengde half bolvormige lens belicht door een verbonden stelsel van doorlatende sleuven die coherent gevoed wordt. Voor veiligheids- en telecommunicatie

systemen wordt een geïntegreerde dubbelschil lens ontwerp besproken waarbij elke voedingselement is geassocieerd aan een stralingspatroon, elk onafhankelijk van elkaar.

Het tweede gedeelte van de thesis richt zich op het scenario waarbij er één pixel per lens wordt gebruikt en focust voornamelijk op THz-astronomie toepassingen. Deze toepassingen vereisen vaak antennes in het brandvalk met meervoudige stralingsbundels, welke bovendien een grote operationele bandbreedte hebben. Veel van de bestaande sub-mm golf instrumenten die zijn ontwikkeld voor dit soort applicaties zijn beoogd voor grote FPAs die gebaseerd zijn op een enkele bundel per antenne met een hoge dichtheid van de antennes in het stelsel. Het antennestelsel is vervolgens gekoppeld aan een reflectorsysteem met een grote F/D ratio. Toekomstige astronomische radiometers, geplaatst op satellieten, zullen hoogst waarschijnlijk gebaseerd zijn op cryogeen gekoelde detectoren om de vereiste sensitiviteit te behalen. Ze zullen tienduizenden ontvangers hebben om een breed gezichtsveld te hebben en tegelijkertijd in een groot portie van de THz-band opereren. Verschillende types van reflectorantennes worden voorgesteld in de literatuur, inclusief de Vivaldi antennes, hoorn antennes en Eleven-antennes. Deze antennes worden echter geoptimaliseerd om de reflector illuminatie efficiëntie te maximaliseren wanneer zij als een enkele reflectorsensor worden gebruikt. Als resultaat van deze optimalisatie is de taper efficiëntie vaak erg slecht welke cruciaal is om de totale systeem prestatie te karakteriseren voor stelsels met een hoge sensordichtheid. Verder zijn er verscheidene problemen bij het fabriceren van duizenden antennestelsel elementen met de huidige fabricatie technieken voor de sub-mm band. Aan de andere kant worden geïntegreerde lens antennes wijd gebruikt in de sub-mm band aangezien het mogelijk is om de antennes en de detectoren op dezelfde chip te integreren. Ruimte-instrumenten die gebaseerd zijn op cryogene vermogens detectoren maken vaak gebruik van antennestelsels gebaseerd op dilektrische lenzen. In de literatuur is de meest gebruikte lens antenne de dubbele-sleuf antenne, welke normaal gesproken gebruikt maakt van een bandbreedte veel lager dan een octaaf en tevens een enkele polarisatie heeft. Kronkelige (English: sinuous) en spiraal antennes zijn ook voorgesteld als breedband lens antenne oplossing. Echter wordt de fabricatie van de ge integreerde voedingslijnen uitdagend in de sub-mm band aangezien ze erg klein moeten zijn om niet de uitgestraalde velden te verstoren. Om deze problemen te overkomen stellen we een erg efficiënte, tweevoudig gepolariseerde breedband leaky-lens antenne voor. Dit ontwerp kan worden geïntegreerd met planaire voedingslijnen op dezelfde chip. Naar ons weten is het voorgestelde ontwerp de enige praktische breedband, tweevoudig-gepolariseerde, antenne oplossing die op dit moment verkrijgbaar is voor sub-mm golf frequenties. Daarmee leent het zichzelf als een extreem bruikbaar alternatief voor de volgende generatie sub-mm golf

ruimte-astronomische instrumenten.

Acknowledgements

This doctoral thesis comprises the research performed by the author within the THz Sensing Group in Microelectronics Department at Delft University of Technology. The work has been accomplished thanks to the help, support, guidance and collaboration of many people.

First and foremost, I would like to thank my promotor, Prof. Andrea Neto. I am grateful that you had accepted me to your group and gave me the opportunity to work on this doctoral thesis. It was an honor and a privilege for me to have been working within your group for four-plus years now. The energy and the ambition you bring to your work as a researcher and a supervisor is truly fascinating.

Special thanks go to my co-promotor, Dr. Nuria Llombart Juan. I am a very lucky person to have a chance to work with you. I think you are one of the most knowledgeable and enthusiastic persons that I have ever seen in my life. You are the one that can always find time for your students no matter how many students you have and how busy you are. You have been always positive and optimistic whenever I came to you with a problem. What else a student could possibly wish for? With your superb supervision and super nice attitude, I should say, you had such a huge impact on this thesis. So, thank you for everything.

I would like to thank Dr. Daniele Cavallo for his supervision, especially in the first year of my PhD. Despite the limited time we had a chance to work together, I am still very happy with the outcome of the work. With your superior and deep understanding in electromagnetics and having such a nice personality, I think that your future students are so lucky to have you as a supervisor. Special thanks go to Dr. Giorgio Carluccio for the useful discussions we had and to Dr. Akira Endo for the proofreading of the astronomy part of the thesis.

I would like to thank my PhD defense committee members for taking out their time and accepting to be a part of my PhD defense committee. I am especially grateful to Prof. Jorge Costa and Prof. Christophe Craeye for their careful review of this dissertation.

Special thanks go to Dr. Juan Bueno and Dr. Jochem Baselmans for the useful discussions. Thanks Juan also for the high quality pictures of the antenna coupled KID prototypes and for the translations of the physics terms into electromagnetics. It was such a nice experience to be working with you both.

As a part of collaboration I have spent six beautiful months in Lisbon. I would like to take this opportunity to thank Prof. Carlos Fernandes and Prof. Jorge Costa for the very nice hospitality and the collaboration during the visit. Although the visit was only for six months, it was a great experience for me that I will never forget in my entire life. It could be that the similarities between Lisbon and Istanbul is one of the reasons why I liked the place so much. My office mates, Eduardo, João, Andela, Catarina, Antonio, thank you all guys for everything!

I would like to thank my former office mates in TU Delft; Waqas, Beatriz, and Alessandro. It was a really nice experience for me to share the same office with you guys, I really enjoyed the time we spent together! Thanks Waqas also for helping me about the PhD defense process. Special thanks go to the valuable PhD students in our group, Sven van Berkel and Nuri Marrewijk, for the translation of the abstract into Dutch. You literally saved me guys, thanks a lot! Thanks to my other fellow colleagues at THz Sensing group as well: Dr. Ioan E. Lager, Dr. Erio Gandini, Dr. Maria Alonso, Dr. Keninchi Karatsu, Shahab Dabironezare, Alejandro P. Laguna, Christina Y. Julia and Sebastian Hähnle.

The group had changed a lot of secretaries during the period of my PhD research. So, in chronological order, I would like to thank Jerney van Ooijen, Roniet Sharabi, Xandra Tober and Karen van Busschbach for their help and support.

I would like to thank Dr. Nurhan Turker Tokan and Dr. Fikret Tokan, first, for letting me know about the PhD vacancy here in TU Delft. The question was actually if I knew someone suitable for the position and, after suggesting myself as a candidate, everything happened so quickly that I found myself in Delft, in such a small place, trying to get used to Dutch winter and food. It was much easier with your help I should say. Thank you for the very nice time we had here in Delft.

I would like to thank my Turkish mate Ismail for being such a great friend since I came to Delft. As a person who had no interest in sports at all, you created a monster! We still should do a triathlon one day by the way. I also want to thank my other Turkish friends, Aslihan, Argun, Burak, Ugur, Reyhan, Tugce. It was a pleasure for me to meet you all guys! Thank you all for your help and support.

Finally, the most importantly, I would like to thank my family. My mother Sevda Yurdu-

seven, my father Demirhan Yurduseven, my brothers Okan Yurduseven and Onur Yurduseven. You always supported me no matter the physical distance. I dedicate this thesis to you for your unconditional love and support. Thank you for everything. I hope I made you proud!

A special mention to my brother, Okan Yurduseven. You always became an example for me with the way how you take your decisions in life, with such a strong determination any fearlessness. Thanks for the help and the support you gave to me from such a long distance! I know that your motivation and desire will lead you to continue in academia, and with the enthusiasm and the determination you have, I am sure that you will do great. Who knows maybe we meet in another conference again!

Dear reader, I would like to thank to you as well for being so patient and reading this until to the end. I wish all the best for you and I hope that the information provided in this thesis will be useful for your work.

Ozan Yurduseven, Delft, 18 June 2016

Contents

CHAPTER 1

Framework for the Thesis

Despite the recent discoveries in sub-mm band astronomy, according to the astronomers many sub-mm galaxies (SMGs) that are enshrouded by the cosmic dust are still hidden to state-of-the art technology. These dusty galaxies cannot be observed by optical telescopes whereas they can be detected by using terahertz astronomy (See App. A). Therefore, the need to develop advanced terahertz cameras with improved sensitivity and resolution capabilities arises.

1.1 Framework of This Thesis

This thesis work has been performed in the THz Sensing Group of TU Delft, where Applied Electromagnetic (EM) experts, astronomic Instrumentation specialists and astronomers collaborate to the goal of pushing the state of the art of EM based, space oriented instruments. The funding for this work was in the frame of ERC Grant number 278794 "Advanced Antenna Architecture for THz Sensing Instruments", AAATSI, with Prof. Andrea Neto as Prime Investigator. The goal of the project was to develop breakthrough antenna technology to revolutionize THz imaging.

The astronomic instrumentation component of the group is driven by official collaboration that the THz Sensing Group has with SRON (Netherlands Institute for Space Research). SRON is one of the few world power houses in sub-mm wave detector technology with its position set by the driving role in the development of the HIFI instrument for the Herschel observation satellite. In the last decade most of the research developed by SRON in the field of sub-mm wave space science has been driven by the prospected Japanese mission SPICA (Space Infra-Red Telescope for Cosmology and Astrophysics telescope). In fact it has been proposed that Europe would support an imaging spectrometer, SAFARI, and this is being developed under the leadership of SRON. SAFARI is an infrared camera with about $6,000$ pixels that can make real "photos" of the sky in three adjacent wavelength areas. Using a Fourier Transform Spectroscopy (FTS) detailed spectral information is obtained, allowing astronomers to determine the chemical composition of the observed celestial sources. One of the key requirements for SAFARI is that it should be a back- ground limited instrument. Its detectors should be so sensitive that their functioning does not introduce significant noise equivalent power (NEP) when compared to the fluctuations intrinsic to the incident fields. These fluctuations are thermally generated by the investigated celestial objects.

The THz Sensing group has been developing Imaging Arrays and Integrated Spectroscopic Sensors for a number of years in preparation for SAFARI or SAFARI like instruments. These investigations have been performed in the framework of a number of projects, which will be soon described, that present a few common requirements that are particularly challenging from the electromagnetic design point of view. The common requirements were:

- Arrays of detectors with extreme sensitivities (well beyond the state of the art)
- Large relative frequency bandwidth (well beyond the state of the art)

Given these clear needs, a task has been created within the AAATSI project to develop wide band array architectures for THz space born investigations. This task results in this

PhD thesis.

The first requirement (array sensitivity) has been tackled by our physicist colleagues, investing in Kinetic Inductance Detectors (KIDs) : these, to date, represent the most sensitive detectors suited to be deployed in large array configurations [1]. The "dark" NEPs of KIDs (that is the NEP that they achieve when not coupled to the quasi optical front end) have been sufficient for SPICA like missions since almost 10 years now, in [1] a dark NEP in the order of $3 \times 10^{-18}\ W/\sqrt{Hz}$ was shown. However, the "optical" NEP is the real parameter on which the detector sensitivity is evaluated. That is the NEP including a possible loss of efficiency due to electromagnetic coupling of radiation to the detector. The "optical" NEP enters defines the imaging speed that a background limited instrument can achieve.

The second requirement, large frequency bandwidth, becomes challenging when taken together with the requirement of high coupling efficiency. The state of the art of sub-mm wave front ends with high efficiency is represented by the twin slot [2] of a bandwidth of about 10% was reported. Evolved versions of the twin slot have been also proposed in [3], [4]. Although these antennas were reported as being able to operate within larger bandwidths, they suffer from the quality of the beam patterns. With this work, possibly the state of the art has been pushed one notch higher, with high efficient sub-mm wave quasi optical front ends exceeding one octave, (66%).

The availability of octave bandwidth efficient front ends should be an eye opener for future infrared mission planners. In fact the main parameters planners looked at are angular resolution and imaging speed. The resolution depends only from the focusing capacity of the telescope, which to a large degree is a mechanical requirement associated to its size. However, the imaging speed that a background limited instrument can achieve is directly proportional to the (bandwidth $\times$ efficiency) of the front end. Consequently the portion of sky that can be imaged in the life time of the mission largely depends on this bandwidth $\times$ efficiency product. Moreover it should be noted that even if an octave has been taken as a driver for the present thesis, no show stoppers have emerged and it is apparent that if astronomers found it necessary, arrays with much larger frequency bandwidth would be easily designed with only limited toll on the achieved efficiency.

1.2 Simultaneous Projects

The projects that have been running, within the THz Sensing Group, simultaneously to the present thesis are SPACEKIDs (European Commission FP7 [5] project), A-MKID (European Research Council project-ERC Starting Grant [6]) and DESHIMA (NWO VIDI

project [7]). These projects constitute steps toward a higher Technology Readiness Level (TRL) for the KID technology, mastered for a long time by Dr. Jochem Baselmans at SRON and more recently also at TU Delft. All these projects served slightly different observatory driven requirements. SPACEKIDs addressed the use of KID technology in satellites for deep space or earth observations. A-MKID and DESHIMA are instead instruments for ground space telescopes.

1.2.1 Kinetic Inductance Detectors

New generation THz space instruments require arrays of thousands of detectors to have a large Field of View (FoV). Despite advances in high sensitivity detectors, [8], [9], array scaling for conventional technologies is strongly limited by the difficulty in reading out simultaneously many pixels (i.e. multiplexing). Kinetic Inductance Detector (KID) arrays have solved the multiplexing challenge maintaining the high sensitivity associated to superconducting detection technologies. To this regard one can note that the A-MKID project [10] showed arrays with about 25k elements based on KID technology.

KIDs [11], [12] can be used to relate the intensity of the incoming THz radiation to the resonance frequency of a microwave resonator. The incoming THz radiation, after being captured by an antenna, is channeled in a transmission line. This transmission line, besides supporting the propagation of THz signals is also a portion of a GHz frequency superconducting resonator whose propagation properties are dependent on the number of Cooper pairs per unit of volume. At low temperatures, most of the electrons are attracted to each other to bound in Cooper pairs in a superconductor. When there is no field applied, these pairs have zero center of mass momentum. In the presence of an incoming field, the pairs get accelerated both in the same direction since they are both charged, yet the center of mass momentum is no longer zero. As a result, the incoming radiation, depending on its spectral content, may break some of the Cooper pairs into quasi-particles. To break the Cooper pairs, the incoming radiation must have an energy that is greater than the binding energy. For each material there is a different energy gap to break a pair.
The binding energy is twice as higher than the energy gap of a superconductor, Δ, and is in the order of $3.52k_BT_c$ for $T << T_c$ where T_c is the critical temperature of the superconductor that is required for the electrons to be bound in a Cooper pair. KIDs measure changes in the quasi-particle population that occur within the volume of a superconducting film when an EM wave of frequency higher than the threshold frequency, $f = 2\Delta/h$, is absorbed. Fig. 1.1 clearly shows the presence of the threshold frequency, being about 320 GHz for a superconductor which is made of Tantalum [13]. For Aluminium (Al) this

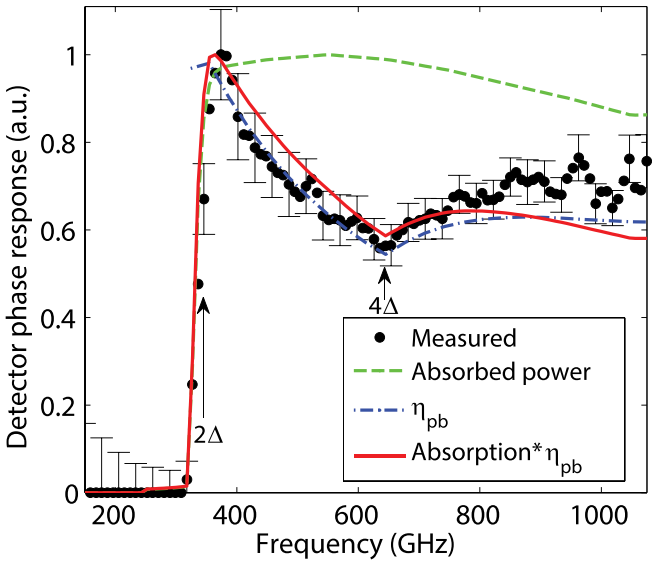

Figure 1.1: Power absorption of a Tantalum superconducting transmission line clearly showing the threshold frequency required for the absorption [13].

frequency is a bit lower, being about 90 GHz [14], whereas it becomes higher for Niobium (Nb), about 670 GHz [15]. As a result of the increment in the quasi-particle population, there is an alteration in the complex impedance of the film related with the increase of the kinetic inductance, L_k, and the loss.

In practice, the variation L_k is so small that, in order to be detected, the film must be fabricated in a microwave resonance circuit with a very high quality factor (Q factor). To create high Q microwave resonators from superconducting films, usually distributed half-wave or quarter wave resonators based on coplanar-waveguide (CPW) structures are used. The resonator is then coupled to a readout line. Figure 1.2 shows a picture of the KID resonator coupled to a planar antenna (a double slot in this case) together with its readout line.

At the resonance frequency, the resonator would normally provides a sharp transmission null in the readout line, readable in the S_{21} characteristic. The THz signal incidence can be observed as a shift of the null in the S_{21} parameter, with the dip moving to lower frequencies, becoming broader and shallower.

The anticipated potential for multiplexing of KIDs relies on fabricating more resonators with slightly different lengths so they can be read out with a train of microwave frequencies. Each of these resonators can be coupled to different antennas or absorbers to form multi-

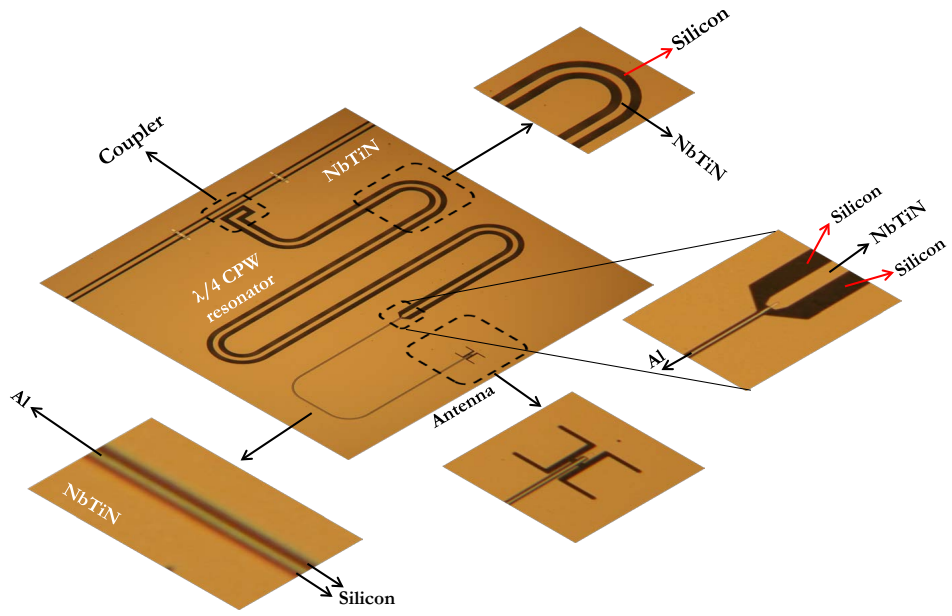

Figure 1.2: Picture of an antenna coupled $\lambda/4$ KID resonator (Single-pixel).

pixel imaging cameras with high sensitivity. Introducing an external coupling system (e.g. silicon lenses) [16] improves the coupling efficiency to a telescope. In this thesis planar radiators, double slot or leaky lens based antennas, will be integrated with the KIDs in order to achieve antenna-coupled KID cameras with thousands of pixels. A schematic of an antenna-coupled KID array that is located at the focus of the silicon lenses is highlighted in Fig. 1.3.

In realistic spaceborne applications, the focal plane of a telescope would host a lens array in which the incoming THz radiation is coupled. Since the number of pixels is anticipated to be very high, the focal distance to diameter (F/D or $f_{\#}$) ratio of the telescope will also be very high to avoid the degradation of the off-focus beams [17].

1.2.2 DESHIMA Project (NWO Vidi Grant 639.042.423)

Normal cameras can produce only 2D images of the sky. This is how the sky appears to the human eye, and it implies that the third dimension, distance, along the line of sight is lost. To compensate for the lack of the third dimension, the optical information intensity needs to be complemented with another type of information: its spectral content distribution.

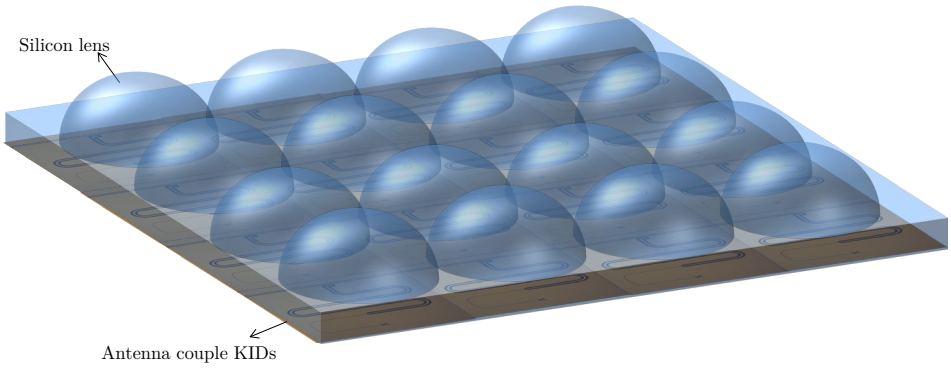

Figure 1.3: Schematic of an antenna based KID array coupled to the silicon lenses.

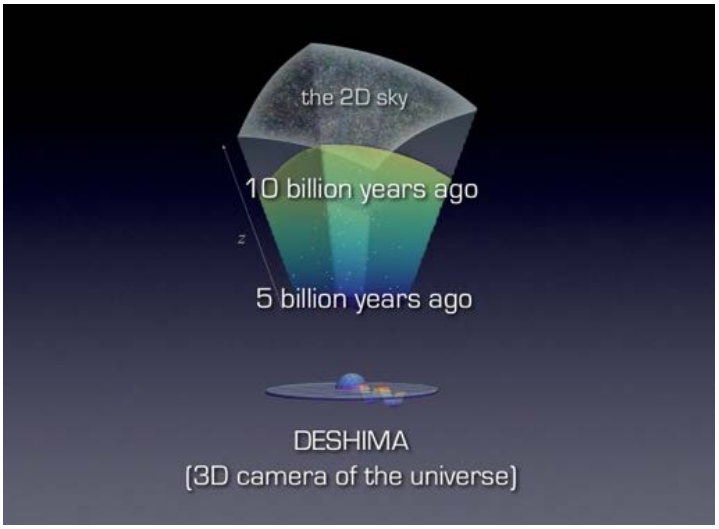

Figure 1.4: DESHIMA instrument is planned to project also the 3^{rd} dimension corresponding the distance, and therefore the age of the SMGs [18].

It is well known that certain molecules radiate and absorb at predefined frequencies: for instance still CO_2 molecules resonate at 1.9 THz. However, when molecules move away from an observer, the observed frequency of this radiation is shifted to lower values, due to the well known Doppler effect. Physicists call this as redshift. This means that observing a certain spectral line in different angular directions, may provide information about the speed at which the universe is expanding in those directions.

Within the THz Sensing Group an instrument dedicated to such type of observations is

being developed by Dr. Akira Endo and Ing. David Thoen. DESHIMA (Deep Spectroscopic High-redshift Mapper) is a novel instrument aiming at discovering tens of thousands of sub-mm wave galaxies (SMGs) and their distances [18]. As a result the instrument will be able to create a 3D map of the SMGs which could provide an enormous amount of information to astronomers about the formation and the evaluation of stars and galaxies. Beyond that, such an observation might even enable to observe giant webs and strings made of SMGs, which trace dark matter distribution. The instrument is mainly developed to perform the measurement of dusty redshift galaxies (also called as sub-mm galaxies) [19]. Standard application of DESHIMA instrument can be listed as [18]:

- Redshift measurements of high-redshift galaxies
- Line survey of distant galaxies
- Sensitive spectroscopy starbust galaxies
- Multi-line spectral mapping of galactic star forming

Technically, DESHIMA is an instrument which targets to cover the entire frequency band from 326 GHz to 905 GHz. An integrated superconductor filterbank made of NbTiN/Al hybrid MKID integrated chip is used in the instrument. The on-chip filterbank illustrated in Fig. 1.5 is the key technology of the DESHIMA instrument. It distinguishes the incoming radiation by their unique wavelength and distributes them into the detectors which have relevant frequency. This is achieved by using superconductor resonators as narrow pass band filters. The detectors located at the output of the filters are known as Kinetic Inductance Detectors (KIDs) and they are also superconductor resonators. With respect to the filter banks, the detector filters actually absorb the sub-mm wave signal, which leads to a quantification of the pertinent spectral component. Only one antenna captures all the sub-mm wave signals, and it has to be integrated with filters and detectors. The antenna will have to operate within the entire large bandwidth, which in relative terms is roughly in $1:3$. This is one of the most challenging and important aspects of the instrument.

1.2.3 A-MKID Project

As anticipated large imaging arrays with high sensitivity as well as large FoV for high spatial resolution will be needed in future imaging instruments.

Within the THz Sensing Group such imagers have been developed by Dr. Jochem Baselmans. The development of the A-MKID instrument is in fact a collaboration between TU

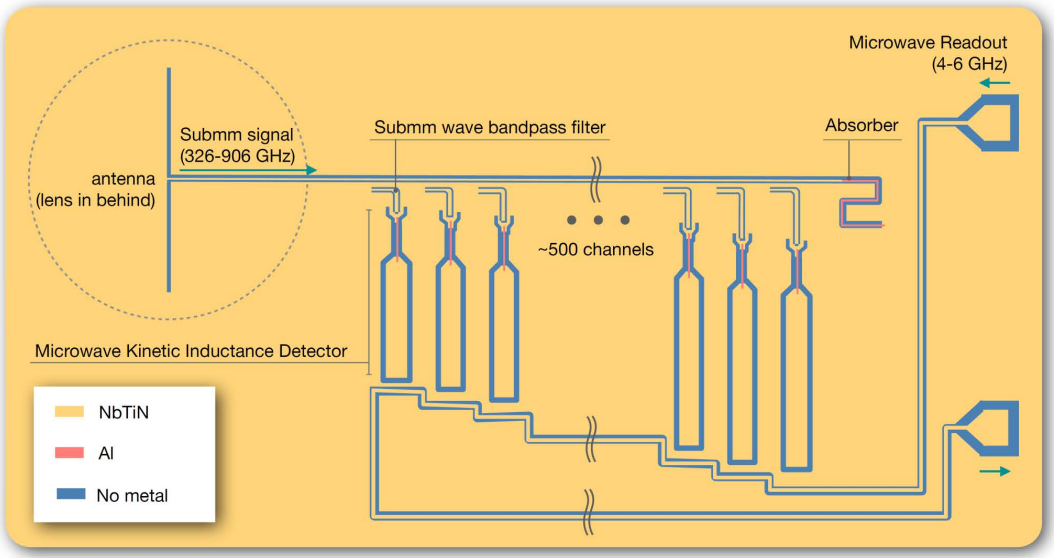

Figure 1.5: Illustration of the on-chip filter bank designed for DESHIMA [18].

Delft, SRON and the Max Planck Institute for Radio Astronomy. The instrument will be deployed at the APEX telescope, in Chile. It will be based on the use of large-format antenna coupled MKID arrays covering, with two separate arrays, two atmospheric windows centered at 350 GHz and 850 GHz. The instantaneous field of view on the sky is 15×15 degrees. Having $\approx$ 16k pixels for the high frequency array and $\approx$ 3500 pixels for the low frequency array, the A-MKID instrument is planned to be the largest submillimeter-wave camera on any telescope ever. The large number of pixels is essential in taking rapid snapshots with high angular resolution and high dynamic range. Among the scopes of A-MKID will be the growth of the cosmic web under the influence of dark matter, the evolution of galaxies throughout the cosmic history, and how dense molecular clouds form new stars, while interacting with larger structures on the galactic scale.

1.2.4 SPACEKIDs Project (FP7 Grant 313320)

The purpose of the SPACEKIDS project, just finished as this document is being redacted, was to develop and demonstrate the capabilities and the suitability of Kinetic Inductance Detectors for use in future space science and Earth observing missions working at far infrared to millimeter wavelengths. Within the THz Sensing Group the key persons were Dr. Nuria Llombart, Dr. Jochem Baselmans and Dr. Juan Bueno. Besides the TS Group

Table 1.1: SAFARI Instrument frequency bands

SAFARI Bands			
Parameter	Band 2	Band 1	Band 0
Band center (μm)	47	85	160
Wavelength range (μm)	34-60	60-110	110-210

FIR Instrument

the project brought together world-leading groups from several European countries, to "*consolidate and extend Europes expertise and capabilities in state-of-the-art far infrared detectors and instrumentation*".

The real goal of the project was to prepare an instrument for the anticipated Japanese SPace Infrared telescope for Cosmology and Astrophysics (SPICA) mission. This satellite, having a large cold telescope cooled to only 6 K, will provide a unique environment where instruments are limited only by the cosmic background itself. A consortium of European and Canadian institutes has been established to design and implement the SpicA FAR-infrared Instrument (SAFARI) an imaging spectrometer designed to fully exploit this extremely low far infrared background environment provided by the SPICA observatory. SAFARI will be an imaging Fourier Transform Spectrometer (FTS) designed to provide continuous coverage in photometry and spectroscopy from 34 to 210 µm. The instrument is anticipated to be divided into three bands as highlighted in Table 1.1. In order to cover the full 34 to 210 µm wavelength range the SAFARI detector system utilizes three large-format detector arrays, [20], [21].

In this thesis, and in the framework of the SPACEKIDS project, we considered an instrument envisioned to operate over an octave bandwidth, from 1.4 to 2.7 THz (Band 0), and coupled to a telescope with $F/D > 10$ with tight feed samplings ($\leq \lambda_0 F/D$).

1.3 Thesis Goal

The objectives of the thesis are given below:

- **Integrated single lens antennas: Multiple feed per lens scenario**

  Part I of this thesis focuses on the design of the lens antennas using a multiple feeds per lens scenario. The aim of the study is to design integrated lens antennas to

achieve frequency stable radiation characteristics to achieve efficient reflector illumination with a wideband operation, typically more than one octave. Due to its wideband characteristics, the connected array of leaky slot antennas have been used as lens feeder. The design is aiming at the Deshima project as a possible application.

Two different approaches have been implemented to achieve frequency independent reflector feeder beams: A coherently fed connected array design with a traditional extended hemi-spherical lens and a double shell lens design integrated into an array where each source element is associated to one beam.

- **Integrated focal plane array antennas: Single feed per lens scenario**

Part II of the thesis focuses on a single feed per lens scenario. Integrated lens array designs aiming at tightly packed focal plane array applications are presented for two specific scenarios: Ground based observation and Space based observation. Starting with an introduction chapter providing a brief discussion on the imaging speed for tightly spaced focal plane arrays, three antenna designs are presented for SPACEKIDs, A-MKID and SAFARI projects. Two antenna concepts have been used in the designs depending on the scenario: A double slot based design for Earth observation, and a dual polarized wideband leaky lens based design for SAFARI-like space observation scenario.

1.4 Methodology

In Part I, where we focus on single lens antennas with multiple feeds, the lens dimensions are typically large in terms of the wavelength. Therefore, the lens surface can be assumed to be in the far-field region. Using a full-wave 3D electromagnetic (EM) solver to simulate the entire lens structure is computationally too demanding or even unfeasible. Moreover, many of such simulations are needed whenever an optimization of the lens and the feeds is required. For this reason, an in-house Physical Optics (PO) tool has been used in the lens analysis in order to perform fast simulations with acceptable accuracy. The details of the tool can be found in [22]. It is important to note that the Fresnel transmission and reflection coefficients do not describe well the radiation when the incident field impinges on the lens interface with angled close or larger than the critical angle. However, in Part I we consider enhanced leaky slots as antenna elements used to feed the lens. These antenna feeds provide directive beams [23], so that mainly the upper part of the lens is illuminated,

whereas low-intensity fields impinge close to total reflection angle.

Part II of this thesis, on the other hand, deals mostly with scenarios with a single feed per lens, which typically require relatively small lens dimensions in terms of the wavelength. It is well know that PO methods cannot provide enough accuracy for structures that have electrically small dimensions and a more detailed approach should be implemented, e.g. in [24], [25]. For this reason, we use a 3D full-wave simulator (CST Microwave Studio [26]) to characterize small lenses in terms of the their radiation patterns and aperture efficiencies.

1.5 Outline of the Thesis

The thesis is organized in eight chapters of which address several aspects of the analysis, the design and the experimental validation the proposed antenna concepts. A brief summary about the contents of each chapter is as follows:

Part I studies integrated single lens & multiple feed antenna solutions to achieve efficient reflector illumination within a wide operational bandwidth.

- **Chapter 2** [1] focuses on the characterization of a broadband array of leaky-wave slots located in the focal plane of a dielectric lens by means of performing a parametric analysis, such as varying the extension length and the off-axis distance. The array is able to generate several independent beams to be used for imaging applications within a large bandwidth, namely over a band exceeding 1 : 4. The main goal of the chapter is to provide some useful design guidelines for the connected array of leaky slot integrated lens antennas.

- **Chapter 3** [2] presents the design of a coherently fed leaky lens antenna specifically aiming at the DESHIMA project. Thanks to the coherent feeding concept the design is able to generate frequency-independent beams for efficient reflector illumination with a stable reflector efficiency for a bandwidth exceeding 1 : 3. Although the chapter focuses on a LF prototype, the design can be easily scaled to the DESHIMA band.

[1] Part of the content has been reported in [J2] (see p. 199)
[2] The content has been reported in [J3] (see p. 199)

- **Chapter 4** [3] provides an alternative design with respect to the concept presented in Chapter 4 to achieve frequency independent beams over a wide bandwidth. In this preliminary study, we present a design based on the integration of a connected array of leaky slot antenna to a double shell lens which is able to generate frequency stable beams within a large bandwidth, typically about one octave.

Part II focuses on the integrated lens antenna designs aiming at a single feed per lens scenario to be used for tightly sampled Focal Plane Array (FPA) applications.

- **Chapter 5** focuses on the scenario of antenna coupled KIDs. It provides a brief information on the direct detection FPAs and investigates the imaging speed for Earth and space based astronomical applications.

- **Chapter 6** discusses the double slot based antenna solutions for SPACEKIDs and A-MKID projects. Taking into account the antenna material stratification (e.g. the kinetic inductance and thickness of the ground plane), we perform a parametric study to provide some design rules for sub-mm double slot antennas coupled to MKIDs and provide the dedicated designs. Beam patterns and antenna coupling efficiency measurements provided by SRON are also shown in the chapter.

- **Chapter 7** [4] proposes a wide-band dual-polarized leaky lens antenna concept that is suitable for tightly packed FPA applications with large $f_{\#}$ reflectors, specifically for SAFARI-like scenario. The proposed design is able to operate within a $1:5$ bandwidth and provides superior antenna aperture efficiencies compared to state-of-the art reflector feeds. Experimental validation of the radiation patterns and antenna optical efficiency obtained by SRON at sub-mm band are included in the chapter.

- **Chapter 8** provides concluding remarks about the results achieved in the thesis and the planned future work.

[3] This work has been carried out during the six months research activity within the framework of NEWFOCUS Grant [27] at Instituto de Telecomunicações in Instituto Superior Técnico (IST), Lisbon, Portugal. The author thanks to Prof. Dr. Carlos Fernandes and Prof. Dr. Jorge Costa for their hospitality and the collaboration during the visit.

[4] Part of the content has been reported in [J1] (see p. 199)

Part I

Single Lens & Multiple Feeds

CHAPTER 2

Parametric Analysis of Extended Hemispherical Dielectric Lenses Fed by A Broadband Connected Array of Leaky slots

In this chapter, we examine the properties of a broadband array of leaky-wave slots located in the focal plane of a dielectric lens, to generate several independent beams for imaging applications. The array performance is investigated over a band exceeding $1:4$. *Parameter analyses, varying the extension length and the off-axis distance, are performed over the wide frequency range and provide useful guidelines for the lens design. A spectral domain approach is used to characterize the field generated by the array, while an accelerated physical optics method is employed for the analysis of the lens. Full-wave electromagnetic simulations performed with CST Microwave Studio are used for the validation of the combined analysis methods. Tapering of the slots can be introduced to reduce both the mutual coupling between the array elements and the cross-polarization levels.*

2.1 Introduction

Dielectric lenses fed by focal plane arrays have been widely proposed in the mm- and submm-wave frequency bands for imaging applications. These include medical imaging [28], non-destructive testing, space observation [1, 29], spectroscopy and security screening [30]. Most of these applications demand high spatial and range resolution of the images, as well as fast acquisition time. To fulfill such requirements, the focal plane arrays need to comprise a large number of elements and be able to operate over broad bandwidths. Moreover, the systems typically require high sensitivity to detect weak signals. Therefore, it is crucial to maintain stable antenna performance over the entire wide bandwidth of operation, since the antenna efficiency has a direct impact on the system signal-to-noise ratio and overall sensitivity.

The most widely used antenna element for feeding dielectric lenses is the double slot presented in [2]. This antenna is planar and simple to design, and generates a highly directive pattern so that only the most efficient part of the lens, its central part, is illuminated. On the contrary, non-directive feeds yield high losses due to reflection at the dielectric-air interface [31]. Despite its advantageous properties, the double slot is a resonant antenna and achieves good efficiency only over a narrow band.

Improved performance is achieved by the enhanced leaky-wave slot antenna presented in [23, 32]. This antenna was shown to achieve good matching and efficient illumination of the lens over a multi-octave bandwidth. Recently, some other attempts to design wideband antenna elements in focal plane arrays were made in [3, 33], by using butterfly-like double slots and spiral elements. However, these designs are limited to about one octave bandwidth.

In this chapter, we investigate the properties of a broadband connected array of leaky-wave slots located in the focal plane of a dielectric lens, as the one shown in Fig. 2.1. This array was recently in [34]. The structure exhibits high efficiency over a band exceeding $1:4$ and can generate several independent beams for imaging applications. In [34] the array was characterized in the presence of a semi-infinite dielectric medium. Here instead we asses the performance of the array when a focusing lens is introduced and we direct our attention for the first time to the optimal design of the lens. This chapter presents a number of parametric analyses similar to the ones in [35,36], obtained by varying the extension length and the off-axis distance over the frequency band of interest. The aim of the investigation is to provide useful guidelines for the design of the extended hemispherical lens (EHL), when fed by the connected array of leaky-wave slots.

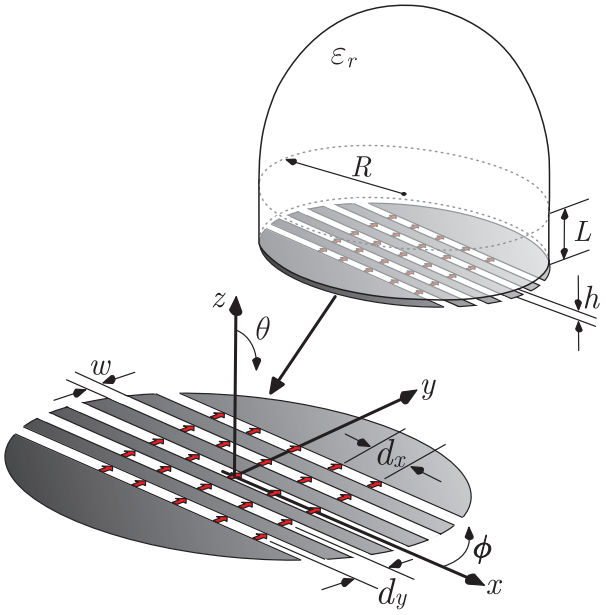

Figure 2.1: Connected array of leaky wave-slots as focal plane array of dielectric lens, with reference system and geometrical parameters.

For the combined analysis of the array and lens, we employ a quasi-analytical method for the representation of the focal plane array [34] and an ad-hoc accelerated physical optics (PO) method for the analysis of the lens. Such method is based on a quadrature rule for numerical integration, which is an extension of the work presented in [37]. Results obtained with CST Microwave Studio [26] are shown for the validation of the combined analysis methods.

Finally, considerations on the effects of tapering the slots are reported. Simulations of tapered slots show a reduced mutual coupling, which for imaging arrays is directly associated with dissipation losses; also, tapered slots yield lower cross-polarization when compared to slots with uniform width.

2.2 Lens Design

The lens and the feed array are shown in Fig. 2.1, together with the characteristic parameters of the structure. We consider an extended hemispherical lens with extension length

L, radius R and relative permittivity ϵ_r. The array plane is placed at distance h from the dielectric lens, where h is a small fraction of the wavelength at the highest frequency of operation. This is a key parameter to ensure highly-directive radiation of the feeds for efficient illumination of the lens [23]. The array consists of a finite number of slots of width w spaced by d_y, each fed in a finite number of points separated by distance d_x. The distance between feeds is considered to be large enough to guarantee low levels of mutual coupling between the elements. Indeed, mutual coupling in imaging arrays is associated with dissipation losses [34]. However, configurations in which the elements are closer and coherently excited can be exploited, as in [38]. All the numerical results presented in the remainder of this paper are obtained as follows:

- The array of feeds is characterized using the quasi-analytical approach described in [34]. This method provides the fields radiated by the array inside the dielectric medium, which is assumed to be a semi-infinite half space.

- These fields are then used to evaluate the equivalent currents on the dielectric-air interface of the lens, as described in [22]. The lens interface is assumed to be in the far-field region of each element of the array.

- Subsequently, the field radiated outside the lens is evaluated with a method based on physical optics (PO). The expression of such field is given in [22] in the form of a radiation integral. This integral is calculated with the numerically efficient method which is briefly described in [22]. Interested readers are suggested to read [39], [40], [41] and [42] for the detailed information on the methodology.

Fig. 2.2 shows the radiation patterns of the central element of a 3×3 array into a silicon half space ($\epsilon_r = 12$), when one element is active and all the other elements are terminated. The geometrical parameters are $w = \lambda_0/30$, $h = \lambda_0/50$, and the periods are $d_x = d_y = \lambda_0/3$, where λ_0 is the free-space wavelength at the lowest frequency f_0. It can be observed that the patterns peak at about 17^0 at $2f_0$ and $4f_0$, which is a peculiarity of the enhanced leaky-wave slot [23]. This effect is less intense at f_0, due to the coupling with neighboring elements, which re-radiate in phase increasing the broadside directivity. It should be noted that, although larger arrays are considered in the remainder of the chapter, the field radiated by each feed can be approximated as if this feed was the central element of a 3×3 array. This is because the mutual coupling with elements farther away is negligible (≤ -40 dB) [34].

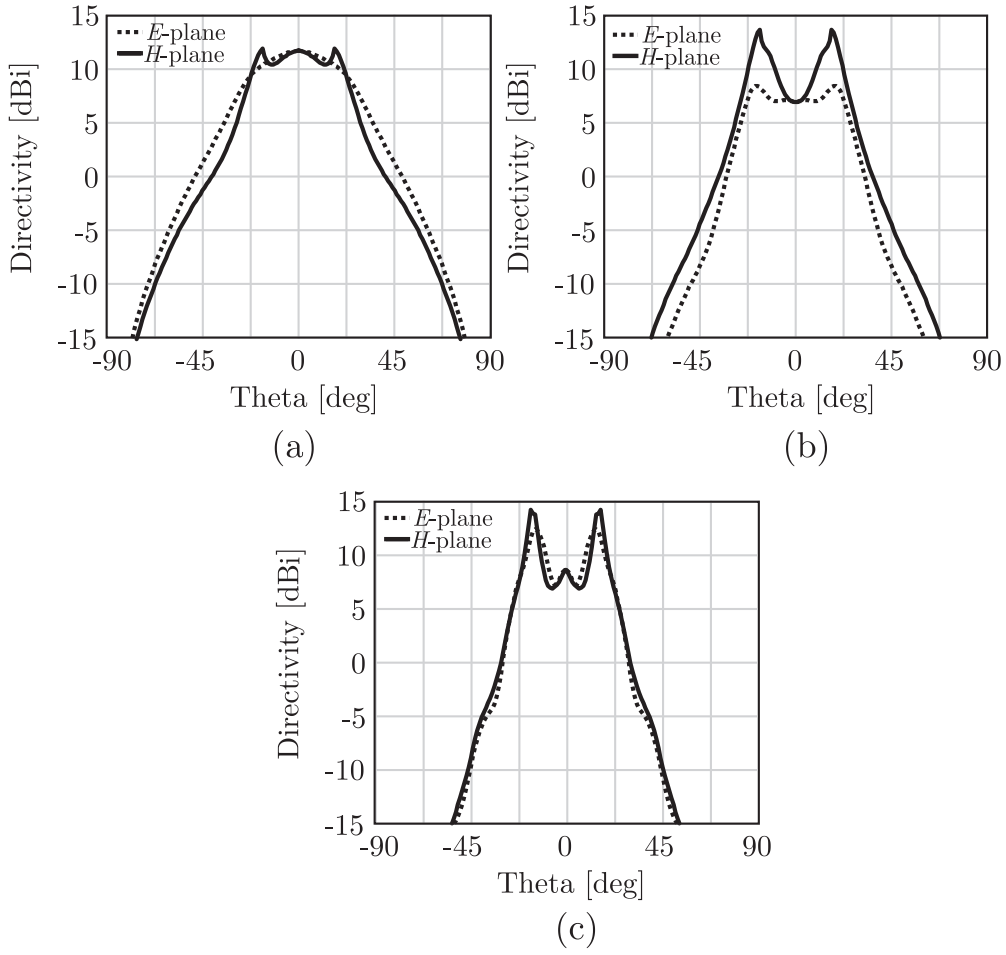

Figure 2.2: E- and H-plane embedded patterns of a leaky-wave slot into silicon at (a) f_0, (b) $2f_0$, (c) $4f_0$.

The primary patterns are then used to evaluate the fields impinging on the dielectric-air interface of the lens, which is assumed to be in the far-field region of each element of the array. Subsequently, in order to evaluate the radiation characteristics in terms of secondary patterns, we employ a method based on geometrical optics (GO) / physical optics (PO), as in [2]. The details of such approach and the description of the algorithm adopted for the efficient evaluation of the PO radiation integral are reported in [22].

2.2.1 Directivity

For the investigations presented in the following, we consider a lens diameter of $25.3\lambda_0$ at the highest frequency ($4f_0$). The displacement of the feed along x (or y) can be related

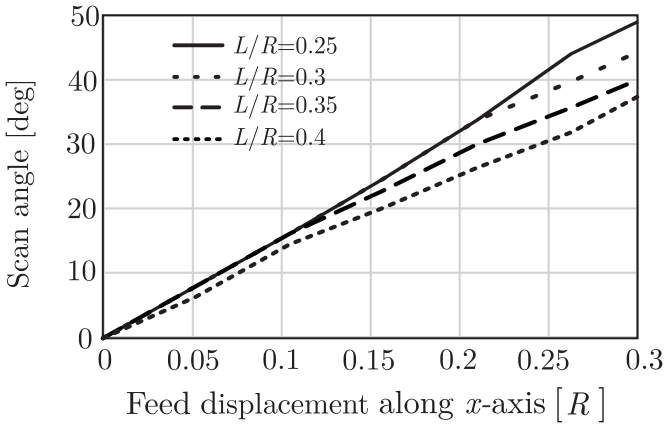

Figure 2.3: Scan angle as a function of the feed displacement along x normalized to the lens radius, for a silicon lens with different extension lengths.

to the scan angle of the secondary pattern outside the lens. The scan angle is reported in Fig. 2.3 as a function of the lateral displacement, for a silicon lens with different extension lengths.

In Fig. 2.4, the maximum directivity is mapped for varying values of the extension length and the off-axis distance, both normalized to the lens radius. The directivity is reported for displacement along x and y and for $4f_0$, $2f_0$ and f_0. It is of interest to note that small variations of directivity ($\leq$ 4 dB) for the element on axis are obtained in the parametric range of values L/R under investigation, even for large lenses ($4f_0$). Much larger variations (16 dB) where observed in [2] for the double-slot antennas feeding a $24\lambda_0$ diameter lens. The reason of the more stable directivity is that the feed considered here is more directive, therefore variations of the extension length have less effect in terms of phase aberration on the lens. Such characteristic is at the cost of a lower maximum directivity achieved by the lens, since the directive pattern in the lens yields a lower lens aperture efficiency.

The directivity contour map in Fig. 2.4 can be used to select the optimal extension length for a specific application. For example, $L/R = 0.35$ maximizes the directivty at broadside at the higher frequencies, while lower values of L/R can be selected to minimize the directivity variation over a certain scan range. Although useful, the directivity gives only information on the phase error due to the lens shape for the specific feed considered for the illumination. For a more thorough analysis, the principal loss factors need to be investigated.

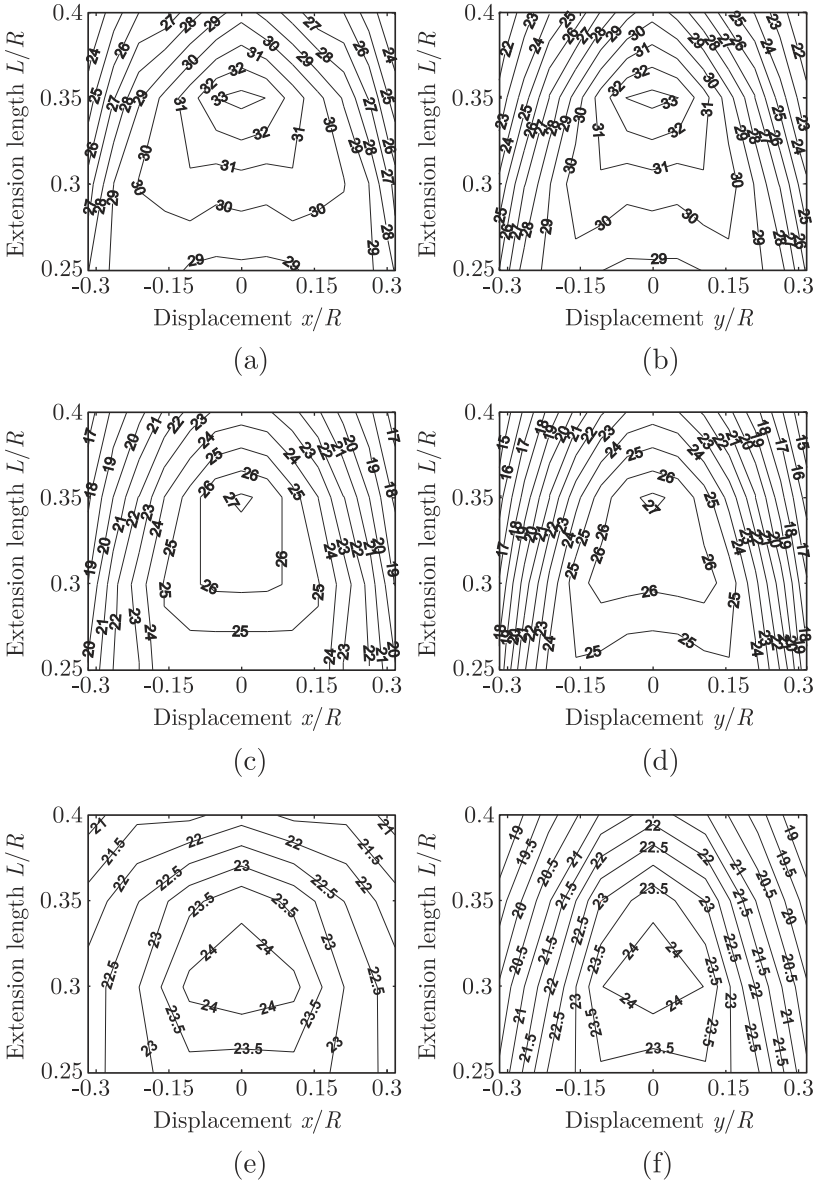

Figure 2.4: Directivity (in dBi) as a function of extension length and lateral displacement: (a), (b) $4f_0$, displacement along x and y, respectively; (c), (d) $2f_0$, displacement along x and y; (e), (f) f_0, displacement along x and y.

2.2.2 Losses

Reflections at Dielectric-Air Interface

For high permittivity materials, such as silicon, internal reflections constitute a significant portion of the total loss. Such losses are shown in Fig. 2.5 as a function of the displacement

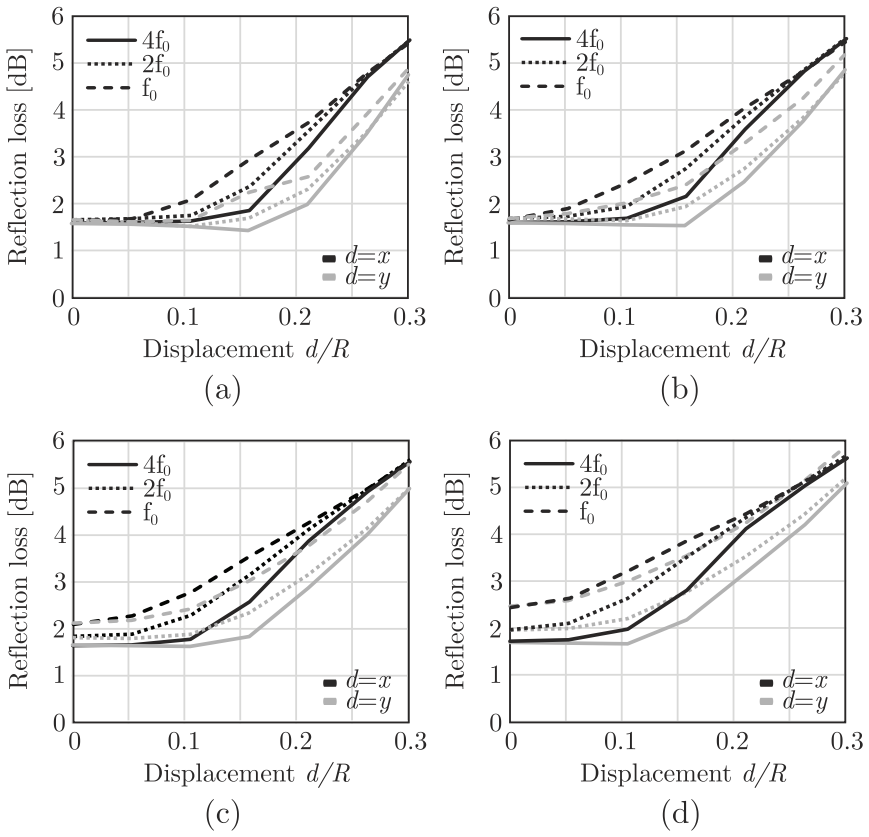

Figure 2.5: Losses for reflection at the dielectric-air interface versus x- and y-displacement and for different frequencies and L/R values: (a) $L/R = 0.25$, (b) $L/R = 0.3$, (c) $L/R = 0.35$, (d) $L/R = 0.4$.

along x and y, for three frequencies and different values of L/R. The reflection increases rapidly with the off-axis distance of the feed, since the lateral part of the lens is increasingly illuminated augmenting the amount of power that undergoes total reflection. When the frequency increases, the pattern radiated by the feed becomes more directive, resulting in a slightly higher radiation efficiency. Also lower L/R implies less reflection at the interface, since the lens surface tends to become hemispherical, so that the incident rays emanating from the feed have directions of propagation closer to the normal to the interface.

Mismatch Loss

The reflection coefficient of one element of the leaky-wave slot array as a function of the frequency is shown in Fig. 2.6, assuming a 80 Ω feeding transmission line, and for different inter-element spacing. Reducing the array period has an effect on the input impedance

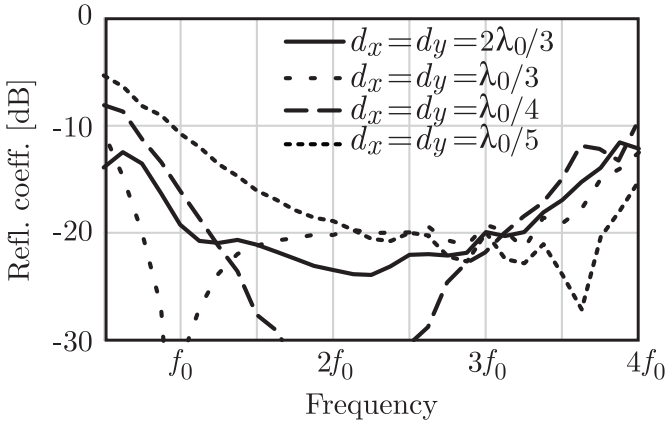

Figure 2.6: Reflection coefficient of one element of the connected array of leaky-wave slots, for different array periods.

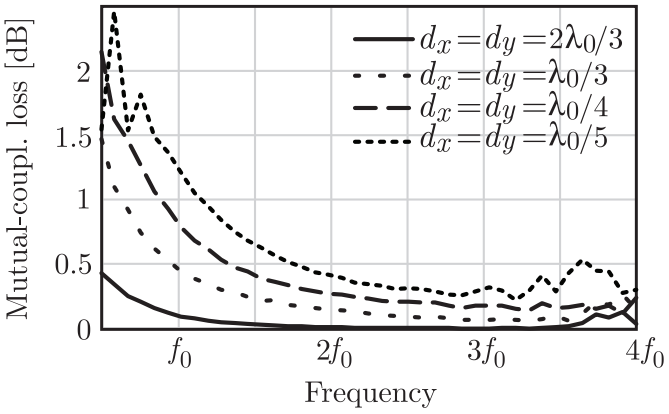

Figure 2.7: Loss due to mutual coupling as a function of the frequency, for different array periods.

of one element, which 'sees' different loadings in its surrounding. However, as previously demonstrated in [23, 32] for a single slot, also in array configuration the leaky-wave slot exhibits very wideband impedance matching, exceeding 1 : 4. Therefore, losses due to mismatch have only a minor impact on the overall efficiency.

Mutual Coupling

Due to their intrinsic nature, connected arrays are characterized by high levels of mutual coupling. While this coupling is beneficial for phased array applications, it constitutes a

loss factor in an imaging array, where each element operates independently. For the widely adopted solution based on the double-slot element, mutual coupling is negligible. However, the inter-element spacing is limited by the physical size of the slots to about $0.35\lambda_0$ at the frequency of operation. This limit does not apply to connected arrays of leaky-wave slots. In fact, one of the advantages of the connected slots with respect to the typically employed antenna elements is the possibility of having very small inter-element distances in such a way to have a closely packed focal plane array for higher spatial resolution of the imaging systems. The possibility of reducing the inter-element spacing is at the cost of non-negligible mutual coupling between elements, as already pointed out in [34]. Figure 2.7 shows the loss in dB for different inter-element distances d_x, d_y. The mutual-coupling loss is lower than 0.5 dB at f_0, when the spacing is 0.3 λ_0.

2.2.3 Gain

The loss factors listed in the previous section can now be included in the calculation of the radiation patterns, to obtain gain plots rather than directivity that have been obtained by using PO approach. Note that the gain defined hereafter does not include ohmic and dielectric losses. However, these are typically known for the specific materials selected for the manufacturing and can be easily included at a later stage for the estimation of the total gain.

To estimate the quality of the patterns radiated by the elements on- and off-axis and their dependence on the extension length and the frequency, Fig. 2.8 reports a set of co-polar gain beam patterns in u-v coordinates, with $u = \sin\theta\cos\phi$ and $v = \sin\theta\sin\phi$. These represent the secondary beam patterns for the element on-axis, the ones displaced by up to three periods along x and y, and the ones displaced by up to two periods along the diagonal (periods are $d_x = d_y = \lambda_0/3$). The position of the maximum, the -3 dB and the -10 dB contours of the beams are shown for each beam, as well as the value of the maximum gain.

Two extension lengths have been selected as $L/R = 0.25$ for Figs. 2.8(a),(b),(c) and $L/R = 0.35$ for Figs. 2.8(d),(e),(f). Restricting the analysis to only two periods displacement along x and y and one period along the diagonal, it can be noted that the solution based on $L/R = 0.25$ exhibits a smaller variation in terms of maximum gain of each beam. Also the -10 dB beam contours are quite circularly symmetric in shape. Larger pattern degradation is observed for the elements displaced by more than $0.25R$ from the lens axis, as expected from the previous analysis on the reflection losses (see Fig. 2.5). In the second case, for which the extension length is $L/R = 0.35$, higher gain is obtained for the on-axis

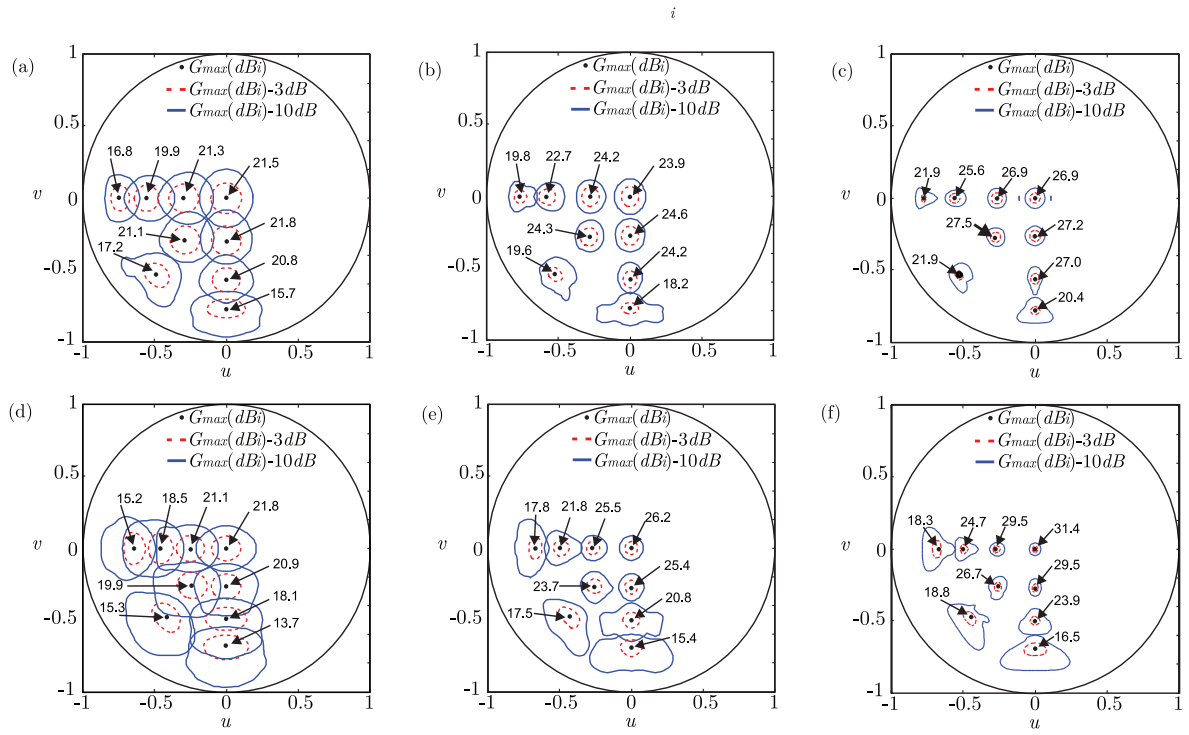

Figure 2.8: Co-polar gain patterns in the u-v coordinates: the position and the value of the maximum, the 3 dB and the 10 dB contours of the secondary beams are shown for the elements in $(x = 0, y = 0)$, $(x = d_x, y = 0)$, $(x = 2d_x, y = 0)$, $(x = 3d_x, y = 0)$, $(x = 0, y = d_y)$, $(x = 0, y = 2d_y)$, $(x = 0, y = 3d_y)$, $(x = d_x, y = d_y)$ and $(x = 2d_x, y = 2d_y)$, with $d_x = d_y = \lambda_0/3$; (a), (b), (c) are pertaining to f_0, $2f_0$ and $4f_0$, respectively, for $L/R = 0.25$; (d), (e), (f) are pertaining to f_0, $2f_0$ and $4f_0$, respectively, for $L/R = 0.35$.

element over the entire frequency range of investigation. This is because such a value of the extension length yields a better approximation of the ideal elliptical lens by the hyper-hemispherical synthesized shape (See Fig. 2.9). While broadside gain is maximized, performance is worse in terms of scan loss and circularity of the 10 dBi beam contours.

The co-polar and cross-polar normalized patterns are reported in Fig. 2.10, for feed displacements of $(x = 2d_x, y = 0)$, $(x = 0, y = 2d_y)$ and $(x = d_x, y = d_y)$, and at the frequencies of f_0, $2f_0$ and $4f_0$. The cross-polar component is normalized to the maximum of the co-polar pattern and the maximum cross-polar level field is indicated in the figure. The cross-polarization levels are lower than -12 dB at f_0, but they increase with the frequency and reach maximum levels of -7.5 dB at $4f_0$, for the element that is diagonally displaced. These relatively high values are associated with the radiation mechanism of the leaky-wave slot feed, and in particular with the air gap of height h that is kept between the

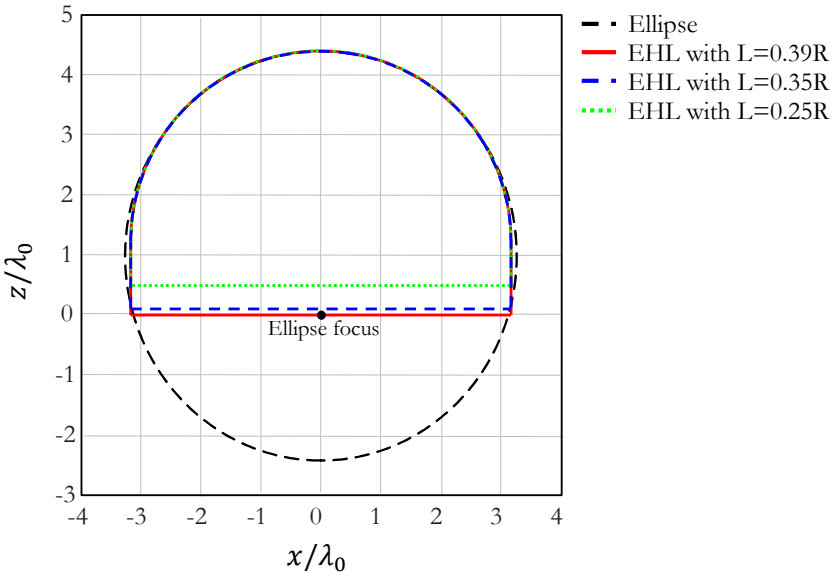

Figure 2.9: 1D drawings of the Extended Hemispherical Lens (EHL) geometries with three different extension lengths, $L = 0.25R$ (green-dotted curve), $L = 0.35R$ (blue-dashed curve) and L=0.39R (synthesized ellipse, red curve), compared to the geometry of an ellipse.

slot and the dielectric lens. The patterns in Fig. 2.10 are calculated choosing the extension length as $L/R = 0.25$. Although not reported here for the sake of brevity, comparable cross-polarization levels were observed for different extension lengths.

2.2.4 Numerical Validation

In order to validate the results, we compare our calculations with CST Microwave Studio [26]. We report in Fig. 2.11 normalized patterns for an on-axis element and for the elements displaced along x and y, assuming, $h = \lambda_0/50$, $\epsilon_r = 12$, $R = 3.16\lambda_0$ and $L/R = 0.25$. The simulated patterns obtained from CST and our in-house analysis tool are in good agreement both for central and offset elements.

One should note that the results from CST simulations in Fig. 2.11 include only the first field contribution transmitted at the lens interface (time-gated data), for the sake of comparison with the PO, which does not take into account multiple reflections. These results are an approximation of those expected in the presence of matching layers used to reduce multiple reflections. To quantify the error introduced by this approximation, as an example, Fig. 2.12 shows CST results of non-gated simulations, with and without matching layers, compared with the gated ones. The data refer to a lens with extension

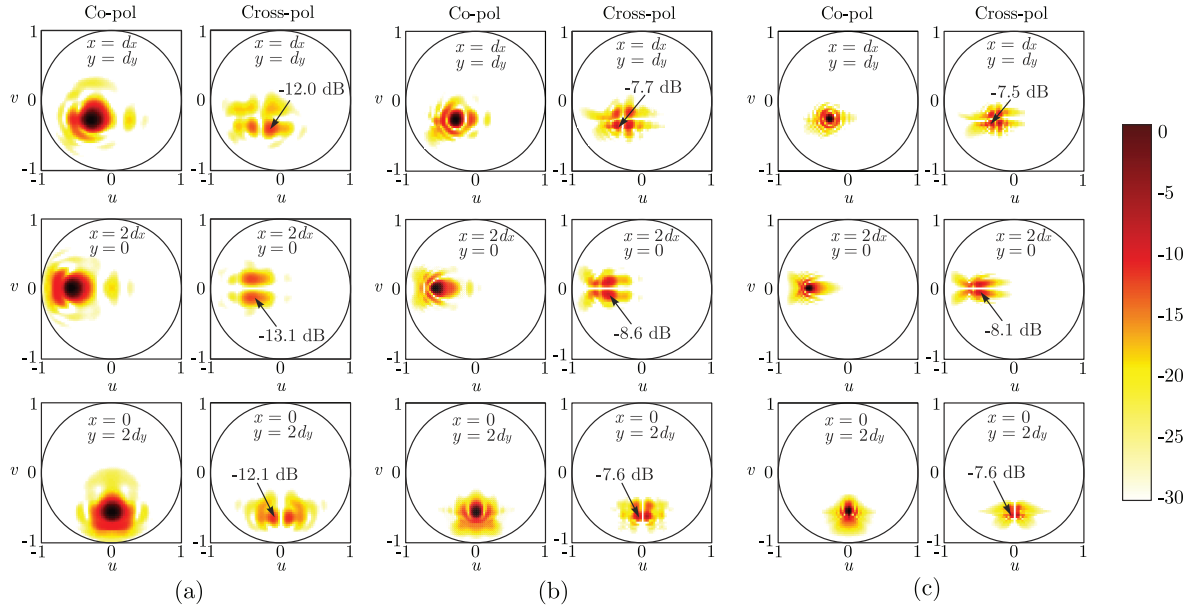

Figure 2.10: Co-polar and cross-polar normalized patterns, for feed displacements of $(x = 2d_x, y = 0)$, $(x = 0, y = 2d_y)$ and $(x = d_x, y = d_y)$, at the frequencies of (a) f_0, (b) $2f_0$ and (c) $4f_0$. The extension length is set to $L/R = 0.25$.

length $L = 0.35R$ at the frequency f_0, for the cases of on-axis and off-axis feeds. The three used matching layers have relative permittivity of 9.7, 6.15 and 2.2, respectively, and thickness of $\lambda_d/4$, where λ_d is the wavelength in each dielectric at the center frequency. It can be observed that the gated results approximate well the non-gated data, only in the case when the lens is coated by the matching layers: despite the inaccurate estimation of the sidelobes, the pattern main lobe is well reconstructed. Higher discrepancy is observed in the absence of matching layers, due to the stronger inner reflections.

2.3 Effects of Slot Tapering

We now investigate the effects of slot tapering on the performance, in particular on the mutual coupling and the polarization purity. We consider a linear taper variation of the slot width characterized by the angle α (see inset of Fig. 2.13).

2.3.1 Mutual Coupling

By tapering the width of the leaky-wave slot, we try to increase the leakage per unit length along the slot, so that the power has effectively leaked away before reaching the

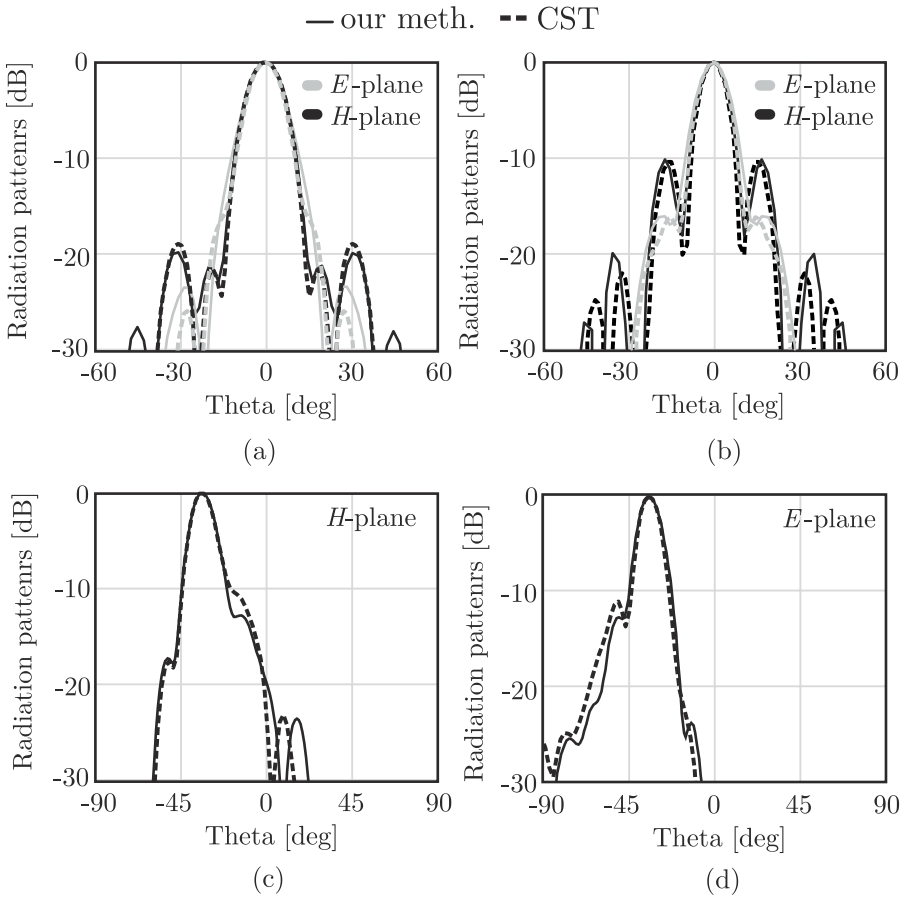

Figure 2.11: Comparison between our method and CST, for only the first transmitted field contribution: radiation patterns for the central element at frequency (a) f_0 and (b) $2f_0$, and for the elements at (c) ($x = 2d_x$, $y = 0$) and (d) ($x = 0$, $y = 2d_y$) at the frequency f_0. For all cases, $L = 0.25R$.

neighboring element. This effect is quantified in Fig. 2.13, which shows the loss due to mutual coupling as a function of the slot taper angle (α). The elements are separated by distance of $\lambda_0/3$. As expected, the loss decreases by widening the slot taper angle, with an efficiency improvement from 90% (0.47 dB loss) to 95% (0.22 dB). Lower mutual coupling would allow to closely pack the elements in focal plane array for high spatial resolution imaging, while keeping very high efficiency. Likewise, for fixed array period, tapering can be used to shift the lower limit of the operational bandwidth of the array towards lower frequencies, without penalty in terms of mutual-coupling loss.

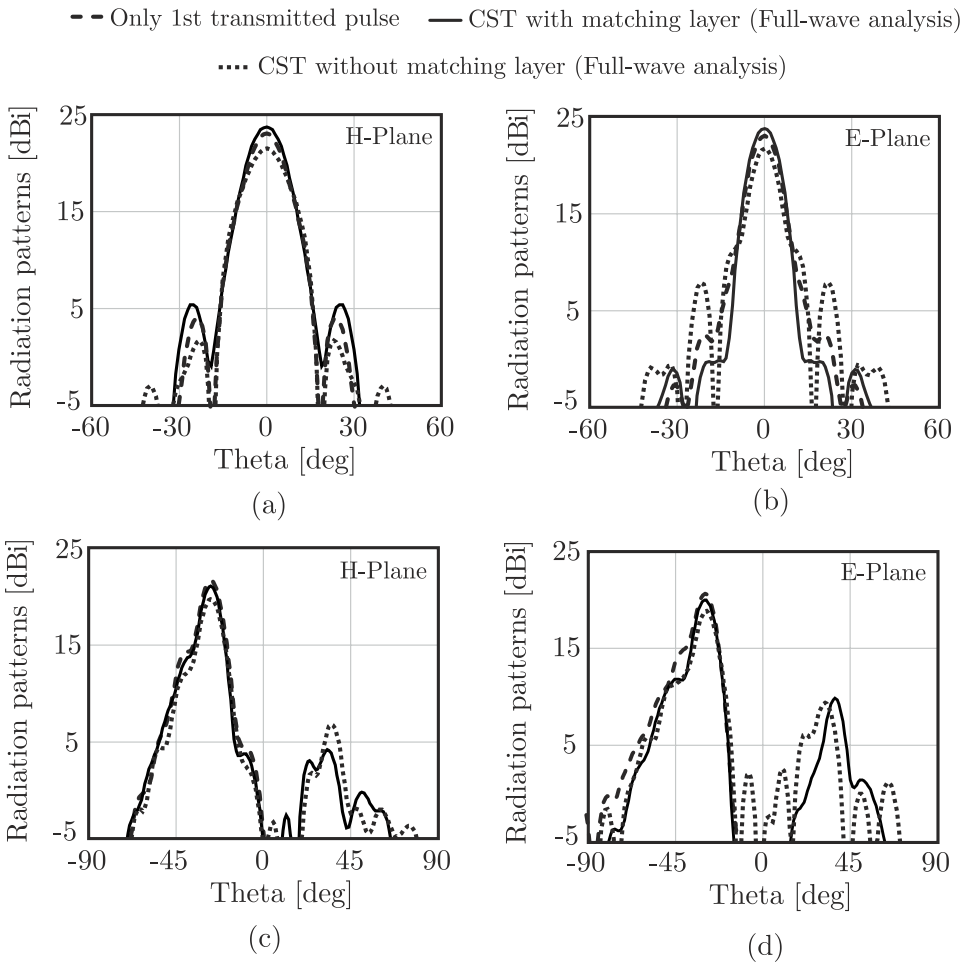

Figure 2.12: Directivity patterns outside the lens ($L = 0.35R$) for only the first transmitted signal contribution and the full wave analysis scenario with and without matching layers at the dielectric-air interface, at f_0 for the feeding positions: (a) and (b) ($x = 0$, $y = 0$) , (c) ($x = 2d_x$, $y = 0$) and (d) ($x = 0, y = 2d_y$).

2.3.2 Cross-Polarization

Besides the improved mutual-coupling efficiency, we investigate how the tapering affects the cross-polarization levels. Here, we just report the simulation results for the patterns obtained when the lens is fed by tapered leaky-wave slots. The field radiated into silicon by the tapered slots has been calculated with CST [26] and then combined with the PO algorithm described in [22] to obtain the secondary patterns. The co-polar and cross-polar components are shown in Fig. 2.14, which refers to the same parameters as in Fig. 2.10, but for slot tapered with angle $\alpha = 35°$. The cross-polar levels are comparable to the ones observed for uniform slots at f_0, but they are considerably lower at higher frequencies. For

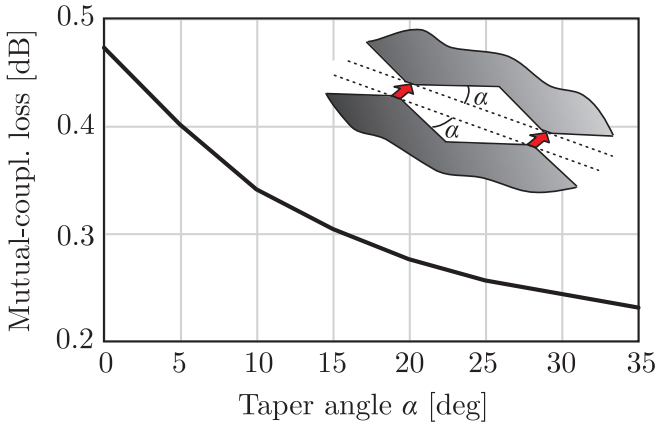

Figure 2.13: Mutual-coupling loss versus slot tapering angle at f_0. The elements are separated by a distance of $\lambda_0/3$.

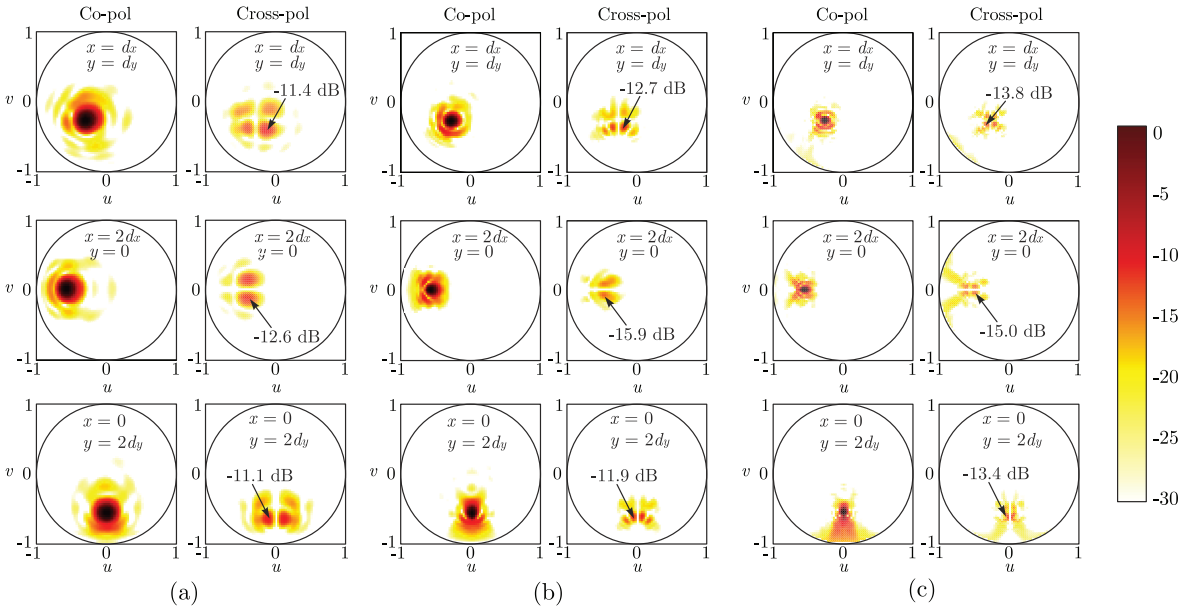

Figure 2.14: As in Fig. 2.10, but for slots linearly tapered with angle $\alpha = 35°$.

instance, the maximum cross-polar level is -13.4 dB at $4f_0$, which represents an improvement of about 6 dB with respect to the uniform slots. The cross-pol reduction by slot tapering does not have an obvious explanation. For this reason, a more rigorous analysis of the propagation and radiation characteristics of tapered leaky-wave slots constitutes a very interesting problem and could be the object of a separate study.

2.4 Conclusions

In this chapter, we investigated the performance achieved by a dielectric lens fed by a broadband connected array of leaky-wave slots. Each feed of the focal plane array exhibits good matching efficiency over a band exceeding $1 : 4$ and is able to generate highly-directive patterns for efficient illumination of the lens. We presented a study of the performance over the entire bandwidth, when varying the characteristic geometrical parameters, such as the extension length and the off-axis distance. The investigation allowed us to identify some useful rules for the lens design, according the specific application.

A combined spectral-domain-approach/physical-optics method allowed the fast analysis of the entire structure, which would be unfeasible with currently available commercial electromagnetic solvers, when the lens is electrically large. Simulation results obtained with CST Microwave Studio, while time-gating only the first transmitted pulse, are shown for the validation of the combined analysis methods for lenses with a size of about 12 free-space wavelengths. It has been demonstrated that the agreement between the simulation results obtained by using PO approach and CST (time-gated data with first transmitted pulse) is quite acceptable. The effect of the multiple reflections have been also demonstrated by further CST simulations and it has been seen that the inner reflections disturb the radiated beams, leading to slightly reduced maximum lens directivities and increased the side-lobe levels for on-axis as well as for off-axis feeds. Finally, some possible advantages of the slot tapering are highlighted, in terms of mutual-coupling and cross-polarization reduction.

CHAPTER 3

Wideband Dielectric Lens Antenna with Stable Radiation Patterns Fed By Coherent Array of Connected Leaky Slots

In this chapter, we present a broadband reflector feed, which consists of a dielectric extended hemispherical lens fed by a connected array of leaky-wave slots. The slot elements are coherently combined to generate directive radiation patterns that mostly illuminate the central part of the lens, the most efficient one. The array is capable of producing secondary patterns with almost constant -10 *dB beamwitdh over a* $1:3$ *bandwidth. This allows efficient illumination of the reflector over a wide frequency range. Performance is estimated in terms of amplitude taper and phase error losses at the reflector, yielding an efficiency of about* 80% *over the entire* $1:3$ *bandwidth. Although the concept is planned to be used in the Terahertz (THz) regime for the DESHIMA instrument, a low-frequency prototype demonstrator has been tested in the* 4 *to* 12 *GHz band, for experimental validation of the concept.*

3.1 Introduction

Reflector systems with wideband antenna feeds are receiving growing interest for applications such as radioastronomy and space observation [1, 18]. For such applications, it is often required to maintain the illumination of the reflector as constant as possible at all frequencies within the large band of operation. Reflector feeds that can operate with high aperture efficiency over wide frequency ranges have been previously developed for low-frequency radio telescopes. Some examples are the focal plane array of tapered slot antennas [43] and the eleven antenna [44]. However, there is currently a need for wideband reflector feeds also at much higher frequencies, for Terahertz (THz) and mm-wave space instruments.

For THz space observation, dielectric lens antennas are typically used, due to their easy integration with the receivers. Elliptical or hyper-hemispherical shapes are frequently employed, which are typically fed efficiently only over a narrow band, e.g. by double slot antennas [2]. An improved solution is the leaky-lens antenna recently proposed in [23,32,45], which can achieve multi-octave bandwidth. This antenna consists of a leaky-wave slot kept at an electrically small distance from the dielectric lens, represented by h in Fig. 3.1(a), in order to obtain directive radiation inside the dielectric material and, consequently, efficient illumination of the lens. Although well matched and with stable phase center over a very wide band, the leaky-lens antenna generates radiation patterns that become narrower and more directive when the frequency increases. For this reason, when used as reflector feed over wide bandwidths, this antenna would not lead to high aperture efficiency at all frequencies.

A solution to obtain frequency independent patterns over a wide bandwidth was presented in [46] and it was based on a double-shell lens design. Here we propose a different solution to the same problem by introducing a novel feed configuration rather than modifying the lens shape. The aim is to improve the reflector illumination efficiency of a single-slot-fed lens antenna by extending the leaky-slot radiation concept to be used in an array configuration, as shown in Fig. 1(b). To maintain the bandwidth wide, the slots are electrically connected so that the array is composed by a finite number of long slots, each excited at a finite number of points. This allows one to obtain high mutual coupling, realizing the so called connected-array concept [47, 48].

The array of connected leaky-wave slots was introduced in [34], where an analysis method for this structure was presented. The formulation was based on a quasi-analytical approach to evaluate the mutual coupling, the radiation patterns, and the voltage distribution on

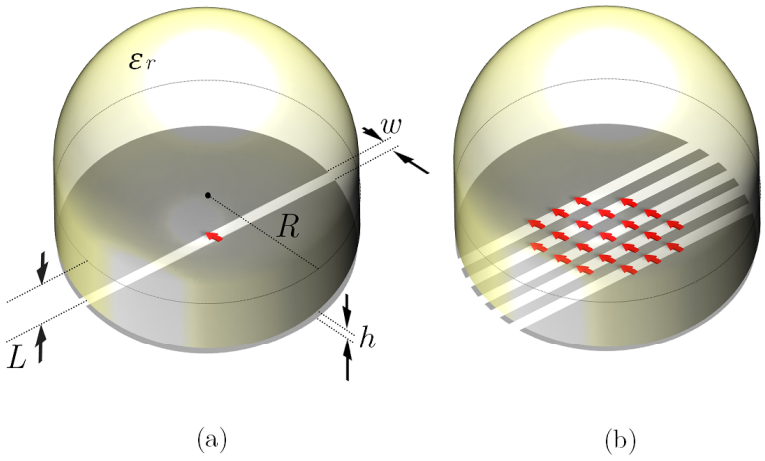

Figure 3.1: (a) Geometry of extended hemispherical lens fed by a leaky-wave slot kept at distance h from the lens; (b) same lens fed by an array of connected leaky-wave slots.

a finite array. The array in [34] was characterized by an electrically large inter-element distance to produce several independent beams, each associated with one element. In this work, we propose a different configuration in which the array elements are not independent, but electrically close and coherently excited. The coherent array concept is used here to design the feed of a focusing lens that has the advantage of generating stable radiation patterns over a broad bandwidth, exceeding 1 : 3 ratios. This characteristic allows wideband illumination of a reflector with high aperture efficiency.

The chapter is organized as follows. In Sec. 3.2 the antenna concept is introduced and the advantages of the proposed structure in terms of radiation pattern stability are qualitatively explained. In Sec. 3.3 we present an example of design of a lens antenna feed, operating from 4 to 12 GHz which is going to be the scaled version of the original sub-mm wave antenna design for the DESHIMA instrument. The simulated performance is reported in terms of matching, predicted aperture efficiency when illuminating a reflector, as well as polarization purity in Sec. 3.4. The experimental validation of the concept (LF prototype) is demonstrated in Sec. 3.5, where measured results from the prototype demonstrator are presented. Finally, conclusions are drawn in Sec. 3.6.

3.2 Antenna Concept

The enhanced leaky-lens antenna [23, 32, 45], sketched in Fig. 3.1(a), is particularly suitable for wideband illumination of a reflector, since it possesses unique properties such as

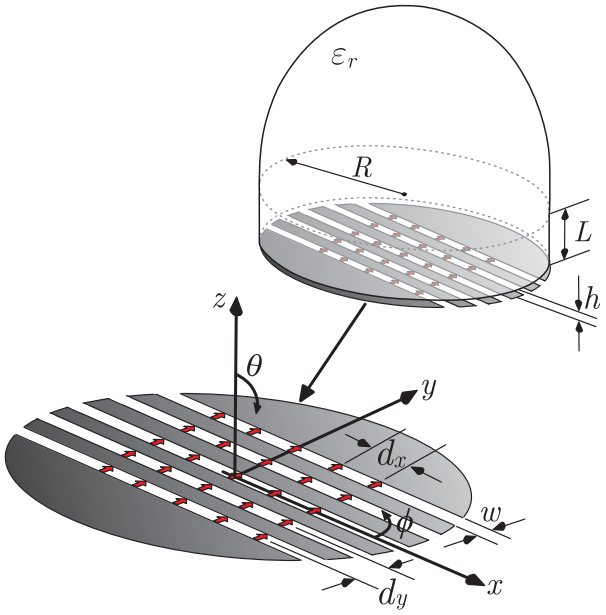

Figure 3.2: Extended hemispherical lens fed by the array of leaky-wave slots, with specified the lens and array geometrical parameters.

frequency-stable phase center and non-dispersive radiation characteristics. However, an additional requirement for wideband reflector feeds is often to be capable of illuminating the reflector with frequency stable radiation patterns, to maximize the aperture efficiency throughout the bandwidth of operation. This property cannot be achieved with the lens fed by a single leaky-wave slot, which produces patterns that are varying with the frequency.

To overcome this problem, we consider an array of connected leaky-wave slots in the focal plane of the dielectric lens, as depicted in Fig. 3.1(b). The geometrical parameters are defined in Fig. 3.2. As an example, let us consider a silicon lens with relative permittivity $\varepsilon_r = 11.9$, radius $R = 4\lambda_0$, with λ_0 being the free space wavelength at the frequency f_0, and extension length $L = 0.35\ R$. The geometrical parameters of the feed array are set to $w = 0.02\lambda_0$, $h = 0.01\lambda_0$, and $d_x = d_y = 0.08\lambda_0$.

The H-plane radiation patterns for a 5×5 array feed are shown in Fig. 3.3 at four different frequencies. The curves include the patterns associated with each element isolated, as well as the pattern sum obtained when all elements are combined in phase. The radiation of an element of the array into the dielectric medium is modeled with the quasi-analytical approach presented in [34], while a physical optics (PO) method is used to include the lens. Note that, since the lens surface is in the far-field region with respect to each single

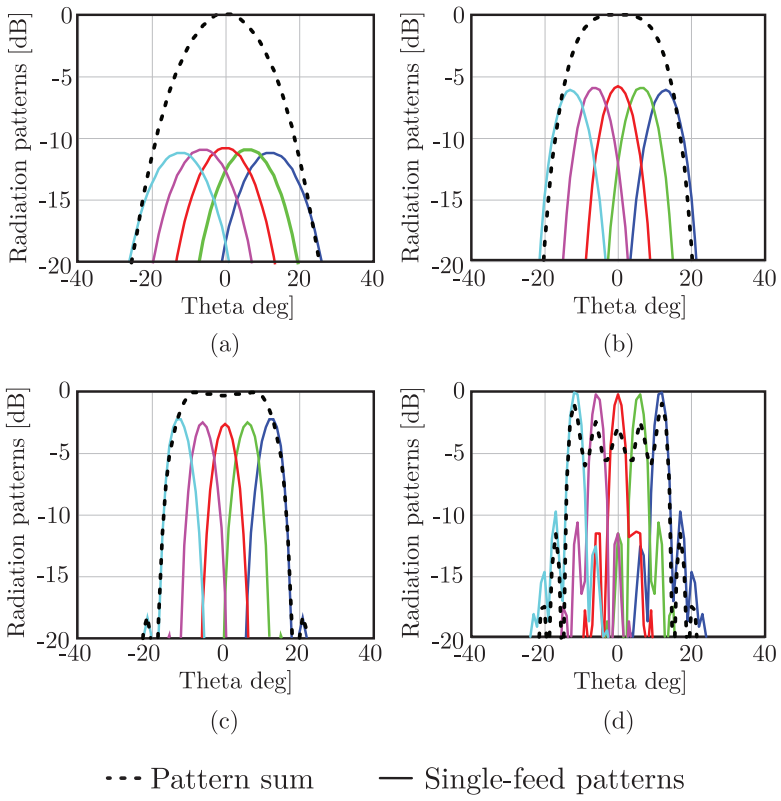

Figure 3.3: H-plane radiation patterns for an array of leaky-wave slots. The dimensions are $R = 4\lambda_0$, $w = 0.02\lambda_0$, $h = 0.01\lambda_0$, $d_x = d_y = 0.08\ \lambda_0$, with λ_0 being the free space wavelength at the frequency f_0. The lens is of silicon ($\varepsilon_r = 11.9$) and with extension length $L = 0.35R$. Patterns generated by the single feeds and by the entire array are shown at the frequencies (a) f_0, (b) $2f_0$, (c) $4f_0$ and (d) $8f_0$.

element, but not with respect to the entire array, the PO calculation is applied to each single feed and the secondary patterns are then summed.

It can be noted that the patterns of the isolated elements become narrower when the frequency increases, just as for the single-slot feed. However, the pointing directions of each beam do not vary, so that the -10 dB beamwidth of the pattern sum remains almost constant with frequency. Oscillations occur at the frequency $8f_0$ because the beams associated with each feed are angularly separated and interfere destructively.

3.3 LF Prototype Design: 4 to 12 GHz Antenna

In this section, we describe a specific design of a connected array of leaky-wave slots feeding a dielectric lens for a 1 : 3 bandwidth operation. The frequency range is chosen to be from

4 to 12 GHz .

The target beamwidth of the secondary patterns generated by the lens is dictated by the focal length-to-diameter (F/D) ratio of the reflector that one wants to illuminate. For example, if we assume an F/D ratio of 0.6, the lens should produce patterns with -10 dB beamwidth of about ± 45 degrees according to the formulation $\theta_0 = 2\tan^{-1}(D/4F)$ [49], where θ_0 is the reflector subtended angle. To achieve the desired beamwidth one can modify the lens size and/or the array total dimensions. However, the following considerations must be kept in mind during the design phase:

- The array period should be small compared to the wavelength to achieve high mutual coupling between the elements and effectively attain the connected array behavior. Typical values for the array spacing are lower than $0.4\lambda_d$ at the highest frequency of operation [48], with λ_d being the wavelength in the dielectric material constituting the lens.

- Obviously, larger sizes of the lens lead to narrower beamwidth values of the secondary pattern. However, given a certain array spacing, the maximum size of the lens should be such that the beams associated with each feed overlap well enough and do not give rise to strong oscillations in the amplitude and the phase of the radiation patterns (as in Fig. 3.3(d)).

- For a given dielectric lens the maximum off-axis distance of the edge elements of the array should not be greater than about one third of the lens radius, to avoid high aberrations in the radiated fields.

- The unit cell size must be large enough to be able to fit the microstrip lines of the corporate feeding network, which is needed to obtain a coherent excitation of the array.

Accounting for the above mentioned aspects, the lens is selected as an extended hemispherical dielectric lens with radius $R = 95$ mm and extension length $L = 30$ mm. The material chosen for the dielectric lens is ECCOSTOCK® HIK 500F [50], with relative permittivity $\varepsilon_r = 12$. The unit cell size has been selected as 7×7 mm^2, with the objective of trading-off the need for high mutual coupling and the necessity for physical space to place the microstrip feed lines.

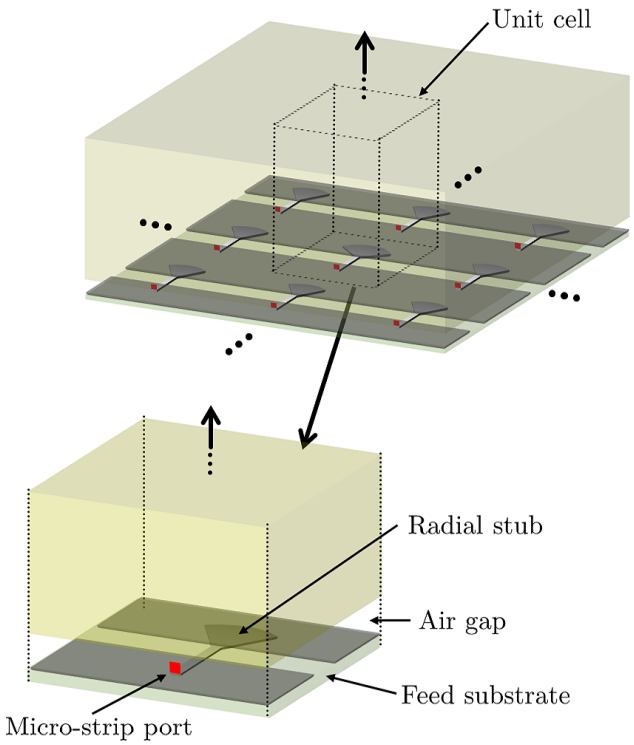

Figure 3.4: Schematic view of the array in the presence of a semi-infinite dielectric medium and details of the unit cell.

3.3.1 Array Unit Cell

Once the unit cell size was fixed, the key parameters that have been optimized to obtain low reflection coefficient within the objective frequency band are the width of the slot w and the height of the air gap h. The slot is fed by aperture coupling with a micro-strip line terminated with an open radial stub, to achieve wideband operation, as shown in Fig. 3.4. The feed substrate is Rogers 6006 with relative dielectric constant of 6.45 and thickness 0.254 mm.

The active reflection coefficient of the unit cell is reported in Fig. 3.5, assuming a 80 Ωtransmission line and selecting the parameters as $w = 1.2$ mm and $h = 0.9$ mm. Simulations of the unit cell have been performed with Ansoft HFSS and show good matching efficiency from 4 to 12 GHz. Note that the lens is, at this stage, approximated as a semi-infinite dielectric medium with relative permittivity $\varepsilon_r = 12$. Therefore, reflections at the dielectric-air interface of the lens are neglected in Fig. 3.5.

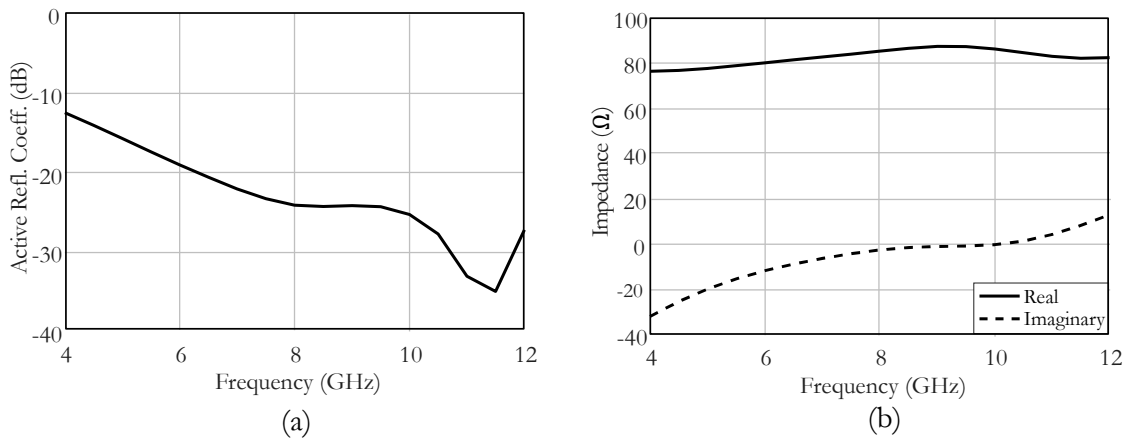

Figure 3.5: (a) Active reflection coefficient for the unit cell and (b) the input impedance in Fig. 3.4.

3.3.2 Array Topology

The total size of the array is chosen conforming to the dimensions of the dielectric lens at our disposal. Specifically, we considered an array with 8×8 elements, with total size of about one third of the lens diameter, to avoid high aberrations in the radiation patterns. The array elements are distributed in a rectangular lattice. However, three elements at each corner are removed to better adapt the field radiated by the lens to the circular aperture of the reflector, yielding a total number of 52 elements in the array (see Fig. 3.6).

3.3.3 Feeding Network

A corporate feed network has been designed to excite all the elements of the array with equal amplitudes and phases (Fig. 3.7(a)). The network includes asymmetric power dividers, tapered impedance transformers and multi-section quarter wave transformers.

The performance of the designed feed structure is presented in terms of the simulated magnitude of the S-parameters in Fig. 3.7(b). It can be observed that the S_{11} parameter at the input port, although rapidly oscillating due to the electrically large length of the transmission lines, remains well below -10 dB, when normalized to a port impedance of 50 Ω which is also the impedance of the connector. The 52 curves pertaining to the S_{j1} ($j = 2, 3, ..., 53$) for the ports representing the array elements are also reported. The losses due to the transmission lines is calculated as about 1.4 dB at the central frequency, 8 GHz. The transmission curves fluctuate around -18.5 dB ($= 10\log_{10}(1/52)$ + losses in the tranmission lines), which is the expected value if all the elements were ideally excited

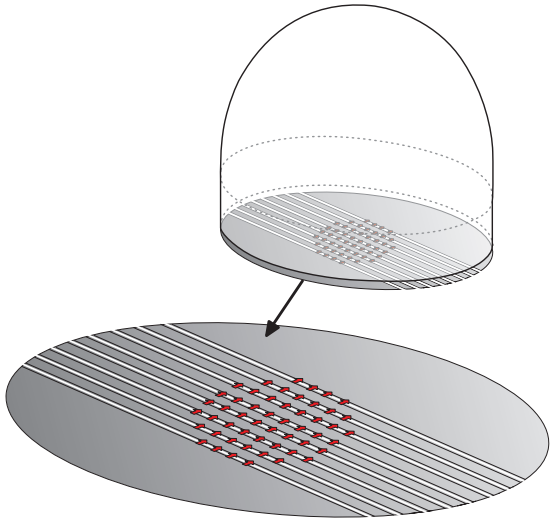

Figure 3.6: Schematic impression of the 52-element array of connected leaky-wave slots in focal plane array of the dielectric lens.

with the same power. Fig. 3.7(c) shows the phase of the transmission coefficients for all the 52 output ports of the feed network. It is apparent that very little difference is present in the phases of the excitation signals reaching the array elements. The simulated results shown in Fig. 3.7(b) and (c) have been calculated by means of Ansoft Designer.

3.4 Simulated Patterns

The radiation patterns generated by the array in the presence of the dielectric lens are presented in this section. The patterns are calculated through full-wave simulations, performed with CST Microwave Studio, of the entire structure including the array and the dielectric lens. The in-house developed physical optics tool, utilized to calculate the patterns in Fig. 3.3, is not adopted here because of the relatively small electrical size of the lens under investigation.

3.4.1 Front to Back Ratio Efficiency

An interesting consideration can be made about the front-to-back ratio efficiency of the array-fed lens antenna. While the single slot couples most of the radiated field to the dense dielectric lens, this is not always the case for the array feed configuration. Indeed, the array produces by itself a directive beam also in the free-space medium, which could cause poor

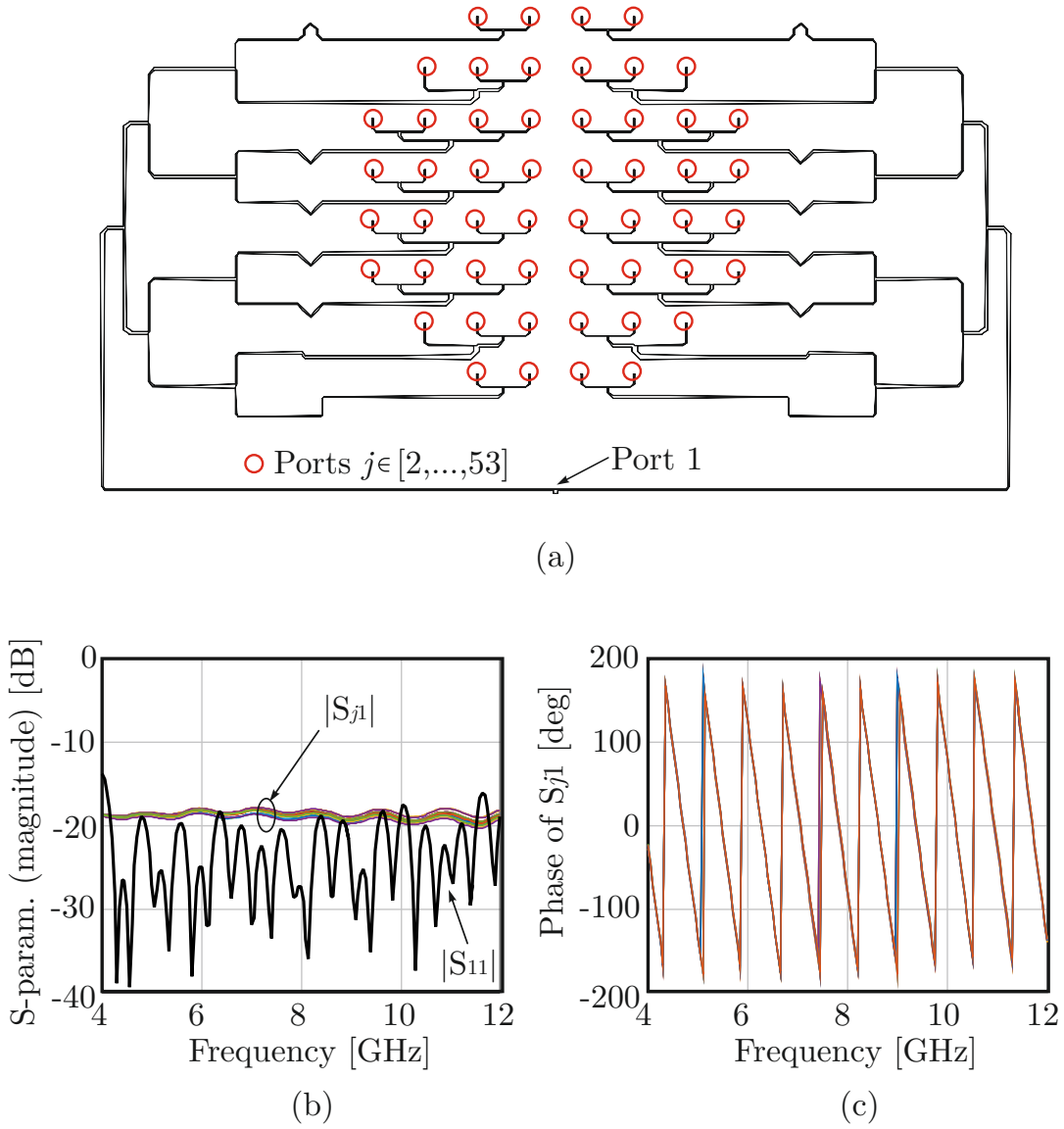

Figure 3.7: (a) Corporate feed network with port definition, (b) magnitude of the reflection and transmission coefficients and (c) phases of the transmission coefficients.

efficiency in terms of front-to-back ratio. For this reason, it is convenient to place a backing reflector at about quarter-wavelength from the array, to ensure unidirectional patterns.

The presence of the dense dielectric medium strongly mitigates the frequency dependence introduced by the back plane, so that the bandwidth remains wide. We compare in Fig. 3.8 the active reflection coefficient of the unit cell with and without the backing reflector,

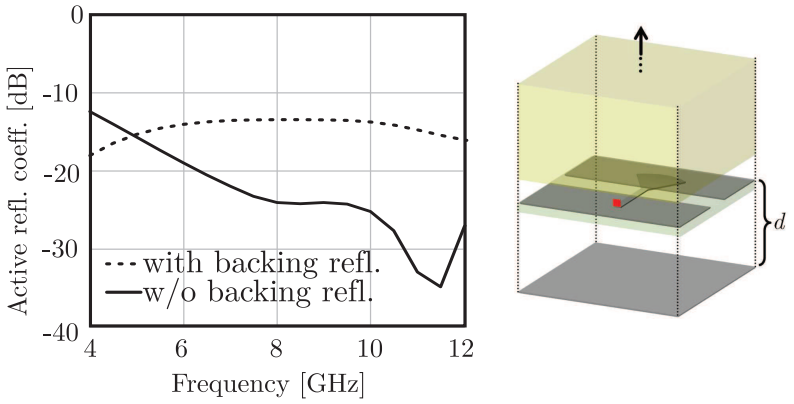

Figure 3.8: Comparison of active reflection coefficient with and without backing reflector.

when the distance from the backing plane is set as $d = 8$ mm. In both cases, the values are lower than -10 dB within the band of interest, normalized to the same impedance value of 80 Ω. Besides the matching performance, the backing reflector should effectively eliminate the back radiation and increase the forward directivity. This aspect is investigated in Fig. 3.9, where the directivity patterns obtained from the array-fed lens are shown, with and without the backing reflector. It can be observed that the presence of the ground plane leads to enhanced directivity in the upper hemisphere, while strongly reducing the power radiated in the lower hemisphere.

3.4.2 2-D Radiation Patterns and Polarization Efficiency

Two-dimensional pattern plots are shown in Fig. 3.10 in the u, v domain, where $u = \sin\theta\cos\phi$ and $v = \sin\theta\sin\phi$, for 4, 8 and 12 GHz. In the co-polar patterns, -20, -10, -3 dB levels are highlighted by contour lines. It is apparent that, over the 1 : 3 bandwidth under investigation, the -10 dB beamwidths remain almost constant at all frequencies. Cross-polar patterns are also reported and they exhibit cross-polarization levels lower than -17 dB.

3.4.3 Aperture Efficiency

By integration of the patterns, we can obtain a more quantitative analysis of the performance by calculating the amplitude taper loss and the phase error loss. The efficiency plots reported in the remainder of the paper include taper, spillover, phase and polarization efficiency. Dielectric losses and internal reflections, while included in the evaluation

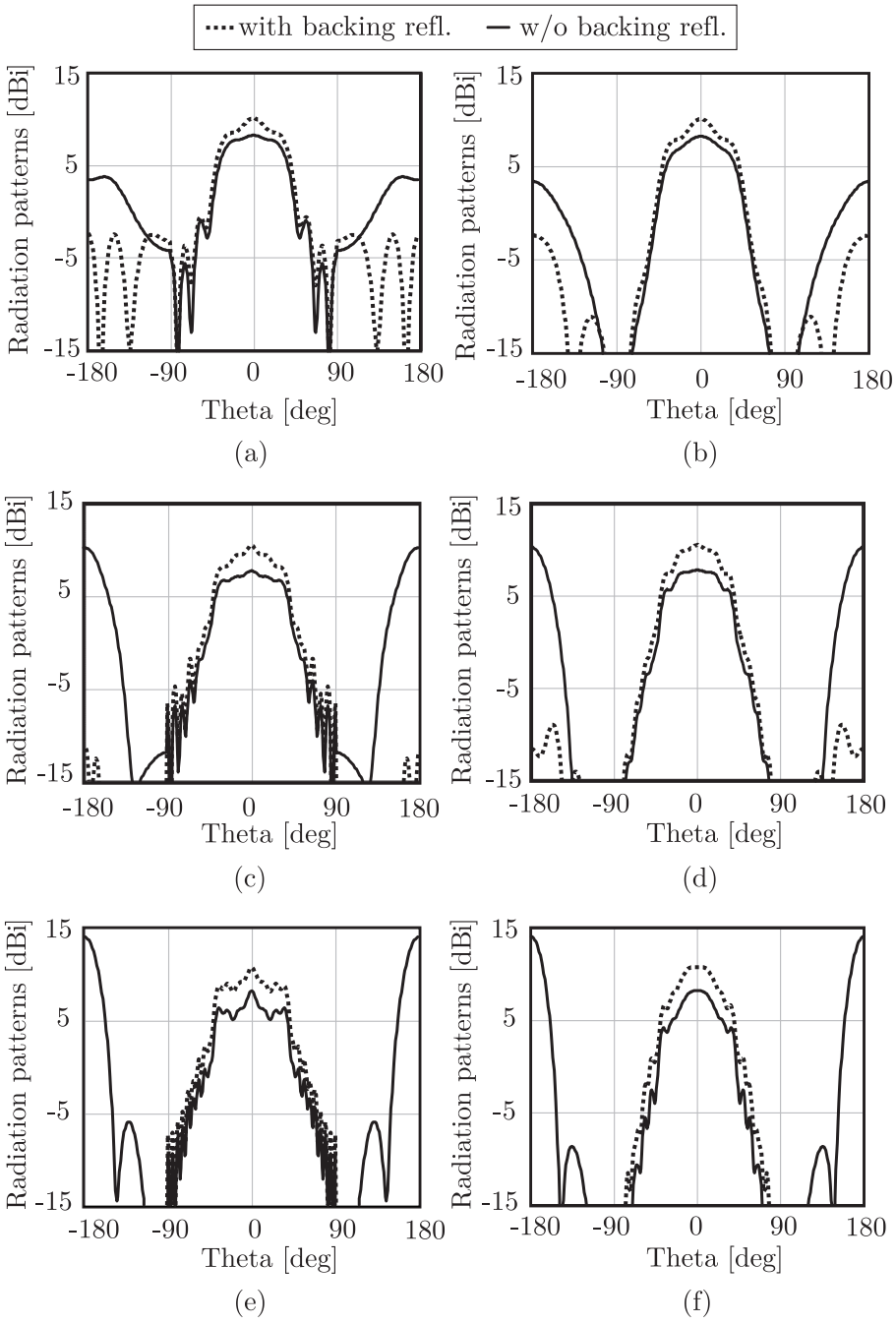

Figure 3.9: Directivity patterns with and without the presence of backing reflector for an array feed with $w = 1.2$ mm, $h = 0.9$ mm, and $d_x = d_y = 7$ mm: (a), (b) are calculated at 4 GHz, (c), (d) at 8 GHz and (e), (f) at 12 GHz; (a), (c), (e) refer to the E-plane, while (b), (d), (f) to the H-plane.

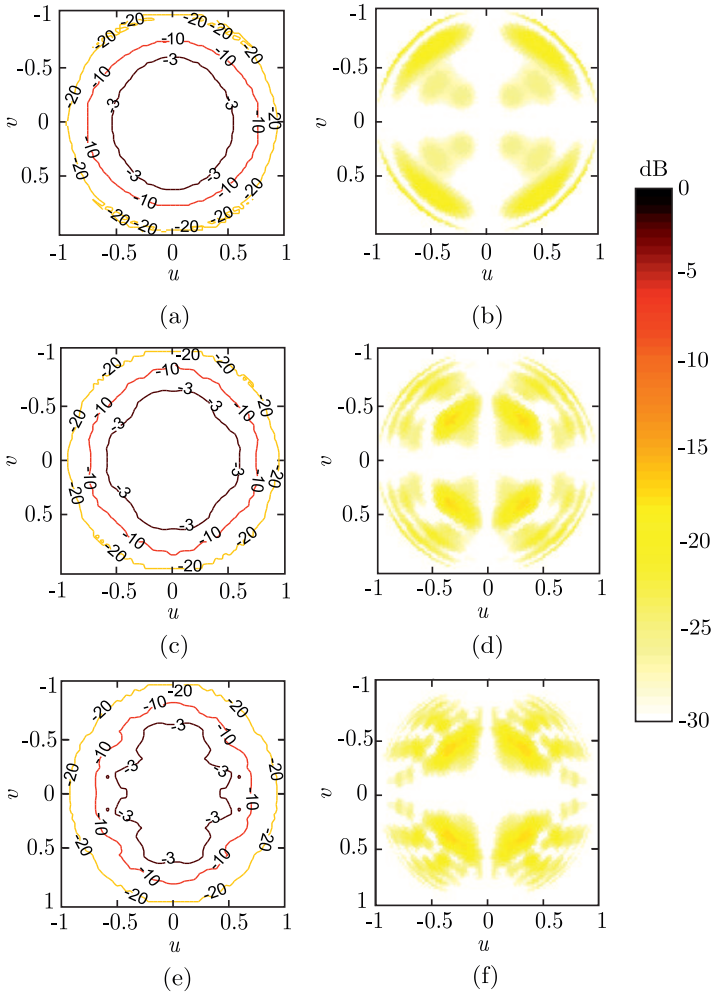

Figure 3.10: Co-polar and cross-polar components of secondary beams after the lens: (a) 4 GHz co, (b) 4 GHz cross, (c) 8 GHz co, (d) 8 GHz cross, (e) 12 GHz co and (f) 12 GHz cross, respectively.

of the radiation patterns, are not explicitly accounted for in the efficiency at the reflector. Also ohmic losses are not consider in the following calculations. However, for the envisaged applications at THz frequencies, the feed network is typically realized with extremely low loss superconducting transmission lines that are kept inside cryogenic cooling systems.

The aperture efficiency, for a reflector characterized by focal length-to-diameter ratio $F/D = 0.6$, is summarized in Fig. 3.11 as a function of the frequency, and compared with the case of single slot. It can be observed that the aperture efficiency, for a single-slot-fed lens, has a maximum of 73% at the central frequency (8 GHz). The efficiency drops to about 50% at high frequency, since the reflector is highly under-illuminated, while at

low frequency the degradation is mainly due to spillover. Instead, the efficiency is nearly constant with the frequency in the case of the array, thanks to the fact that the patterns are much less frequency dependent. The total efficiency is higher than 75% within the entire frequency range under analysis. It can be also pointed out that the maximum efficiency for the single slot is slightly lower than for the array case. We observed that the main reason for such difference is the fact that the array feed exhibits lower cross-polar levels with respect to the single-slot feed. These efficiency numbers are realistic in the presence of matching layers covering the lens.

3.4.4 Tertiary Patterns

Finally, we evaluate the pattern radiated by a reflector illuminated with the lens antenna feed proposed in this article. As an example, we consider a reflector with diameter of 1 m and focal distance of 0.6 m. The resulting patterns are calculated using GRASP and shown in Fig. 3.12, for both the co-polar and the cross-polar components. The side-lobe level is lower than -20 dB and the cross-polar level is lower than -30 dB in the entire field of view.

3.5 Experimental Validation

A prototype demonstrator has been manufactured and tested. The top and bottom views of the array feed are shown in Fig. 3.13, together with the dielectric lens. The lens and the

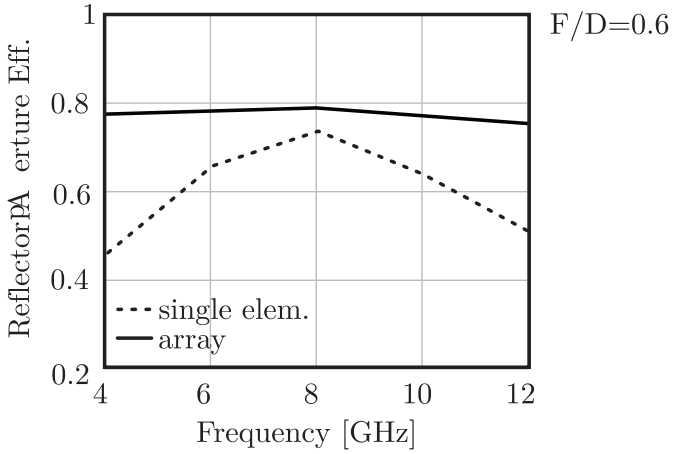

Figure 3.11: Comparison of the simulated reflector aperture efficiencies of the proposed array-fed lens antenna and the single-slot-fed one.

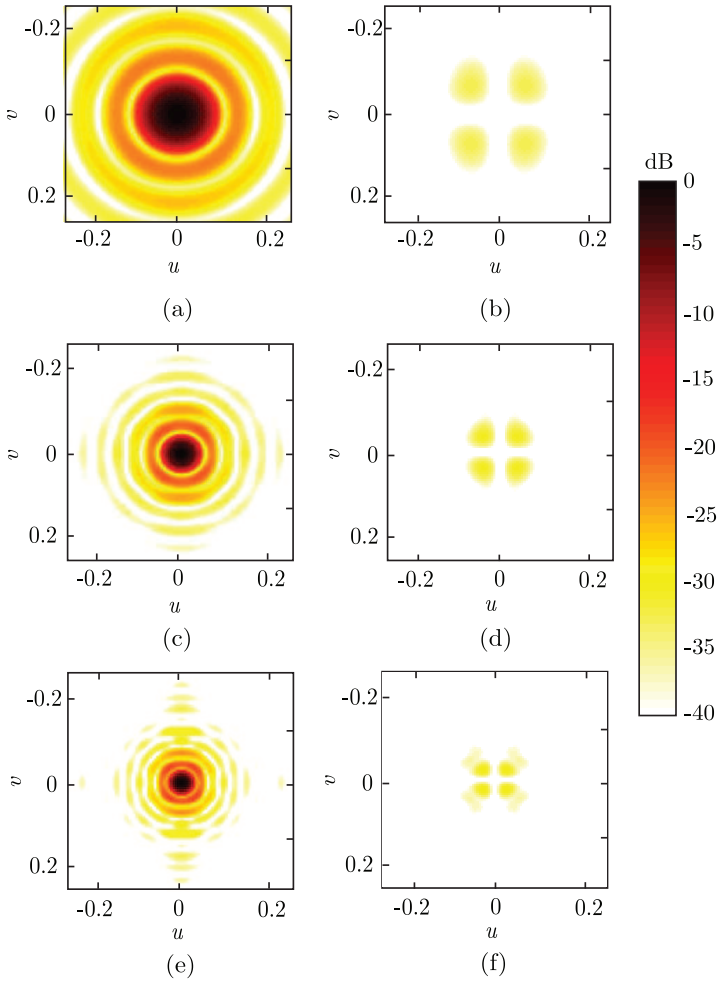

Figure 3.12: Radiation patterns after the reflector: (a), (b) are calculated at 4 GHz, (c), (d) at 8 GHz and (e), (f) at 12 GHz; (a), (c), (e) show the co-polar components, while (b), (d), (f) refer to the cross-polar components.

array are equipped with a supporting structure which allows to micrometrically tune the distance between the printed circuit board and the dielectric lens, in order to implement the desired air gap.

The measured reflection coefficient is shown in Fig. 3.14, remaining lower than -9.5 dB over the entire band under investigation. We also highlight the estimated S_{11} in Fig. 3.14. Estimated reflection coefficient is obtained by means of taking into account the effect of the inner reflections due to the silicon-air interface on the lens surface when the antenna is fed by a lumped port in CST simulations. The difference in S_{11} obtained by the simulation with the first reflection only and the simulation with multiple reflections is calculated

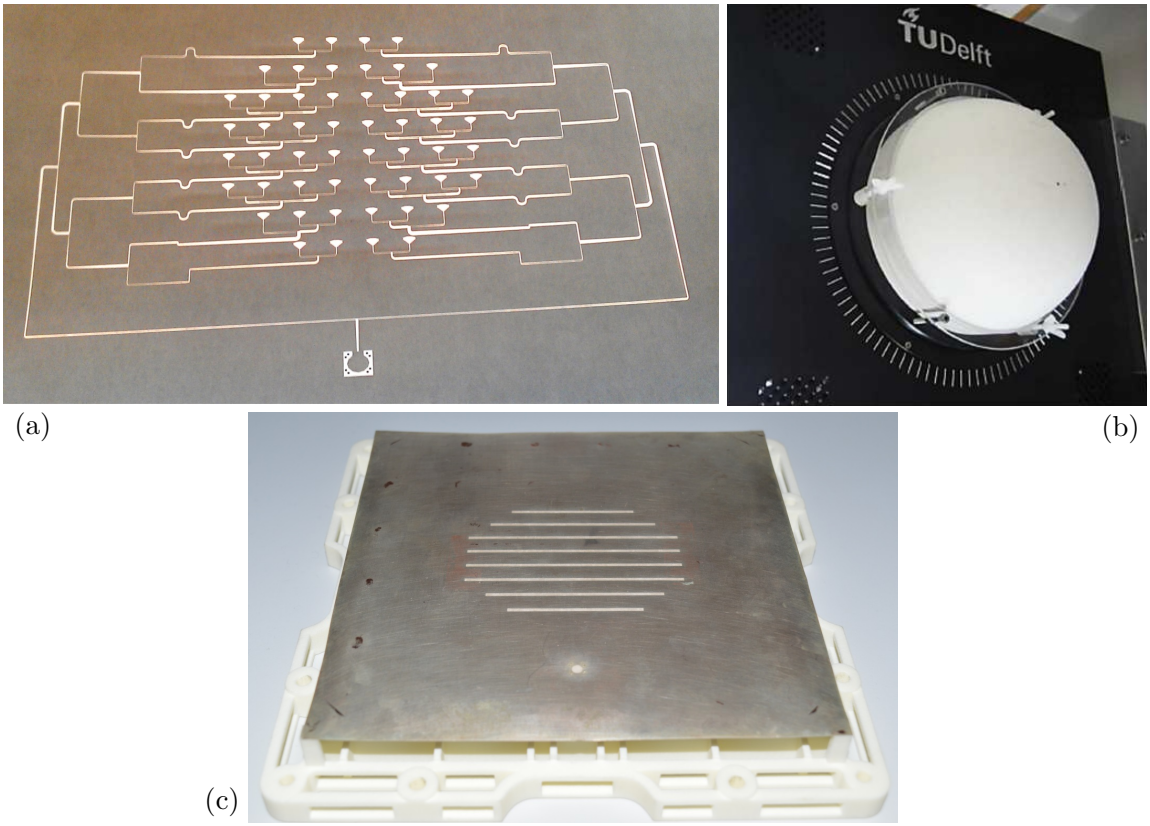

Figure 3.13: (a) Close-up bottom view of the antenna array printed circuit board and (b) dielectric lens located on the top of the antenna and (c) Top view of the ground plane including the slots.

and then included into the active reflection coefficient given Fig. 3.7(b). The agreement between the measured and the estimated reflection coefficients is acceptable. Then the measured patterns are compared with the simulated ones in Figs. 3.15 and 3.16 for main planes and diagonal plane, respectively. The comparison exhibits a fair agreement between simulation and experiments. Low values of cross polarization are observed in the main planes and even in the diagonal plane, where the maximum cross-polar component of the radiated fields is -12 dB.

The capability of this structure to maintain the beamwidth weakly dependent from the frequency is also confirmed from the measured results. The variation of the phase center along the lens axis has also been investigated. By placing the origin of the reference system on the array plane, we obtain the phase patterns shown in Fig. 3.17, for the E- and H-plane at 4, 8 and 12 GHz. The phase oscillates in a range of about 30 degrees at all frequencies for

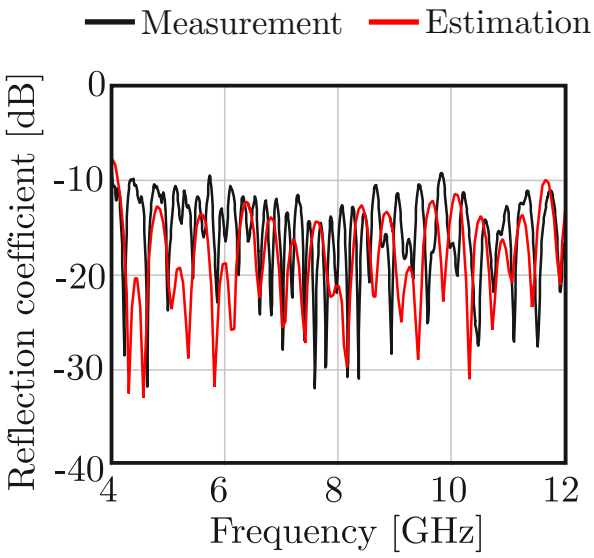

Figure 3.14: The measured and the estimated reflection coefficients of the prototype antenna .

observations within the main lobe, defined by the angle subtended by the reflector. These variations lead to small phase error loss on the reflector. Indeed, in Fig. 3.18 we report the aperture efficiency calculated by integration of the measured patterns, compared with simulation results. The efficiency includes amplitude taper, phase error, cross-polarization loss and spillover. The measured efficiency is higher than 70% in the target frequency range and it is up to $\pm$ 5% lower than the simulated levels. Such discrepancy is congruent with the difference between the measured and simulated patterns shown in Figs. 3.15 and 3.16.

3.6 Conclusions

We proposed a connected array of leaky-wave slots as feed of a dielectric lens. Thanks to the properties of the connected arrays, the array is well matched over a large bandwidth. The coherent array of slots is able to generate secondary patterns with almost constant -10 dB beamwitdh over a bandwidth exceeding $1:3$. This allows efficient illumination of the reflector over a wide frequency range. Such a property was demonstrated both with simulations and measurements from a demonstrator operating from 4 to 12 GHz. The measured secondary radiation patterns also exhibit remarkably low values of cross polarization, even in diagonal planes ($\phi = 45°$), which is always lower than -12 dB within the whole band of operation. This is, in our knowledge, among the lowest measured cross

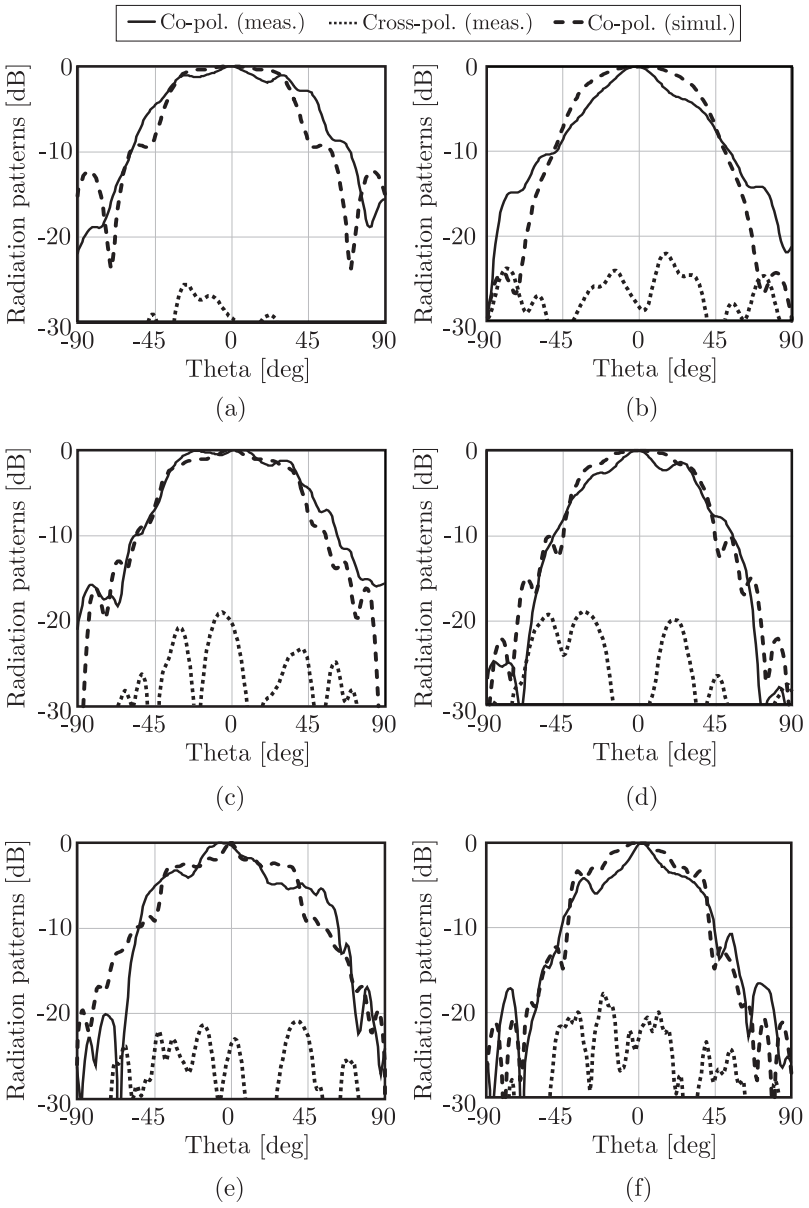

Figure 3.15: Comparison of measured and simulated co-pol and cross-pol patterns at the frequencies: (a) and (b) 4 GHz, (c) and (d) 8 GHz, and (e) and (f) 12 GHz, respectively; (a), (c), (e) refer to the E-plane, while (b), (d), (f) to the H-plane.

polarization ever reported for broadband dielectric lens antennas.

Designs characterized by wider bandwidth can also be achieved with larger lenses, since the lower limit of the band is mainly dependent on the lens size. We believe that the proposed concept represents a useful solution for THz space applications which require the

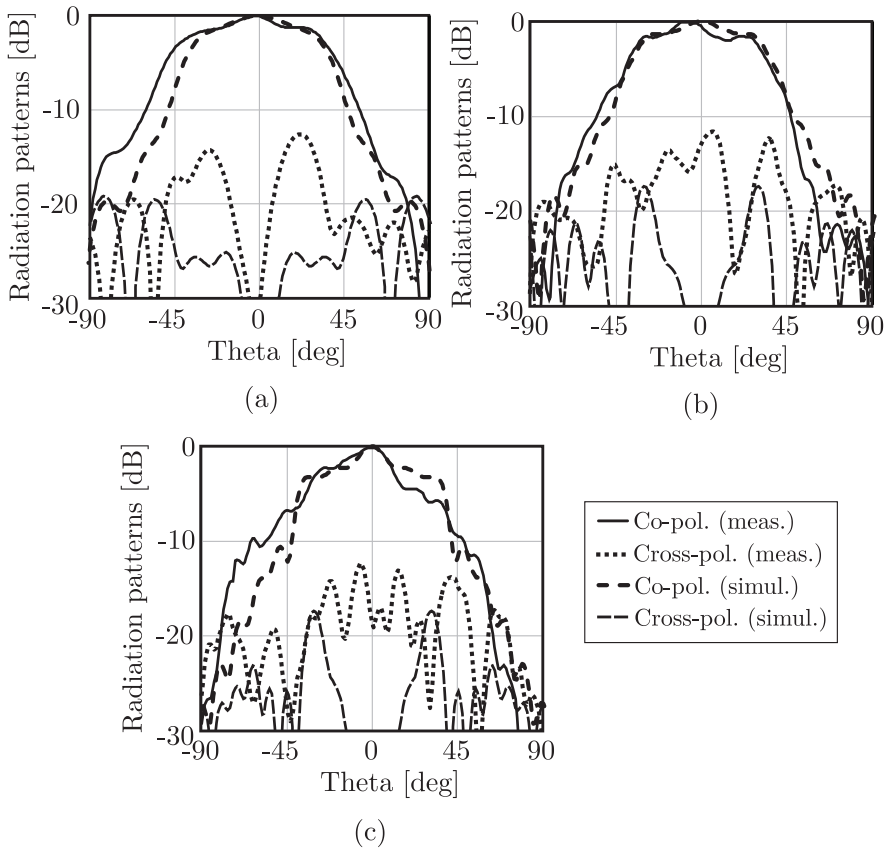

Figure 3.16: Comparison of measured and simulated co-pol and cross-pol patterns on the diagonal plane at (a) 4 GHz, (b) 8 GHz, and (c) 12 GHz, respectively.

illumination of a given reflector aperture with high efficiency over a large frequency band.

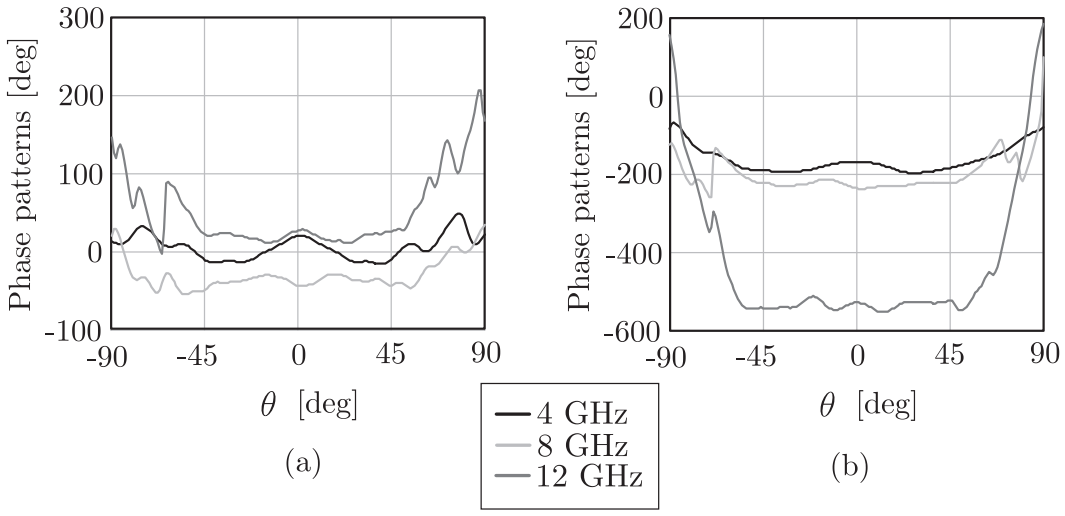

Figure 3.17: Measured phase patterns for the lower, central and upper frequency within the target bandwidth, for the (a) H- and (b) E-plane.

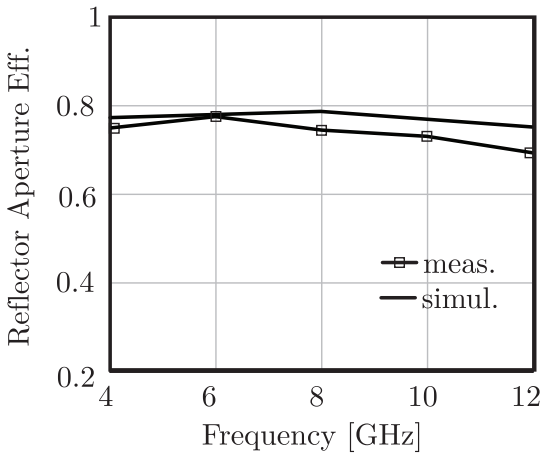

Figure 3.18: Comparison of the measured and simulated reflector aperture efficiencies of the proposed array-fed leaky lens antenna.

CHAPTER 4

Double Shell Lenses: An Alternative Wide-band Design Approach To Achieve Frequency Stable Beams

In this chapter we propose an alternative design concept based on the integration of a connected array of leaky slot antenna to a double shell lens that is able to generate frequency stable beams within a large bandwidth, typically about one octave. Starting from the feed array design, we show the beam stability performance from the optimized lens geometry when the lens is excited by on-axis feed as well as off-axis feeds to highlight the scan capabilities of the array design. Finally, we compare the performance of the proposed lens antenna design with a conventional extended hemispherical single shell lens in terms of beam stability and scan loss within the band of operation.

4.1 Introduction

The instruments used in radio astronomy and space observation mostly benefit from wideband feeds with frequency stable illumination to maximize the aperture efficiency on the reflector aperture within the band of operation. In order to achieve high reflector illumination efficiency over the desired bandwidth, we proposed a concept in Chapter 3 based on the design of a coherently fed leaky lens antenna. The concept provides a solution by means of introducing a novel feed configuration rather than modifying the lens shape. The aim is to improve the reflector illumination efficiency of a single-slot-fed lens antenna by extending the leaky-slot radiation concept to be used in an array configuration, can be seen from Fig. 4.1. The elements in the array are coherently excited, so that they are associated with a single beam outside the lens. However, in this scenario, the reflector is illuminated by only a coherently combined single beam. In other words the concept is not suitable for the applications that require electronic beam steering. An alternative design approach to the one presented in Chapter 3 could be to design a multiple shell lens such that the refraction interfaces from the shells are adequately shaped to form frequency stable patterns [46]. Using the Double Shell Lens (DSL) concept given in [46], the aim of this chapter is to design an integrated connected array of leaky lens antenna with large number of array elements such that each element is able to generate a frequency independent beam within an octave bandwidth.

In this chapter, we will use an integrated DSL concept which, in principle, can be used either as a reflector feed or directly as an imager itself. Here, we target a direct imager scenario for broadband security applications, namely over an octave bandwidth. The antenna concept that we are proposing is sketched in Fig. 4.2. The feed array is located on the focus of the DSL and used as a lens feeder where each pixel is associated with an independent beam illuminating the DSL surface.

The chapter is organized as follows. In Section 4.2, we will explain the specifications of the work. Section 4.3 will demonstrate the optimized feed geometry to be used for the illumination of the inner shell of DSL. The optimized lens geometry will be demonstrated in Section 4.4. In Section 4.5, we will show the performance of the proposed DSL antenna design in terms of beam stability and scanning loss. Performance comparison with respect to a conventional extended hemispherical Single Shell Lens (SSL) will be also shown in order to provide reference data for performance comparisons. Lastly, we will provide the concluding remarks and possible future work in Section 4.6.

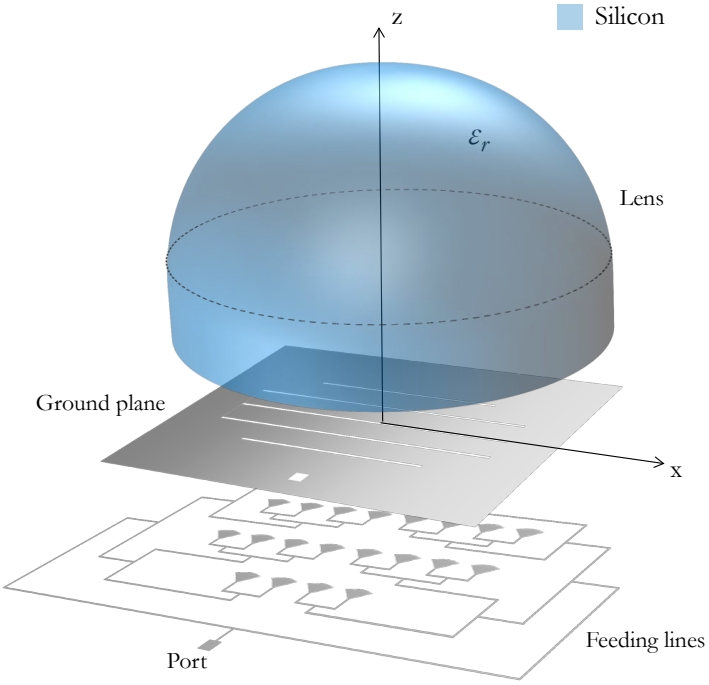

Figure 4.1: Illustration of the coherently fed connected array concept for wideband frequency stable beam applications.

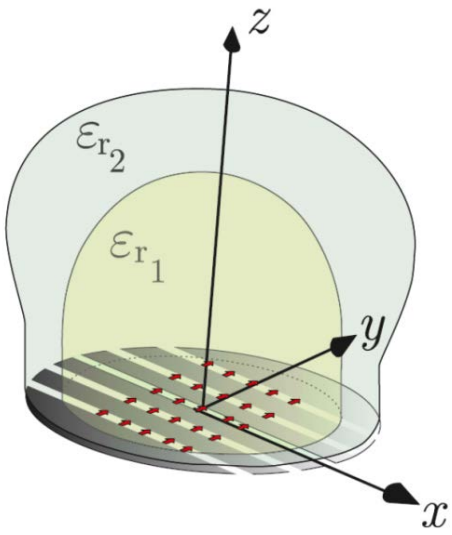

Figure 4.2: Schematic view of a double shell lens antenna fed by a connected array of leaky slot.

4.2 Project Requirements

The project requirements are listed below:

- The design is planned to be used directly as an imager itself, which means that the secondary beams after the lens should be highly directive. Namely, the desired gain is about 45 dBi and the corresponding half-power beamwidth (HPBW) is about 1^0,
- The imager has a bandwidth of one octave. More precisely, it should cover a band starting from 0.3 THz to 0.6 THz,
- The initial goal is to have a total number of pixels about 529 with a total scan angle of about 22^0 (11^0 from each side),
- Frequency stable beams after the lens for on-axis feed as well as off-axis feeds within the proposed band. The design should be able to provide high scan loss performance (Namely less than -1.5 dB).

4.3 Feed Design

Regarding the requirements listed above, we will first focus on the design of a connected array of leaky antenna to be used as a lens feeder within the proposed frequency band. In order to avoid high lateral lens illumination, which leads to significant inner reflections, we assume that the inner shell of the DSL is made of silicon with relative a permittivity of $\epsilon_{r_1} = 11.9$. Considering the electrically large inner shell dimensions, the antenna design is done in the presence of a semi-infinite silicon brick located on top, being separated from the ground plane with an electrically small air-gap with a thickness of h (See Fig. 4.3). In order to achieve efficient lens illumination we used an electrically small airgap between the antenna array feed and the lens due to the radiation mechanism of the leaky slot antenna [23]. Here, the airgap is chosen to be $0.03\lambda_0$, where λ_0 is the free-space wavelength at the lowest frequency, $f = 0.3$ THz. The stratification used in the feed optimization process is shown in Fig. 4.3.

The feed geometry is illustrated with its design parameters in Fig. 4.4. The elements in the array have been packed very close to each other, with a separation of 0.3 λ_0, where λ_0 is the free-space wavelength at the lowest frequency, i.e. 0.3 THz. As one can see from the figure, we introduced tapering in the slots to optimize the mutual coupling between the feed elements and to improve feed cross-polarization performance as was mentioned in

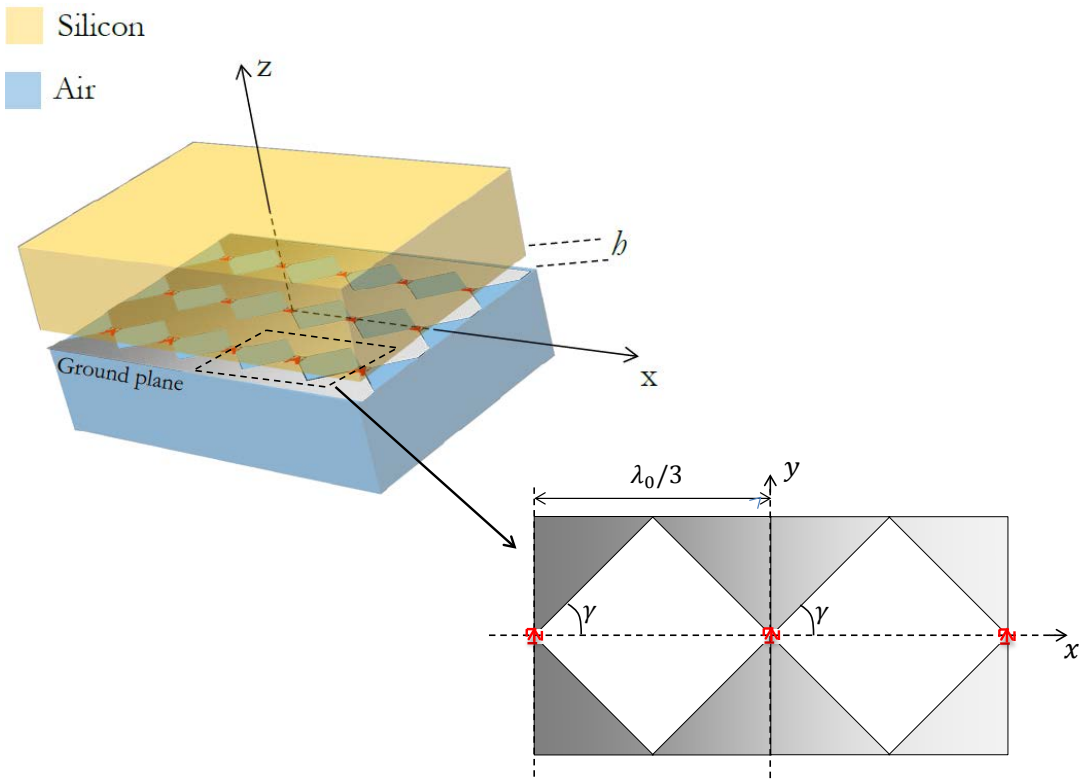

Figure 4.3: Stratification used for the antenna optimization. The thickness of the airgap is represented by h.

Chapter 2. This tapering angle is chosen to be $\gamma = 45^0$ (See Fig. 4.3). In the analysis, we first evaluated the embedded S-parameters, exciting only one element when the feed is surrounded by matched loadings. Assuming a port impedance of 125 Ω, the S-parameters are reported in Fig. 4.5. As can be seen from the figure, the feed is well matched within the operational frequency band. We also investigated the mutual coupling between the array elements and highlighted in in Fig. 4.5. The result shows that the array has a maximum mutual coupling level about -14 dB, which is defined between the adjacent elements along the slot axis. The loss due to the mutual coupling between the elements have been evaluated and found out to be less than 0.55 dB within the operational bandwidth.

4.4 Lens Design

As a next step, the lens optimization is performed considering the project requirements. In this study, in order to get fast and accurate lens optimization, an Integrated Lens Antenna Shaping tool (ILASH) [51] is used. It includes a GO tools for quick design of these

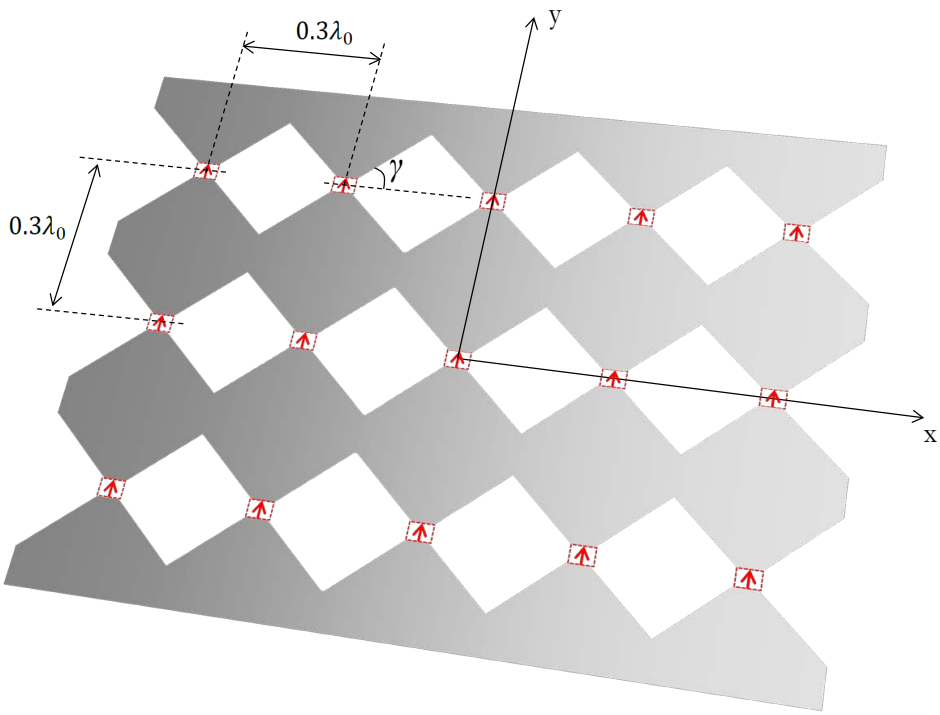

Figure 4.4: Perspective view of the connected leaky slot array.

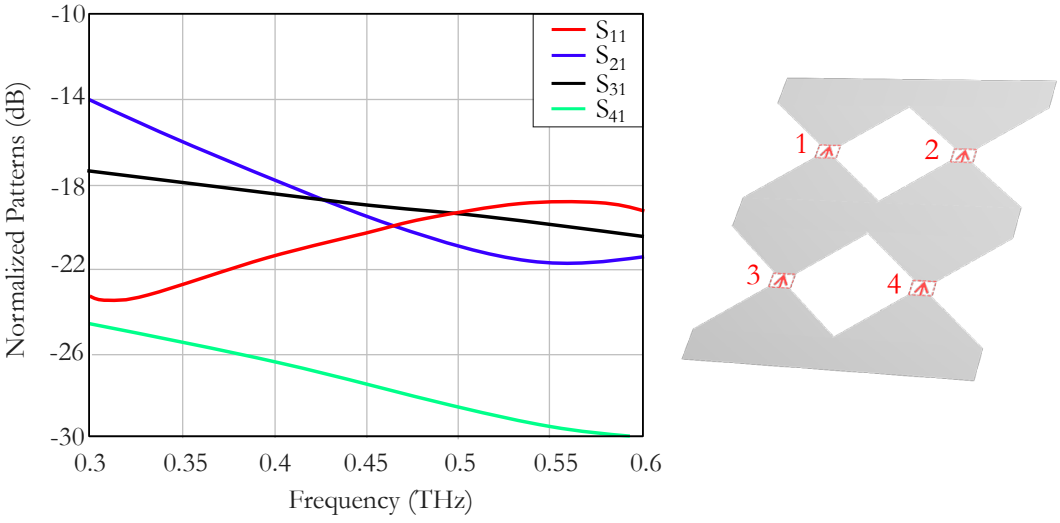

Figure 4.5: Embedded S-parameters of the antenna array as a function of frequency.

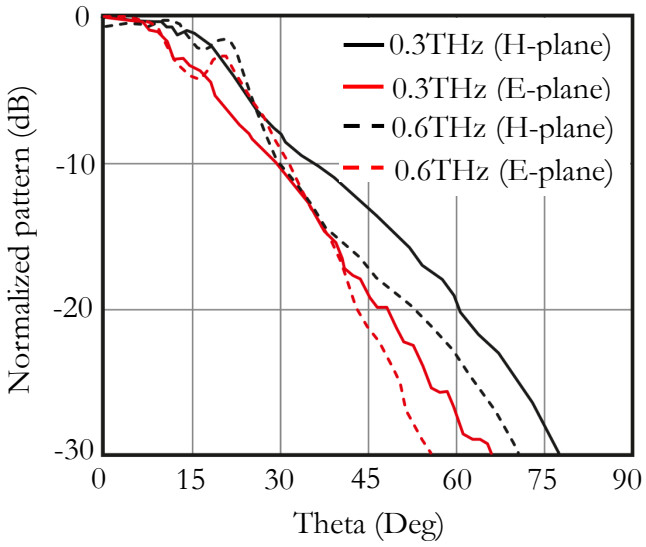

Figure 4.6: Primary fields radiated into semi-infinite silicon dielectric located on top.

types of lenses subject to a number of different target specifications, GO/PO tools for the computation of the lens equivalent surface currents and radiation pattern, and a Genetic Algorithm (GA) optimization tool for advanced lens design.

We followed the following steps during the optimization:

- Far-field beams inside the semi-infinite silicon radiated by the central array element (in the presence of its surroundings) is simulated by CST and the results are imported into ILASH,
- A cost function is defined to create a mask for the desired secondary beams in terms of HPBW and side-lobe radiation for 0.3, 0.45 and 0.6 THz,
- Using a modified Abbe lens based design, GA tool is used in order to optimize the inner and outer shell geometries by means of minimizing the cost function,
- The optimized geometry is then used in the second stage of optimization as an initial geometry,
- At this stage, reference system in CST is changed accordingly to export the radiation due to offset feed position (The furthest element located in the edge is taken into account).

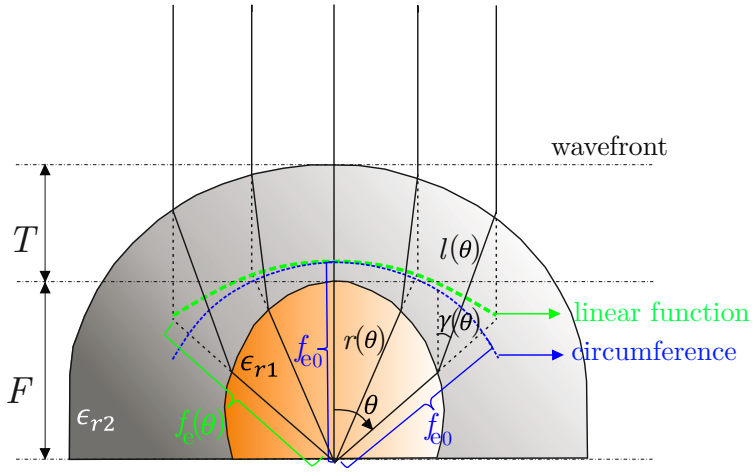

Figure 4.7: Ray distribution from a modified Abbe sine lens with an intersection curve defined as a linear function (highlighted with a green-dashed curve) defined between the inner and outer shells. A circumference curve with a fixed radius of f_{e0} from an Abbe sine lens (blue-dashed line) is also highlighted for the sake of comparison.

- Two beam masks are defined for the new optimization: One for the central element and one for the offset feed (the last element in the array) to maximize the scanning performance of the lens,

- Having minimized the cost function, we finalize the lens optimization process.

Due to the requirements of the project, the lens should provide collimated radiation not only for the on-axis feed but also for off-axis feed elements. Lens geometries satisfying Abbe sine condition are reported to provide high performances in terms of beam stability and beam scanning performance for reasonable off-axis feed displacements [52]. The Abbe sine condition imposes that the extended rays departing from the on-axis source and the corresponding extended transmitted rays intersect on a circumference, with a fixed radius of f_{e0}, which is centered at central feed [52]. The abbe sine condition can be written as [52]:

$$(f_{e0} - r(\theta))sin(\theta) = l(\theta)sin(\gamma(\theta)) \tag{4.1}$$

Where $r(\theta)$ represents the length of the inner shell, $l(\theta)$ represents the length of the outer shell and $\gamma(\theta)$ represents the angle of the rays (See Fig. 4.7). One can consider to modify the Abbe sine condition in such a way that the rays' intersection curve is not a circumference anymore but a linear function that can be calculated as [52]:

$$f_e(\theta) = f_{e0} - \Delta f_e(cos(Q\theta)) \tag{4.2}$$

By replacing the Abbe sine circumference with a modified Abbe lens intersection curve, one can achieve a wider scan angles with providing better efficiency [52], [46]. Therefore, we started the optimization process by using a modified version of a conventional Abbe lens. Cross section of a modified Abbe sine lens can be seen from Fig. 4.7. The figure shows that the intersection points of the projection of the rays departing from the on-axis feed and the corresponding extended transmitted rays from the point source all lie on a on a linear function with a length of $f_e(\theta)$ from the central source. Thanks to this intersection curve, the rays coming out from the outer shell are parallel to each other and they produce a planar phase front, which ensures frequency stable beams not only for broadside radiation but also for reasonable scan angles for electrically large lenses [46].

The optimized double shell lens geometry can be seen form Fig. 4.8a with its design parameters. The material of the inner lens is silicon ($\epsilon_{r1} = 11.9$) and it has a height of $F = 40$ mm with having a radius of 27 mm. Outer shell, on the other hand, is made of fused quartz ($\epsilon_{r2} = 3.8$) with a thickness of $T = 40$ mm and a radius of 55 mm. In order to evaluate the performance of the optimized DSL, an extended hemispherical single shell lens (SSL) made of silicon is also designed as a reference solution. For the sake of fair comparison, SSL geometry is designed such that it provides similar gain and beamwidth as the double shell one at the center frequency, 0.45 THz. The SSL geometry and its design parameters are shown in Fig. 4.8b. The lens has a radius of $R = 44.6$ mm and an extension length $L = 0.35R$. We used the same airgap between the ground plane and the lens as it was used for the feed array design in Section 4.3.

To get an initial idea about the performance of the lens, as a first step, we evaluated the ray distribution inside and outside the lens in ILASH. For this purpose, firstly, a point source is located at the center of the feed plane whereas, in the second case, the source is shifted by $3.3\lambda_0$ which corresponds to the last pixel of the 23×23 feed array. The ray distributions are shown in Fig. 4.9a and b for on-axis and off-axis feed positions, respectively. As can be seen from the figure, the rays due to a point source exit the lens parallel for both scenarios, as expected.

4.5 Numerical Results

First, we report the secondary beams radiated by the SSL in Fig. 4.10a and b for H and E-planes, respectively. In the figure, each beam is associated to one single array element

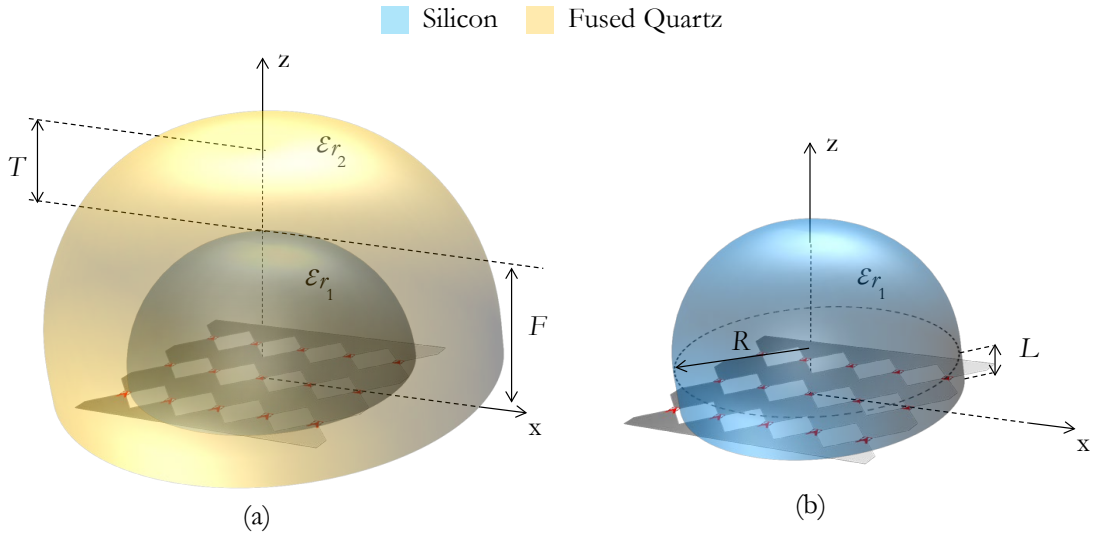

Figure 4.8: Lens geometries with their design parameters for: (a) DSL design, and (b) SSL design to be used as a reference geometry.

that is being excited whereas all the surrounding array elements are terminated by loadings. Assuming all the scan angles and the frequencies, the results show that the maximum gain variation in the secondary beams radiated by SSL design is significant, almost 6dB. The gain variation from the optimized DSL antenna is highlighted in Fig. 4.11, also for H and E-planes. One can easily see the improvement, with having a maximum variation of 2.7 dB, considering all the beams in both planes. Compared to the conventional SSL design, it is quite clear that the proposed DSL based design is able to provide much more stable secondary beams in terms of gain variation within the frequency band.

Fig. 4.11 also shows that the level of the side lobes generated by the optimized DSL structure seems to be higher compared to the SSL design, especially at the highest frequency. This could be associated to the phase modification phenomena that occurs between the two shells of the DSL. Since the desired antenna gain is relatively high and the antenna dimensions are very large in terms of wavelength, it is difficult to adjust the phase accordingly on the shells. However, the side-lobes are extremely narrow and less than 7 dB with respect to the maximum gain associated to the adjacent pixel at the worst case scenario.

One other important parameter for the proposed design, as mentioned before, is the scan loss which should be minimized for off-axis feeds to satisfy the requirements of the proposed imager. For this purpose, we evaluated and reported this loss for the proposed DSL and the reference SSL designs in Table 7.1 at frequency points 0.3 THz, 0.45 THz and 0.6 THz. According to the table, DSL design improves the scanning loss significantly compared to

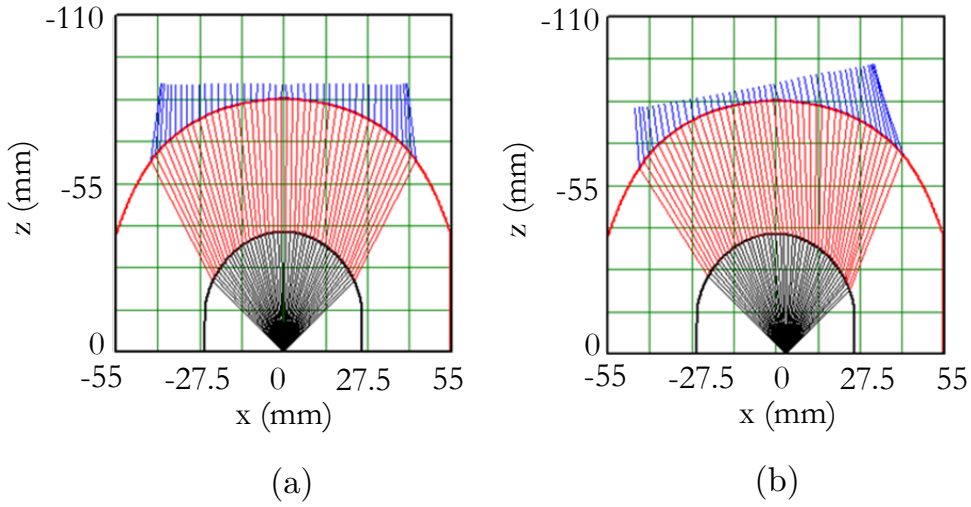

Figure 4.9: Ray distribution inside and outside the optimized double shell lens due to a point source located at (a) the center of the lens and (b) $x = 3.3\ \lambda_0$ (corresponds to the position of the feed located at the edge).

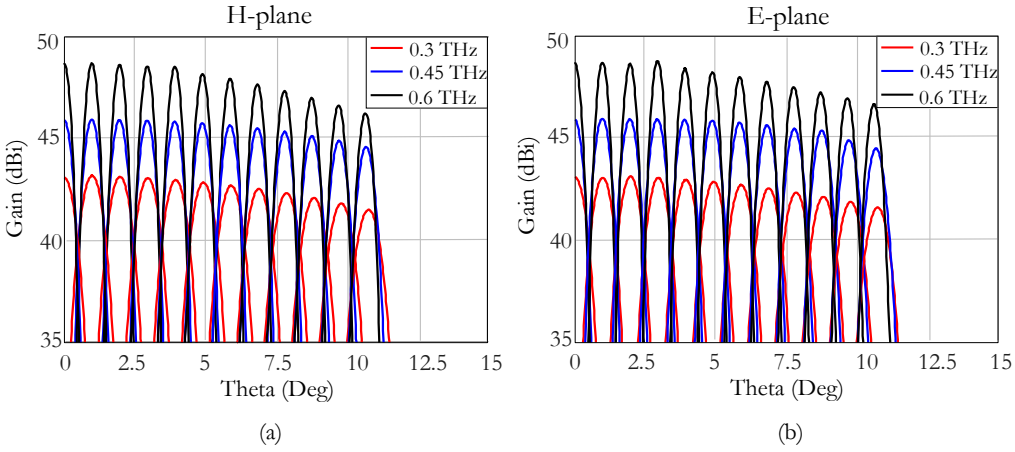

Figure 4.10: Secondary beams obtained by the conventional SSL design for: (a) H-plane, and (b) E-plane at 0.3 THz, 0.45 THz and 0.6 THz.

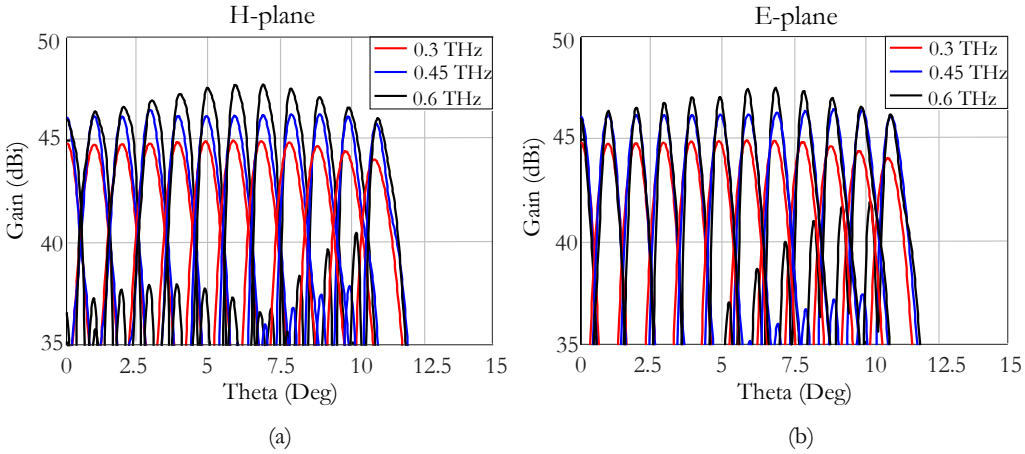

Figure 4.11: Secondary beams obtained by the optimized DSL design for: (a) H-plane, and (b) E-plane at 0.3 THz, 0.45 THz and 0.6 THz.

Table 4.1: Scan loss comparison between the proposed DSL antenna and the conventional SSL design

H-plane

Frequency (THz)	DSL	SSL	Improvement (dB)
0.3	-0.81	-1.69	**0.88**
0.45	-0.29	-1.4	**1.11**
0.6	-1.37	-2.46	**1.09**

E-plane

Frequency (THz)	DSL	SSL	Improvement (dB)
0.3	-0.88	-1.53	**0.65**
0.45	-0.33	-1.44	**1.11**
0.6	-1.46	-2.04	**0.58**

the SSL design. More precisely, in average, we observed an improvement of about 1.02 dB and 0.78 dB in the H and E-planes, respectively.

As a result of improved gain variation and scan loss, one can expect to have stable beamwidth as a function of feed position and frequency. To see how much DSL solution improves the performance in terms of the beamwidth stability compared to reference SSL design, we highlight HPBW variation as a function of feed position for SSL and DSL

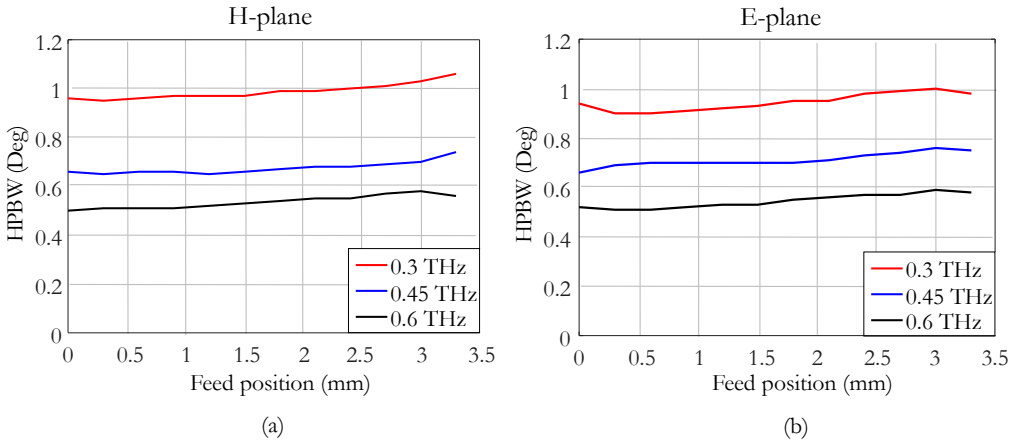

Figure 4.12: Beamwidth variation obtained by the SSL design as a function of feed position for three frequencies within the band for (a) E-plane, and (b) H-plane.

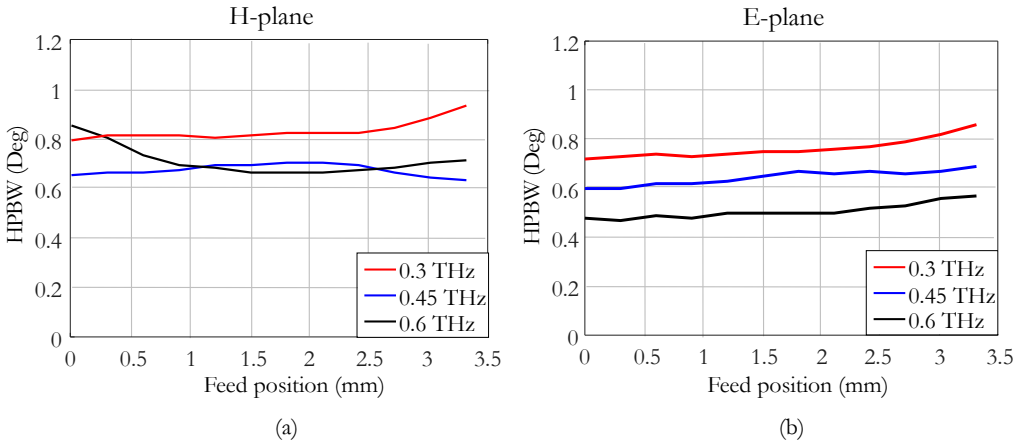

Figure 4.13: Beamwidth variation obtained by the proposed DSL design as a function of feed position for three frequencies within the band for (a) H-plane, and (b) E-plane.

designs in Fig. 4.12 and Fig. 4.13, respectively, at 0.3, 0.45 and 0.6 THz. It is clear that the beamwidth variation in the secondary beams obtained by the proposed DSL design is much less than the variation one can achieve by using a conventional extended hemispherical SSL design.

4.6 Conclusion

In this chapter, we performed a preliminary study to provide a design concept that can be considered as an alternative approach described in the previous chapter. The concept is

based on the integration of a connected array of leaky slot antenna, as a lens feeder, to a double shell lens to achieve frequency stable beams within an octave bandwidth. We have demonstrated that the proposed concept improves the frequency stability of the beams significantly compared to the conventional SSL based design. In addition to the on axis feeding, scanning performance is also evaluated and have been shown that the proposed DSL based concept is able to provide better beam scanning performances with respect to conventional SSL design within the band of operation. It should be noted that, at this stage, this preliminary study does not take into account the dielectric losses in the lens materials. This issue needs to be investigated as a future work.

Part II

Integrated Lens Antennas for tightly spaced FPA Applications

ANTENNA COUPLED KIDs

Part II of this thesis will focus on a scenario using a direct detection imager based on an antenna coupled KID array. Future astronomic THz radiometric systems require tens of thousand receivers to achieve high sensitivities and to provide a large Field of View (FoV). Here we consider a design based on a tightly spaced Focal Plane Array (FPA) with thousands of pixels located at the focal distance of a telescope. A sketch of the proposed FPA antenna design which will be dealt with in the following chapters is shown in Fig. 4.14. The system is characterized by a large $f_{\#}$ (F/D) telescope to avoid significant performance degradation for peripheral elements.

We will use integrated lens antennas as FPA elements, to serve as a reflector feed, since

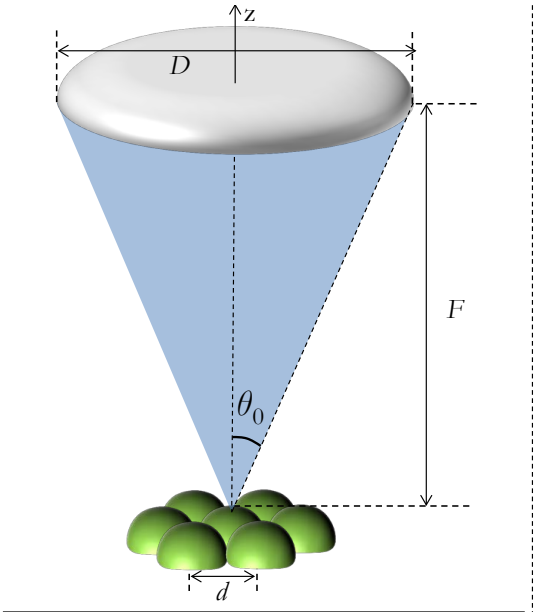

	Space instrument	Earth based instrument
F/D	≈21	≈9
Frequency band	1.4-2.7 THz	0.8-0.9 THz
Lens material	Silicon	Sapphire wafer+Silicon
Df	1.55mm	1.55mm
d	1.6mm	1.6mm

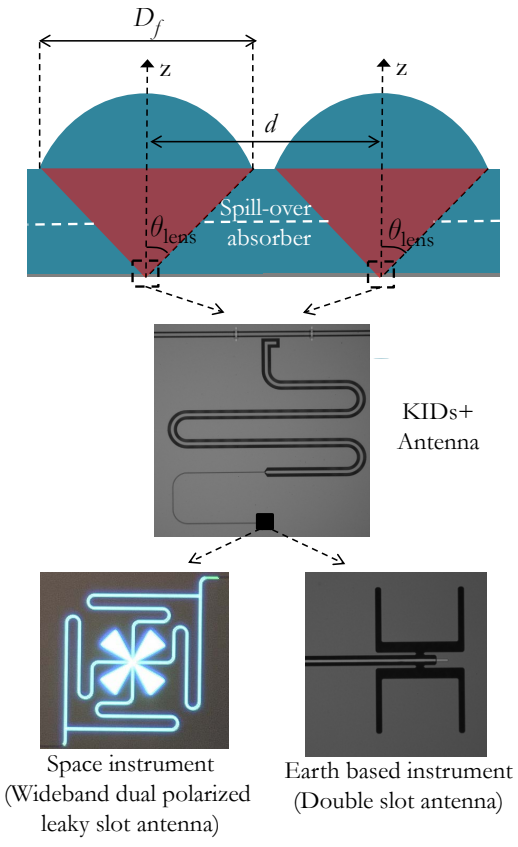

Figure 4.14: The schematic of antenna coupled KIDs scenario. Tightly packed lenses located at the focal distance of a reflector with large $f_{\#}$ are highlighted on the left hand side. On the right hand side, cross section of the lenses are shown together with their feed and a mesh absorber between the lenses to suppress lateral radiation inside the lens array due to the feed spill-over.

they can provide practical solutions and are easy to manufacture in tightly spaced FPAs. Fig. 4.14 shows the lenses together with their feeding, being located at the lens focus to form feed per lens scenario. The FPA elements are separated by a distance d that is typically in the order of $d \leq \lambda_0 F/D$ where λ_0 is the free-space wavelength at the center frequency, f_0. Considering such small FPA element separations, a lens truncation angle, θ_{lens}, may help to achieve closely packed FPAs. One problem for tightly packed FPAs could be the superior coupling that may occur between the FPA elements due to spill-over radiation. To reduce the coupling between the lenses due to feed spill-over, we use a mesh absorber to suppress the lateral radiation inside the lens array. The details of the spill-over absorber design are explained in Appendix D.

Two antenna concepts are used depending on the application type: A double slot based design and a leaky slot based design. Chapter 6 will be focusing on the design of a FPA based on double slot antenna concept, specifically aiming at applications for Earth-based

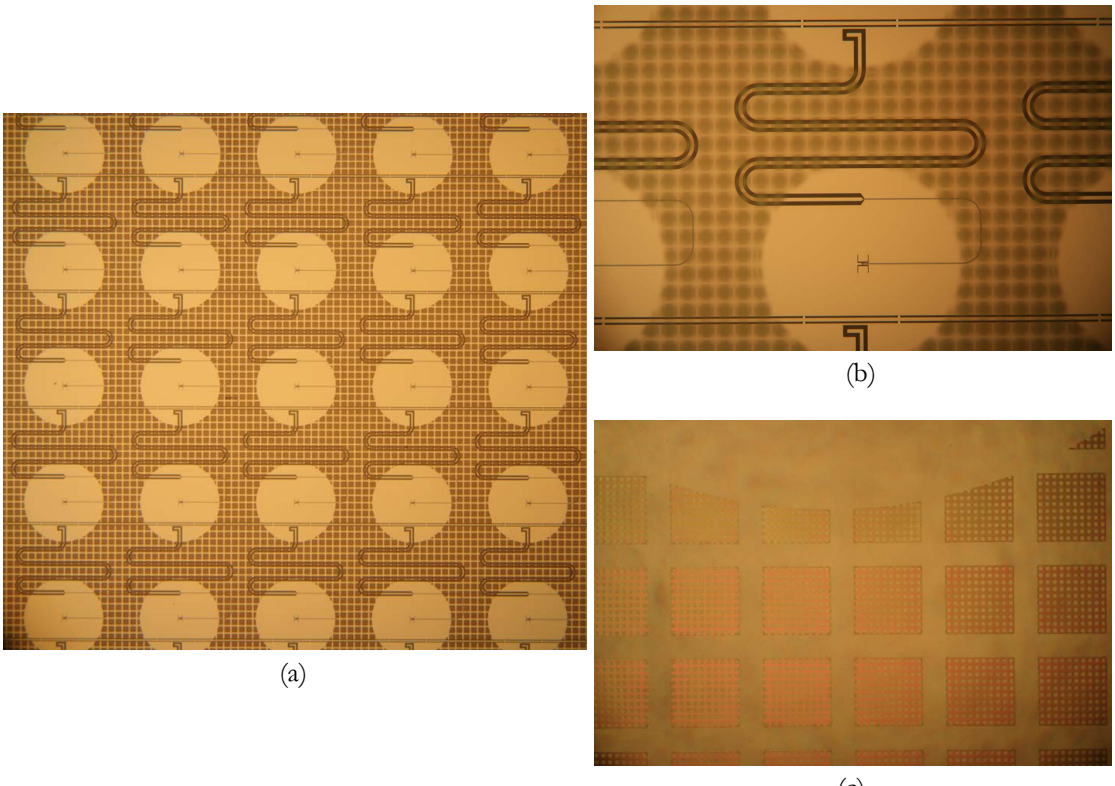

(a) (b) (c)

Figure 4.15: The picture of the fabricated double slot antenna geometry together with KIDs: (a) Top view of the antenna array (b) focusing at a single pixel and (c) the mesh absorber (Courtesy of SRON).

Figure 4.16: The picture of the fabricated dual-polarized leaky slot array coupled KIDs (Courtesy of SRON).

observation where the need of bandwidth is less stringent. In Chapter 7, on the other hand, we will aim at a wideband dual-polarized leaky lens antenna design to achieve superior sensitivities, aiming at applications for Space-based observation. The antennas are coupled to KIDs, which allows a single readout unit for thousands of pixels [10]. The images of the fabricated antenna coupled KID arrays have been shown in Figs. 4.15 and 4.16 for the double slot and the dual-pol leaky antennas, respectively. The following chapters will focus on the design and the experimental characterization of these two antennas to be used in tightly spaced FPA applications.

Part II of the thesis consists of three chapters:

- Chapter 5 provides a brief discussion on the imaging speed for Earth and space based observations.
- Chapter 6 gives some design rules for double slot antennas at sub-mm range and provides three double slot based antenna designs for the SPACEKIDs and A-MKID projects.
- Chapter 7 provides a dual-polarized wideband leaky slot based lens antenna design

for space based astronomical instruments (SPICA/SAFARI like scenario).

CHAPTER 5

Direct Detection Focal Plane Arrays: On the Imaging Speed

Next generation imaging systems based on direct detection mostly benefit from large format antenna arrays located at the focal distance of a telescope with large $f_{\#}$ (F/D). They typically require cryogenically cooled detectors to reduce undesired additional noise and to maximize the sensitivity of the imaging system. This chapter will focus on the investigation of the imaging speed for such systems for different scenarios including earth and space based applications.

5.1 Introduction

The trend in THz radiometric systems is the use of large focal plane (staring) arrays. Specifically future, satellite based, astronomic THz radiometers will be most likely based on cryogenically cooled detectors to reach the highest sensitivities, will consist of tens of thousands receivers to provide a broad field of view and could address simultaneously a broad portion of the THz band. A cornerstone in the dimensioning of these systems is the study [53]. This study addresses the most important signal to noise and sampling considerations that could lead to a preference for absorbers based architectures rather than antennas when the instruments and the detectors are photon noise limited (the instrument including the optics is cold).

The specific scenario addressed in this chapter is shown in Fig. 4.14. It is characterized by a large $f_{\#}$ reflector. The large $f_{\#}$ is chosen to realize images with thousands of pixels without significant degradation of the performances of peripheral elements. A view of the instrument is depicted in Fig. 5.1. The radiometric system is enclosed in an instrument box cooled at a temperature T_{IB}, whereas the detectors are placed in what is typically referred as cold box at a temperature T_{CB}. These two boxes can make a contribution to the noise of the instrument when the detectors are background limited. The directivity of the antenna will play then a significant role to reduce the impact of this noise on the imaging speed.

5.2 Imaging Speed for Distributed Sources

In astronomy, radiometry is the primary tool used to characterize the electromagnetic power spectrum of emission due to sources distributed in space. The purpose of imaging radiometers is to measure such spectral radiation for every direction in the sky. The key observable parameter is the brightness $B_{sky}(\theta, \phi)$. Planck equation defines the brightness at frequency f as a function of the sky temperature $T_{sky}(\theta, \phi)$ in every angular direction.

$$B_{sky(f,\theta,\phi)} = \frac{f^2}{c^2} \frac{2hf}{\frac{hf}{e^{k_B T_{sky}(\theta,\phi)}} - 1} \tag{5.1}$$

where $h = 6.626068 \times 10^{-34}$ Joules sec. is the Plancks constant, $k_B = 1.380 \times 10^{-23}$ m^2 kg s^{-2} K^{-1} is the Boltzmann constant, $c = 2.99 \times 10^8$ m/s is the speed of light speed and $T_{sky}(\theta, \phi)$ the equivalent temperature of the investigated direction of the sky.

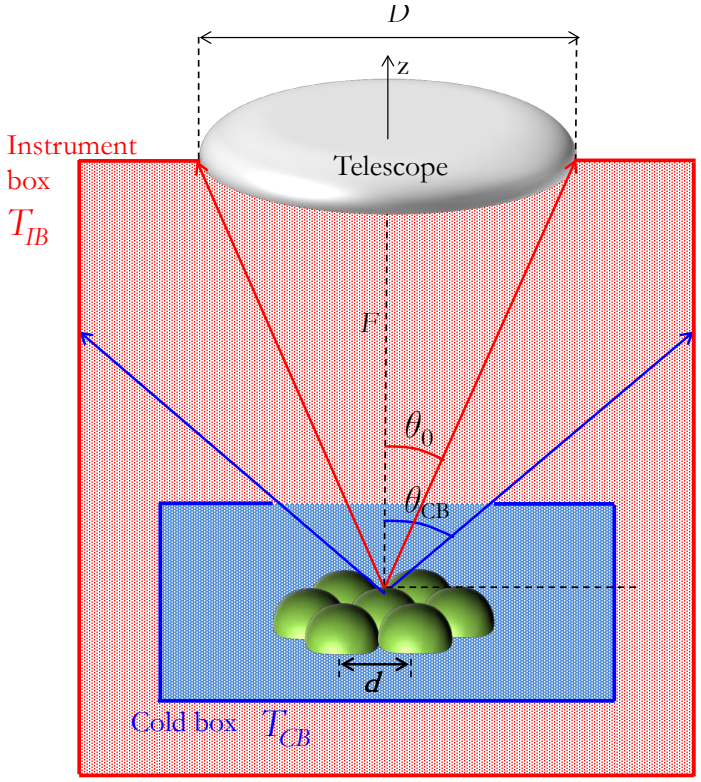

Figure 5.1: Schematic of the radiometric imaging instruments.

An instrument able to perform radiometry is composed by a large telescope to collect the signals from the sky and focal plane array of sensors. Each of these sensors is composed by a radiation coupler (antennas or absorbers) and a detector that transforms the THz electromagnetic signal into low frequency electrical one. Later in the thesis, we will be focusing on the antenna design for different instruments for the projects that have been briefly explained in the introduction chapter.

The scope of the investigation is restricted to direct detection schemes, for which cryogenically cooled superconducting detectors can provide extremely high sensitivity [54] and large format arrays. The signal to noise in such systems can be expressed as

$$\frac{S}{N} = \frac{p^{sky} BW}{NEP} \sqrt{t_i} \tag{5.2}$$

Where t_i is the integration time, NEP is the Noise Equivalent Power of the detector and p^{sky} is the received power by the detector, from the sky, over a bandwidth BW:

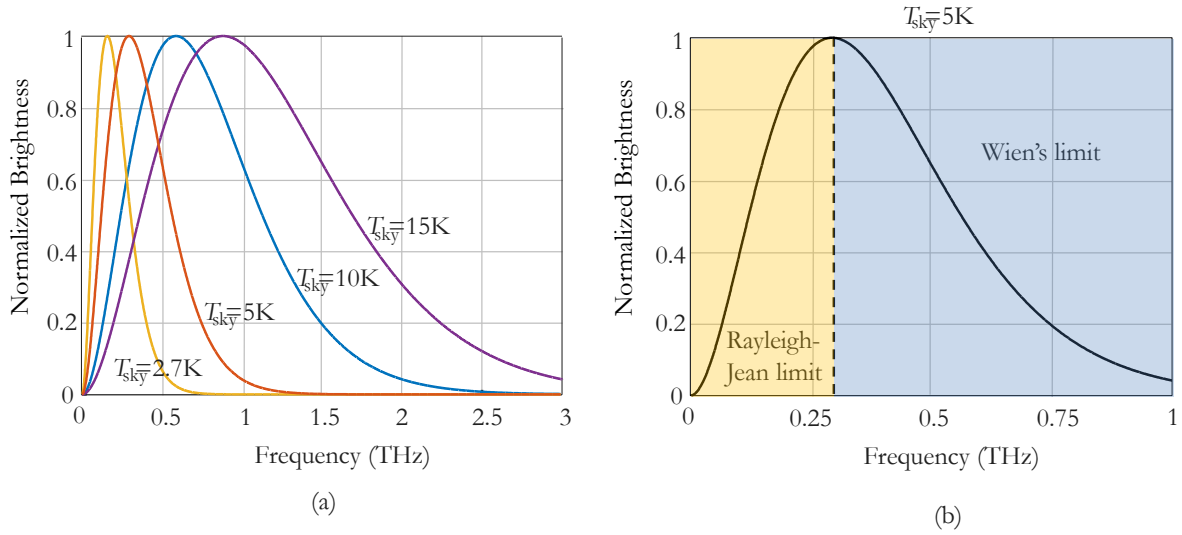

Figure 5.2: Normalized brightness as a function of frequency for various sky temperatures, T_{sky}.

$$p^{sky} = \frac{1}{BW}\int_{f_0-BW/2}^{f_0+BW/2} P^{sky}(f)df \tag{5.3}$$

Appendix A shows the spectral power received from a distributed black body of a certain angular dimension, Ω_s, can be expressed as:

$$P^{\Omega_s} = \frac{2hf}{\frac{kf}{e^{k_B T_{sky}(\theta,\phi)}} - 1}\eta_{co}^{\Omega_s}(f) \tag{5.4}$$

where $\eta_{co}^{\Omega_s}(f)$ is antenna coupling efficiency due to a distributed source within Ω_s solid angle. It includes spill-over efficiency ($\eta_{so}^{\Omega_s}$), antenna feed efficiency (η_{feed}) and the efficiency associated to the detector losses (η_{det}) (See Appendix B). It should be noted that, in Eq. 5.4, factor of 2 comes from the dual-polarized operation of the antenna system. If the antenna has a single polarization only, then, one has include a factor of 0.5 in the antenna coupling efficiency, $\eta_{co}^{\Omega_s}$.

In case of imaging radiometers, the following different incoherent sources are of relevance. Each of these contributions can be express using the same procedure as described in the Appendix B:

- The signal of interest is the sky radiation (including the possible effect of the optics) referred to the reflector solid angle, Ω_{ref}

$$P_{sky}^{ave}(f) = \frac{2hf}{e^{\frac{hf}{k_B T_{ave}}} - 1} \eta_{co}^{\Omega_{ref}}(f) \tag{5.5}$$

- The total undesired noise power for the central feed (assumed to be representative for the entire array), $P_{und}(f) = P_{IB}(f) + P_{CB}(f)$, is given by the superposition of powers due to two statistically independent type of rays reaching the receivers: rays arriving from instrument angular region, Ω_{IB}, and rays coming from the cold box angular region, Ω_{IC} (see Fig. 5.1):

$$P_{IB}(f) = \frac{2hf}{e^{\frac{hf}{k_B T_{ave}^{IB}}} - 1} \eta_{co}^{\Omega_{IB}}(f) \tag{5.6}$$

$$P_{CB}(f) = \frac{2hf}{e^{\frac{hf}{k_B T_{ave}^{CB}}} - 1} \eta_{co}^{\Omega_{CB}}(f) \tag{5.7}$$

The NEP can be basically divided in two terms: The detector intrinsic noise and the background noise (associated to P^{sky}, P_{IB} and P_{CB}):

$$NEP^2 = NEP_d^2 + NEP_b^2 \tag{5.8}$$

For observations from a given beam pointing direction a useful parameter to quantify the performance of a telescope is its speed of acquisition, imaging or mapping speed. This latter can be defined as the inverse, speed=$1/t_i$ of the acquisition time necessary to obtain a certain SNr. Using eq. 5.2, simple algebra shows that

$$speed = \frac{1}{SNr^2} \frac{(p^{sky} BW)^2}{NEP_d^2 + NEP_b^2} \tag{5.9}$$

While the purpose of radiometric imaging is to measure the angular distribution of the sources of the brightness in the sky, $B_{sky}(\theta, \phi)$, this distribution is eventually estimated by performing a discrete Fourier Transformation of the samples of the amplitudes acquired in a focal plane populated by many receivers (antennas). In order to be able to reconstruct the original brightness via such Fourier Transformation with the maximum resolution allowed by the reflector system, the sampling of the focal plane must be related to the $f_\#$ (also indicated as F/D) of the reflector system. It is well known [55] that the sampling, d, must be $d = 0.5\lambda f_\#$ for incoherent imaging. Denser sampling is not useful because it is the antenna diameter that limits the resolution. Scarcer samplings lead to lower resolutions. However,

the samples do not need to be acquired simultaneously. This means that larger focal plane samplings can be useful too. Giggling is the process of re-pointing the reflector to different directions in order to acquire all the useful samples that are necessarily skipped with samplings larger than $d = 0.5 f_{\#} \lambda$. Fig. 5.3a shows a graphical representation considering three different sampling configurations that are typically adopted/proposed. $d_p = 0.5 f_{\#} \lambda$, $d_f = 2d_p = f_{\#} \lambda$ and $d_e = 2d_f = 4d_p = 2f_{\#} \lambda$. Note that in d_p, p indicates power sampling because it is the required sampling if one can only detect the power spectrum of the incoming signal (the case in radiometry); in d_f, f indicates field sampling, because it would be the appropriate sampling if one was able to detect a signal in both its amplitude and phase (never in radiometry), while in d_e indicates the efficient sampling because it is the sampling that leads to the maximum power detected from a point source aligned with the reflector system.

It is apparent from Fig. 5.3b that the antenna needs to be re-pointed four times if one uses a focal plane that is sampled at field sampling period. Generalizing if n' is the total number of pixels needed according to power sampling, in order to reconstruct a given field of view, and N is the factor by which n is divided in the realized implementation, $n' = n/N$, the acquisition time of the n' configuration is $\tau' = \tau N$, where τ is the time of acquisition of a each pixel. So while the power sampling is simply characterized by a certain integration time τ_p, the field and efficient samplings, with receiver characterized by integration time τ_f, and τ_e, lead to total observation time $\tau'_f = 4\tau_f$, and $\tau'_e = 16\tau_e$ respectively.

The speed ratio between two FPA configurations, with a sampling of $N_s = N^2$ (e.g. 1, 4, 16) each, will then be given by:

$$\frac{speed_1}{speed_2} = \frac{N_2}{N_1} \frac{(p_1^{sky})^2}{(p_2^{sky})^2} \frac{NEP_{d2}^2 + NEP_{b2}^2}{NEP_{d1}^2 + NEP_{b1}^2} \tag{5.10}$$

In case of an astronomical instrumentation, the instruments are designed such that they are limited by the background noise and not the detector. Therefore the speed ratio becomes

$$\frac{speed_1}{speed_2} = \frac{N_s^2}{N_s^1} \frac{(p_1^{sky})^2}{(p_2^{sky})^2} \frac{NEP_{b2}^2}{NEP_{b1}^2} \tag{5.11}$$

In such case, for a certain thermal source T incident on the antenna, assuming a system operating over a relative small bandwidth BW centered at f_0, the NEP can be expressed as [54]:

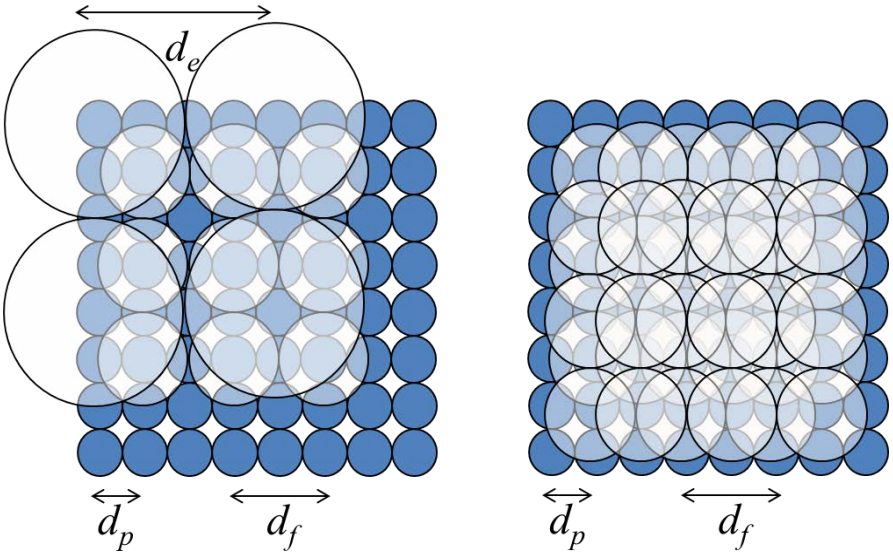

Figure 5.3: (a) Three different focal plane sampling configurations, d_p: $d_f = 2d_p$ and $d_e = 2d_f = 4d_p$, and (b) giggling needed to reconstruct with a field sampling period.

$$NEP_T = \sqrt{2p_T BW(1 + \eta_{ave}\frac{1}{e^{\frac{hf_0}{k_B T}} - 1})hf_0} \tag{5.12}$$

where p_T is any of the incoherent source contributions (Eq. 5.5, 5.6, 5.7) and η_{ave} is the average antenna efficiency over the bandwidth which can be calculated as

$$\eta_{ave} = \frac{1}{BW}\int_{f_0-BW/2}^{f_0+BW/2} \eta_{co}^{\Omega_s}(f)df \tag{5.13}$$

Let us now consider an ideal antenna feed with a circular aperture with the same diameter as the focal plane array spacing, d, having 100% aperture efficiency and receiving two polarizations. In this case, $\eta_{feed}(f) = 1$ and $\eta_{taper}(f) = 1$ over the full bandwidth. The efficiency of the radiometer is then determined by the illumination efficiency of the reflector. Fig. 5.4 shows this efficiency as a function of $d/\lambda f_{\#}$. One can appreciate that the efficiency is low and determined by the spill over at small samplings. For $0.5\lambda f_{\#}$ and $\lambda f_{\#}$ samplings, the spill-over is 5.77 and 1.8 times lower than $2\lambda f_{\#}$ sampling, respectively.

Let us consider an earth based astronomical instrument looking to the sky with no contributions from the instrument or cold box. In this case, the background NEP is given

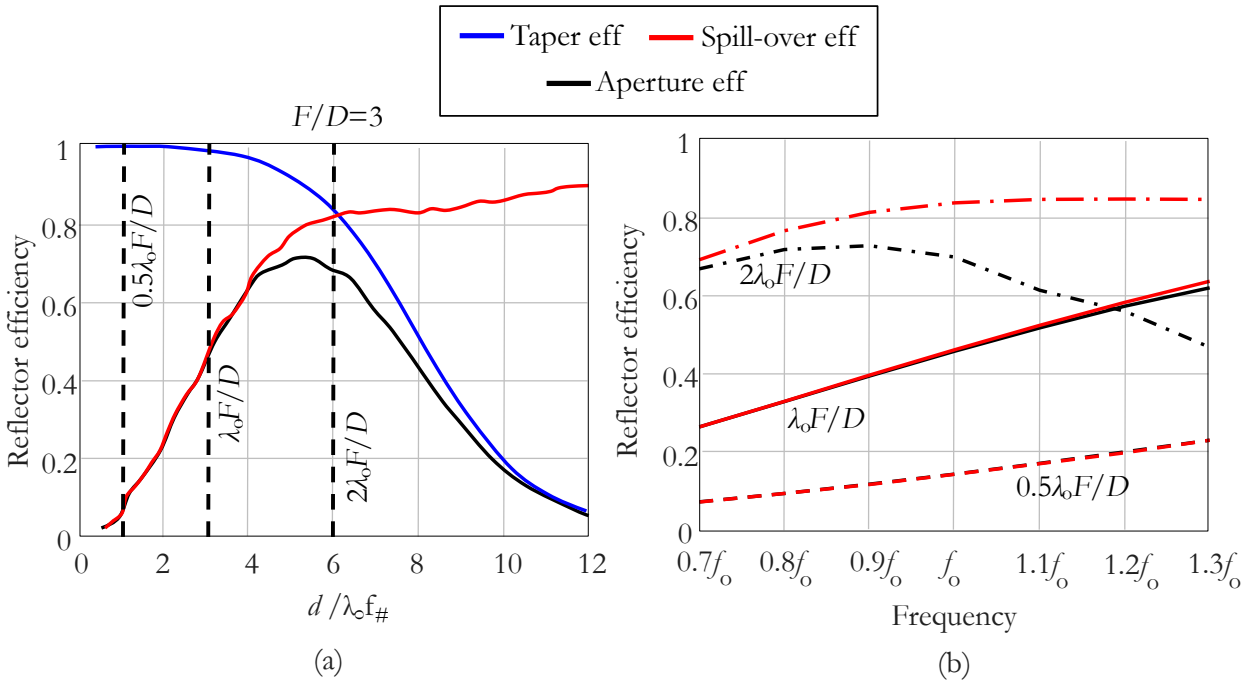

Figure 5.4: (a) Reflector efficiency calculations (a) as a function of the feed aperture and (b) as a function of the frequency for three different feed samplings, all obtained by using a uniform feed aperture.

by the sky temperature directly. In case of instruments operating in the Rayleigh-Jeans (RJ) limit (See Fig. 5.2a), one can do some approximations on the received spectral since $\frac{hf}{e^{\frac{hf}{k_BT}}-1} \approx k_BT$ leading to standard microwave radiometry where

$$p_{ave}^{sky} = \frac{1}{BW}\int_{f_0-BW/2}^{f_0+BW/2} \frac{2hf}{e^{\frac{hf}{k_BT_{ave}}}-1}\eta_{co}^{\Omega_s}(f) \approx 2k_BT_{sky}\eta_{ave} \tag{5.14}$$

The second term in the NEP in eq. 5.12 is the dominating one for high antenna efficiency since $\frac{1}{e^{\frac{hf_0}{k_BT_b}}-1} >> 1$. So the background NEP is proportional to the average antenna efficiency and the square root of the RF bandwidth as in standard microwave radiometery:

$$NEP_b^{RJ} = 2k_BT_{sky}\eta_{ave}\sqrt{BW} \tag{5.15}$$

In this limit, the speed ratio is proportional only to the ratio of jiggling positions:

$$\left.\frac{speed_1}{speed_2}\right|_{sky}^{RJ} = \frac{N_s^2}{N_s^1} \tag{5.16}$$

For high frequencies and low temperatures, representative of sub-millimeter wave space instruments, the black body radiation is determined by the Wien's limit (See Fig. 5.2) where $\frac{2hf}{e^{\frac{hf}{k_BT}}-1} \approx 2hfe^{-\frac{hf}{k_BT}}$. One can relate this expression to the standard Rayleigh approximation by defining an equivalent temperature, T^e, such that $hf_0e^{-\frac{hf_0}{k_BT}} = k_BT^e$. In this case, the spectral power received from the sky will be

$$p_1^{sky} \approx 2k_BT_{sky}^e\eta_{ave} \tag{5.17}$$

where

$$T_{sky}^e = \frac{hf_0}{k_B}e^{-\frac{hf_0}{k_BT_{sky}}} \tag{5.18}$$

The NEP in the Wien's limit is determined by the first term in (8) and it depends on the square root of the antenna efficiency:

$$NEP_b^W = 2\sqrt{k_BT_{sky}^e\eta_{ave}BWhf_0} \tag{5.19}$$

Therefore, in this case, the antenna efficiencies will impact the speed ratio linearly:

$$\left.\frac{speed_1}{speed_2}\right|_{sky}^{W} = \frac{N_s^2}{N_s^1}\frac{\eta_{ave}^1}{\eta_{ave}^2} \tag{5.20}$$

Fig. 5.5 shows the speed ratio for tight samplings ($0.5\lambda_0 f_\#$) for the considered scenarios with respect to the efficient sampling as a function of the temperature of the source, T. The calculations have been done at a single frequency, 850 GHz. The figure shows that the speed advantage for tight samplings is proportional to the jiggling positions and converges to the N_s^2/N_s^1 as the source temperature T increases. The reason why the speed ratio does not become $N_s^2/N_s^1 = 16$ is due to the fact that the speed advantage for tight samplings is reduced when the RJ approximation cannot be considered in the noise.

Fig. 5.5 also shows the speed ratio for tight samplings for low source temperatures where the black body radiation is determined by the Wien's limit. According to the figure, it is still advantageous to do the power samplings since the spill-over for $d = 0.5\lambda f_\#$ is only 5.5 times lower than the $2_\#$ sampling that has a speed penalty of having to do 16 jiggling positions.

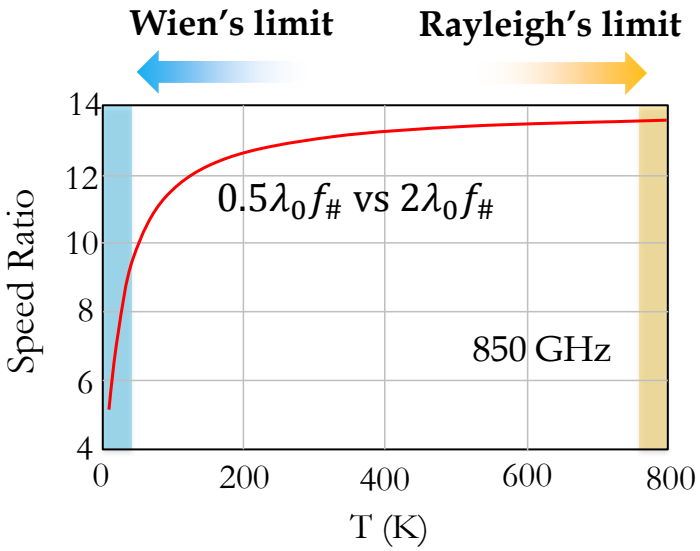

Figure 5.5: Speed ratio calculations as a function of source temperature T at a single frequency, 850 GHz.

CHAPTER 6

Double slot based design

Achieving fully sampled Focal Plane Arrays (FPAs) of direct detectors typically require tightly spaced FPAs for deep space instrumentation in sub-mm wavelengths. For this purpose, highly sensitive microwave kinetic inductance detectors (MKID) with kilo-pixel arrays have been proposed in the literature. Kinetic Inductance Detectors (KIDs) are able to provide superb sensitivity in the sub-mm region combined with ease of operation. Double slot antennas are one of the most commonly used antenna solutions in the literature since they can provide high aperture efficiencies and provide planar lens integrated solutions, leading to easy fabrication process also in sub-mm band. In combination with MKIDs, to reduce the ohmic losses, the antennas are typically made of superconductive materials characterized with having a certain kinetic inductance. In this chapter we perform a parametric study to provide some design rules for sub-mm double slot antennas coupled to MKIDs to have a benchmark reference for the wideband antenna design.

6.1 Double Slot Antenna Coupled to KIDs

6.1.1 State-of-Art Double Slot Design

Double slot antenna shown in Fig. 6.1a is one of the most commonly used antenna since they provide highly efficient planar integrated lens antenna solutions. The concept was first introduced in [2]. The antenna geometry is highlighted in Fig. 6.1a and it consists of two slots with a length of $L = 0.28\lambda_0$ and a slot separation of $S = 0.16\lambda_0$, where λ_0 is the free-space wavelength at design frequency, f_0 [2]. The beams radiated into a silicon dielectric in E, D and H-planes are shown in Fig. 6.1b. In [2], the antenna geometry is optimized in terms of radiation patterns in a semi-infinite dielectric to achieve effective lens illumination.

Double slot antennas coupled to integrated bolometers have been extensively studied in [56]- [57]. Fig. 6.2a shows a double slot antenna with an integrated bolometer, which can be considered as a lumped resistance, with a CPW line connecting the two slots with the bolometer. An RF circuit model of such design is shown in Fig. 6.2b [56]. Thanks to the small dimensions of the receiver, the feeding lines can be fabricated very close to each other leading to similar radiation characteristics to the ones shown in [2].

Starting from the design given in [2], in this chapter, we will aim at providing some design rules for a double slot antenna integrated to MKIDs in sub-mm band. For this purpose we will investigate the integration of a double slot design to a distributed absorbing line (KID resonators in our case) instead of a lumped resistance, taking into account different material stratification used for developing the KID technology, i.e. superconducting ground plane (GP) and sapphire dielectric.

6.1.2 Double Slot Impedance Match

Fig. 6.3a shows a double slot antenna together with a distributed CPW transmission line attached to the center of the slot. An RF model for such design is highlighted in Fig. 6.3b, following the same approach as in [56]- [57]. The RF circuit consists of three parts: The slots, a CPW line that connects the slots (k_{01}, Z_{01}) and a distributed CPW transmission line to serve as an absorbing line (k_{02}, Z_{02}) in reception (or a feeding line for an excitation port defined in transmission). On the other side of the absorbing line, there is a short-circuited stub with an impedance of Z_{stub} attached to the antenna to adjust the imaginary part of the antenna input impedance. The stub can be considered as a series inductance.

We first start with the impedance of the slots alone when they are separated from the CPW line. As mentioned before, we focus on the antenna coupled KIDs scenario in sub-

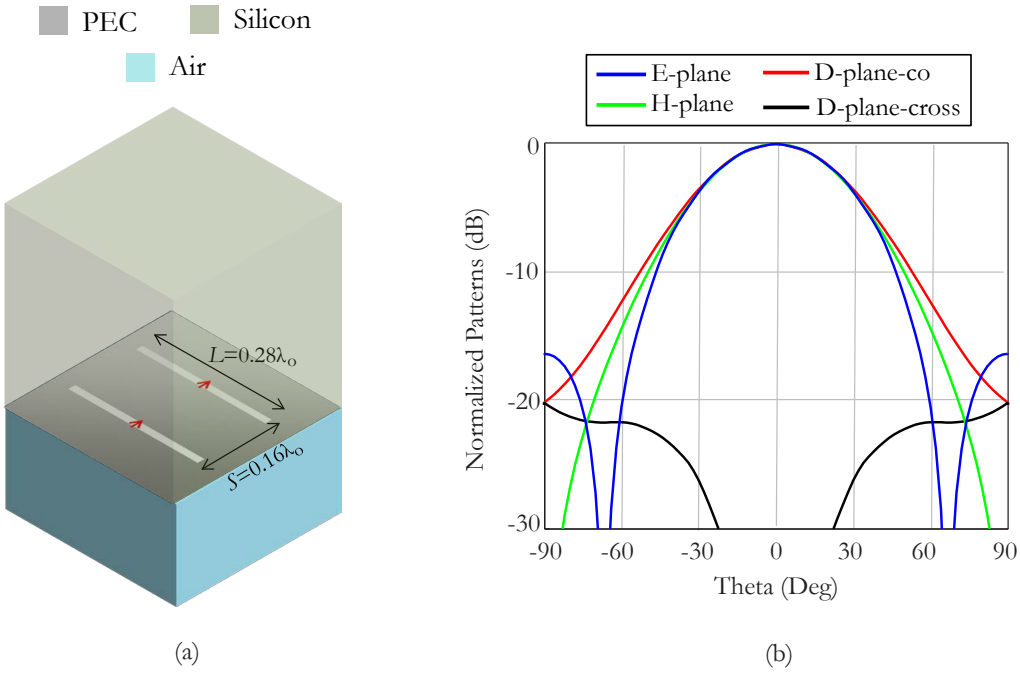

Figure 6.1: (a) Double slot antenna geometry [2] and (b) radiated beams into semi-infinite dielectric.

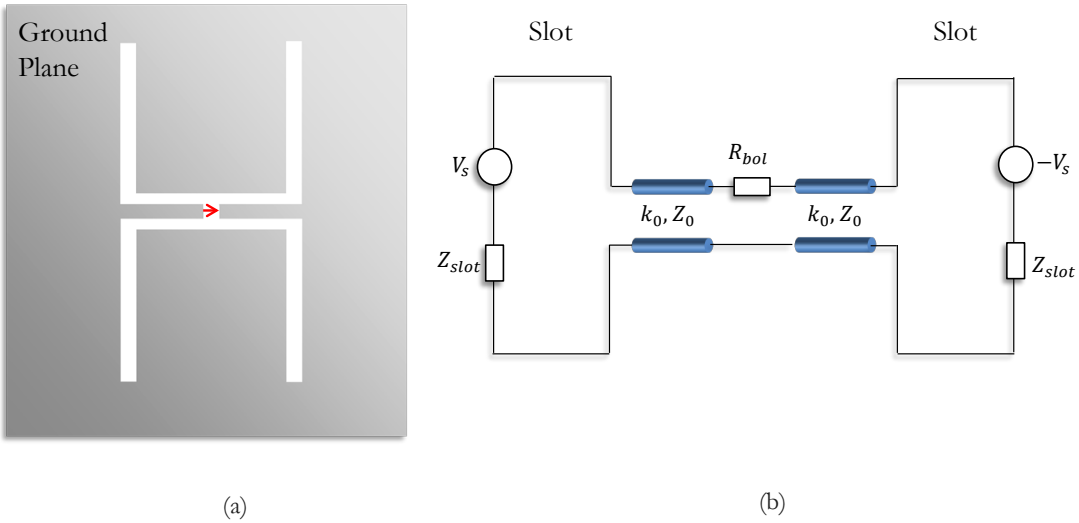

Figure 6.2: (a) A double slot antenna with a bolometer attached to the center of the slot, and (b) its RF equivalent circuit [56].

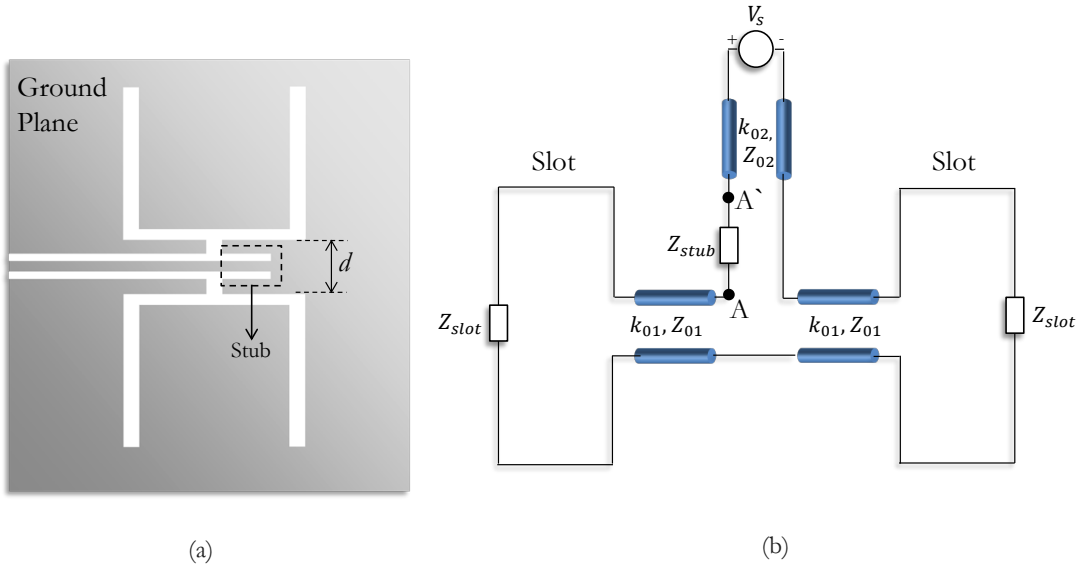

Figure 6.3: (a) A double slot antenna integrated to a distributed CPW line attached together with a matching stub, and (b) its RF equivalent circuit.

mm band with a superconductive material to serve as GP in the presence of a semi-infinite dielectric stratification. The GP has a thickness of about 0.45 µm and is made of NbTiN material which has a kinetic inductance of about 0.4pH/sq. The double slot impedance, Z_{slot} will be evaluated for various antenna material stratification including PEC and NbTiN GP with and without any thickness to provide a guideline for the double slot impedance characterization in sub-mm band. All these effects may be relevant for a resonant antenna such as the double slot. It is useful to mention here that CST does not allow to define a superconductive material with a certain thickness and we followed steps highlighted in Fig. 6.4 to perform a fast characterization of the antenna.

The impedance of the double slot alone in the presence of a semi-infinite silicon medium is highlighted in Fig. 6.5 as a function of frequency for different kinetic inductance and thickness values used to define the GP. One can clearly see that antenna material stratification has a negligible effect on the double slot impedance.

Another important point is the fabrication issues of the CPW lines that are connecting the two slots. It may not be feasible to fabricate the lines small enough in order not to impact the antenna radiation performance as it was the case with the integrated bolometers (Fig. 6.2). This implies that a double slot antenna with larger separation d between the slots is usually necessary. As a result, this separation will have an effect on both the antenna

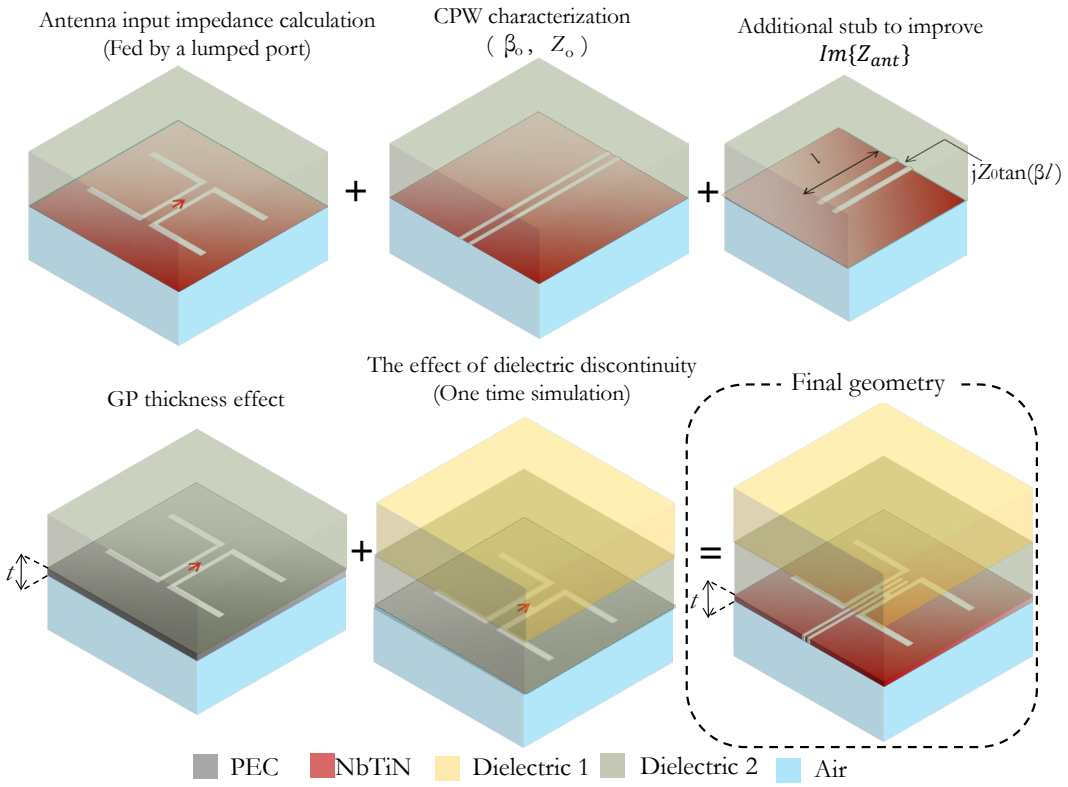

Figure 6.4: Steps followed to evaluate the antenna matching performance.

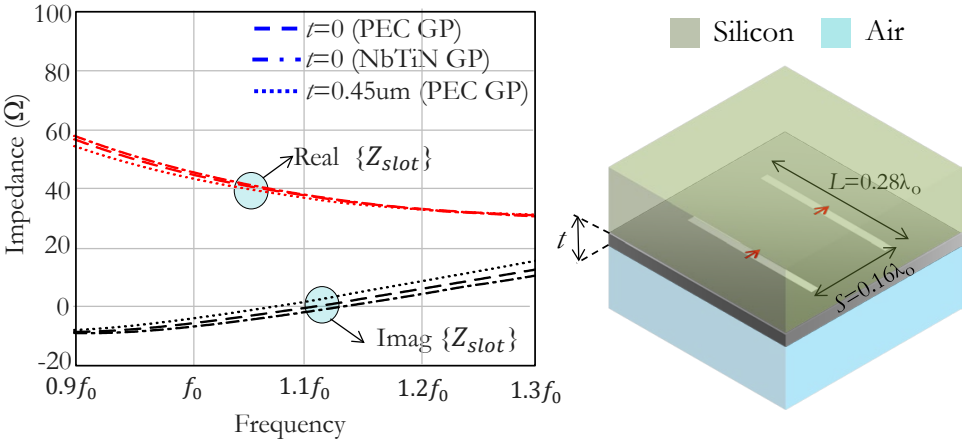

Figure 6.5: Antenna input impedance variation for different (a) PEC GP thickness, (b) dielectric stratification, and (c) GP kinetic inductance values.

impedance and the radiation characteristics of the antenna. To characterize this, assuming the GP is made of PEC, we investigate the electrical properties of the CPW line connecting the two slots (Z_{01}, k_{01}) including the attenuation constant (α), the propagation constant (k_{01}) and the characteristic impedance (Z_{01}) for various vertical slot separation values d by using a tool described in [58]. The results are highlighted in Fig. 6.6 as a function of frequency. According to the figure, larger slot separations lead to higher attenuation constants and lower characteristic impedance values. Higher attenuation constants are associated to the increased radiation losses that eventually will impact the cross-polarization performance of the double slot. Figure 6.6 also includes the case when the GP is made of a superconductive material with a certain a kinetic inductance (NbTiN with an inductance of 0.4 pH/sq in our case) when the slot separation is fixed to $d = 0.033\lambda_0$ to highlight the effect of the GP material. The figure shows that the kinetic inductance of the GP has a significant impact on the propagation constant of the CPW line. Due to its resonant behavior of the double slot geometry, the variation in the k_{01} will introduce a strong shift in the antenna resonance frequency and the reduction in α_{01} will reduce the superior radiations that are associated to the CPW line.

Having investigated the two slots and the CPW lines separately, we then integrate them to investigate the effect of slot separation d on antenna input impedance Z_A, the impedance seen from the input of CPW integrated double slot geometry (See Fig. 6.3b). Assuming the GP is made of PEC and the presence of a silicon semi-infinite dielectric on top, the antenna input impedance variation is highlighted in Fig. 6.7 as a function of d. The figure shows that narrower slot separations lead to significantly higher $\mathfrak{Re}(Z_A)$ and $\mathfrak{Im}(Z_A)$ values at the resonance frequency.

Assuming the slot separation is $d = 0.033\lambda_0$, we highlight the effect of the material stratification on the antenna input impedance Z_A in Fig. 6.8. According to the simulation results, using a PEC GP with a thickness of 0.45 µm introduces a shift with a factor of 1.031 in frequency and 0.93 in Z_A compared to the case when the PEC GP does not have any thickness. Using NbTiN superconductor with a kinetic inductance of 0.4pH/sq as a GP material (no thickness) introduces a shift of 0.948 in frequency and 1.069 in Z_A compared to PEC GP. Finally, taking the semi-infinite silicon stratification as a reference, we obtained a shift of 1.049 and 1.192 by replacing the silicon with sapphire.

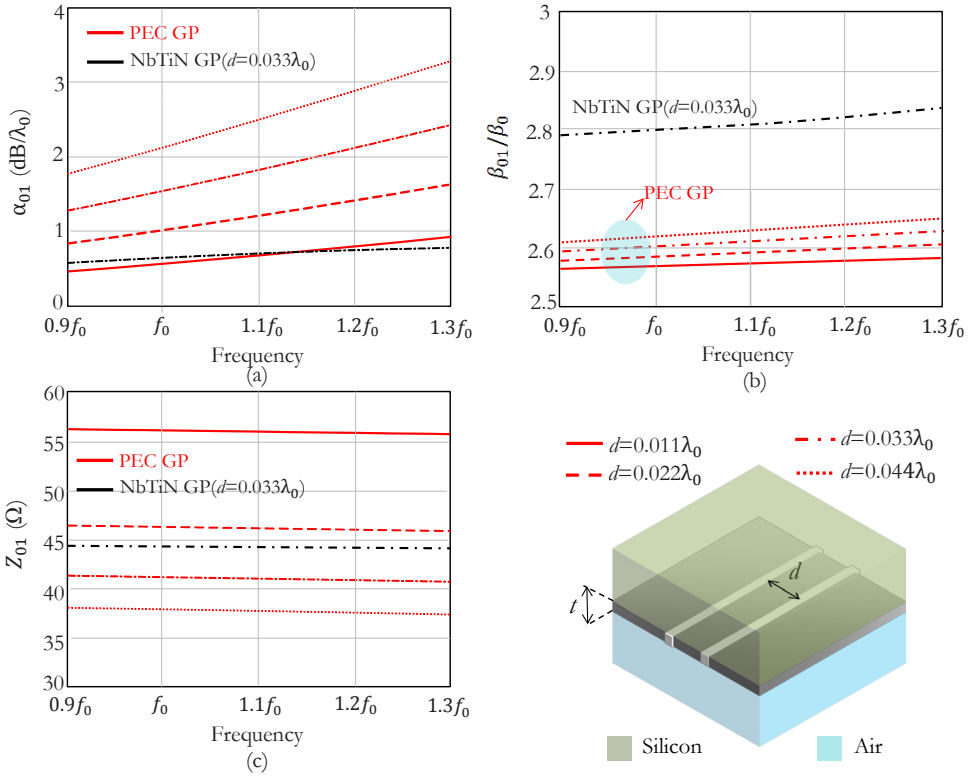

Figure 6.6: Variation of the electrical properties of a CPW line for various slot separations: (a) Attenuation constant (b) propagation constant and (c) CPW characteristic impedance.

Important

- Antenna material stratification does not have any significant impact on the double slot impedance (See Fig. 6.5),
- Larger CPW separations, d, lead to the greater line attenuation constants, α_{01}, (See Fig. 6.6) which worsens the cross-pol performance of the antenna,
- Larger d values reduce the transmission line characteristic impedance Z_{01} and slightly increase the real part of the propagation constant of the line β_{01} (See Fig. 6.6),
- GP with a kinetic inductance leads to lower α_{01} and significantly higher β_{01} values for the CPW in comparison to PEC GP (See Fig. 6.6).

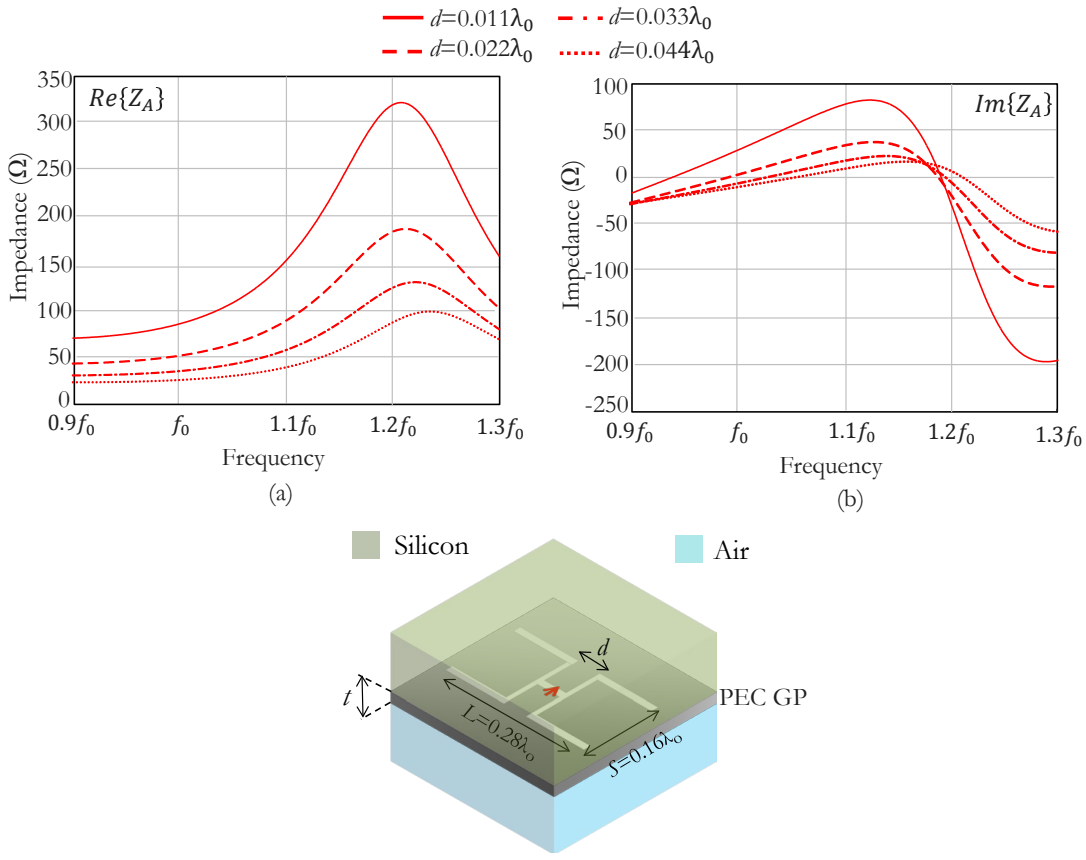

Figure 6.7: Antenna input impedance variation for different slot separations as a function of frequency: (a) Real part and (b) imaginary part.

Using the steps described in Fig. 6.4, we simulated a CPW fed double slot geometry with a slot length of $L = 0.28\lambda_0$, a horizontal slot separation of $S = 0.16\lambda_0$ and a vertical slot separation $d = 0.033\lambda_0$. In the simulations, for the sake of genereric dielectric stratification, we assumed that an anisotropic sapphire wafer ($\epsilon_{x,y} = 9.3, \epsilon_z = 11.5$) with a thickness of about λ_0 is located between the GP and a semi-infinite silicon brick. The antenna matching is highlighted in Fig. 6.9. One can appreciate the comparison between the approximated S_{11} and simulated S_{11} obtained by CST with the entire antenna material stratification. We also show the matching with and without the matching stub to highlight the shift in the resonance frequency f_0.

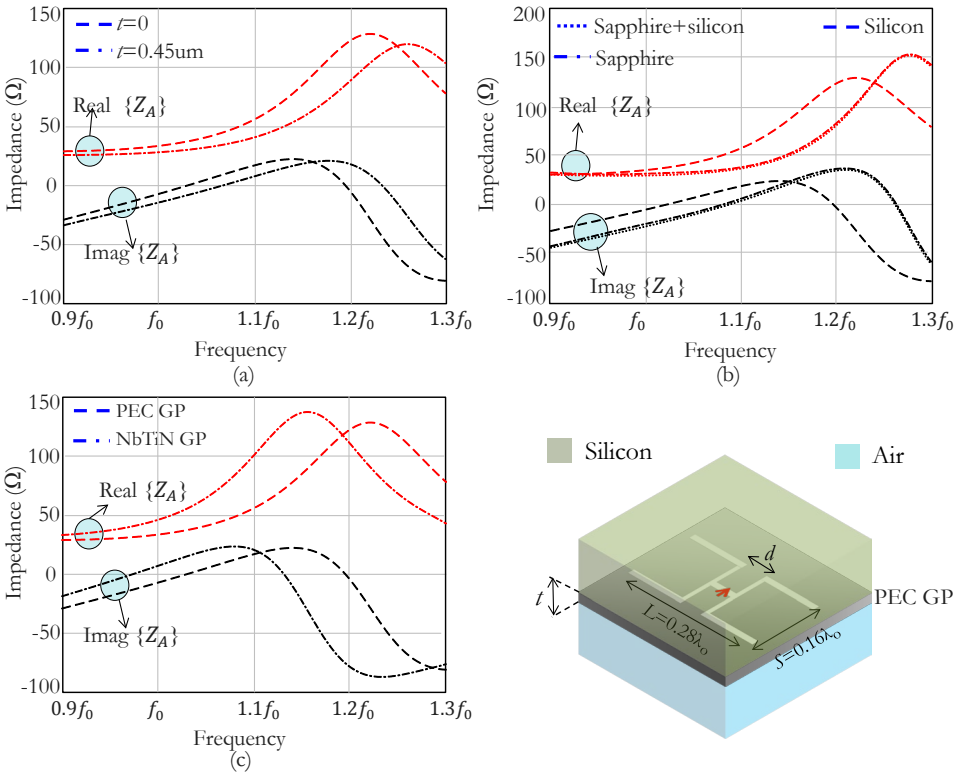

Figure 6.8: Antenna input impedance variation of the CPW integrated double slot antenna with $d = 0.033\lambda_0$ for different (a) PEC GP thickness, (b) dielectric stratification, and (c) GP kinetic inductance values.

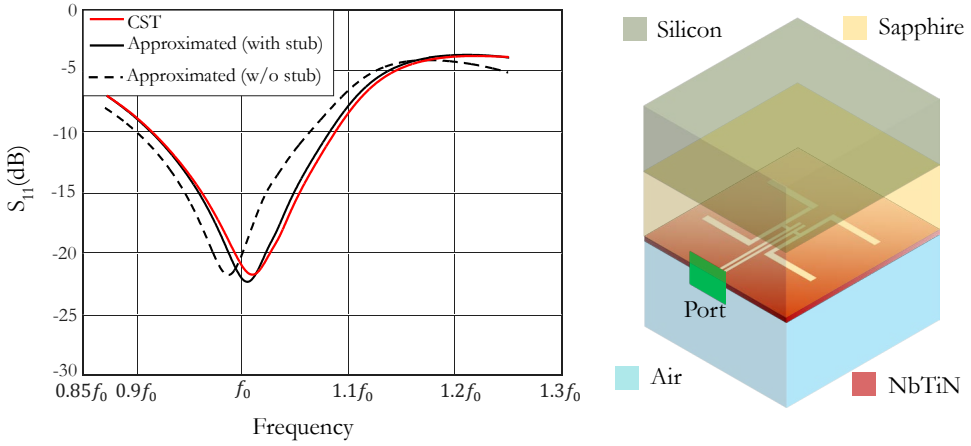

Figure 6.9: Comparison of S_{11} seen from the input port obtained by the approximation and full-wave simulation with the entire antenna material stratification.

Table 6.1: Design specifications for astronomical missions

	SpaceKIDs antenna	**A-MKID antenna 1**	**A-MKID antenna 2**
Frequency band	800-900 GHz	330-364 GHz	800-900 GHz
Lens type	Elliptical lens (Fixed)	Elliptical or EHL*	Elliptical or EHL*
Wafer material	Sapphire	Silicon	Silicon
Wafer thickness	350um	>375um	>350um
Lens material	Silicon	Silicon	Silicon
Lens thickness	0.776mm	<1.2mm	<1.2mm
ML type	λ/4 Parylene coating	λ/4 Parylene coating	Grooved silicon
GP material	NbTiN (0.4pH/sq)	NbTiN (0.37pH/sq)	NbTiN (0.4pH/sq)
FPA spacing	1.6mm	2mm	1mm

* EHL: Extended hemispherical lens

6.2 Double Slot Based Prototypes

Using the methodology given in the previous chapter, we have performed a parametric study to design three optimized double slot antennas to be used for three specific scenarios as benchmarks:

- SPACEKIDs project (850GHz center frequency).
- A-MKID project (350GHz center frequency).
- A-MKID project (850GHz center frequency).

Each scenario has its own fabrication limits. We summarize the antenna specifications in Table 6.1. It is important to state here that SPACEKIDs design has pre-defined lens dimensions and stratification including a 350 µm anisotropic sapphire wafer printed between the silicon lens and the GP. The antenna for A-MKID intrument, on the other hand, has a lens that is entirely made of silicon. The GP including the double slot design parameters is highlighted in Fig. 6.10. Taking the fabrication constraints into account, we report the final dimensions of the optimized designs in Table. 6.2.

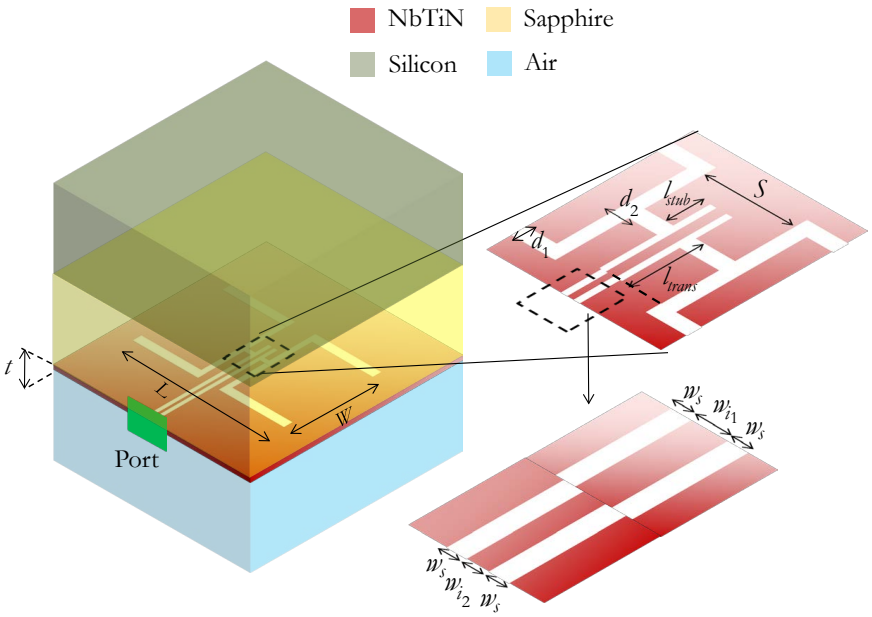

Figure 6.10: Double slot geometry with its design parameters.

The antenna matching performances have been highlighted in Fig. 6.11. One can clearly see that the optimized antennas are well matched within a bandwidth exceeding the requirements given in Table 6.1.

Normalized fields radiated in the presence of a semi-infinite dielectric due to the CPW fed double slot antennas are highlighted in Fig. 6.12. Magnitude of the co and cross polarized radiation in E, D and H-planes can be seen on left hand side whereas the phase distributions in the E and H-planes are demonstrated on the right hand side. Looking at the fields, one can easily notice the effect of the anisotropic sapphire wafer: The primary fields obtained from the SPACEKIDs antenna are narrower than A-MKID antenna #1 and #2. Besides, SPACEKIDs antenna provides a phase variation that is significantly higher compared to other ones, especially in the H-plane. A-MKID antennas have quite stable phase variation in E and H-planes which is kind of similar to the ones given in [2]. Obviously the SPACEKIDs antenna suffers from the anisotropic sapphire wafer located between the GP and semi-infinite silicon due to the fact that it introduces different behavior to different polarizations. However, please note that, the lens used for SPACEKIDs antenna design has fixed dimensions and material stratification unlike the A-MKID design where we can also optimize the lens together with the double slot geometry. For this reason, one can assume that SPACEKIDs design has an optimized double slot geometry used illuminating

Table 6.2: Optimized double slot antenna design parameters

	SpaceKIDs antenna	**A-MKID antenna**	**A-MKID antenna**
Optimization frequency	800-900 GHz	330-364 GHz	800-900 GHz
L	98.82um	240 µm	98.82 µm
W	56.47 µm	137.14 µm	56.47µm
d_1	3 µm	12 µm	6 µm
d_2	6 µm	12 µm	6 µm
S	12 µm	25 µm	12.4 µm
w_{i1}	2 µm	2 µm	2 µm
w_{i2}	2 µm	1.6 µm	1.6 µm
w_s	2 µm	2.2 µm	2.2 µm
w_f	2 µm	6 µm	4 µm
l_{stub}	8.75 µm	25.75 µm	12.65 µm
l_{trans}	-	40 µm	40 µm

an '*unmatched lens*'.

Fig. 6.13, we highlight the spill-over efficiency defined on the lens aperture for SPACEKIDs and A-MKID antennas as a function of lens subtended angle θ_{lens}. Using same θ_{lens}, one could expect to get higher spill-over efficiencies from SPACEKIDs antenna since the primary fields are more directive than A-MKID design. Lens subtended angle, θ_{lens}, however, differ for SPACEKIDs and A-MKID designs. Considering the fabrication constraints and the spill-over performance highlighted in Fig. 6.13, we chose a lens truncation angle of $\theta_{lens} = 55^0$ and $\theta_{lens} = 46.3^0$ corresponding to a lens spill-over efficiency $\eta_{pill-over}$ of about 0.82 and 70% for A-MKID antenna #1 and #2, respectively. Corresponding aperture diameters are $D_f = 1.55$ mm ($D_f = 4.3\lambda_0$), $D_f = 1.9$ mm ($D_f = 2.33\lambda_0$) and $D_f = 0.94$ mm ($D_f = 2.83\lambda_0$) for SPACEKIDs design, A-MKID antenna #1 and #2, respectively. The lens design parameters are highlighted in Fig. 6.14. It should be mentioned here that such dimensions cannot be considered in the far field zone. Therefore, the efficiencies highlighted in Fig. 6.13 are obtained by near field evaluation. Far field evaluation is also performed and about 5% deviation is observed between near and far field evaluations.

As it is shown in Fig. 6.14, A-MKID antenna #2 does not have a typical $\lambda/4$ ML made

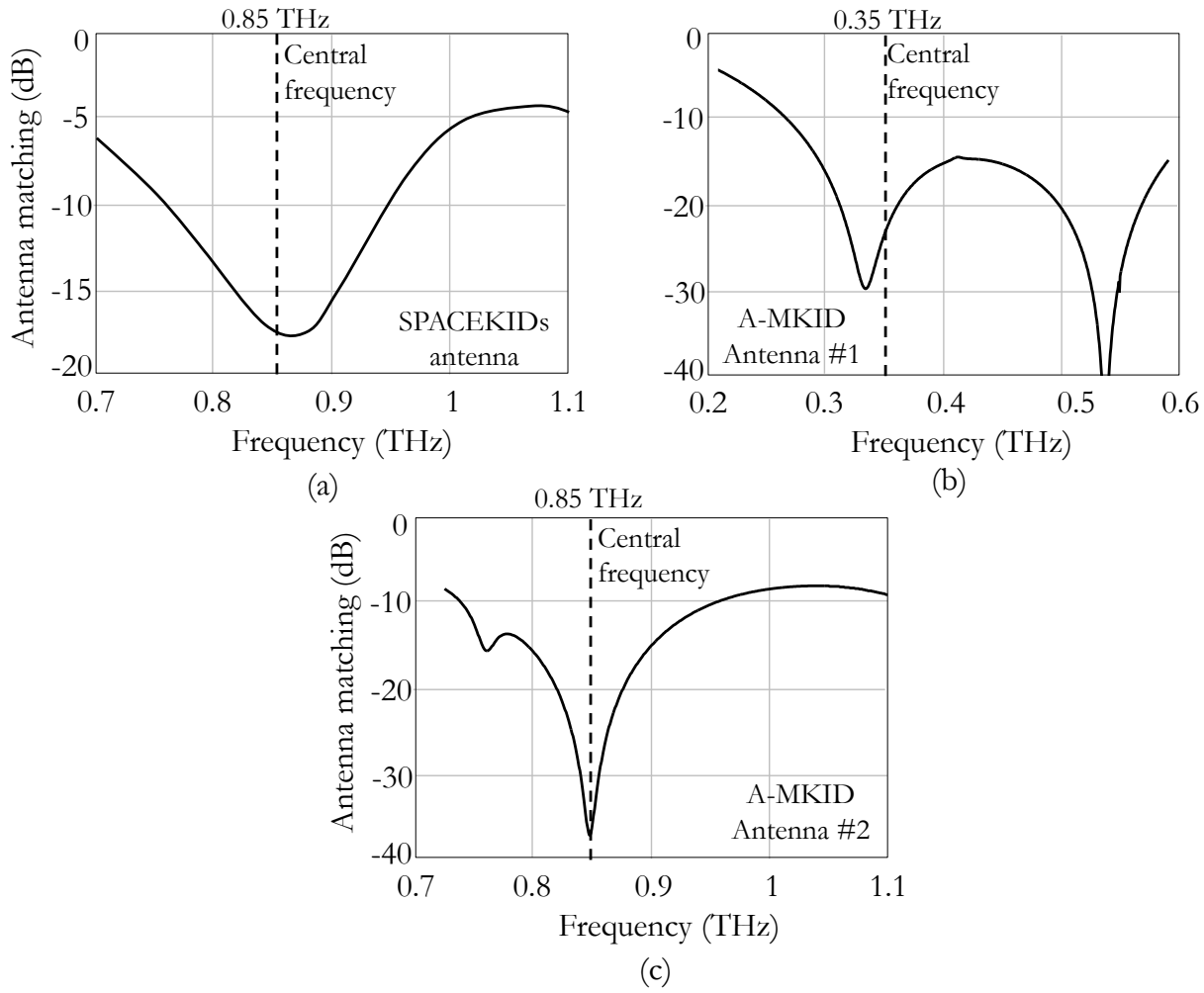

Figure 6.11: Antenna input matching S_{11} obtained by (a) SPACEKIDs antenna (b) A-MKID antenna #1 and (c) A-MKID antenna #2.

of Parylene material as SPACEKIDs and A-MKID #1 antenna designs have. Instead, a grooved silicon ML is designed and integrated on top of the silicon lens. Information on the design of the grooved ML is given in Appendix E.

Considering the radiation inside the lens highlighted before, the phase variation observed in SPACEKIDs antenna will certainly have an impact on the secondary beams, and eventually, on the feed aperture efficiency. We highlight the secondary beams from the selected lenses in E, D and H-planes obtained by the SPACEKIDs, A-MKID #1 and #2 antennas in Fig. 6.15a, b and c, respectively. The figure shows that the beams are quite symmetrical and the cross-polarization level is less than -20dB for A-MKID design. However, the

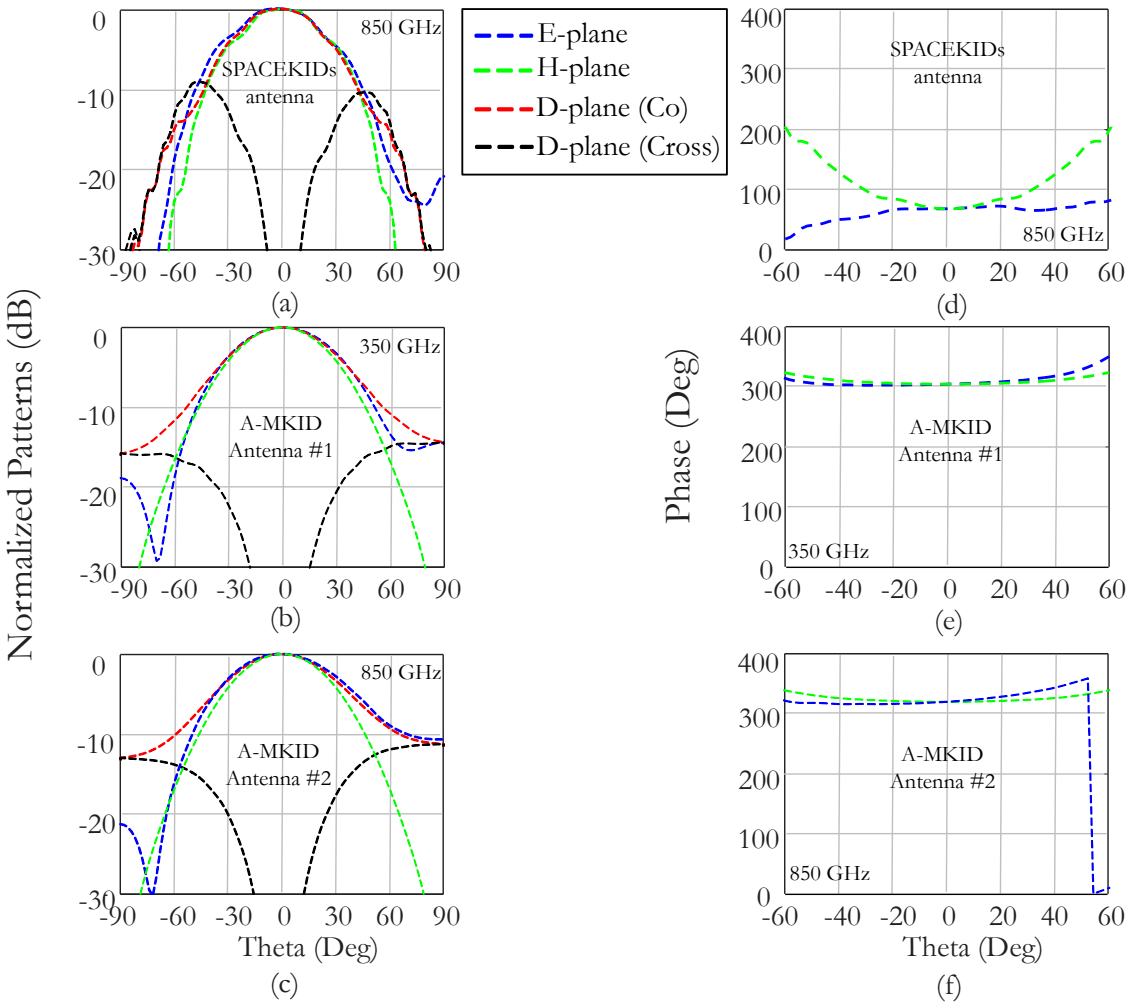

Figure 6.12: Primary fields obtained by the optimized double slot designs for: (a) SPACEKIDs antenna (b) A-MKID antenna #1 and (c) A-MKID antenna #2.

beams from the SPACEKIDs design is slightly larger in the H-plane than E-plane as a result of significant phase variation in the H-plane in the primary fields. Anistoropic sapphire wafer also impacts the cross-polarization performance of the SPACEKIDs antenna design.

The antenna aperture efficiency for all the designs is reported in Table 6.3. One can notice the effect of the phase variation on the taper efficiency. The SPACEKIDs antenna suffers from taper efficiency, providing an aperture efficiency about 53% whereas it goes up to around 76% and 58% for A-MKID antenna designs #1 and #2, respectively. One can also notice that AMKID antenna #2 suffers from radiation efficiency, being the lowest amongst

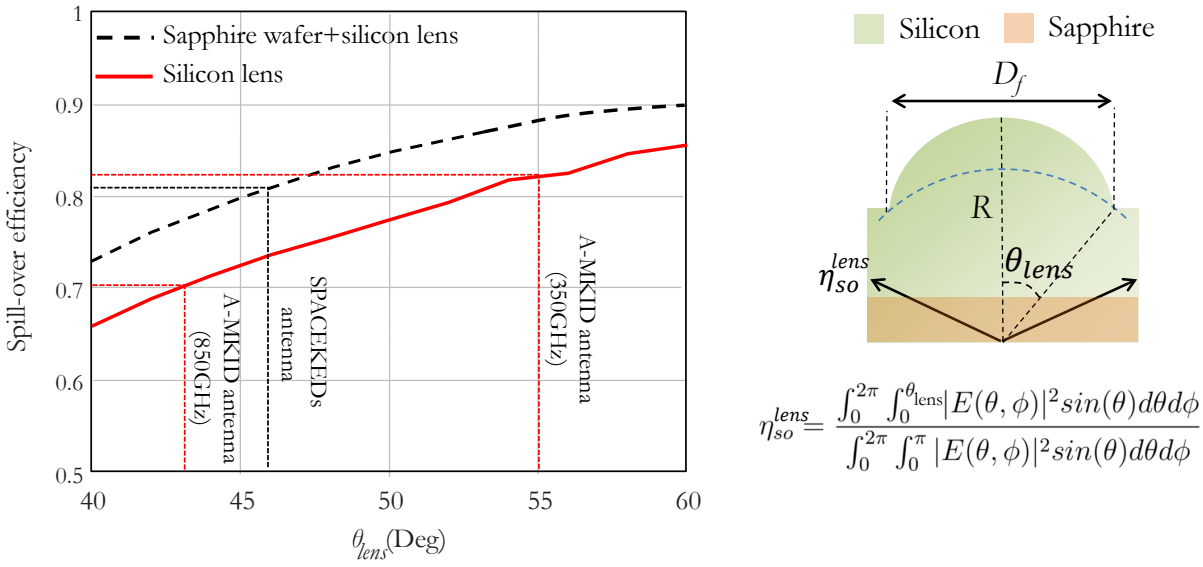

Figure 6.13: Spill-over efficiency calculations representing the fraction of power captured by the lens aperture with a diameter of D_f. The evaluations are performed within the near-field region.

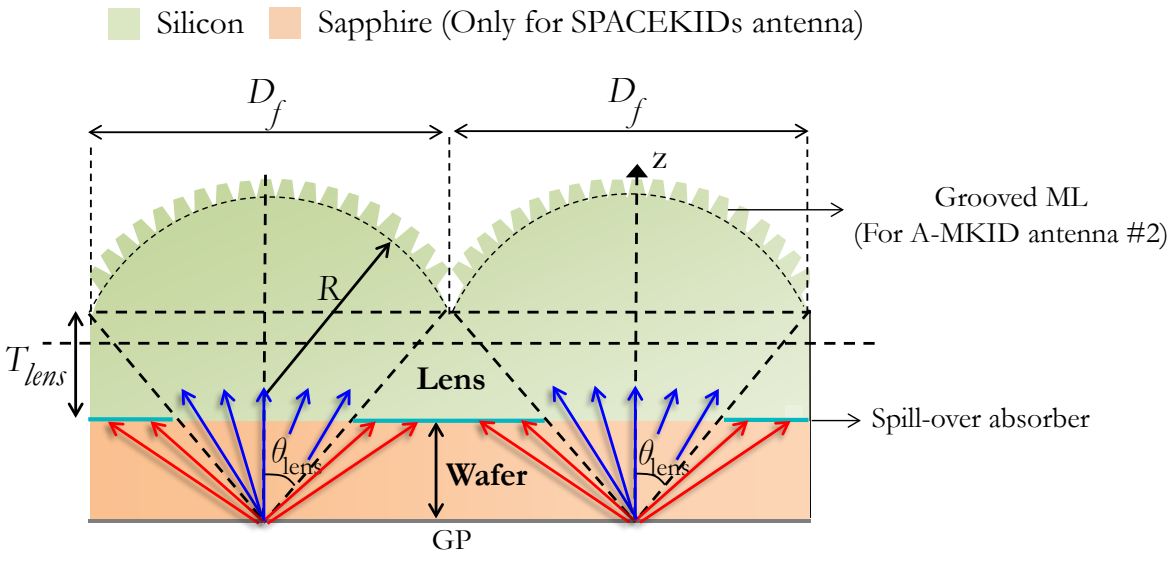

Figure 6.14: Sketch of the lens geometry including the lens design parameters. Note that Sapphire wafer is only used for SPACEKIDs lens whereas grooved ML is only for A-MKID antenna #2 design.

all. This is because of the low spill-over efficiency as a result of using a quite low lens truncation angle, θ_{lens} since the lens thickness T_{lens} should be less than 150 µm due to

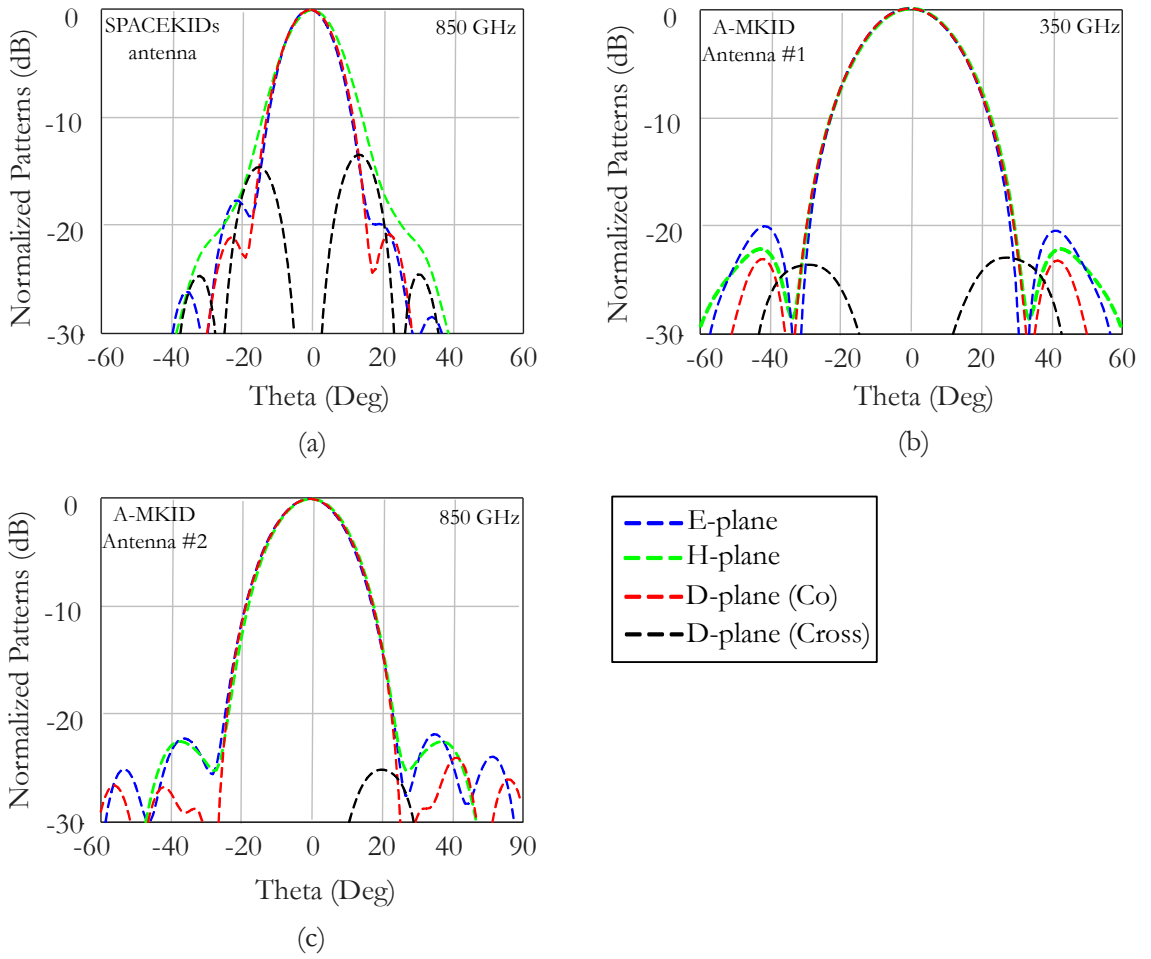

Figure 6.15: Secondary beams after the lens obtained by the optimized double slot designs for: (a) SPACEKIDs antenna (b) A-MKID antenna #1 and (c) A-MKID antenna #2.

the fabrication constraints. Table 6.3 also includes an efficiency term η_{5umgap} due to the gap between the sapphire wafer and silicon lens for 850GHz SPACEKIDs antenna. This gap is estimated to be around 5 µm in the fabrication process. To investigate the effect of this gap on the antenna efficiency, we did some simulations for various gap values and reported the secondary beams in the H-plane in Fig. 6.16. One can clearly see the effect on the lens antenna directivity, and according to our calculations, using 5, 10 and 20 µm gap values reduces the antenna efficiency of about 0.963, 0.79 and 0.5 times compared to the case when there is no airgap between the chip and lens.

The schematic of the tightly spaced FPA scenario can be seen from Fig. 4.14 in Chapter 5. The lenses are hexagonally oriented and a single layer mesh absorber is used in order to

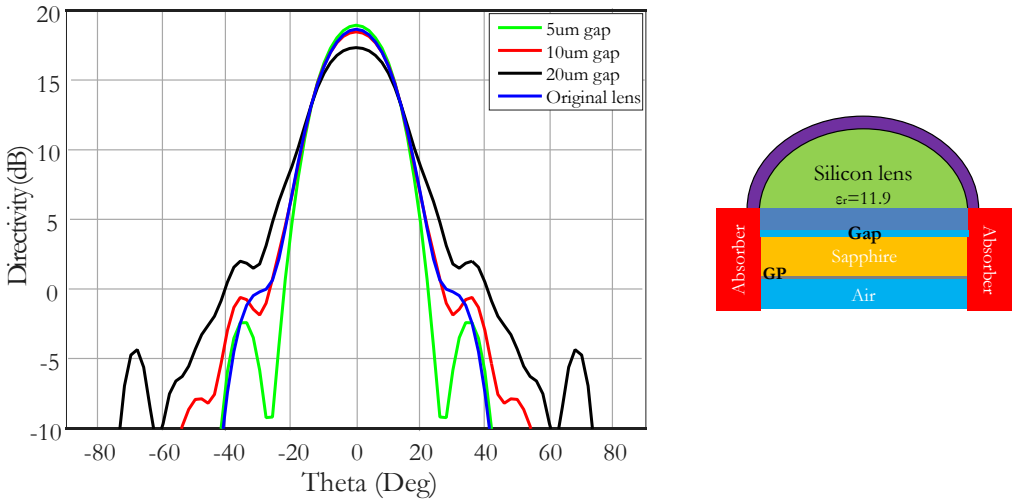

Figure 6.16: Directivity variation in the secondary beams for various airgap values between the sapphire wafer and silicon lens

Table 6.3: Aperture efficiency calculations for double slot based designs

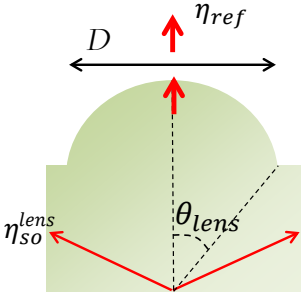

Efficiency			SPACEKIDs antenna (850GHz)	AMKID antenna (350GHz)	AMKID antenna (850GHz)
		η_{taper}	0.715	0.92	0.94
η_{feed}^{det}	η_{feed}	η_{rad}	0.835	0.84	0.68
		η_z	0.98	0.99	0.99
	η_{det}	η_{rad}^{CPW}	0.94	0.99	0.91
		η_{5umgap}	0.963	-	-
		η_{ap}	**0.529**	**0.757**	**0.575**

suppress the radiation launching into the neighbor lenses due to the spill-over of the lens feed (See lens cross-section in Fig. 6.14). Detailed information on the optimization and the design of the SO absorber together with the performance AMKID #2 antenna array

is given in Appendix D.

6.3 Experimental Verification

In this section, we analyze the measured antenna coupling efficiency ($\eta_{co,m}^{\Omega_s}$) due to a blackbody source within a source solid angle of Ω_s and compare it with the simulated antenna coupling efficiency ($\eta_{co,s}^{\Omega_s}$) that is related to the coupled power from the lens antenna into a far-field aperture within a solid angle of Ω_s. Appendix A provides brief information on the calculation of the simulated coupling efficiency while Appendix C briefly explains the methodology used in order to obtain the coupling efficiency from the measurements. Fabrication of the antenna and the measurements have been done by SRON. Here we just report the measurement results to validate our CST simulations.

The schematic of the measurement setup with the lens array and the coupling aperture can be seen in Fig. 6.17. In the measurements $1x4$ SPACEKIDs antenna array is used as it is highlighted in Fig. 6.17. The top view of the lens array can be seen from Fig. 6.18 whereas the picture of the fabricated antenna integrated to the KID resonator and the readout line is shown in Fig. 6.19. The antenna layout is shown in Fig. 6.20. Fig. 6.20a includes the entire mask with readout electronics whereas Fig. 6.20b focuses on only one KID with the antenna. In the measurement setup the antenna array is aligned along x-axis. One can notice that the center point is aligned somewhere between lens #2 and #3, being close to the mid point. This can be considered an uncontrolled shift and we include this shift also in our calculations. The simulated and measured coupling efficiencies for all of the lenses are highlighted in Fig. 6.21. One can appreciate the good agreement between the the simulated and measured coupling efficiencies.

The frequency response of an antenna can be measured by using Fourier Transform Spectrometer (FTS). The FTS looks into a blackbody source with an angular extension much larger than the antenna beam. Therefore the obtained power is proportional to the antenna feed efficiency η_{feed}. Fig. 6.22 shows the normalized frequency response of the antenna. According to the figure there is a quite good agreement between the simulated and measured FTS.

The comparison of the measured and simulated beams after the lens are highlighted in Fig. 6.23. A blackbody source that make a 2D grid scan with a 0.85THz filter is used as a source to illuminate the lens. The simulations take into account the first transmitted pulse from the lens surface. According to Fig. 6.23 there is a reasonable agreement between the

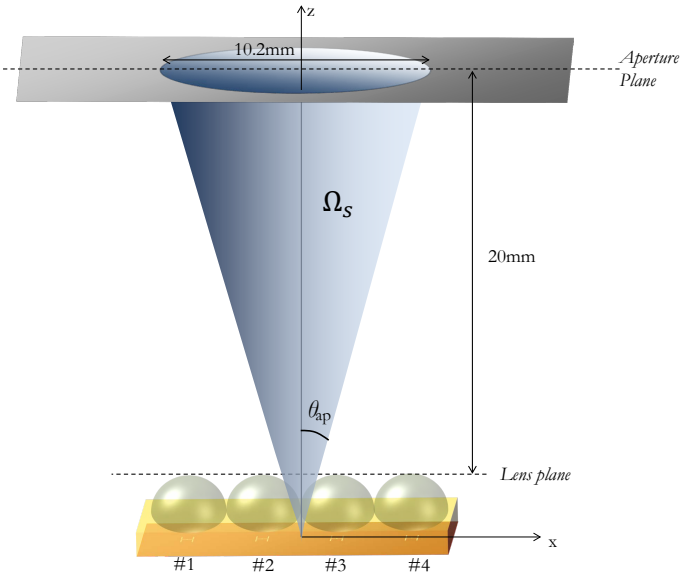

Figure 6.17: Schematic of the lens array used for the coupling efficiency measurements.

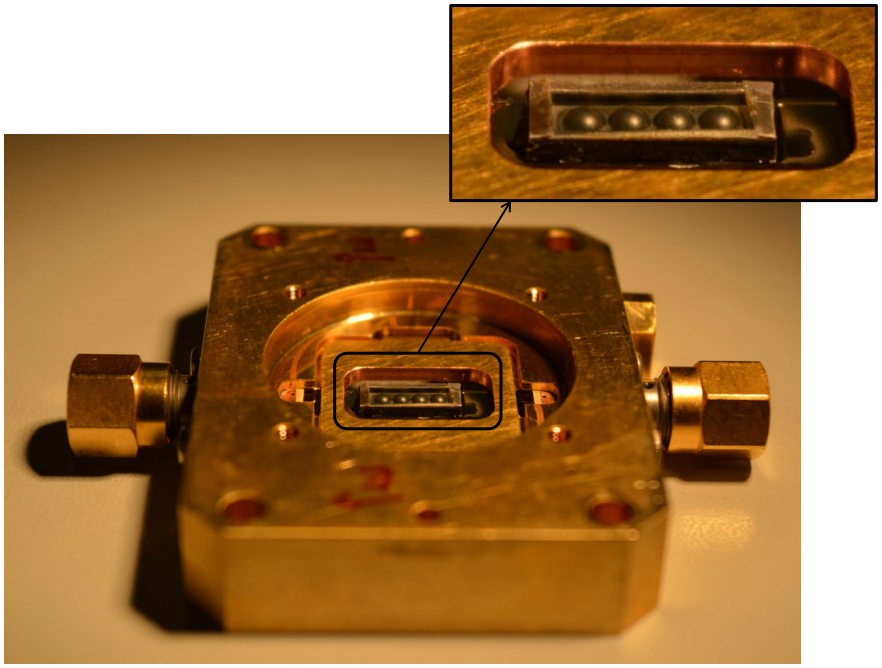

Figure 6.18: Top view of the fabricated antenna including the zoomed version of the lenses.

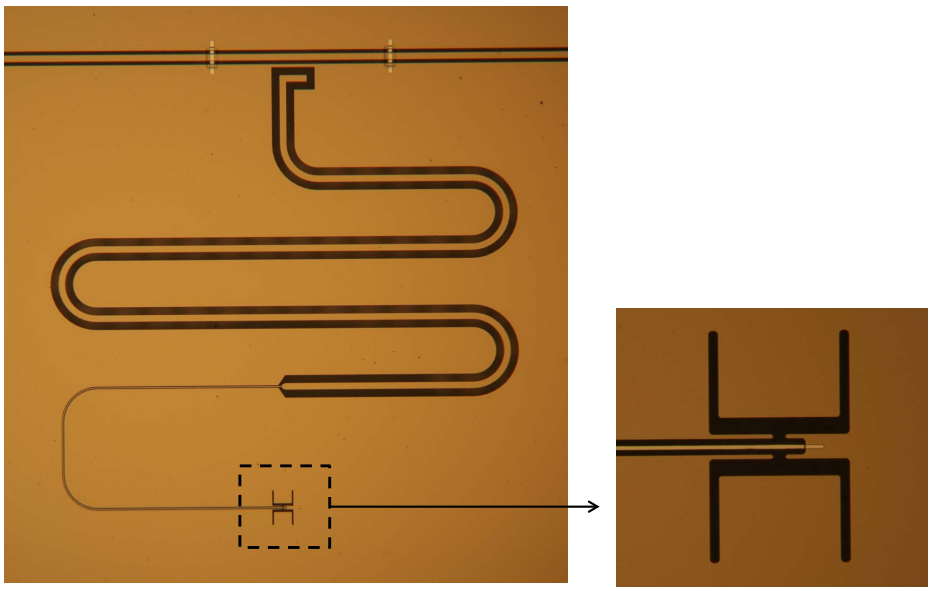

Figure 6.19: Picture of the fabricated double slot antenna for SPACEKIDs project (Focusing on a single pixel).

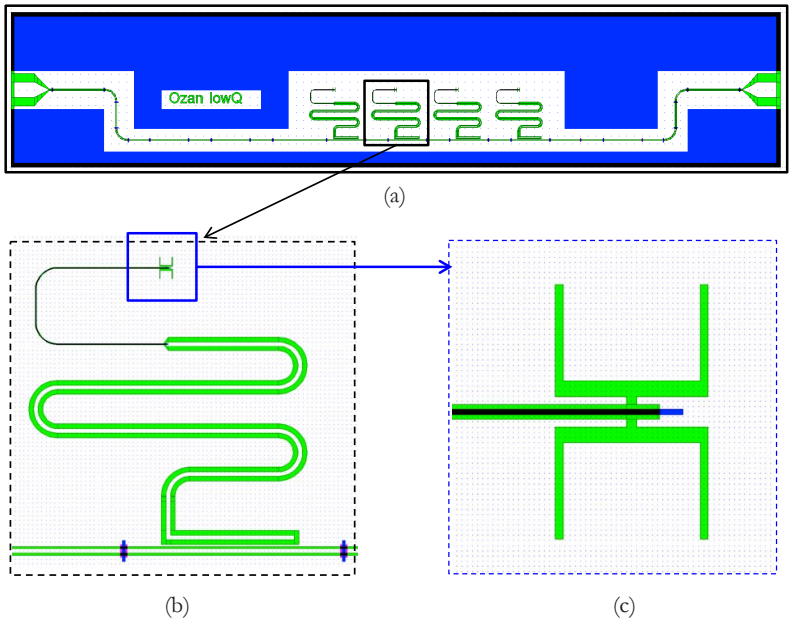

Figure 6.20: Antenna mask including the antenna, $\lambda/4$ resonator and the coupler.

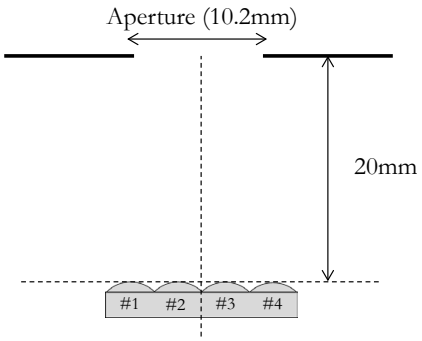

Lens #	Measured	Simulated			
	$\eta_{BB}^{\Omega s}$	η_{so}	η_{feed}^{det}		$\eta_{CO}^{\Omega s}$
			η_{feed}	η_{det}	
1	**0.39**	0.609	0.818	0.905	**0.45**
2	**0.54**	0.7	0.818	0.905	**0.518**
3	**0.55**	0.7	0.818	0.905	**0.518**
4	**0.39**	0.609	0.818	0.905	**0.45**

Figure 6.21: Comparison of the measured and calculated antenna coupling efficiencies of the lens array.

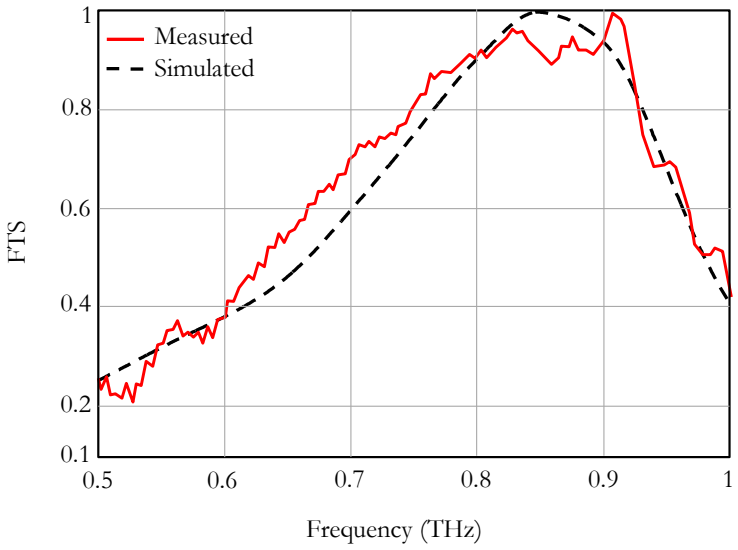

Figure 6.22: Comparison of the measured and the simulated FTS of the antenna.

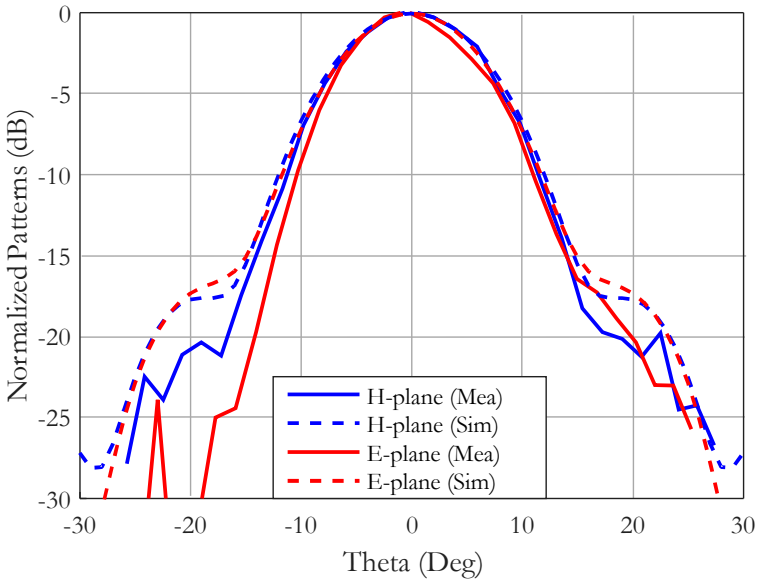

Figure 6.23: Comparison of the simulated and measured secondary beams in E and H-planes at 0.85 THz.

simulated and measured beams.

CHAPTER 7

A Wideband Dual-Polarized Tightly Packed Focal Plane Array

This chapter presents the design and measurements of a wideband dual polarized leaky lens antenna suitable for tightly spaced focal plane arrays. The antenna is composed by two crossed leaky slots fed by two orthogonal microstrips or CPWs to realize dual polarization operation. The crossed feeding structures are fed differentially in order to couple the radiation into the slots. The slots are then coupled to a dielectric lens to achieve directive patterns suited for feeding large F/D reflectors. In this work, the proposed leaky lens antenna is optimized to achieve high aperture efficiency with clean symmetric patterns in both polarizations exceeding an octave bandwidth. The concept is validated by the measurements of the primary fields inside the lens at low frequency and the secondary beams at THz frequency.

7.1 Introduction

Applications in imaging, radio astronomy and space science typically require antennas that are able to provide multi-beam solutions with large operational bandwidths. Many of the instruments done for this kind of applications are based on antenna arrays located on the focal plane of a large reflector. Future scientific instruments operating in the sub-millimeter band of the spectrum are envisioned to have large format focal plane arrays (FPA) that are based on single beam per feed and tight sampling and are coupled to reflector systems with large F/D ratios (> 3) [1], [20].

For microwave frequencies, several wide bandwidth single reflector feeds such as ridged horn antennas [59], eleven antennas [44], a coherently fed connected array of slots coupled to silicon lenses [38] and studies with optimized lens profiles in [46], [60] have been proposed with nearly frequency stable patterns coupled to small F/D ratios. Single feed solutions, however, are optimized for efficient reflector illumination over wide bandwidths. As a consequence, this type of feed solutions are typically characterized by a low taper efficiency of the reflector feed. Instead, for focal plane arrays, Vivaldi [61], [62], corrugated horn [63]- [64] or spline horn antennas [65], [66] are the most widely used antennas at low frequencies. These later antennas can provide relatively low-sidelobes and cross polarization levels at a moderate bandwidth with higher taper efficiencies than the single feed systems. When the instruments require tightly spaced FPAs for full sampling of the focal field, the taper efficiency of the feed antennas becomes particularly critical for the overall system performance since it affects the spill over from the reflector [55]. The aim of this work is to design a tightly sampled wideband dual-polarized FPA feed with high aperture efficiency that could be used at high frequencies where large F/D ratios are typically preferred.

Lens antennas are widely used in the sub-mm band since they allow the integration the antenna and detector on the same chip. Space instruments based on cryogenic power detectors often use focal plane arrays based on dielectric lenses. In [10], a astronomical instrument based on about 25k FPA elements based on Kinetic Inductance Detectors (KIDs) slot antennas coupled to silicon lenses has been developed. Achieving the mentioned number of array elements is a challenging target for any kind of horn antennas with the fabrication techniques available nowadays. In the literature, the most commonly used lens feed is a double slot antenna, which typically operates in a bandwidth much less than one octave and with single polarization [2]. Other slot based lens feeds have been proposed to improve the impedance bandwidth [67], [68], [69], [4], typically at the cost of the quality

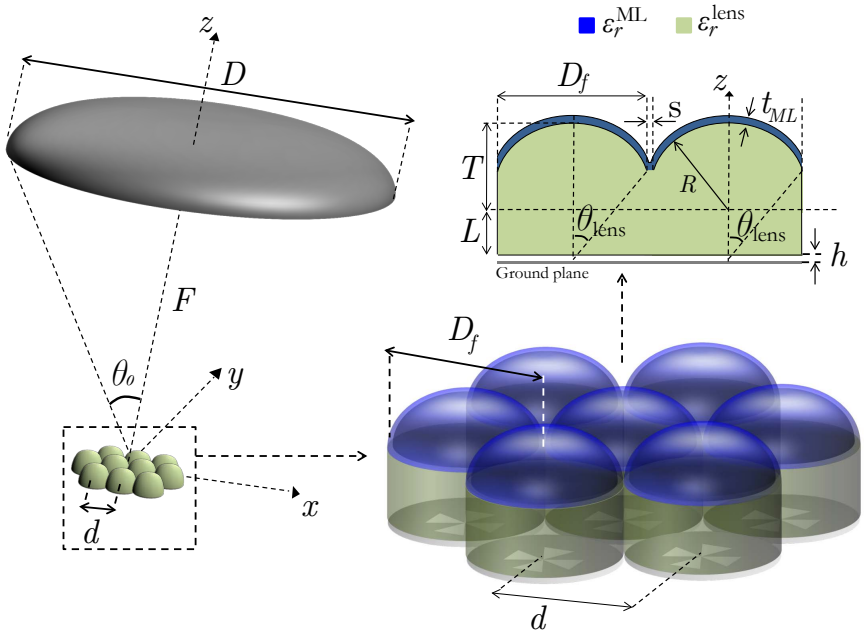

Figure 7.1: Schematic of the FPA design with its design parameters.

of the patterns. Sinuous antennas and spiral have been also proposed in [70], [71] to provide wideband solutions. The main limitation of these antennas is the difficulty to integrate them with planar transmission lines [72]. A new lens feed concept was proposed in [23] able to operate at multi-octave bandwidths. This antenna consists of a leaky-wave slot kept at an electrically small distance from the dielectric lens in order to improve the lens illumination. Recently, the combination of this leaky lens antenna with KIDs has been proved to give nearly independent frequency response from 350 GHz up to 1.2 THz [73]. However such antenna had a very low aperture efficiency, only being suitable for single feed systems.

In this chapter, we present the optimization of a tightly spaced FPA based on such concept, see Fig. 7.1. Improving on the antenna concept presented in [23], we propose a dual polarized extension that is able to provide high feed aperture efficiency over an octave bandwidth. It consists of two orthogonal slots coupled into the two independent microstrips, which can be easily integrated to differential receivers or KIDs. To our best knowledge, the proposed leaky lens antenna is the only practical wideband dual polarization solution that can be integrated to planar feeding lines on the same chip presently available at high frequencies.

The chapter is organized as follows: In Sec. 7.2, we briefly mention about the state-of-art solutions proposed for tightly spaced FPAs and compare their performances. In Sec. 7.3,

Table 7.1: Reflector Feeds for FPA applications

Antenna type	Frequency range	Aperture efficiency	PFL*	Polarization	Directivity (central f)	X-pol
Corrugated horn [63]	1 : 1.5	Between 38%-53%	No	Linear**	$\approx$ 20.5dB	< -30dB
[74]	1 : 1.6	Between 38%-58%	No		$\approx$ 18.66dB	< -20dB
Spline horn [65]	1 : 1.16	Between 49%-54%	No	Linear	$\approx$ 26.4dB	< -28dB
Double slot antenna [2]	1 : 1.15	Between 60%-75%	Yes	Linear	$\approx$ 30dB	< -20dB
X-slot antenna [67], [68]	1 : 2	Between 40%-50%	Yes	Linear	$\approx$ 28.7dB	< -12dB
Sinuous antenna [70]	1 : 4 (@12GHz, @24GHz)	Between 39%-50% (Estimated) (50%, 43%) (Estimated)	Yes***	Dual	$\approx$ 22dB	< -17dB
This work	1 : 2.5 1 : 5.25	Over 60% Over 50%	Yes	Dual	$\approx$ 28.7dB	< -12dB

*PFL: Planar feeding lines

** Dual polarized version may also be possible

*** Beam distortion due to the radiation of planar feeding lines unless the lines are extremely tiny in terms of wavelength

we introduce the antenna concept and explain the slot excitation mechanism. This section mainly focuses on a parametric study to optimize the antenna radiation in the presence of a semi-infinite silicon stratification to maximize feed taper efficiency on the lens aperture. In Sec. 7.4, we show the experimental validation of the radiation patterns inside semi-infinite silicon. Sec. 7.5 focuses on FPA lens optimization where we show the performance of leaky lens antenna array together with the reflector illumination. Finally, the conclusions are given in Sec. 7.9.

7.2 State-of-Art in Tightly Spaced FPAs

In this section, we provide a detailed summary of the different antenna geometries that could be used in wideband and tigthly spaced FPAs. Table 7.1 shows the summary of the operational bandwidth and aperture efficiency values that can be obtained by the most widely used geometries in the literature. When some of these parameters were not explicitly given, we give our best knowledge estimation. The information on the type of the antenna polarization and possibility to integrated with planar feeding lines is also given.

Vivaldi antennas have been proposed for wideband imaging applications ([61], [62]) since they are matched within a bandwidth in the order of several octaves and able to provide

stable beams over an one octave [75]. Used in single feed per beam scenarios, Vivaldi antennas suffer from strong coupling [55]. Therefore, they are typically used as phased arrays for multiple feed per beam scenarios with F/D ratios typically less than 1 [61], [62].

Pyramidal and conical horns, common at high frequencies, are characterized by a aperture efficiencies of about 50%-60% [76]- [77] and offer a bandwidth up to 1 : 1.5. In order to achieve high reflector illumination efficiency, corrugated horn antennas have been proposed in the literature [63]- [64]. These antennas typically present low side-lobe and cross polarization levels. The aperture efficiencies of corrugated horns presented in [63] and [74] are comparable to the conventional ones since they are optimized for $2\lambda F/D$ feed spacing. The manufacturing difficulties are significant for corrugated horn based FPAs at mm and sub-mm frequencies. As an alternative solution, smooth-walled spline horn antennas have been proposed in [65], [66]. Although this kind of smooth-walled horns are typically characterized by slightly better aperture efficiencies compared to corrugated horns, they can only provide narrower operational bandwidth than corrugated ones due to their increased lengths.

Integrated lens antennas, on the other hand, can provide more practical solutions since they are easier to manufacture in tightly sampled FPAs [10]. A double slot antenna is the most widely used lens feed [2]. It provides an aperture efficiency of 75% at the center of the bandwidth. This later is limited by to about 1 : 1.15 by the impedance matching. Similar designs have been investigated in [4], [78]. Wideband lens feeds such as the X-slot [67]- [68], a broadband slot feed so-called XETS antenna [69], sinuous antenna [70], [71] and spiral antennas [72] have been also proposed in the literature. The X-slot antenna can operate over an octave bandwidth with an aperture efficiency between 40%-50% [68]. XETS antenna also provides an octave bandwidth with a linear polarization only [69]. A wideband and dual polarized lens feed was proposed in [70]. The feed is based on a sinuous antenna with nearly frequency independent patterns. Using the data provided in [70], we calculated the taper efficiencies, at 12 and 24 GHz, to be 69% and 66%, respectively. Including a matching layer, this sinuous antenna will have a peak of about 50% aperture efficiency. When it comes to feeding mechanism, either integrated or the differential feeds can be used with sinuous antennas [70]. However, the use of planar feeds disturbs their radiation characteristics significantly [72], unless the width of feeding lines are much smaller than the wavelength. A scaled version of the sinuous antenna presented in [71] was used to operate continuously within a frequency band starting from 60 GHz up to 240 GHz. It is able to provide dual polarization with planar feeding lines. The width of the microstrip transmission lines used in [71] is about $\lambda_0/2000$, where λ_0 is free-space wavelength at the

highest frequency in the design. The requirement of extremely small feeding lines limits the use of these antennas at higher frequencies.

The table also includes the performance of our proposed design based on a leaky lens concept. The details of the antenna optimization are given in the coming sections. The proposed dual polarized leaky lens antenna provides a peak aperture efficiency of 70% and it is higher than 50% within a bandwidth of $1:5.25$ while it exceeds 60% for a bandwidth $1:2.5$. Moreover, the proposed antenna does not suffer from significant coupling to the feeding lines affecting the radiation patterns since it has a much larger ground plane than the sinuous antenna. The microstrip width in the present design is about $1/86\lambda_0$ at the highest frequency. The design can be extended to coplanar waveguide feeding lines with a dimensions of $1/39\lambda_0$ [79]. Based on these results, the proposed leaky antenna solution offers a viable path for tightly spaced and widband integrated FPAs at high frequencies.

7.3 Single and Dual polarized leaky slots

In this section, first, we will focus on the optimization of the fields radiated into semi-infinite dielectric by a single polarized leaky slot antenna. Then, using the optimized single polarized leaky slot, we will modify the it accordingly to achieve the proposed dual-polarized leaky slot design.

The geometry of the proposed dual-polarized leaky slot antenna is sketched in Fig. 7.2. It consists of a semi-infinite dielectric with a permittivity of ϵ_r^{diel} fed by the leaky slot that is etched on a ground plane located on top of a membrane. The membrane is placed at a certain electrically small distance h from the bottom part of lens. It has a permittivity of ϵ_r^{memb} and a thickness of h_m. On top of the membrane, an electrically long tapered slot is printed with a length of l_s, an initial width of w_0 and a final width of w_s. A microstrip transmission line with a length of l_m and a width of w_m printed on the other side of the membrane is used to couple the radiation into the slot as it can be seen from Fig. 7.2c.

In the optimization process we used a semi-infinite dielectric medium with a permittivity of $\epsilon_r^{diel} = 11.9$. In order to optimize the radiation patterns from the dual-pol leaky slot, a parametric study is performed for a bandwidth $1:2.5$, namely starting from 8 to 20 GHz. In order to maximize the lens antenna aperture efficiency, for each of the polarizations, the leaky wave slot should ideally generate a top hat pattern, inside the dielectric, with low cross-polarization. The shape of the pattern is directly related to the leaky wave propagation constant, $\beta - j\alpha$ [23]. Typically the pattern generated in silicon by a long slot in the presence of an air cavity has two pronounced peaks at $\theta = \pm sin^{-1}(\beta/k_d)$, where k_d is

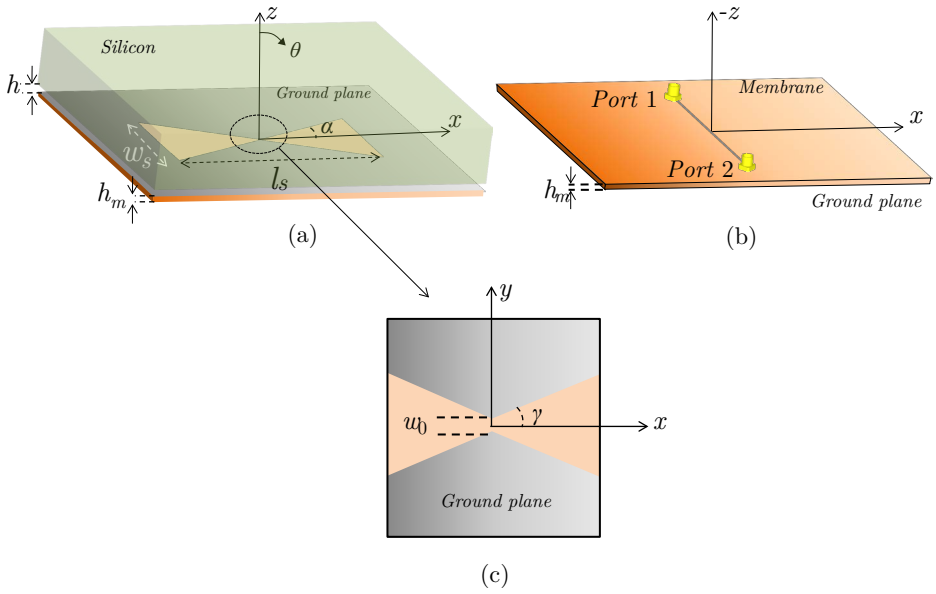

Figure 7.2: Schematic drawing of the microstrip fed single polarized leaky lens antenna showing; (a) The perspective view of the antenna with a semi-infinite silicon dielectric located on top, separated by an airgap, h, from the ground plane, (b) the central part of the crossing slots, and (c) the microstrip transmission lines printed on the bottom side of the membrane to couple the radiation to the orthogonal slots.

the wave number in the silicon. Fig. 7.3 shows the radiated field inside the semi-infinite silicon dielectric medium simulated with CST MWS [26] at 15 GHz for various airgap and slot tapering angle values.

The leaky wave propagation constant can be controlled by changing the height of the air cavity, h, and the width of the slot w_s. Larger cavity heights lead to leaky waves with smaller attenuation constants α. Fig. 7.4a shows the difference between the maximum directivity of the antenna (D_{max}) and the directivity at broadside ($D(0,0)$) as a function of the cavity height. Therefore the gap should be small, typically limited by the fabrication constrains. The cross-polarization level is instead influence by two parameters: the cavity height and the slot tapering angle. Figure 7.4b shows the difference between the maximum level of the co (Co_{max}) and cross polarization (Cross_{max}) components as a function of the cavity height whereas Fig 7.4c and d show the impact of the slot tapering angle. The larger tapering angle is, the lower the cross polarization level. The upper limit for the tapering angle is then given by -10 dB beam-width for a proper lens illumination [2] and azimuthal symmetry of the radiated fields.

The leaky wave propagation constant can be controlled by changing the height of the air

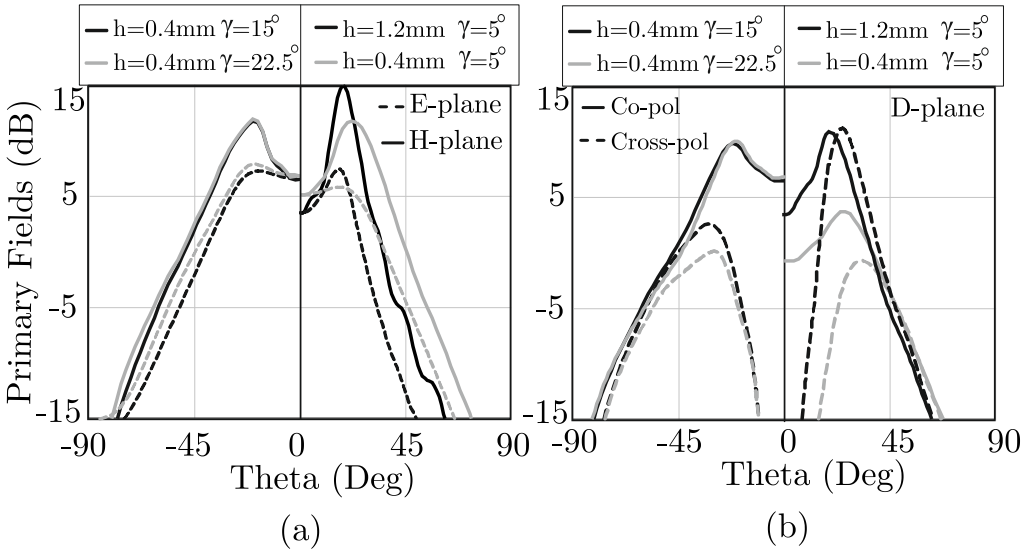

Figure 7.3: Primary field variations inside the semi-infinite dielectric that is separated from the ground plane with an airgap h for various airgap and slot tapering angles, γ, at $f = 15$ GHz. (a) includes co-polar beams in E and H-planes and whereas (b) highlights co and cross-pol radiation in D-plane.

cavity, h, and the width of the slot w_s. Larger cavity heights lead to leaky waves with smaller attenuation constants α. This will imply more pronounced peaks. Fig. 7.4a shows the difference between the maximum directivity of the antenna (D_{max}) and the directivity along the broadside ($D(0,0)$) as a function of the cavity height. It is clear from Fig. 7.4a that, indeed, larger cavity heights lead to higher peaks that are associated to the lower attenuation constants. The cavity height has also an impact on the cross-polarization. Fig. 7.4b shows the difference between the maximum level of the co (Co_{max}) and cross polarization (Cross_{max}) components in dB. According to the figure, the higher cavity distance is being used in the design, the more cross-pol radiation one gets from the antenna. Fig. 7.4c and d show the results for different slot tapering angles for a fixed cavity height. Larger slots lead to stronger leaky wave attenuation. Therefore, the use of taper slots reduces the level of the leaky wave peaks as well as the cross-polarization level.

The -10 dB beamwidth of the radiation inside a semi-infinite silicon medium is highlighted for various tapering angles in Fig. 7.5a and b for E and H-planes, respectively. According to the figure, increasing slot tapering angle yields to more symmetric beams in both planes. On the other hand, due to the fact that larger slots provide higher attenuation constants, eventually the beams become wider as the tapering angle increases. This, however, is not the desired behavior for this particular design since it may be an issue considering

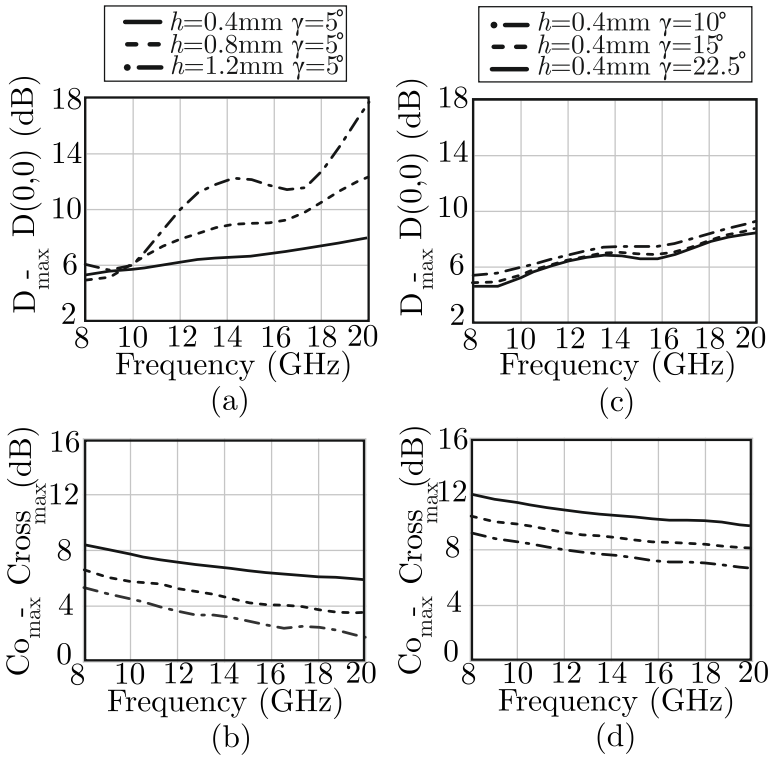

Figure 7.4: Maximum directivity (D_{max}) with respect to to broadside directivity ($D(0,0)$) as a function of a) airgap distance, b) tapering angle, and, the difference between the maximum of co and cross polarizations for primary fields inside the semi-infinite dielectric for different c) airgap values, and d) tapering angles.

the antenna will radiate significant field towards to the lateral part of the lens that will end up with having strong inner reflections from the dielectric-air boundary. One should be careful about these reflections since they may change antenna radiation characteristics significantly. As a result, the optimum performance has been obtained for $h = 0.4$ mm, $w_0 = 0.24$ mm and $w_s = 23$ mm, which corresponds to a slot tapering angle, $\gamma \approx 15^0$. The radiated pattern for these conditions is also shown in Fig. 7.3 and it will be representative both for dual and single polarized antennas.

The phase center variation of the primary fields is also studied and the results were highlighted as a function of frequency in Fig. 7.6 for E and H-planes. The phase center location is calculated by using CST MWS where -10 dB radiation angle for the primary fields that was highlighted in Fig. 7.5 were taken as a reference. As expected, the phase center of the leaky slot antenna is located underneath the ground plane and Fig. 7.6 shows that the single-pol leaky antenna provides a reasonably stable phase center within the entire bandwidth, with having a maximum variation about 5 mm and 2 mm in the H and E-planes,

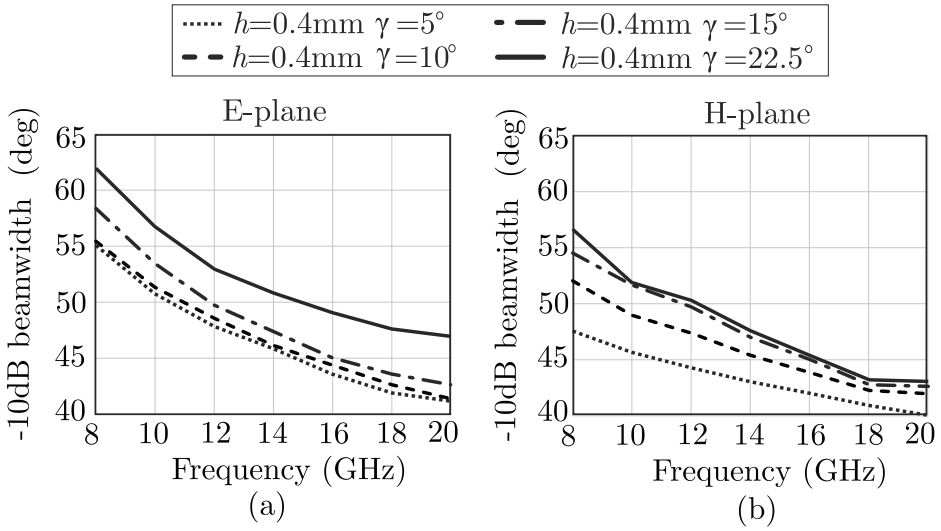

Figure 7.5: -10 dB beamwidth variations for the primary fields inside the semi-infinite dielectric for various slot tapering angles γ for a) H-plane and b) E-plane.

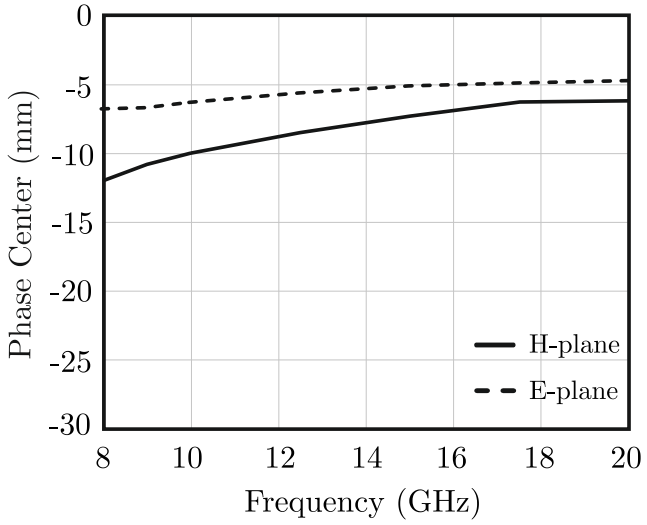

Figure 7.6: Phase center variation of the beams radiated into semi-infinite silicon in E and H-planes as a function of frequency.

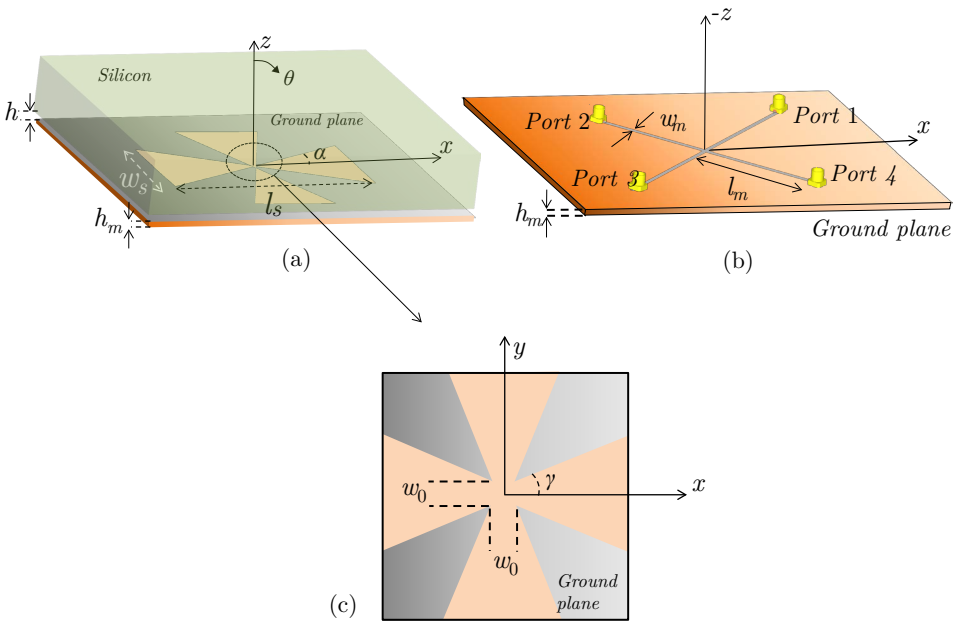

Figure 7.7: Schematic drawing of the microstrip fed dual polarized leaky lens antenna showing; a) an extended hemispherical lens fed by a membrane placed at a certain distance, h, from the ground plane, b) the geometry of the dual polarized tapered slot fed by two crossed microstrips, and, c) the central part of the crossing slots.

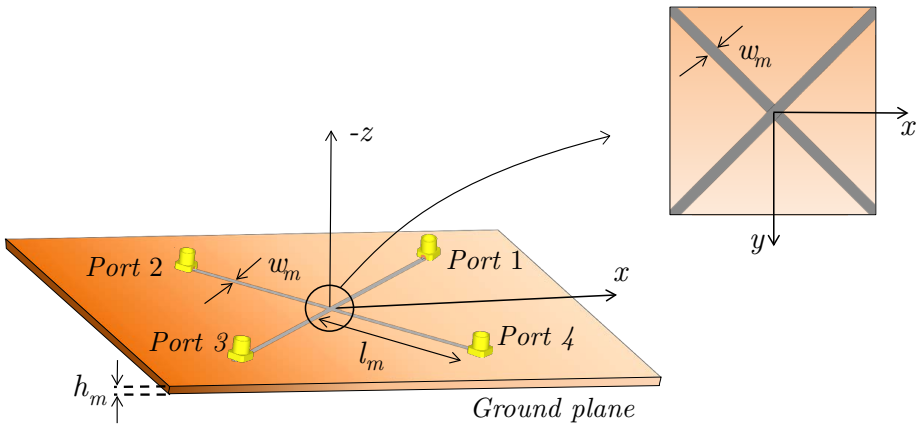

Figure 7.8: Schematic of the microstrip transmission lines located underneath the membrane. The crossing microstrips are connected in the center.

respectively.

Having optimized the radiation characteristics of the single-pol leaky slot antenna, we now

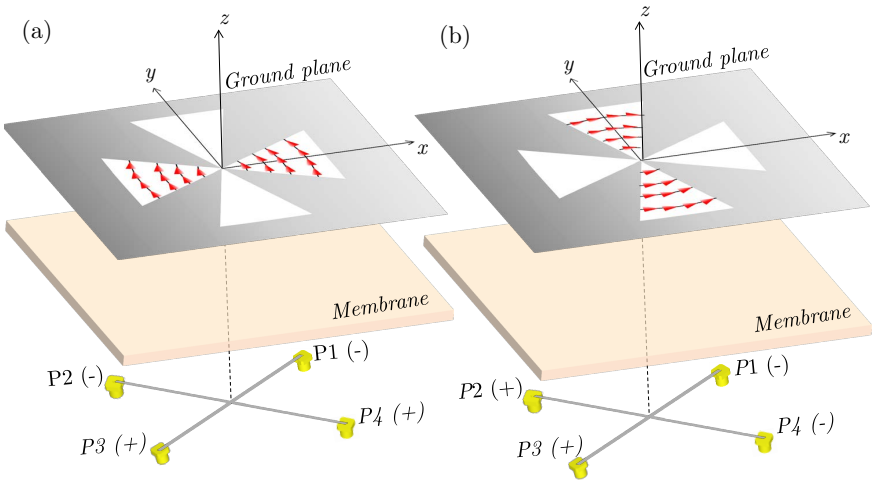

Figure 7.9: Demonstration of the excitation mechanism of the dual-pol leaky antenna depending on port the excitation signals.

propose the dual polarized version of the optimized design by means of introducing an orthogonal slot into the design shown in Fig. 7.2. The orthogonal slots are coupled, in turn, by two orthogonal microstrips printed on the other side of the membrane as it can be seen from Fig. 7.8. Since the two slots are fed symmetrically, the performance of two polarizations is the same. In order to generate the two polarizations, the microstrip transmission lines are fed by Port 1, Port 2, Port 3 and Port-4 simultaneously. Fig. 7.9 highlights the electric field distribution across the slots depending on the port excitations. To excite one polarization at a time, the ports should be fed by using one of the following schemes:

- Port 1= $-V$, Port 2= $-V$, Port 3= $+V$ Port 4= $+V$ (In order to excite the slot aligned along x-axis).

- Port 1= $-V$, Port 2= $+V$, Port 3= $+V$ and Port 4= $-V$ (In order to excite the slot aligned along y-axis).

where V is the amplitude of voltage excitation defined for the ports in the simulations.

To prove we have similar radiation characteristics from the single and dual polarized leaky slot antennas, in Fig. 7.10, we compare the primary fields from these two designs in E and H-planes at 10 and 15GHz, respectively. As one can notice from the figure, the two antennas provide almost identical beams as expected.

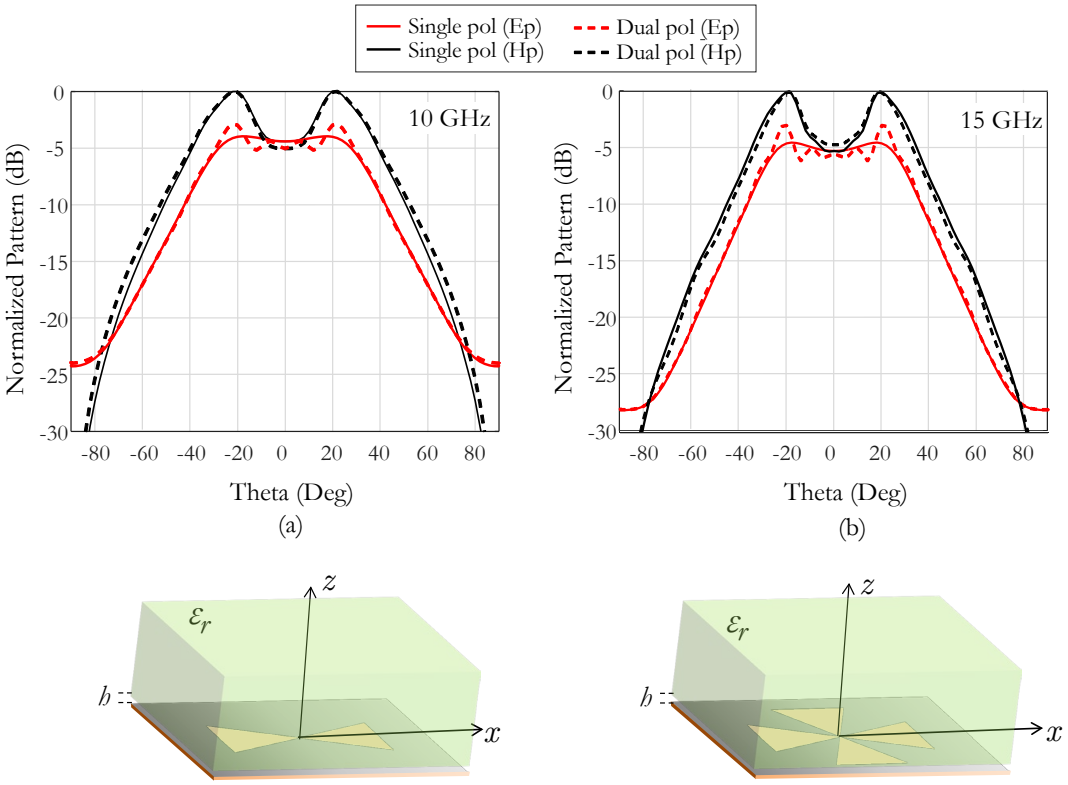

Figure 7.10: The dimensions of the optimized lens. The lenses are tightly packed to form an hexagonal array to be used as a FPA.

7.4 Experimental Validation of the Primary Fields

The dual-polarized slot has been manufactured using standard printed technology and it is shown in Fig. 7.11. The air cavity has been created by using a grid structure of ceramic material with a height of $h = 0.4$ mm and a permittivity of 3.55. Thanks to the gridded structure, the effective permittivity is close to $\epsilon_{eff}^{grid} = 1$. The membrane was made with Rogers RT6002 with a permittivity of $\epsilon_r^{memb} = 2.94$ and a thickness of $h_m = 0.127$ mm. The transmission lines have a width of $w_m = 0.175$ mm with a length of $l_m = 30$ mm (From the connector to the center of the slot). The antenna presented is well matched to a microstrip line with a characteristic impedance of 75 Ω over a bandwidth larger than two octaves. The active reflection coefficient is measured and has good agreement with the CST simulations, as shown in Fig. 7.12.

In order to measure the radiated fields inside the dielectric, a near field broadband waveguide probe operating from 9 to 26 GHz is located on the top of a half dielectric sphere with

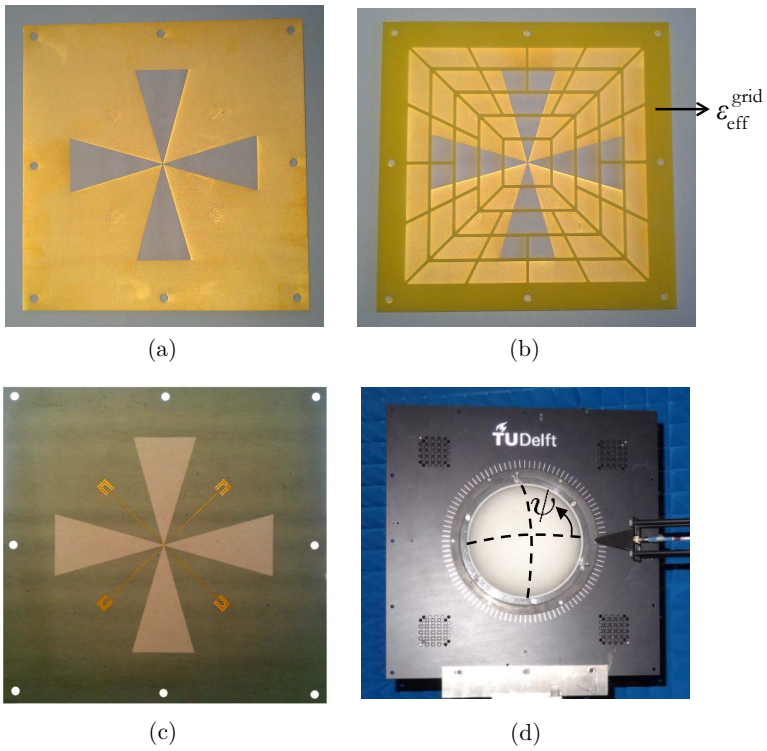

Figure 7.11: Images of the low frequency prototype: a) ground plane, b) ceramic grid located on the top of ground plane to serve as an airgap, c) microstrip feeding lines located underneath the membrane, and d) the dielectric lens located on the top of the dual pol leaky wave antenna.

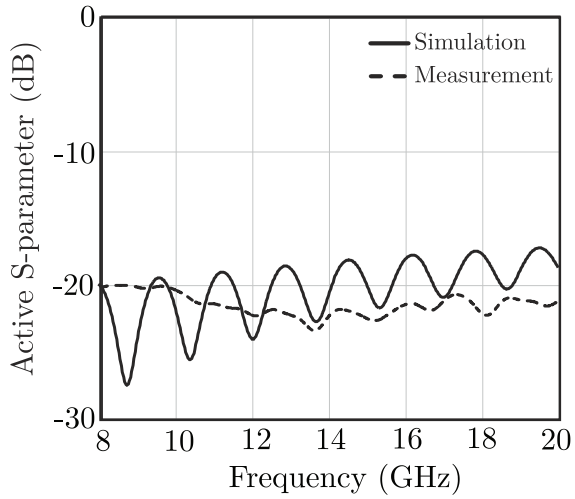

Figure 7.12: Comparison of the measured and simulated active S-parameters.

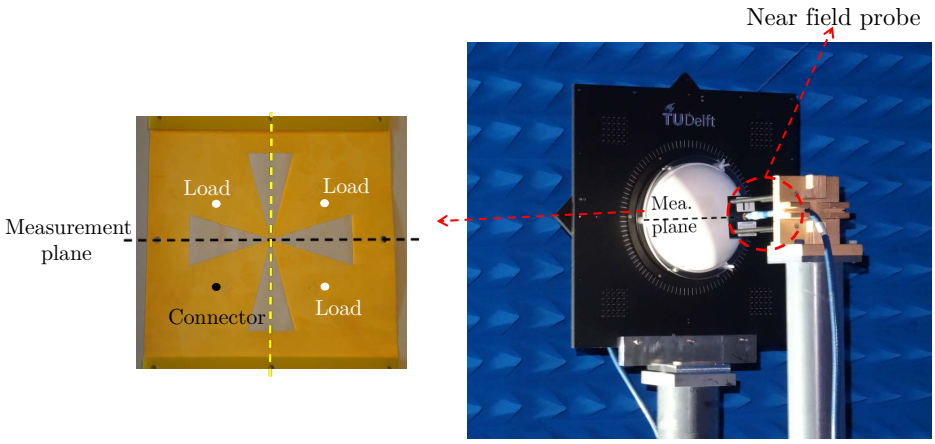

Figure 7.13: A near field probe is positioned just above the hemispherical lens in order to measure the primary fields from the proposed dual-pol leaky slot antenna.

a radius of $R = 95$ mm. The dielectric sphere is made of ECCOSTOCK HIK 500F ® [50], with relative a permittivity of 11.9. The antenna is fed by only one port at a time while all the other ports are terminated with matched loads (See Fig. 7.13). The contributions from the other ports are taken into account by superposing the fields measured at each port. θ and ϕ-components of the field are measured by rotating the probe by 90^0 along its axis. The dielectric sphere is not covered by a matching layer and the inner reflections at the dielectric-air interface are time gated in the post processing.

During the measurement campaign, we found out that the sphere material was not uniform and presents an anisotropic behavior. Therefore the measurements were repeated three times by rotating the dielectric sphere, only, along ψ as highlighted in Fig. 7.11d. The measured radiated fields inside the dielectric are compared with the simulated ones at three frequencies, 10, 15 and 20 GHz in Fig. 7.14 and Fig. 7.15 for the H and E-plane, respectively. Due to the anisotropy, Figs. 7.14 and 7.15 include the measured fields at three different ψ sphere rotations. As it can be seen from the results, there is a good agreement between the measurements and CST simulations for H-plane whereas the agreement becomes worse for the E-plane. For this field polarization, the measured results depend strongly on the dielectric sphere rotation.

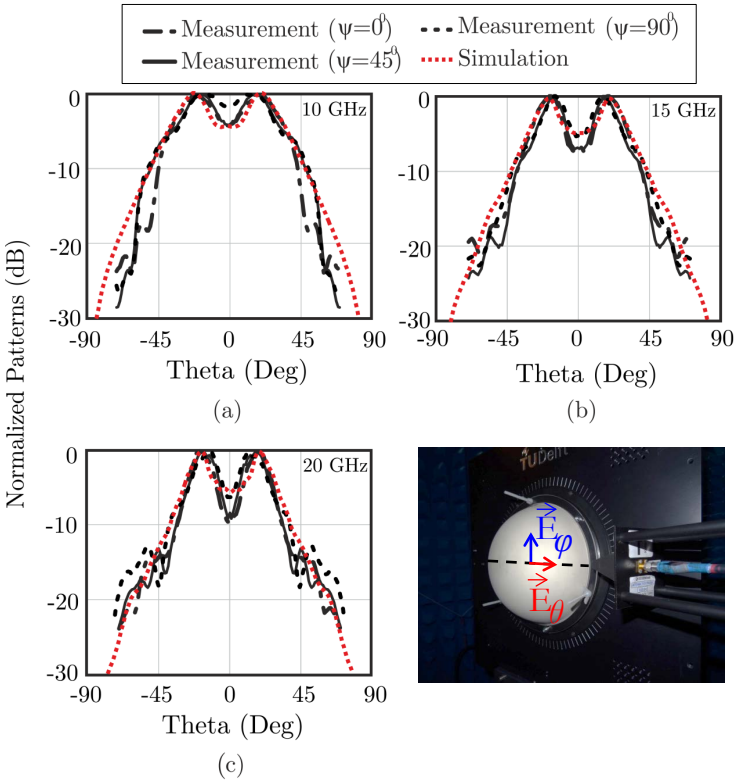

Figure 7.14: Comparison of the H-plane measured patterns for three lens rotation angles, ψ, for the frequencies at: a) 10 GHz, b) 15 GHz, and c) 20 GHz.

7.5 THz FPA Optimization

In this section, we present a practical implementation of a tightly packed FPA based on directive leaky lens feeds. The application of the proposed antenna is sub-mm astronomical observations with reflector systems of $F/D > 3$. For the lenses fed by directive feeds, the impact of the mutual coupling in the radiation pattern can be neglected. The lens antennas has been analyzed by using a numerically efficient Physical Optics (PO) algorithm [22]. The schematic of the final lens geometry is highlighted in Fig. 7.1. The lens material has the same permittivity as the semi-infinite dielectric medium used for the slot optimization ($\epsilon_r^{lens} = \epsilon_r^{diel} = 11.9$) with having a radius of R, an aperture of D_f, an extension length of $L = 0.31R$, and a lens truncation angle of θ_{lens} (See Fig. 7.1). The lens is coated by a $\lambda_d/4$ matching layer made of Parylene material ($\epsilon_r^{ML} \approx 2.62$), where λ_d is the wavelength at inside the dielectric at the center frequency, f_0.

In Fig. 7.16, the proposed leaky lens antenna aperture efficiency, η_{ap}, as a function of frequency is highlighted. The lens antenna has a maximum aperture efficiency about 70%

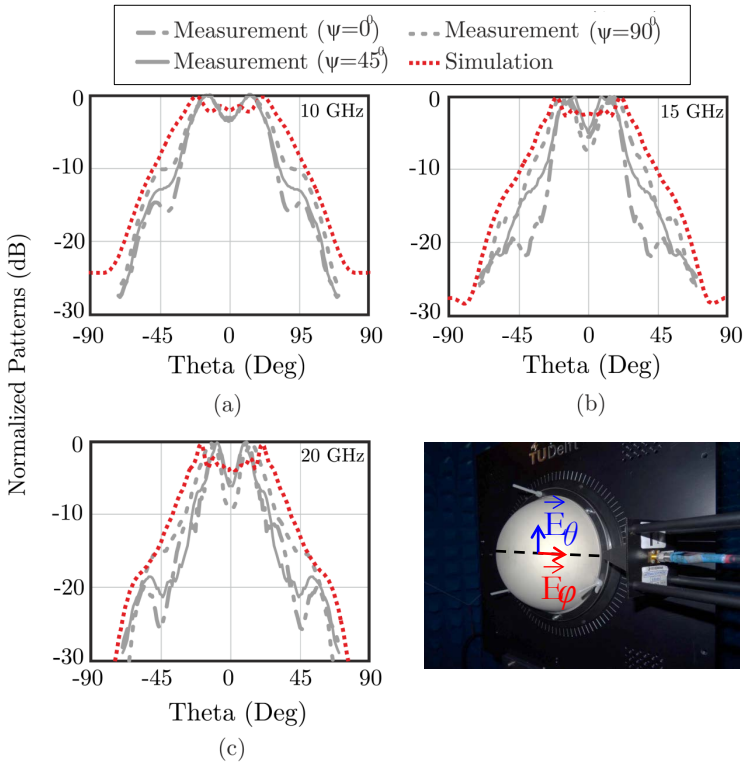

Figure 7.15: Comparison of the E-plane measured patterns for three lens rotation angles, ψ, for the frequencies at: a) 10 GHz, b) 15 GHz, and c) 20 GHz.

while it is higher than 60% within a bandwidth of about 1 : 2.5. Moreover it remains higher than 55% over the entire bandwidth (See Fig. 7.16). The simulated aperture efficiencies obtained by full-wave CST simulations have been also shown in Fig. 7.16 at six discrete frequency points (highlighted by black dots) obtaining good agreement between PO and CST simulations.

As a specific example, here, we consider a proposed sub-mm wave space astronomical instrument envisioned to operate over an octave bandwidth from 1.4 to 2.7 THz and coupled to a telescope with $F/D > 10$ [20], [21]. Different feed samplings ($d = 0.5\lambda_0 F/D$, $d = \lambda_0 F/D$) of the focal plane are under consideration. Here λ_0 is the free-space wavelength at the center frequency, f_0. The proposed FPA design has a feed separation of $d = 1.6$mm with the lenses having an aperture of $D_f = 1.6$mm (which corresponds to $D_f = 10.66\lambda_0$), a radius of $R = 0.9$mm (See Fig. 7.1), an extension length of $L = 0.31R$ and a lens truncation angle of $\theta_{lens} = 46.3^0$.

The Co and cross polar radiations patterns of the proposed lens antenna are shown in Fig.

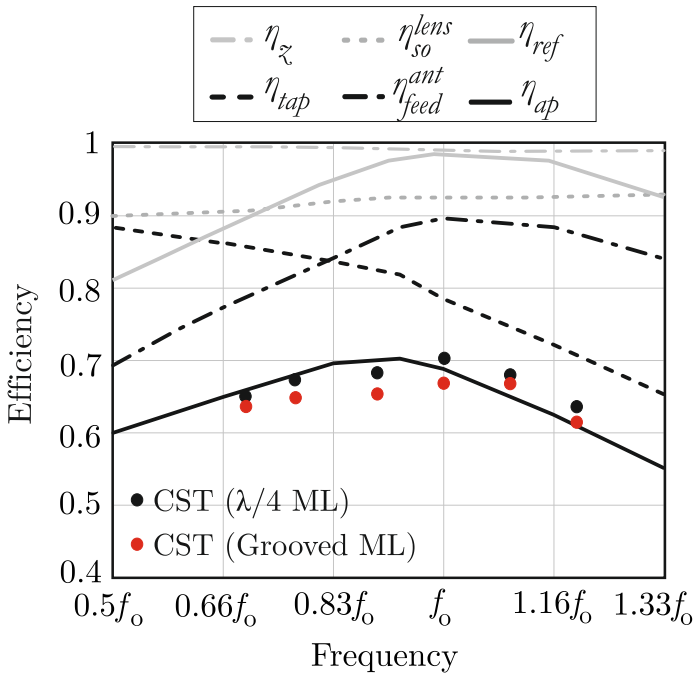

Figure 7.16: Aperture efficiency of the proposed lens antenna as a function of frequency.

7.17 for $0.66f_0$, f_0 and $1.33f_0$, respectively. Fig. 7.17 shows that the beams after the lens are quite symmetric in E, H and D-planes. The lens antenna has a cross-polarization less than -12 dB within an octave bandwidth. Phase distribution of the reflector feed patterns can be seen from Fig. 7.17d for E and H planes, at the same frequency points.

7.5.1 Reflector Simulations

In Fig. 7.19, we compare the reflector illumination efficiencies, simulated with GRASP, obtained by the proposed design and a feed with a uniform aperture current distribution ($\eta_{ap} = 100\%$) for $d = 0.5, 1$ and $2\lambda_0 F/D$ feed spacings as a function of frequency. The $2\lambda_0 F/D$ is also included in Fig. 7.18 for reference. The ratio of the reflector efficiencies ($\eta_{leaky}/\eta_{uniform}$) for feed samplings $d \leq \lambda_0 F/D$ is basically the feed aperture efficiency reported in Fig. 7.16. This is because the reflector illumination efficiency is solely dominated by the reflector spill-over efficiency for tightly spaced FPAs ($d \leq \lambda_0 F/D$). Therefore, for such small feed samplings, one has to maximize the feed taper efficiency. Instead for $d = 2\lambda_0 F/D$, the reflector efficiency is a trade off between spill over and taper efficiencies, and therefore the reflector feeds are typically optimized for high Gaussicity [2].

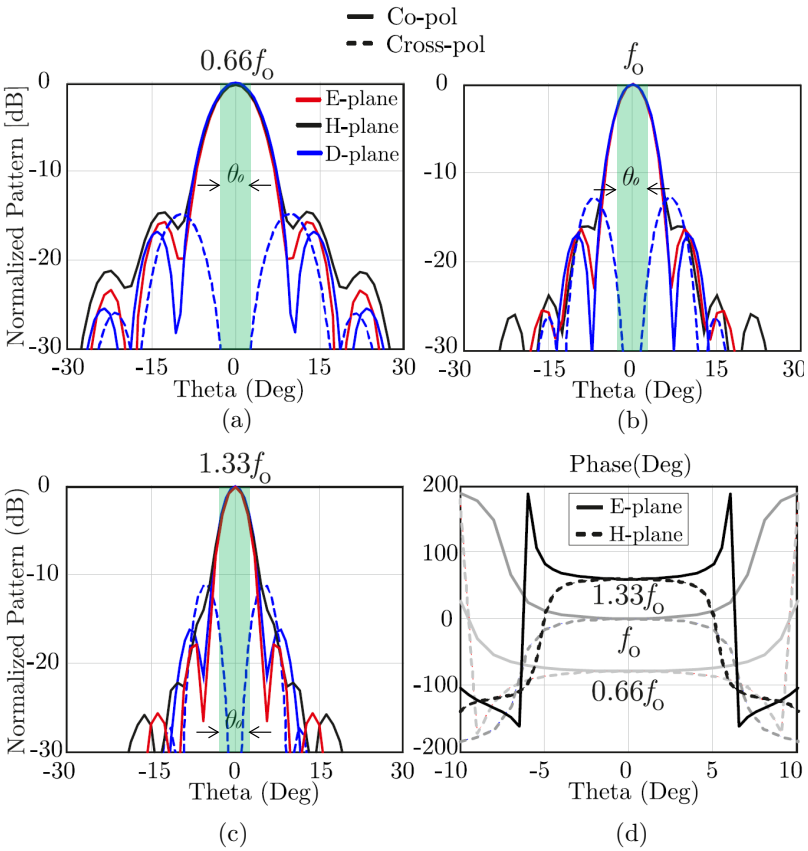

Figure 7.17: Co and cross-pol radiation of the reflector feed with a lens aperture of $D_f = 10.66\lambda_0$ at the frequencies of (a) $0.66f_0$, (b) f_0, and (c) $2f_0$, in E, H and D-planes. The region confined by the reflector subtended angle θ_0 corresponding to FPA feed separation of $d = \lambda_0 F/D$ is also highlighted together with the beams. Here (d) shows the phase distribution of the secondary beams in E and H-planes at the same frequency points.

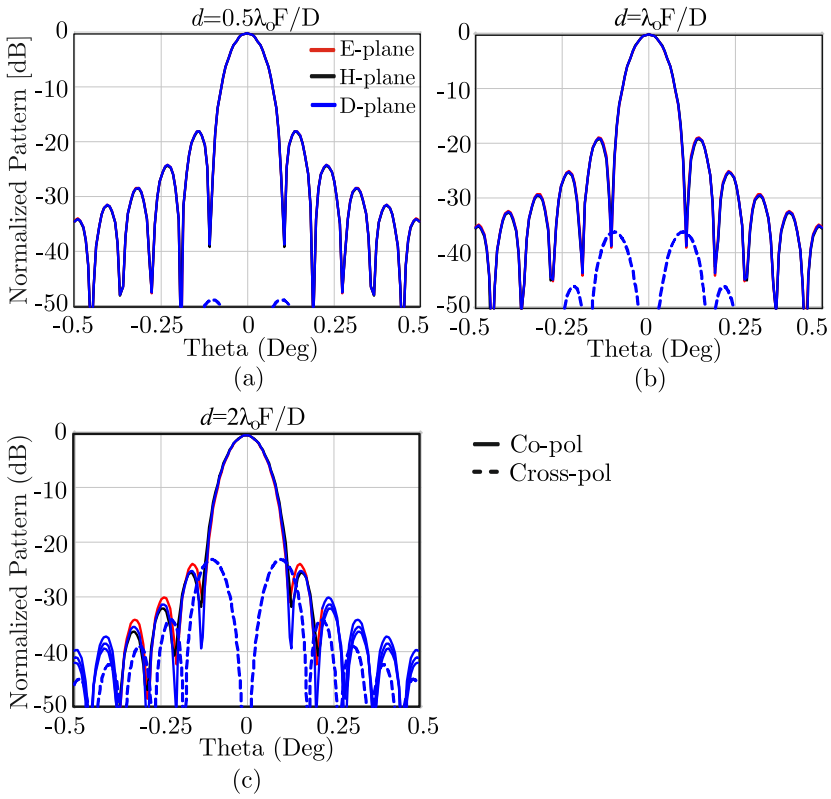

Figure 7.18: Co and cross-pol components of the reflector patterns obtained by the proposed lens antenna design with a fixed aperture diameter of $D_f = 10.66\lambda_0$ for three feed samplings: (a) $d = 0.5\lambda_0 F/D$ (b) $d = \lambda_0 F/D$, and (c) $d = 2\lambda_0 F/D$.

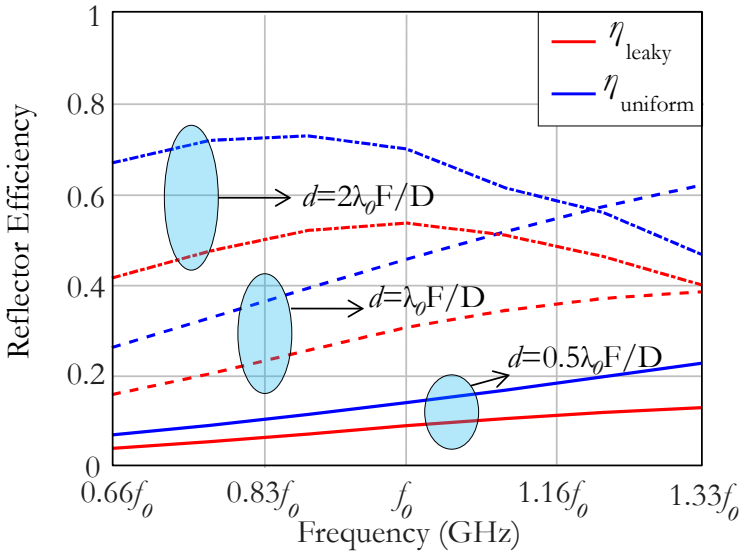

Figure 7.19: Reflector efficiency comparisons (including the feed efficiency, η_{feed}) between the proposed leaky slot and an ideal uniformly excited feed for different feed separations d in the FPA as a function of frequency.

The radiated patterns from the considered telescope are shown in Fig. 7.18 for $d = 0.5\lambda_0 F/D$ and $\lambda_0 F/D$. It shows that tight samplings lead to lower cross-polarization levels in the telescope radiation patterns since the feed cross polarized fields do not reach the telescope (i.e. smaller subtended angle, θ_0, as shown in Fig. 7.17). Therefore, for tightly spaced FPA, the achieved cross polarization level in the proposed antenna system is less than -35dB.

7.6 THz Prototype

In this section, we will show the performance of the design to be used within SAFARI band (1.4 THz to 2.7 THz). To do so, as a first step, the dimensions of the optimized prototype will be scaled down accordingly. Here, we use a dimension scaling factor of 1/133. Then, as a second step, we replace microstrip transmission lines with CPW transmission lines in order to make the GP planar. This means that the KID resonator and the antenna can be etched on the same layer (See Fig. 7.20) which makes the fabrication process much easier in sub-mm band. In principle, assuming that there is no radiation coming form the CPW lines, these two design should provide radiation patterns. To prove this, we also simulated the design with CPW lines and according to our simulations, indeed, using CPW line in-

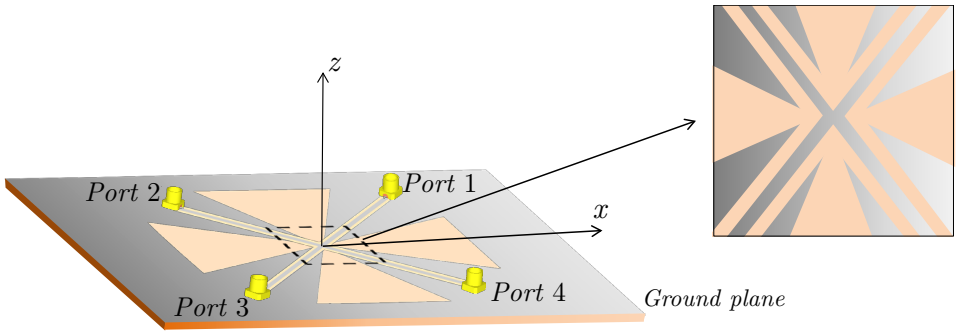

Figure 7.20: Drawing of the antenna fed by two crossing CPW transmission lines etched on the same layer.

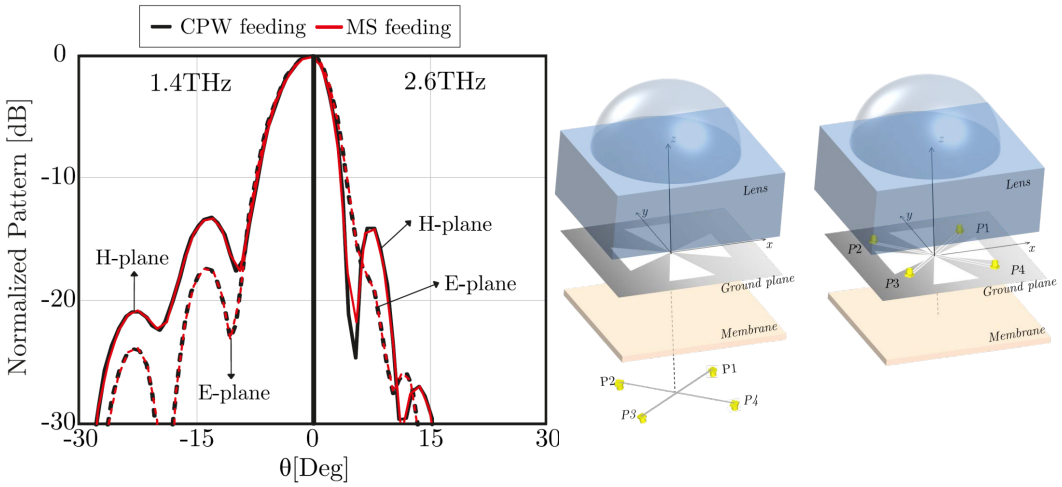

Figure 7.21: Radiation pattern comparisons for the optimized antenna with CPW and MS transmission lines at 1.4THz and 2.6THz, providing almost same radiation patterns in transmission.

stead of MS line does not alter the radiation patterns it is highlighted in Fig. 7.21.

Secondly, we introduce a spill-over (SO) absorber to suppress uncontrolled power launching in the lens array. Finally, as a last step, due to the fabrication limitations, we replace the Parylene $\lambda/4$ ML with an alternative grooved ML design that is entirely made of silicon to serve as a wideband ML in sub-mm prototype. We have followed the similar steps described in Appendix D and E for the SO absorber and grooved ML designs, respectively. The unit cell dimensions of the optimized SO absorber and the grooved ML are highlighted in Fig. 7.22. We simulated the optimized single lens when it is coated with the grooved ML and compared with the simulation when the lens is coated with the Parylene $\lambda/4$ ML in CST. In the simulations, an E-field probe is located on top of lens and the simulations

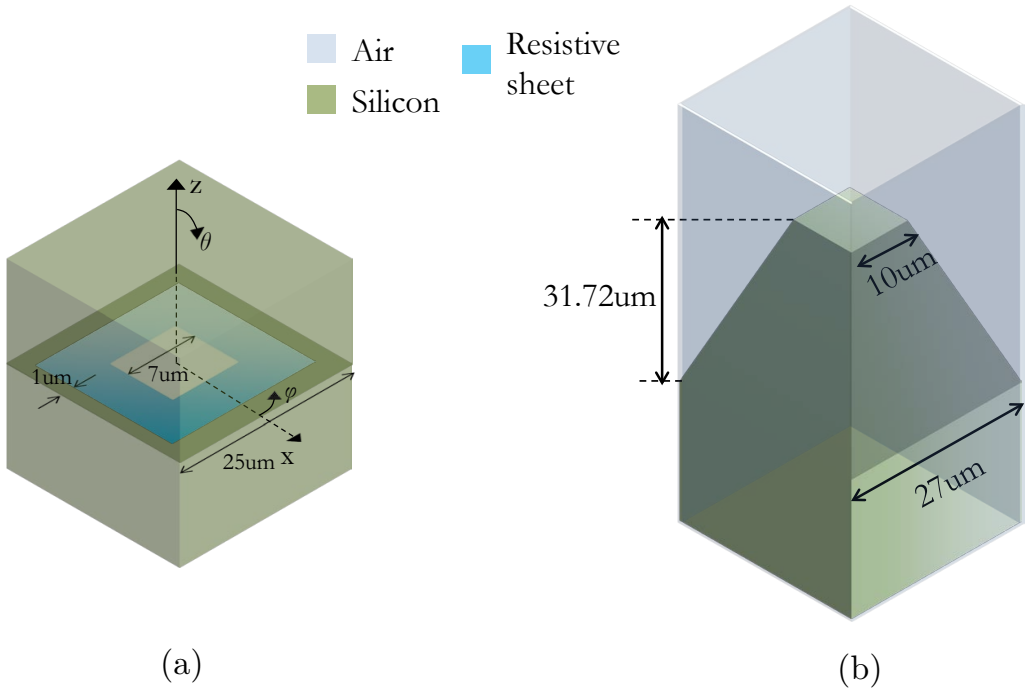

Figure 7.22: Unit cell dimensions of (a) the spill-over absorber and (b) grooved ML.

are stopped after first pulse is transmitted. The spill-over (η_{so}^{lens}) and the reflection (η_{ref}) efficiencies defined on the lens with both ML designs are highlighted in Fig. 7.23. As one can see, we have a very good agreement between the grooved ML and the Parylene $\lambda/4$ ML. This proves the proposed grooved ML design works properly within the proposed band.

After finalizing the grooved matching layer and SO absorber design, we can demonstrate the final geometry of the HF antenna array. The cross section of the design is highlighted in Fig. 7.24. Aperture efficiency obtained by the final prototype with the grooved ML and SO absorber is highlighted in Fig. 7.16.

7.7 Experimental Validation

In this section, we will validate the simulated ($\eta_{co,s}^{\Omega_s}$) and measured ($\eta_{co,m}^{\Omega_s}$) antenna coupling efficiencies of the single-pol leaky lens antenna (See Appendix A and B for the detailed information on the methodology). The measurements have been done in SRON and a single polarized version of the proposed design have been used in the measurements. The fabricated array has 1k pixels and a picture including some of them is shown in Fig. 7.25.

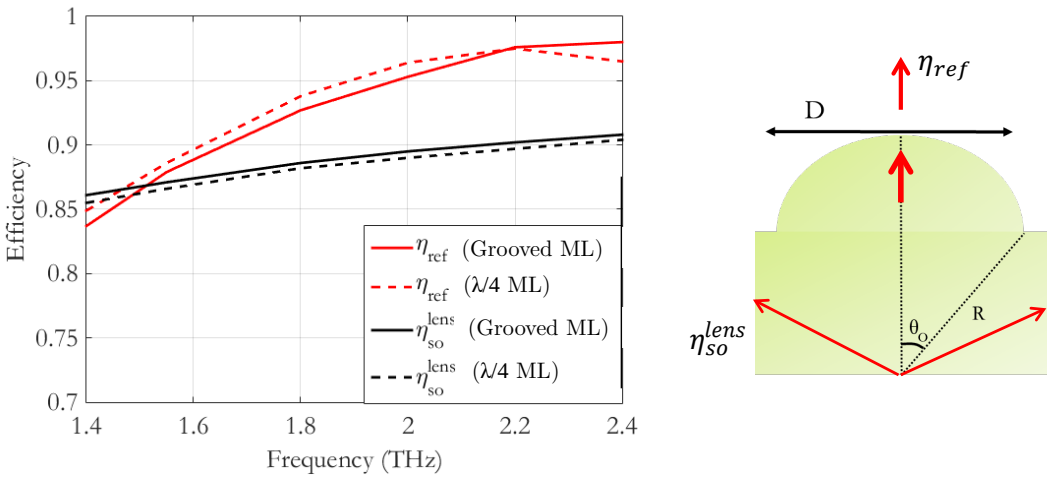

Figure 7.23: Efficiency comparisons obtained from the lenses coated by grooved ML (solid lines) and $\lambda/4$ ML (dashed lines) designs.

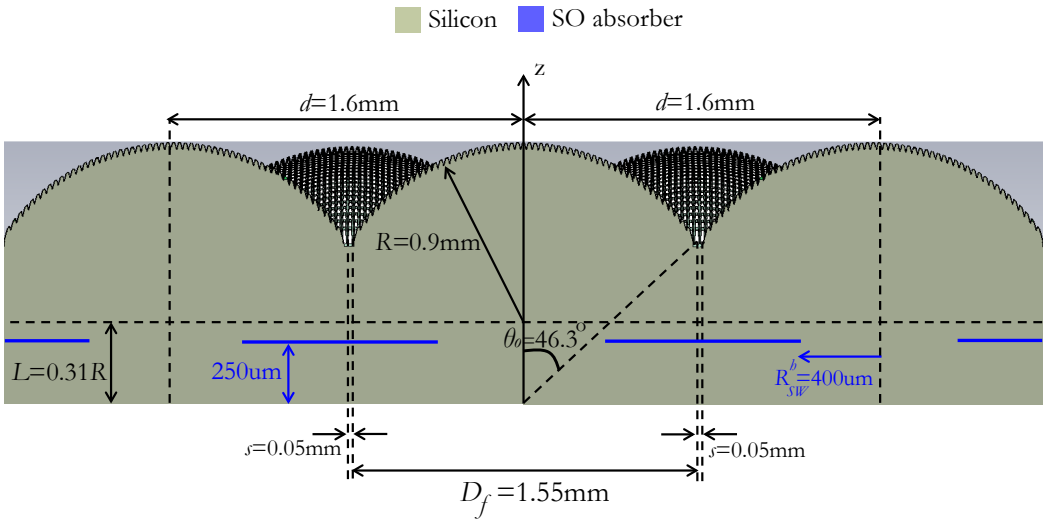

Figure 7.24: Cross section of hexagonally oriented HF prototype with its design parameters.

Figure 7.25: Picture of the fabricated single polarized leaky array (Courtesy of SRON).

The measurements have been done by using a single pixel of the proposed array and the lens is not coated by a ML. As mentioned before, one should expect similar results from proposed dual-pol leaky lens antenna since they provide almost identical beams as demonstrated in Sec. 7.3.

Similar steps have been followed as in Chapter 6 to validate the antenna coupling efficiency. The simulated $\eta_{co,s}^{\Omega_s}$ and measured $\eta_{co,m}^{\Omega_s}$ coupling efficiencies are highlighted in Fig. 7.26. It is important to remind here that the lens is not covered by a ML. Fig. 7.26 includes the scenarios where the lens is exactly located in the center and a 20 µm shift is introduced between the GP and the lens. This is due to the uncertainty in the fabrication process. It is very difficult to know exactly if the leaky slot is centered with the lens or, if not, the exact shift introduce in the measurement setup. Fig. 7.26 shows that the simulated antenna coupling efficiency varies between 0.102 and 0.158 within a tolerance of 20 µm shift. The measured coupling efficiency is about 0.11. It is fair to say that we have a quite good agreement between the simulated (with 20 µm shift) and measured antenna coupling efficiencies.

The comparison of the measured and simulated FTS data of the single polarized leaky lens antenna has been shown in Fig. 7.27. In the figure, the dashed black curve represents the raw measured FTS data which includes the effects coming from the filters that are present

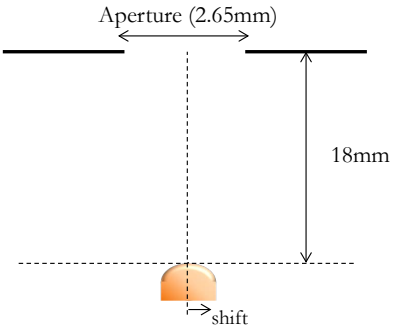

Measured	**Simulated**				
$\eta_{co,\,m}^{\Omega s}$		η_{so}	η_{feed}	η_{det}	$\eta_{co,\,s}^{\Omega s} = \eta_{so}\,\eta_{feed}\,\eta_{det}$
0.11	**Centered**	0.449	0.534	0.659	**0.158**
	20um shift	0.27	0.571	0.659	**0.102**

Figure 7.26: Comparison of the simulated and measured antenna coupling efficiencies obtained by the isolated single polarized leaky lens antenna at 1.55 THz.

in the measurement setup. Solid black line shows the measured FTS with the corrections after eliminating filter effects. The measured FTS datas show the wideband behavior of the proposed leaky lens antenna design. However, the presence of the water molecules in the measurement setup and possible standing waves between the source and aperture still have an impact on the FTS data. In fact, in Fig. 7.27, the oscillations in the measured FTS results are mainly associated to the water absorption lines due to the presence of the water molecules in the setup. Using the data provided in [80], the frequencies where the water absorption line effect is significant are highlighted by red-dashed curves in Fig. 7.27.

Following, we highlight the comparison of the simulated and measured secondary beams in Fig. 7.28a at 1.55 THz since we have the measured data only at 1.55 THz. In the measurement setup, a blackbody source that can make a scan in 2D plane and equipped with a 1.55 THz filter is used as a source to illuminate the lens. It should be mentioned here that the measurement setup has an aperture stop to suppress the incoming radiation outside the solid angle of about 12^0. Figure 7.28a shows that the agreement between the simulated and measured beam is quite good. For the sake of completeness, we also highlight the simulated beams after the lens at 2 THz and 2.6 THz in Fig. 7.28b and c, respectively.

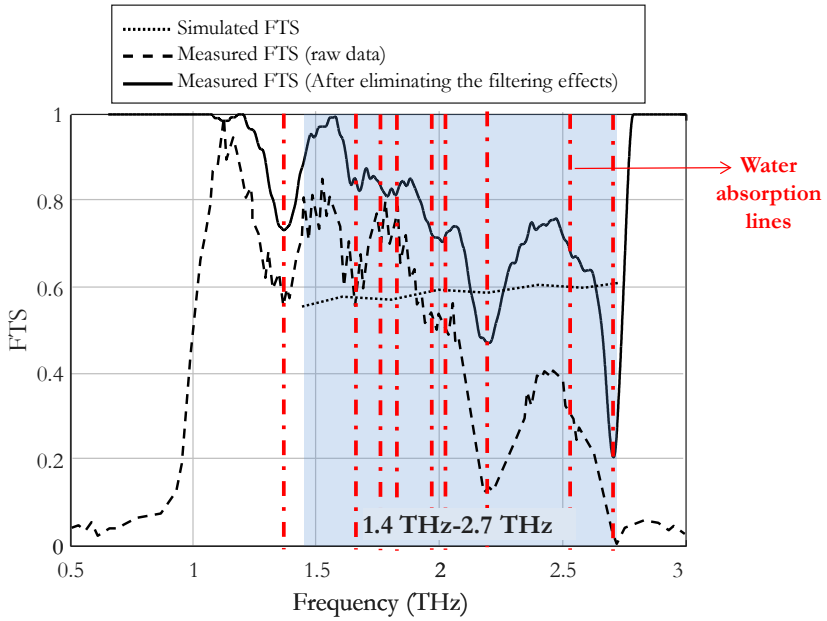

Figure 7.27: Comparison of the simulated and measured FTS datas obtained by the isolated single polarized leaky lens antenna.

7.8 Dual Polarized Antenna Operation in Reception

Since we do not have measurement results from the proposed dual-polarized leaky lens design yet, in this section, we will evaluate the performance of the dual polarized leaky lens antenna in reception by using CST MWS in terms of antenna efficiency and beam patterns. We directly use the HF design with CPW transmission lines. In order to analyze the antenna in reception, one has to launch separate simulations for each of plane waves impinging to the antenna surface with a certain incident angle, θ_i. The simulations takes much longer time in reception compared to the scenario when the antenna is operating in transmission. Therefore we will perform the simulations for only E and H-planes with 4 incident angles, $\theta_i = 0^0, 5^0, 10^0$, and 15^0, respectively (See Fig. 7.29) which is quite enough to characterize the main beams in reception. Also, we use a scaled version of the lens given in the previous section with a scaling factor of $1/1.75$ in order to accelerate the simulations.

It is important to state here that within the proposed bandwidth of SAFARI instrument, the reception mechanism of the antenna is slightly different than the antennas designed for A-MKID or SPACEKIDs projects since we use a thicker GP and CPW transmission line, about 75nm and they are both made of Aluminum. Direct measurements from SRON proved that Al film has some lossess within the proposed band. Therefore, for this design,

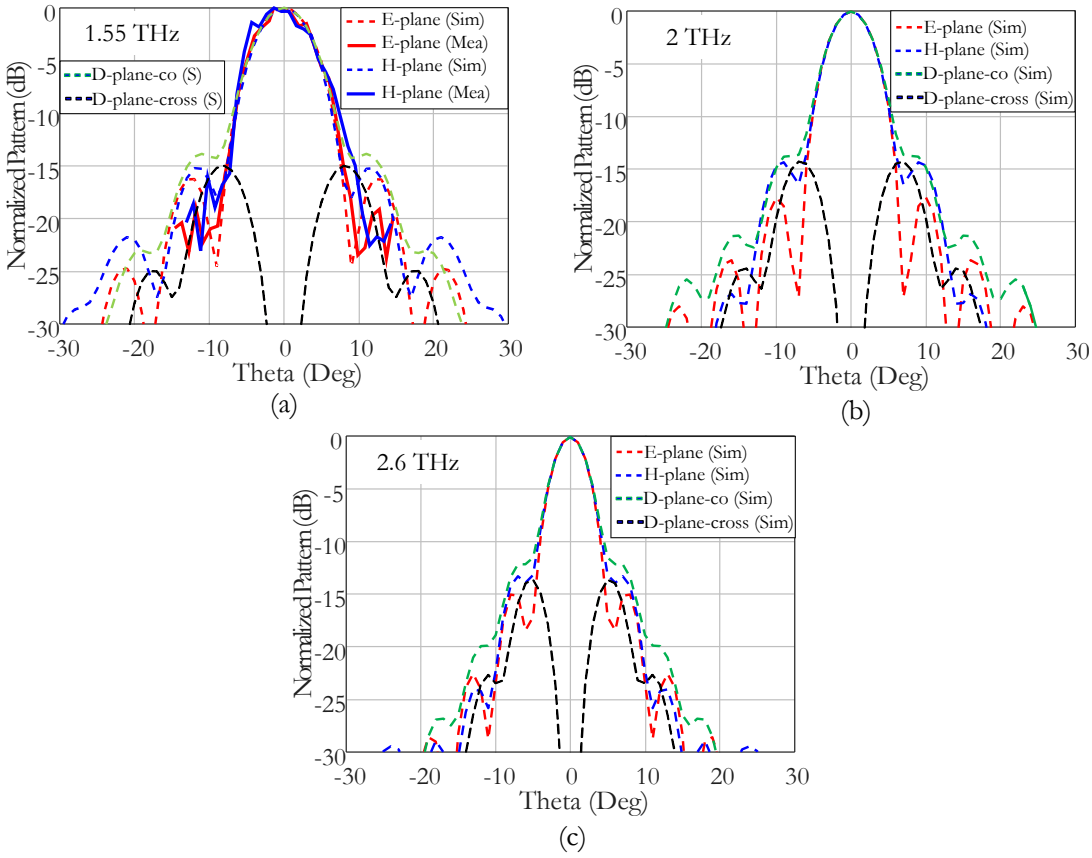

Figure 7.28: Radiated beams from the isolated single polarized leaky lens antenna: (a) Comparison of the simulated and measured secondary beams at 1.55 THz, (b) simulation results at 2 THz and (c) simulation result at 2.6 THz in E, H and D-planes.

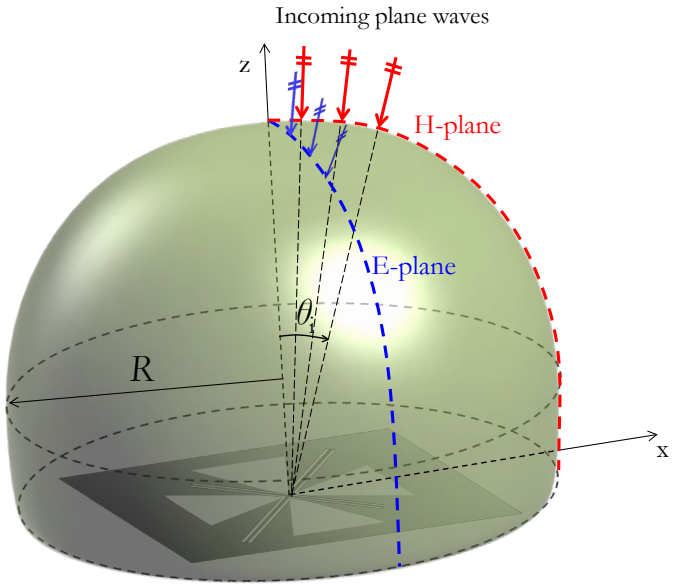

Figure 7.29: Incoming planes waves defined for E and H-planes with incident angles of $\theta_i = 0^0, 5^0, 10^0$ and 15^0.

the incoming radiation captured by the antenna will not be absorbed solely by the lossy CPW line but some part of it will be dissipated inside the GP. However, the detector is only sensitive to the power absorbed on the inner CPW line. As a result, one needs to evaluate two parameters obtained from CST reception simulations:

- The power absorbed by the ground plane (P_{abs}^{GP})
- The power absorbed only inside the lossy CPW inner conductor (P_{abs}^{CPW})

Here, we are interested in the antenna efficiency (η_{ap}^{Rx}) and the angular pattern of the antenna ($F(\theta_i)$) in reception. Once we know P_{abs}^{GP} and P_{abs}^{CPW}, they can be calculated as:

$$\eta_{ap}^{Rx} = \frac{P_{abs}^{GP}(\theta_i = 0)}{P_{RMS}^{PW}} \tag{7.1}$$

and

$$F(\theta_i) = \frac{P_{abs}^{CPW}(\theta_i)}{P_{abs}^{CPW}(\theta_i = 0)} \tag{7.2}$$

where P_{RMS}^{PW} refers to the total RMS inward power on the lens aperture due to the broadside plane wave incidence. Assuming a constant electric field distribution along the aperture

1.4 THz	Tx	Rx
Taper	0.8302	
Reflection	0.8799	
Spill-over	0.8764	
CPW Rad loss	0.969	
Matching	0.991	
Total	**0.615**	**0.58**

(a)

1.8 THz	Tx	Rx
Taper	0.7725	
Ref	0.9573	
Spill-over	0.8826	
CPW Rad loss	0.9635	
Matching	0.989	
Total	**0.622**	**0.61**

(b)

2 THz	Tx	Rx
Taper	0.7716	
Ref	0.9778	
Spill-over	0.8847	
CPW Rad loss	0.948	
Matching	0.982	
Total	**0.622**	**0.608**

(c)

Figure 7.30: Antenna efficiency comparison in transmission and reception for 1.4THz, 1.8THz and 2THz.

with a magnitude of E_0, it can be calculated as:

$$P_{RMS}^{PW} = \frac{E_0^2}{2\eta} A_{ph} \tag{7.3}$$

Where A_{ph} is the physical area of the lens aperture.

In principle, the proposed antenna can be used for the applications that require the antenna to serve either as a transmitter or as a receiver. Indeed, due to the reciprocity theorem one may assume that these two scenarios, antenna being used in transmission or reception, should yield to same beam patterns. In transmission, as explained in Section 7.3, the antenna is excited by the ports with a certain symmetry (See Fig. 7.9). In reception, the symmetry of the excitation happens only in the presence of a plane wave impinging to the lens along broadside ($\theta_i = 0^0$). Therefore, one can expect to achieve similar antenna aperture efficiencies when the antenna is operating in Tx and Rx where an incident plane wave along broadside is used to illuminate the lens. To show this, we have evaluated the antenna aperture efficiencies in transmission and in reception at 1.4 THz, 1.8 THz and 2 THz and reported in Fig. 7.30 at each frequency point. According to the result, we have an excellent agreement between total antenna efficiencies obtained in transmission and reception.

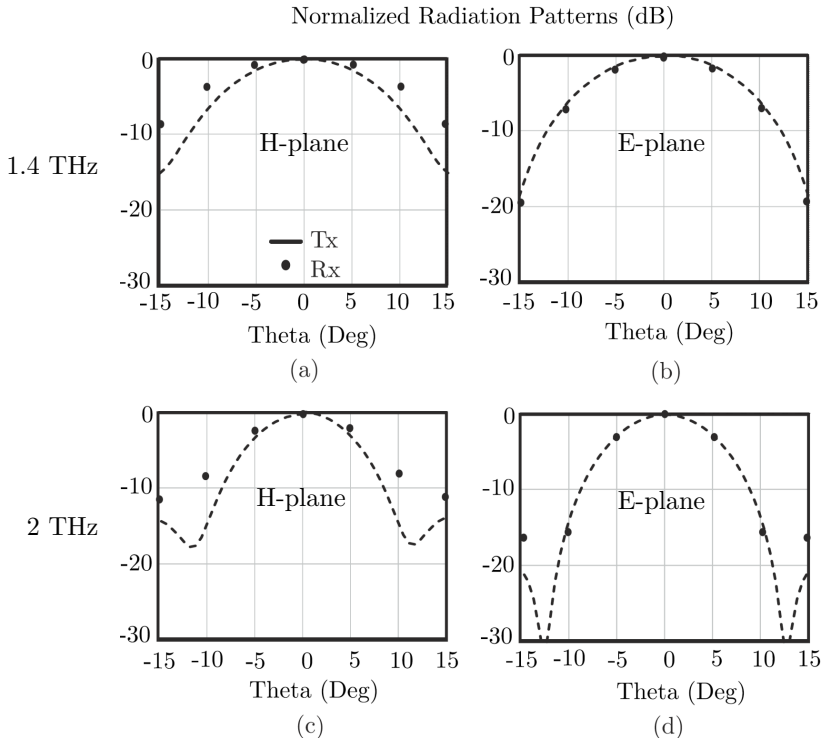

Figure 7.31: Comparison of the antenna beams in reception and transmission at 1.4THz and 2THz.

When it comes to the beam patterns, however, one has to evaluate the lens antenna with an incoming plane waves at oblique incidence ($\theta_i \neq 0^0$). Since the excitation of the symmetry does not hold for oblique incidence anymore, one can expect to have some differences in the beams obtained in transmission and reception scenarios. To prove this, the antenna beams in Tx and Rx are evaluated and compared in Fig. 7.30 for 1.4 THz and 2 THz. Fig. 7.31a and b show the normalized beam at 1.4 THz, whereas Fig. 7.31c and d highlight the patterns at 2 THz for H-plane and E-planes, respectively. Although the angular distribution of the antenna beams in transmission can be obtained by a single CST simulation, the simulations in reception have to be launched for each specific observation angle which is time consuming. As mentioned before, here, we evaluated the beams in reception at 0^0, 5^0, 10^0 and 15^0 and highlighted with dots in Fig. 7.31. It can be seen that there is an excellent agreement in the E-plane, both for 1.4 THz and 2 THz. However, the difference in the H-plane is significant. The beams obtained in reception is about 1.4 times wider than the beams in transmission. This result is not trivial, in fact, kind of expected due to the reason given above.

One of the possible solutions to hold the excitation symmetry also for the oblique incidence

(a) (b)

Figure 7.32: Proposed CPW fed dual polarized leaky slot geometries: (a) The ordinary design and (b) the modified design with airgap located at the center, seperating the crossing CPW lines.

scenario in reception is to decouple the CPW transmission lines in the center by means of using an air bridge in the center of the antenna as it is shown in Fig. 7.32b. Same simulations in reception are launched for the modified antenna design with an air-bridge in the center and the results are highlighted in Fig. 7.33. The figure clearly shows that the modified antenna provides the same beams in reception and transmission both for E and H-planes.

7.9 Conclusion

The dual polarized leaky lens antenna presented in this contribution is able to provide clean symmetric beams with high aperture efficiencies for a bandwidth more than one octave. The proposed antenna provides a planar integrated solution which allows easy and low cost manufacturing process unlike the horn antenna solutions since they suffer from these issues, especially for higher mm and sub-mm wavelengths. The design has a maximum lens aperture efficiency of 70% while it operates within a bandwidth over $1:5$ with an aperture efficiency more than 50% or $1:2.5$ where the aperture efficiency is more than 60%. The entire antenna system has a very good cross polarization performance. Namely the maximum cross polarization level is less than -35 dB for $d = \lambda_0 F/D$ sampling whereas it remains even lower, less than -49 dB, for $d = 0.5\lambda_0 F/D$.

According to the results highlighted in the text, we believe that the proposed antenna design lends itself as an extremely useful alternative for next generation sub-mm wave space astronomical instruments.

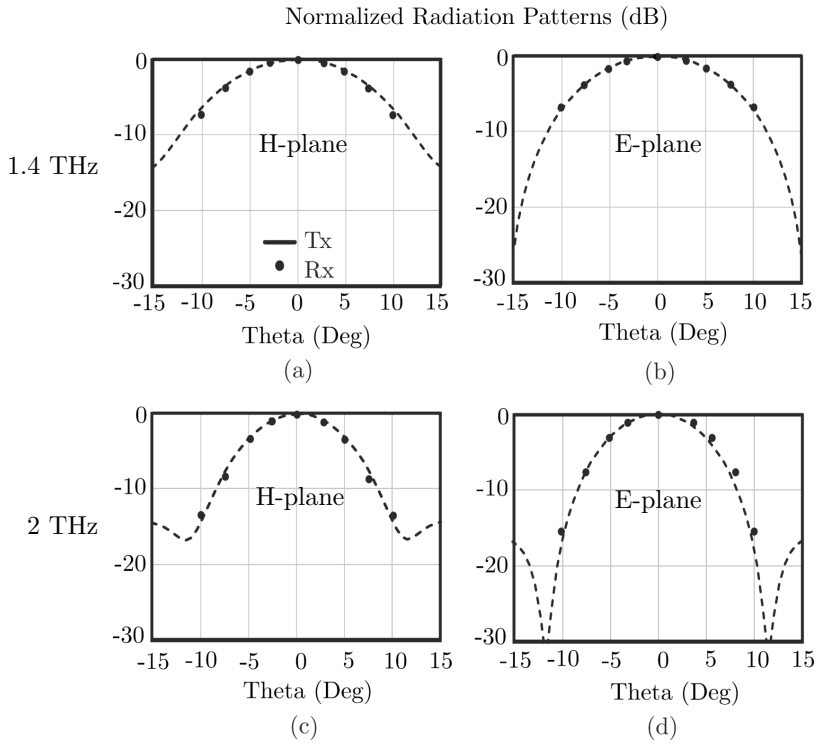

Figure 7.33: Comparison of the antenna beams obtained from the modified antenna in reception and transmission at 1.4THz and 2THz.

CHAPTER 8

Conclusions and future work

The last chapter of this thesis will summarize the scientific results have been discussed within the previous chapters and explains the possible future research lines.

8.1 Conclusions

This thesis has focused on the development of high performance integrated lens antenna solutions to be used for sub-mm wave & THz astronomical observations. The work is divided into two parts: The first part aimed at a single lens fed by multiple feeds to achieve frequency stable radiation for effective reflector illumination. Part II, on the other hand, focused on a single feed per lens scenario, specifically targeting at tightly spaced FPA applications. Two scenarios have been considered for FPA design: Earth based and space based astronomical observations. Depending on the requirements of the instruments, a double slot based approach has been used for Earth based astronomy whereas a dual polarized wideband antenna design has been proposed for space based observation.

8.1.1 Single Lens Scenario

First, we performed a parametric study in order to characterize an extended hemi-spherical lens fed by a connected array of leaky slots within a bandwidth ratio of 1:4. A spectral domain approach has been used to characterize the field radiated by the array whereas an accelerated PO method is employed in the lens analysis. We started investigating the radiation characteristics of the lens as a function of the feed position and the length of the lens extension. It turned out that extension lengths close to $0.35R$ (R being the radius of the lens) lead to maximum directivity values from the lens antenna for higher edge of the frequency band whereas the extension length tends to be lower for lower frequencies, being about $0.3R$. The investigation of the reflection losses on the lens surface showed that increasing the lens extension length provides slightly higher scan losses. Fixing the lens extension length, higher frequencies lead to lower reflection losses since the directivity of the beams inside the lens is proportional with the frequency.

The study of losses due to mutual coupling between the array elements showed that $0.3\lambda_0$ spacing between the elements provide a loss below 0.5 dB at the lowest frequency, f_0. One can use tapered slots instead of straight ones to reduce the mutual coupling losses even further. This may allow one to pack the elements tightly for FPA applications where high spatial resolution is needed. Besides, it has been demonstrated that introducing slot tapering in the array helps to improve antenna cross polarization performance.

Having studied the radiation characteristics of a connected array of leaky slot antennas, a coherently fed leaky slot array is introduced as a lens feeder within a bandwidth of about $1:3$. The proposed lens antenna is able to provide frequency stable beams to maximize the reflector illumination efficiency within the band of operation. Performance is estimated in

terms of amplitude taper and phase error losses at the reflector, yielding a reflector aperture efficiency of about 80% over the entire 1 : 3 bandwidth. A LF prototype covering a band from 4 to 12 GHz has been fabricated. The simulated antenna performance has been validated with the measurements from the prototype. The measured antenna beams and reflector illumination efficiency have a quite agreement with the ones predicted by the simulations. Although the results of the LF prototype is shown, the antenna can be easily scaled accordingly for sub-mm band and it satisfies all the specifications required by the DESHIMA instrument.

Another approach to achieve frequency stable beams could be to use the Double Shell Lens (DSL) concept instead of using the concept of feeding the array elements coherently. For this purpose, a connected leaky slot array with 23×23 feeding elements have been integrated to an optimized DSL. It has been demonstrated that the antenna is able to provide quite stable beams within a bandwidth of one octave both for on-axis feed and off-axis feedings. A conventional silicon extended hemispherical lens has been used as a reference design. According to the results the proposed DSL based antenna has a gain variation of 2.7 dB whereas it becomes about 6 dB for the conventional lens design. Using a DSL also improved the scan loss by about 1 dB within the band.

8.1.2 Tightly Spaced FPA Scenario

When it comes to tightly spaced FPA, it has been demonstrated that the feed aperture efficiency becomes crucial to maximize the total system performance, and therefore, the imaging speed.

For this purpose, first, a double slot based antenna design have been proposed for Earth based observation. This scenario includes two project: SPACEKIDs project and A-MKID project. Depending on the requirements of each project three double slot antennas have been designed. The antennas have been optimized to maximize their feed aperture efficiency at the optimization frequency which is 850 GHz for SPACEKIDs and A-MKID band 2 and 350 GHz for A-MKID band 1. The simulated feed aperture efficiencies are 53%, 76% and 58% for SPACEKIDs and A-MKID antennas No. #1 and #2, respectively. The proposed double slot based design for SPACEKIDs project has been fabricated by SRON. The simulated antenna performance has been validated by measurements performed at 850 GHz by SRON. For a FF aperture with an opening angle of $\theta_0 = 14.3^0$, the simulated and measured antenna coupling efficiencies are about 52% and 54%, respectively. Besides, the beams after the lens and FTS of the antenna have been compared with measurements and very good agreements have been obtained between the simulations and measurements.

A wideband dual polarized antenna has been proposed for a SAFARI-like scenario within the SPACEKIDs project. The scenario has an operational bandwidth from 1.4 THz to 2.7 THz. It has been demonstrated that the antenna is able to provide a feed aperture efficiency of more than 60% within a bandwidth of $1:2.5$ whereas it exceeds 50% for a $1:5$ band. The instrument has an optical telescope with a large F/D (f) ratios, typically $F/D > 10$. To achieve full focal plane field sampling, tightly spaced feed arrays have been investigated with various feed samplings including $d = 0.5\lambda_0 F/D$, $d = \lambda_0 F/D$ and $d = 2\lambda_0 F/D$. The reflector beams have been demonstrated and the results show that the antenna system has a maximum cross polarization value of -35dB and -48dB for $d = \lambda_0 F/D$ and $d = 0.5\lambda_0 F/D$, respectively. A single polarized version of the proposed antenna has been fabricated and measured by SRON at 1.55 THz to verify the simulated antenna beams and coupling efficiency results. Very good agreements have been obtained between the simulations and measurements.

Finally we evaluated the surveying speed ratio obtained with the proposed single polarized version of the dual polarized leaky slot antenna for $d = 0.5$, 1 and $2\lambda_0 F/D$ feed samplings where λ_0 is the free-space wavelength at the center frequency of f_0. In the calculations the double slot based A-MKID antenna #2 design is taken as a reference. The leaky lens and the double slot antenna feed efficiencies are highlighted in Fig. 8.1 within an octave bandwidth together with the reflector spill-over efficiencies obtained for $d = \lambda_0 F/D$ sampling. The proposed leaky slot based design has a feed efficiency above 75% within the entire band whereas the double slot based design suffers from this efficiency especially at the edges of the band. Using the efficiencies reported in Fig. 8.1, the ratios are highlighted as a function of the instrumental noise contribution T_{IB} for Rayleigh's and Wien's limits in Figs. 8.2a and 8.2b, respectively. One can see that the leaky slot based design has a significant advantage in terms of speed compared to the double slot based design for tight feed samplings, especially for low instrumental noise conditions. The advantage drops as the instrument noise increases.

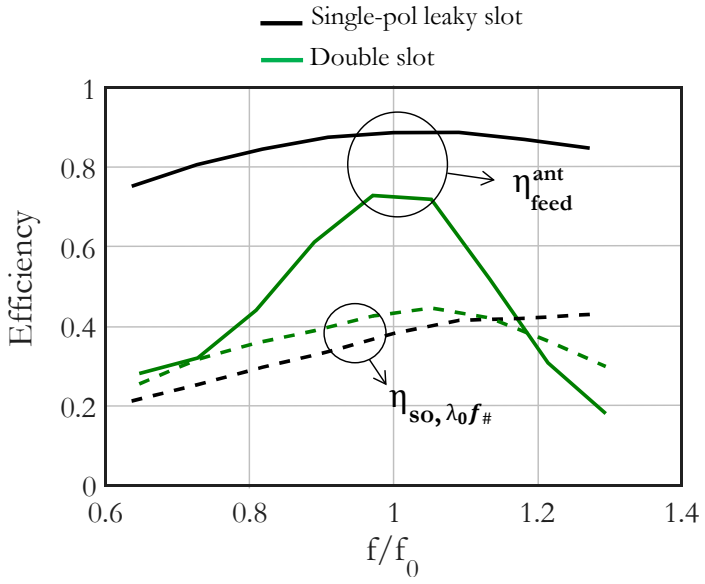

Figure 8.1: Speed ratio calculations obtained by the single polarized version of the proposed dual polarized leaky lens antenna as a function of the instrumental noise (T_{IB}), taking the double slot based A-MKID antenna #2 with a sampling of $d = \lambda_0 F/D$ as a reference.

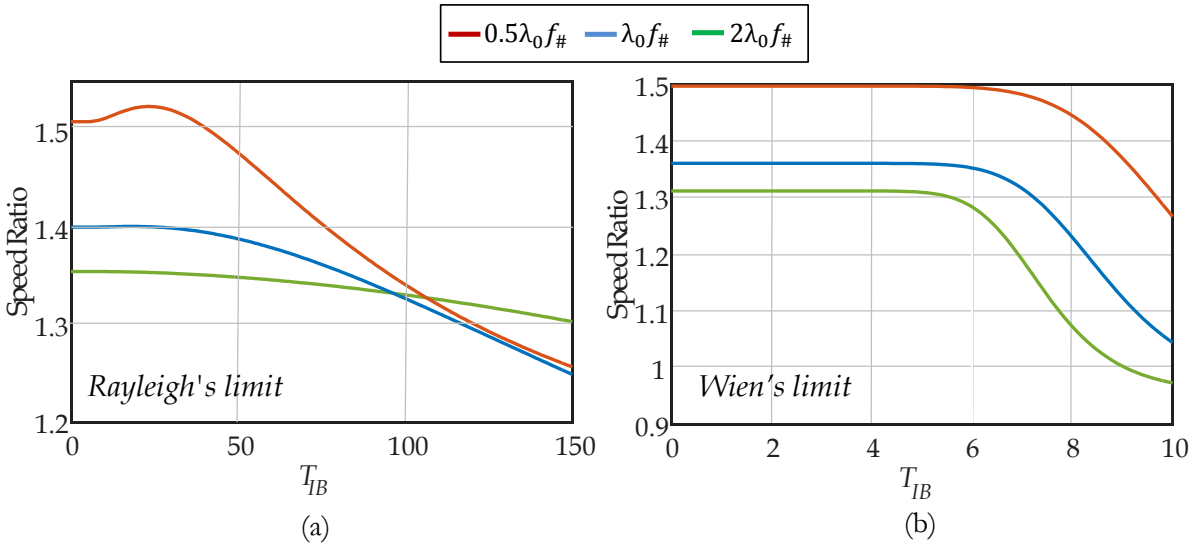

Figure 8.2: Speed ratio calculations obtained by the single polarized version of the proposed dual polarized leaky lens antenna as a function of the instrumental noise (T_{IB}), taking the double slot based A-MKID antenna #2 with a sampling of $d = 2\lambda_0 F/D$ as a reference.

8.2 Future Research Lines

There are several research lines that can be thought as a continuation of the work presented in this thesis which are enlisted below:

- In Chapter 3, a LF prototype of the coherently fed leaky lens antenna has been demonstrated to validate the simulation results. The antenna is planned to be used for the DESHIMA instrument as a future work and measurements of the scaled version of the proposed design will be performed in the DESHIMA band.

- Firstly, as was mentioned in Chapter 4, the study of the DSL based antenna concept provides only a preliminary design since dielectric losses are neglected in the lens materials. A study on the material choice should be carried out and the lens optimization explained in Chapter 4 has to be repeated accordingly, while including the dielectric losses of the lenses.

- Chapter 6 provides three antenna solutions to be used for SPACEKIDs and A-MKID projects. The SPACEKIDs antenna has been fabricated and measured at 0.85 THz. A-MKID antenna #1 and #2 will be fabricated and the antenna beams, the coupling efficiency and Fourier Transform Spectrometer (FTS) measurements will be performed by SRON as future work.

- A proposed single polarized version of the dual polarized FPA antenna explained in Chapter 7 has been fabricated and measured by SRON at 1.55 THz. The fabrication of the array version of the single pol antenna has been finalized and the beam pattern and the FTS measurements will be performed soon.

Finally, the antenna designs have been presented in this thesis could be easily employed at sub-mm wave frequencies. The proposed dual polarized leaky slot antenna that can be integrated to planar transmission lines (in our case KIDs) which could enable astronomers to design advanced THz cameras with tens of thousands of arrays located at focal plane to achieve broad Field of View (FoV). Thanks to its capability of dual polarization, large bandwidth of operation and high aperture efficiencies, the design could improve the sensitivities of the state-of-the-art instruments significantly. The design concepts have been introduced in this thesis are extremely suitable for THz deep space instrumentation where the applications mostly require superior detector sensitivities, improved resolution capabilities and higher imaging speeds. In fact, a prototype at SAFARI band of the dual-polarized leaky slot antenna is currently being fabricated and pending to be measured by SRON,

which opens up the possibilities to revolutionize the next generation THz astronomical instruments.

APPENDIX A

Seeing the Invisible: Sub-mm Wave & Infrared Radiation

An invisible type of radiation beyond the red portion of the visible spectrum was discovered by Sir William Herschel in 1800. He then called this type of radiation as infrared, meaning "below" red. This discovery can be considered as a first step in forming the electromagnetic spectrum. Considering the energy emitted by all objects in the universe, infrared radiation and visible light are just two types produced energy. Having a complete picture about the creation of the universe and understanding how it is changing is only possible by means of studying all of these kinds of radiation types.

We can learn a lot about the universe just by using our eyes. Consider all the information you can obtain by simply looking at the world around you. Our eyes serve as sophisticated detectors which have biologically evolved to "detect" visible radiation. However, there are numerous types of radiation that we cannot detect without using technology. Only a few types of radiation is allowed to penetrate through our atmosphere and visible radiation is one of them. We can see only a tiny amount of electromagnetic radiation compared to what we can possibly get within the entire electromagnetic spectrum by using high technology instruments.

Radio waves, microwaves, infrared, visible, ultraviolet, X-rays and Gamma rays form the electromagnetic spectrum. They only differ by their wavelength or frequency. The wavelength decreases and frequency (as well as temperature and energy) increases from radio waves to Gamma-rays. In free-space all of these radiation types travel with the same speed, at the speed of light. Not only the visible light but also radio, infrared (some portion), and a tiny amount of ultraviolet energy can travel to the Earth's surface from space. It is

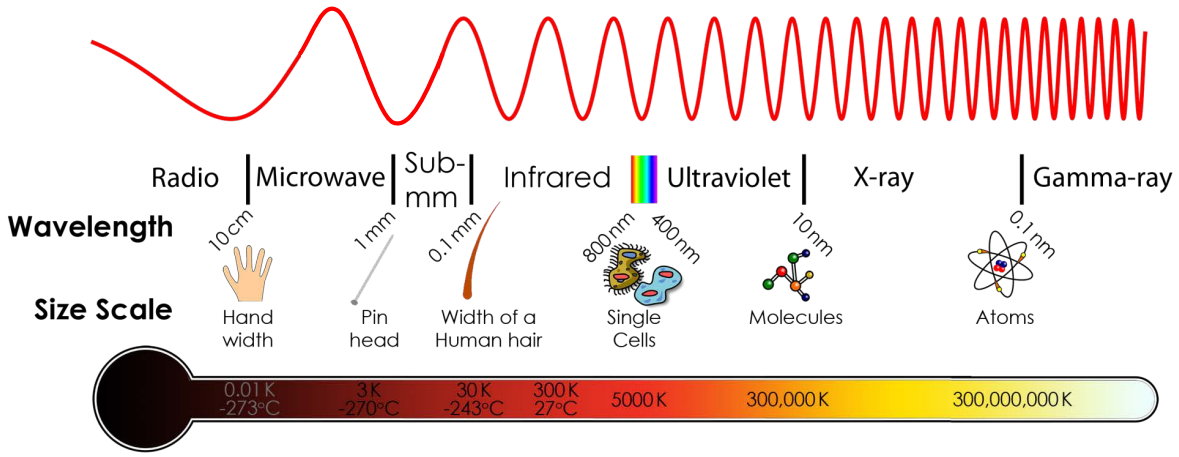

Figure A.1: The electromagnetic spectrum (From http://planck.cf.ac.uk/science).

fortunate for us that our atmosphere blocks the rest of the radiation, many of them being dangerous for life on Earth.

The electromagnetic spectrum is highlighted in Fig. A.1. Infrared radiation is located between the microwave and visible portions of the electromagnetic radiation. Infrared radiation has wavelengths shorter than microwaves and longer than visible radiation. Correspondingly Infrared has frequencies that are higher than microwaves and lower than visible light. Thermal radiation or the heat is the primary source that emits infrared energy. It is generated by the fluctuations of atoms and molecules in an object. The lower the temperature, the less the molecules move and the less infrared radiation they emit. Infrared radiation is emitted by all objects, even the objects that we may consider as being very cold (i.e an ice cube) emit infrared energy. If an object does not radiate visible light since its temperature is not high enough, then it emits most of its energy in the from of infrared. Objects radiate more infrared energy as they become warmer.

In our daily life we are exposed to the infrared radiation all the time. For example the heat due to sunlight, a radiator, a fire are mostly infrared. Our bodies also radiate infrared energy with a wavelength peaking at about 10um. Detection of the infrared radiation leads to significant benefits and discoveries, providing more and more understanding about our world and the Universe thanks to the development of superior infrared detectors. From security, medicine, navigation and rescue, to the weather, the atmosphere and the cosmos, it has not only saved lives, but has lead to an endless, new world to explore.

Infrared radiation is divided in three sub regions: Near (NIR), middle (MIR) and far-infrared (FIR). The range between the microwave and FIR regions of the spectrum is considered as sub-mm wave range (See. Fig. A.1). Typically it covers a frequency band starting from 300GHz to 1 THz of the spectrum. Sub-mm wave portion of the spectrum is relatively less studied and it has a huge potential to change the view upon the universe.

A.1 Terahertz Astronomy

Although the information in different sources may vary, roughly speaking, the Terahertz portion of the spectrum is assumed to be starting from about 300 GHz up to about 3 THz. It includes the entire sub-mm band and extends up to the long-wavelength edge of the FIR spectrum. At such frequencies, technological developments over the last decades resulted in superior detectors with improved performance of capturing the radiation that is not visible to human eyes. Besides, telescopes can be placed on satellites or on high-flying airplanes to avoid the attenuation and the optical emission caused by the Earth's atmosphere on the radiation emitted by celestial objects. Although all the objects existing in the Universe emit THz radiation, only a tiny amount of the radiated THz signals can be captured by ground-based observatories due to the strong atmospheric attenuation. Therefore, using space based observatories launched directly in space or located at high-flying aircrafts has revolutionized our knowledge about the universe. Most of the THz observations require special kind of detectors that are cooled down to extremely low temperatures. This is because sub-mm & FIR emissions are primarily in the form of heat radiation and therefore the detectors should provide high sensitivity to the thermal fluctuations.

THz radiation can be used to observe the deep Universe as well as star-forming regions since it can penetrate through the thick dust regions that exist in space. Moreover, cold interstellar clouds and cool stars can be also observed in the THz whereas they are not visible in visible spectrum. Many interstellar molecules (including organic molecules) can be also included in the list. These types of observations can also be made towards the very early Universe.

A.2 Atmospheric Transmission

Excluding our local solar system, all the information we can obtain about the Universe comes from the observation of the radiation emitted by the distant objects existing in space. In other words, astronomy is totally based on remote sensing to provide information upon

which our theories and knowledge rest. Knowing the possibility of getting immense amount of data from the Universe by means of observing the emitted radiation from celestial objects, it is kind of disappointing that only a tiny of it could reach to us due to the fact that most of the information is absorbed by the Earth's atmosphere. This is because the presence of the gases and the water vapor existing in our atmosphere introduces strong absorption. Figure A.2 shows the atmospheric transmission as a function of the frequency of the incoming signal up to 1 THz measured at Llano de Chajnantor, Chile at an altitude of about 5km from sea level. It shows that most of the radio-waves emitted by the celestial objects can travel to the surface of the Earth without almost no absorption, which has been discovered from the observations in the twentieth-century. Similar to the radio-waves, visible light can also penetrate through the Earth's atmosphere, diminished a bit but not totally absorbed. Since ancient time human race has been always extremely curious to know more about space, staring at the stars, the Moon and making observations to see celestial objects such as different planets and so on. The effort of trying to make the unknown known would only be possible thanks to the transparent behavior of our atmosphere to the visible light. The reasons explained above explains why radio and optical astronomy are already widely developed and well-known to study the Universe. Unfortunately, this is not true for THz observation since it not as straightforward as optical and radio astronomy due to the fact that most of THz radiaton cannot penetrate our atmosphere. As a result, THz astronomy has been overshadowed by optical and radio astronomy so far.

Apart from visible radiation and radio-waves, a small portion of the ultraviolet radiation and some infrared radiation can reach us. The rest of the wavelengths emitted by the celestial objects, however, are absorbed by our atmosphere and cannot reach ground-based telescopes.

The reason why our atmosphere is transparent to specific wavelengths and not to the rest is completely related to its atomic and molecular constituents. For example, the radio waves with a wavelength less than about one centimeter is strongly absorbed by the atmospheric gases like oxygen and water vapor (H_2O). When it comes to infrared radiation, other gasses such as CO_2 together with H_2O introduce strong absorption for most of IR radiation. However, there are some narrow windows in the IR spectrum that the astronomers can make some observations such as the radiation with a wavelength of about 10um and 20um. To overcome these difficulties, a solution could be to perform the infrared observations by means of launching the telescopes at the altitudes of about $30 - 35$km by using large balloons or directly positioning them on space based satellites.

Moving to the lower band in frequency, one can observe similar transmission behavior

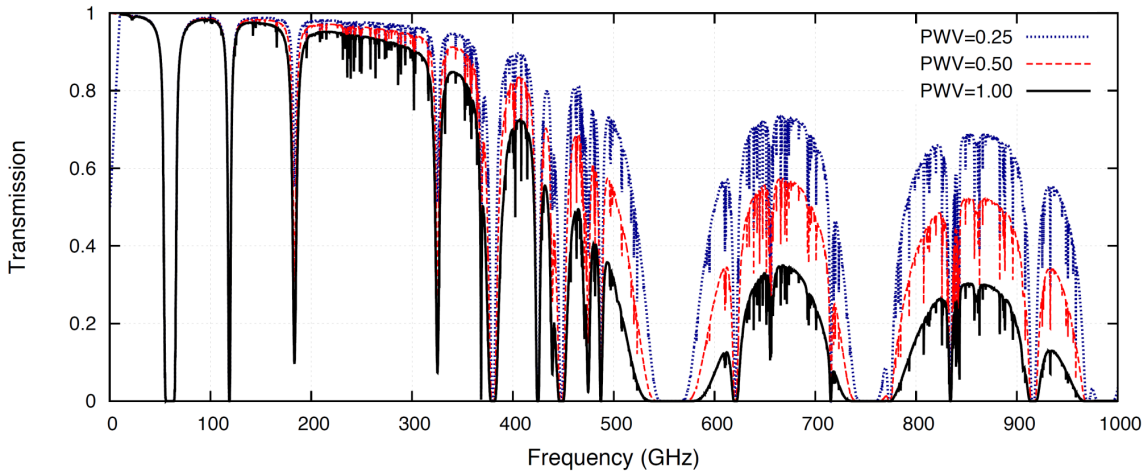

Figure A.2: Atmospheric transmission as a function of wavelength measured at Llano de Chajnantor, Chile, at the altitude of 5040m (From http://almascience.eso.org).

also for FIR and sub-mm wave regions due to the strong absorption by the constituent atmospheric gasses almost within the entire band. However, there is an exception for two frequency windows corresponding to about 350GHz and 850GHz that could be suitable for astronomers to perform sub-mm observations from ground based observatories.

A.3 Why THz Astronomy is Important

THz astronomy is crucial when it comes to understanding the universe and its content. The fundamental reasons for this can be listed as below:

A.3.1 Observing the Galaxies Hidden by Dust

A census of any galaxy, including the ones that are characterized as spiral galaxies (i.e. the Milky Way), not only reveals billions of luminous stars, but also a medium filling the deep space between the stars. This is called as Interstellar medium (ISM) and it mainly consists of gas atoms, molecules and solid dust particles. For example, in the solar neighborhood of the Galaxy, typically there is only one atom of gas per cubic centimeter and hundreds of dust grains per cubic kilometer. However, on galactic scales, the effects due to the gas and dust are apparent. The dust grains are composed of carbon and silicate matter and tend to be tiny, typically smaller than 0.1um in diameter. They can reflect and absorb the surrounding visible and ultraviolet light generated by the stars, producing a dimming and

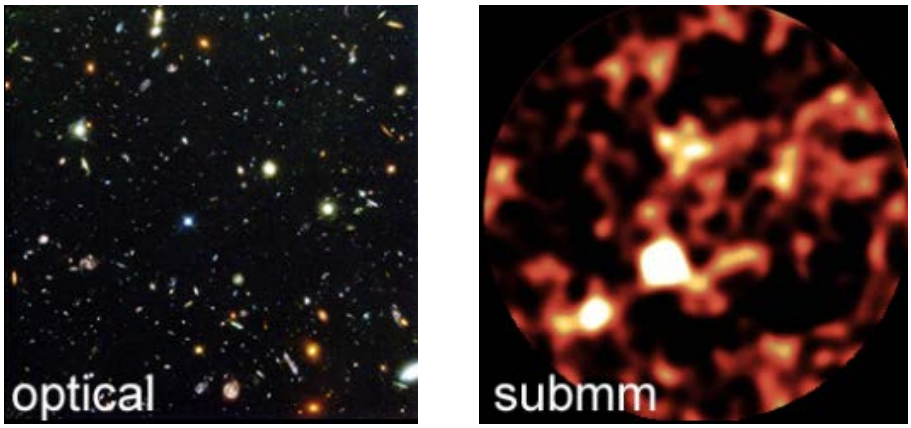

Figure A.3: (a) Optical image of Hubble Deep Space and (b) the SCUBA image of HDF obtained at 350 GHz sub-mm observation showing dusty galaxies [81] that are not visible in optical observations (From http://herschel.cf.ac.uk).

reddening effect.

In 1996, a picture taken by the Hubble Space Telescope revolutionized astronomy. It was the most detailed optical picture of the Universe mankind have ever had. The picture is known as Hubble Deep Field (HDF) and it is shown in Fig. A.3a. Thousands of galaxies are visible in the image, the faintest ones being located at further distances. However this picture was not the entire story. Second revolution, after Hubble, was the sub-mm wave array camera SCUBA on the James Clerk Maxwell Telescope (JMCT) [82], being one of the highest-impact astronomical instruments between $1997 - 2003$. Further observations from SCUBA proved that the galaxies hidden by the huge amount of dust are missing in Fig. A.3a. Figure A.3b shows the 850 um SCUBA image of the dusty view of the HDF. Compared to optical image shown in Fig. A.3a, the number of galaxies are much smaller (seen as white spots) in the sub-mm image and it is totally different from what one can obtain from the optical observations.

As a consequence, it is clear that the observations at sub-mm wave & far-infrared wavelengths has a lot to offer when it comes to the detection of sources that are hidden by the cosmic dust.

(a) (b)

Figure A.4: Rosette nebula seen in (a) visible light and (b) FIR spectrum (Image credit: ESA/PACS and SPIRE consortia).

A.3.2 Witnessing Star Formation

Dust hides not only the distant galaxies from our view but also the newborn stars. The ISM can be considered as a reservoir from which matter for new stars can be drawn. Almost 99% of the ISM is composed of either atomic gas (i.e. hydrogen) or molecular gas (i.e. hydrogen, water, ammonia and carbon monoxide). The concentrations of gas and dust are thousands of times greater than elsewhere in molecular clouds existing within the ISM. They usually appear as a dark nebula against a blanket of background stars in an astronomical observation.

These clouds are capable of generating hundreds of stars inside their cores. For example, the Orion Nebula which can be easily seen through binoculars, is one of the richest nurseries of star formation. The newborn stars are surrounded by dense clouds of gas and dust so they are often hidden from view. FIR and sub-mm radiation is the clearest way to observe the newly formed stars that are still embedded in their clouds. Infrared radiation due to the heat from the stars can penetrate through the dark, nebulous clouds and could provide us a picture regarding to the formation of the stars, which is unlikely for visible radiation since it is blocked. As an another example, the picture of Rosette Nebula is shown in visible light and FIR region in Fig. A.4a and b, respectively. Only the FIR image is able to show the dust glowing due to the heat generated by the young stars inside within.

A.3.3 Exploring the Early Universe

Terahertz astronomy can help astronomers to obtain more information about the early Universe and the evolution of the galaxies. Our Universe is expanding since the Big Bang explosion, a theory that assumes to be the beginning of our universe, and most of the galaxies are moving away from each other since then as a result of the expansion of the Universe. Astronomers have observed that the further away the galaxies are, the faster they move. This movement has an interesting effect that could be very useful for astronomers. It is proven that as an object is moving further away, the emitted radiation is "redshifted" which means that the frequency of the emitted radiation shifts to lower band. In other words, the expansion of the universe stretches the light traveling within intergalactic space which results in a cosmological redshift in the wavelength to longer wavelengths. Although it is not exactly the same, this cosmological redshift is somewhat similar to the Doppler shift that we can observe in our daily life. For higher redshifts, most of the infrared radiation radiated by distant sources such as stars and galaxies are red-shifted into the sub-mm band by the time they are reach to our telescopes [81].

In the universe, the objects with high redshifts can be observed as they existed long ago. The deeper the distance, the greater the redshift, and consequently, the further "look back" in time that we observe the Universe as it was. As an example, Fig. A.5 demonstrates the matter distribution in the Universe for different redshifts, z, values. The frames demonstrate the evolution of the dark matter model in 140 million light year box from a redshift of about 30 to the present epoch, $z = 0$. It is quite exciting to see how the matter density variation changes, being almost homogeneous when the Universe was less that 1% of its current age and forming smaller bright clusters as a result of the gravitational force as time goes on. One can also notice that as the redshifts get closer to $z \approx 0$, the matter distribution does not change that much. This is because the gravitational force cannot compete with the acceleration provided by the dark energy as the Universe expands, typically corresponding at $z < 1$. Investigation of the dark matter evolution could result in important discoveries. By using the Atacama Large Millimeter/submillimeter Array (ALMA), astronomers had discovered a nest of monstrous baby galaxies located about 11.5 billion light-years away [83]. The young galaxies seem to be located at the junction of gigantic filaments in a web of dark matter. This discovery supports the current galaxy formation theories which predict that these monstrous galaxies form in areas where dark matter is concentrated. However it is not possible to observe them in visible spectrum since these galaxies are often hidden in dust. On the other hand, they do emit strong radiation in the sub-mm band. This recent study shows that further sub-mm observations

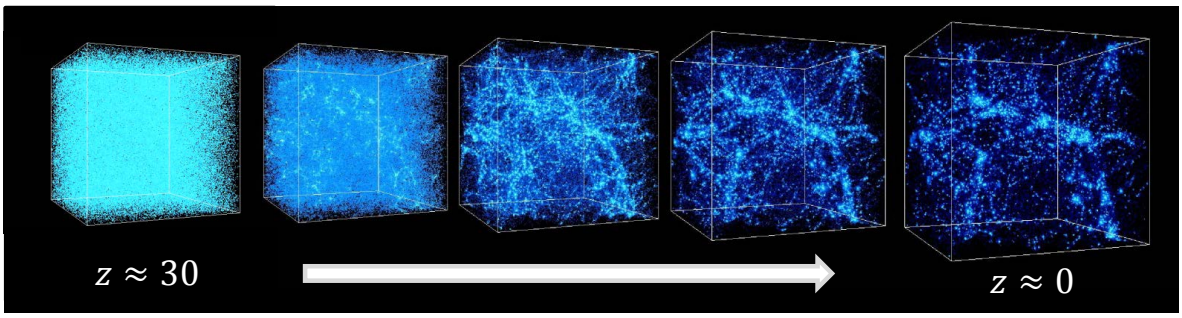

Figure A.5: Frames showing the evolution of the dark matter distribution in the universe in a box model for various ages (From http://cosmicweb.uchicago.edu).

are required to look back even further into the deep space to reach a deeper understanding about the evolution of the early Universe.

As a result, the Universe works as a cosmic time machine which means the deeper the astronomers look into the space, the further they go back in time. We have enough reasons to believe that THz astronomy has a tremendous potential to provide us valuable data to have more understanding on the formation and the evolution of the stars and dusty galaxies, which can yield a new view upon the early Universe. However, all of these discoveries are only possible with the help of further astronomical observations made by the telescopes with superior sensitivities and higher resolutions.

APPENDIX B

Spectral Power Received from an Incoherent Distributed Source

B.1 Antenna Coupling Efficiency

Let us assume that for each receiver the targeted plane waves are those distributed over the solid angle defined by the source dimension, θ_s. Accordingly it is convenient to express the desired power received from a central feed from the sky in terms of the effective area of the telescope as

$$P_{sky}(f) = \int_0^{2\pi} \int_0^{\theta_s} B_{sky}(\phi, \theta) A_{eff}^{tel}(\phi, \theta) sin\theta d\theta d\phi \tag{B.1}$$

where

$$A_{eff}^{tel} = A\eta_{feed}^{det}\eta_{taper}^{tel} \tag{B.2}$$

and

$$\eta_{taper}^{tel} = \frac{D(0,0)}{D_{max}} = \frac{D(0,0)}{4\pi A}\lambda^2 \tag{B.3}$$

Where A represents the physical area of the antenna, η_{taper}^{tel} is the reflector taper efficiency related to the antenna directivity at broadside $D(0,0)$ and η_{feed}^{det} is the detector feed efficiency (See Section B.2).

One cannot anticipate the radiation distribution $B(\phi, \theta)$, since it is the object of the investigation. However to characterize the performance of a system one can assume that power is received from a constant distribution of sources over the field of view (FoV):

$$B(\phi,\theta) = \frac{f^2}{c^2}\frac{2hf}{e^{\frac{hf}{k_B T_{ave}}}-1} \tag{B.4}$$

Introducing the normalized directivity function $F^a(\phi,\theta) = D(\phi,\theta)/D(0,0)$ such that

$$P^{ave}_{sky}(f) = B^{ave}_{sky}(f)A^{tel}_{eff}(0)\int_0^{2\pi}\int_0^{\theta_s} F^a(\phi,\theta)sin\theta d\theta d\phi \tag{B.5}$$

Therefore, we can obtain the following relationship:

$$A\eta^{det}_{feed}\eta^{tel}_{taper}\int_0^{2\pi}\int_0^{\theta_s} F^a(\phi,\theta)sin\theta d\theta d\phi = A\frac{D(0,0)}{4\pi A}\lambda^2\int_0^{2\pi}\int_0^{\theta_s} F^a(\phi,\theta)sin\theta d\theta d\phi \tag{B.6}$$

From the definition of directivity in antennas, we know that

$$D(0,0)\int_0^{2\pi}\int_0^{\pi} F^a(\phi,\theta)sin\theta d\theta d\phi = 4\pi \tag{B.7}$$

Therefore, combining eq. B.6 and eq. B.7, we can express eq. B.5 as

$$P^{ave}_{sky}(f) = B^{ave}_{sky}(f)\eta^{det}_{feed}\lambda^2\frac{\int_0^{2\pi}\int_0^{\theta_s} F^a(\phi,\theta)sin\theta d\theta d\phi}{\int_0^{2\pi}\int_0^{\pi} F^a(\phi,\theta)sin\theta d\theta d\phi} \tag{B.8}$$

The ration of the integral is an efficiency term, multiplying the λ^2 throughout, and it is related to how much power is coupled into the source angular dimension:

$$\eta^{\Omega_s}_{so}(f) = \frac{\int_0^{2\pi}\int_0^{\theta_s} F^a(\phi,\theta)sin\theta d\theta d\phi}{\int_0^{2\pi}\int_0^{\pi} F^a(\phi,\theta)sin\theta d\theta d\phi} = \frac{\Omega_s}{\lambda^2}A \tag{B.9}$$

Note that in eq B.9, the antenna physical area is used. The extra losses (i.e. ohmic, impedance matching, lens illumination efficiency and the detector losses) are included in the $\eta^{det}_{feed}(f)$ term. Considering these simplification the average spectral power received by an antenna from a distributed source with an angular dimension of Ω_s is given by:

$$P^{ave}_{sky}(f) = B^{ave}_{sky}\eta^{det}_{feed}(f)\eta^{\Omega_s}_{so}(f)\lambda^2 = \frac{2hf}{e^{\frac{hf}{k_B T_{sky}(\phi,\theta)}-1}}\eta^{\Omega_s}_{co,s}(f) \tag{B.10}$$

Here we define $\eta^{\Omega_s}_{co,s}$ as simulated antenna coupling efficiency that can be obtained by using full-wave CST simulations:

$$\eta^{\Omega_s}_{co,s} = \eta^{det}_{feed}(f)\eta^{\Omega_s}_{so}(f) \tag{B.11}$$

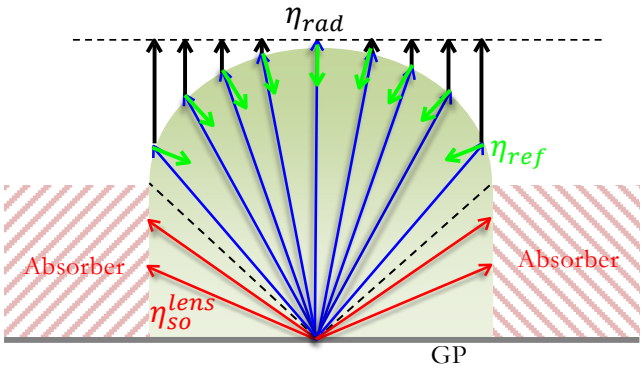

Figure B.1: Graphical illustration of the efficiency terms used in the appendix.

$\eta_{co,s}^{\Omega_s}$ will be used as a benchmark between simulated and the measured antenna coupling efficiencies reported in Chapter 6 and 7 (See Appendix C for the detailed information on the derivation of the measured antenna coupling efficiency, $\eta_{co,m}^{\Omega_s}$).

B.2 Lens Antenna Efficiencies

Assuming we have a lens antenna as a reflector feed, here we provide the definitions of the efficiency terms that have been used to characterize the antenna performance. We start with the lens antenna aperture efficiency which will be represented as η_{ap} and can be evaluated as

$$\eta_{ap} = \eta_{taper}^{feed}\eta_{feed} \tag{B.12}$$

where η_{feed} and η_{taper}^{feed} refer to lens antenna feed efficiency and lens taper efficiency, respectively. Taper efficiency is ratio of the broadside directivity and the maximum directivity that one can achieve by using the same size aperture with a uniform field distribution.

Lens antenna feed efficiency η_{feed}, on the other hand, can be calculated as

$$\eta_{feed} = \eta_{rad}\eta_z \tag{B.13}$$

Here η_{rad} refers to the antenna radiation efficiency, η_z refers to the efficiency due to antenna impedance matching. Antenna radiation efficiency η_{rad} is defined as the fractional radiated power and can be directly evaluated by CST simulations with multiple inner reflections. Using PO approach, one can also evaluate η_{rad} separately after the first transmitted pulse as below

$$\eta_{rad} = \eta_{ref}\eta_{so}^{lens} \tag{B.14}$$

where η_{ref} refers to antenna reflection efficiency due to the dielectric-air interface on the lens surface, and η_{so}^{lens} refers to spill-over efficiency defined on the lens surface (See Fig. B.1).

It should be mentioned here that the efficiency η_{feed} given in Eq. B.13 is only associated to the antenna itself. In other words it could be representative for an ideal detector scenario. In reality, however, this is never the case and the losses associated to the detector itself should be included in Eq. B.13 as well. By doing so, we define detector feed efficiency η_{feed}^{det} as

$$\eta_{feed}^{det} = \eta_{feed}\eta_{det} \tag{B.15}$$

Here η_{det} refers to the detector efficiency and includes any kind of losses due to the detector such as the losses due to radiation of the CPW line, GP material and the gap between the wafer and the silicon lens due to fabrication process.

APPENDIX C

Optical Efficiency Measurements

The optical efficiency measurements are performed by Netherlands Space Institute Research (SRON). Here we provide brief information about the measurements and how we relate the measurement data to our CST simulations. The setup where the MKID array is evaluated using a cryogenic system with a box in a box cold stage design is shown in Fig. C.1. The boxes highlighted in red, orange and blue curves are used to shield the sample to from the radiation due to the environmental temperature directly or through the coax lines. In addition, the inside of the outer box is coated with carbon loaded epoxy and SiC grains to effectively prevent reflections of light entering through the filters. As a result, the array is fully enclosed in a 100 mK environment with the exception of a far-field aperture. This aperture is isotropically illuminated by a large temperature controlled blackbody mounted on the 4K stage [14]. Three stacks of metal mesh filters provide a minimum rejection of 40 dB at all wavelengths outside bandpass region of about $0.95f_0 < f < 1.05f_0$ which is centered at f_0. The rest of the detector enclosure is a 100 mK absorber that has a negligible emission at f_0.

In generic case, for any kind of detector, the total NEP can be calculated as:

$$NEP(T_{BB}) = \sqrt{NEP_b(T_{BB})^2 + NEP_d^2} \tag{C.1}$$

where $NEP_b(T_{BB})$ is the background limited NEP and NEP_d refers to detector NEP. In case of KIDs, the total NEP can be assumed to be limited by NEP_b for very small blackbody source temperatures, T_{BB} (See Fig. C.1). Then one can assume

$$NEP(T_{BB}) \approx NEP_b(T_{BB}) \tag{C.2}$$

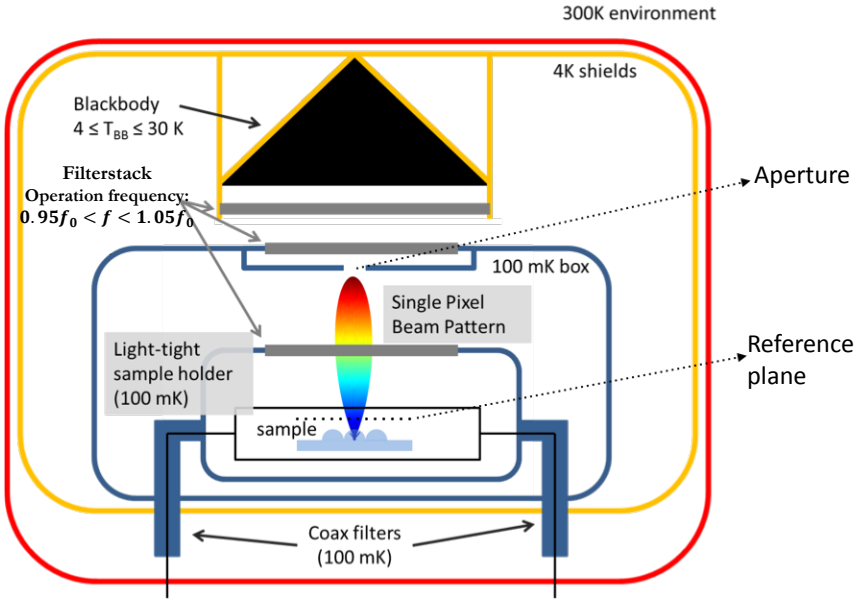

Figure C.1: Schematic of the measurement setup for optical NEP measurements.

Since the target of this thesis is sub-mm wave astronomical observations, NEP_b is determined by the Wien's limit. Then the background limited NEP is only defined by the absorbed sub-mm power. Assuming a system operating over a relative small bandwidth centered at f_0, as given in Chapter 5, the background limited NEP in the Wien's limit can be evaluated as

$$NEP_b(T_{BB}) = \sqrt{k_B T_{BB} \eta_{ave} BW h f_0} \tag{C.3}$$

Eq. C.3 can be used up to a bandwidth in order of one octave. In the measurement setup, a filterstack with a bandwidth much less than one octave, typically about 10%, is used in front of a blackbody source (See Fig. C.1). For such narrow bandwidths one can assume

$$\eta_{ave} = \frac{1}{BW} \int_{f_0+BW/2}^{f_0+BW/2} \eta_{co,m}^{\Omega_s}(f) df \approx \eta_{co}^{\Omega_s}(f_0) \tag{C.4}$$

Then Eq. C.3 becomes

$$NEP_b(T_{BB}) = \sqrt{k_B T_{BB} \eta_{co}^{\Omega_s}(f_0) BW h f_0} \tag{C.5}$$

Here $\eta_{co}^{\Omega_s}(f_0)$ refers to antenna coupling efficiency to the blackbody source with a solid angle of Ω_s at the center frequency f_0. The measured antenna coupling efficiency $\eta_{co,m}^{\Omega_s}$ can

be evaluated by means of using the simulated antenna coupling efficiency $\eta_{co,s}^{\Omega_s}$ [54]. To do so, one can calculate the ratio of the measured NEP and estimated NEP as following

$$\epsilon = \frac{NEP_b^m(T_{BB})}{NEP_b(T_{BB})} = \frac{\sqrt{k_B T_{BB} \eta_{co,m}^{\Omega_s}(f_0) BW h f_0}}{\sqrt{k_B T_{BB} \eta_{co,s}^{\Omega_s}(f_0) BW h f_0}} = \frac{\sqrt{\eta_{co,m}^{\Omega_s}(f_0)}}{\sqrt{\eta_{co,s}^{\Omega_s}(f_0)}} \tag{C.6}$$

As a result

$$\eta_{co,m}^{\Omega_s}(f_0) = \eta_{co,s}^{\Omega_s}(f_0)\sqrt{\epsilon} \tag{C.7}$$

Here ϵ represent the deviation of the measured coupling efficiency compared to the simulated one due to the possible fabrication tolerances and additional noise contribution associated to the detector. If $\epsilon = 1$ then $\eta_{co,m}^{\Omega_s}(f_0) = \eta_{co,s}^{\Omega_s}(f_0)$ which means that the fabricated antenna works as expected by the CST simulations.

APPENDIX D

The Desgin of the Spill-over Absorber

When it comes to tightly packed lens arrays, one problem could be lens coupling due to the significant uncontrolled power launched in the lens array. This could be directly associated to spill-over loss and may result in significant variation in the antenna side lobe levels. One way to suppress the impact of the uncontrolled power in the lens array is to design a spill-over (SO) absorber. This appendix will focus on the optimization of a specific scenario, A-MKID lens antenna #1, but the concept can be extended to all lens designs shown in the thesis.

Due to the fabrication reasons, we will optimize a single layer absorber. The absorber is located on top of silicon chip, at a distance of 375 µm from the GP which corresponds to about $0.43\lambda_0$ at 350 GHz. In order not to affect the entire antenna coupled KID structure, especially readout electronics that operates at microwave range, the SO absorber should have a high-pass filter characteristic in terms of absorption performance.

Unit cell SO absorbing structure with its design parameters is highlighted in Fig. D.1. To maximize its absorption performance within the required band, we performed a parametric study as a function of H, P and g for broadside plane-wave incidence as well as for the incoming plane-waves with various oblique incidences, θ_i both for TE and TM modes. The parametric study yields the optimized dimensions as reported below:

- $P = 100$ µm (corresponds to $0.4\lambda_d$ at 350GHz)

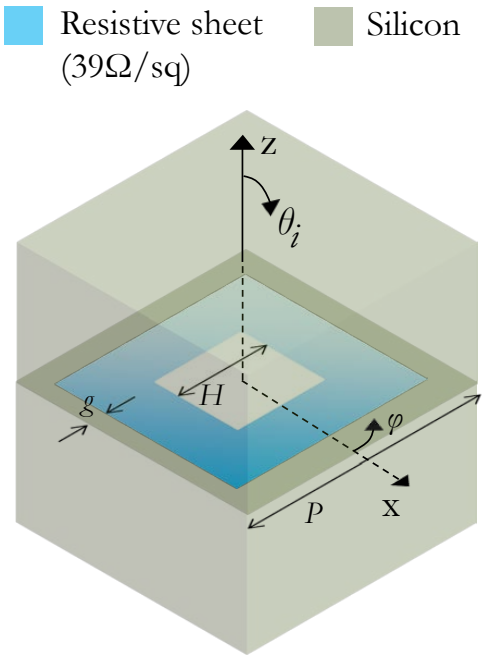

Figure D.1: The design parameters of the unit cell spill-over absorbing structure.

- $H = 30.8\,\mu m$
- $g = 3.31\,\mu m$

The absorption performance of the optimized SO absorber can be seen from Fig. D.2. Fig. D.2a and b show the absorption for different oblique incidences as a function of frequency for TE and TM polarizations, respectively. Fig. D.2c, on the other hand, focuses on the absorption for TE and TM polarizations as a function oblique incidence angle at the optimization frequency, 350 GHz. The figure shows that the optimized SO absorber is able to provide an absorption ratio higher than 40% for scanning angles $\theta_i \leq 50^0$ at 350 GHz. Considering the maximum theoretical broadside absorption could be 50% for a single layer design, we accepted this performance of the proposed design as sufficient.

The SO absorber cannot be printed across the entire plane otherwise it also absorbs the main beam of the lens feed which, in the end, will reduce lens antenna aperture efficiency. Therefore circular gaps with a radius of R have to be introduced on the absorber plane. To define this radius, as a first step, we plot the magnitude of the electric field distribution at the absorber plane with different contours representing -8, -10, -12, -14 and -16 dB

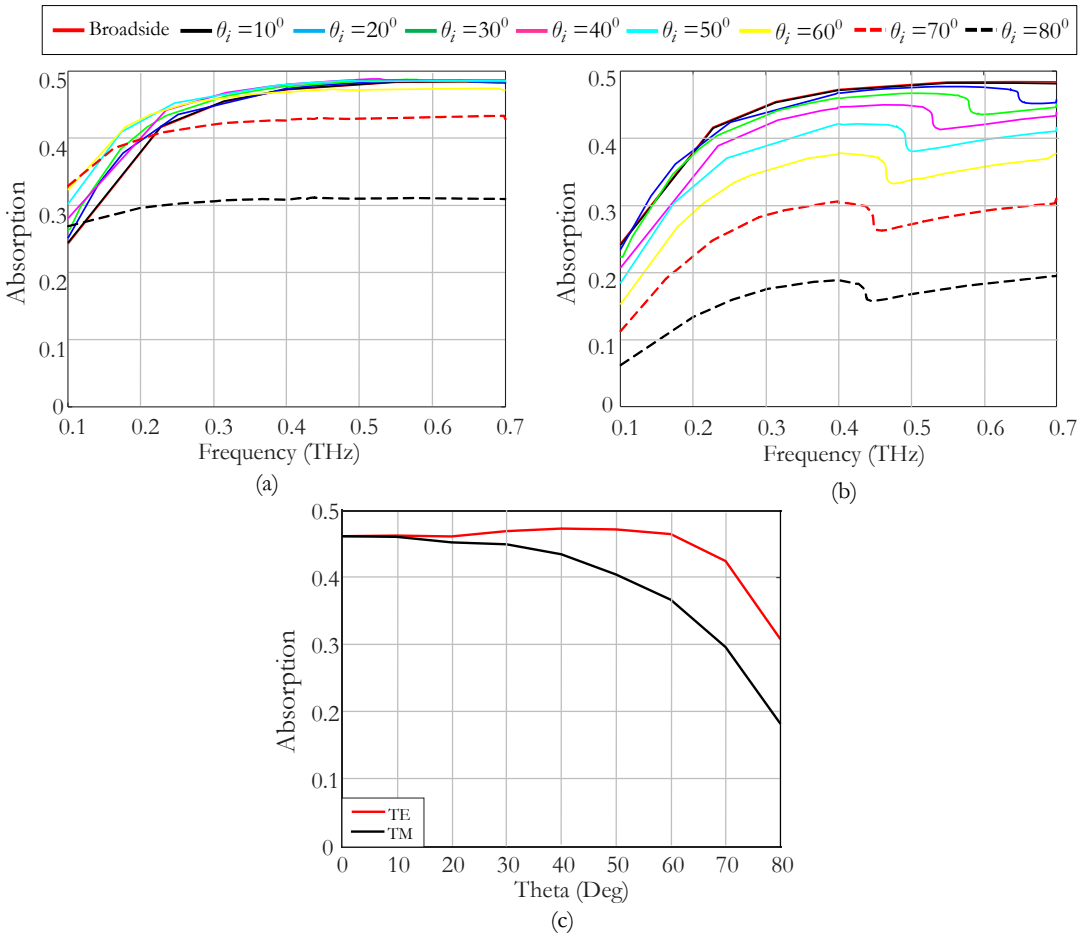

Figure D.2: Absorption performance of the SO absorber: (a) and (b) shows the absorption as a function of frequency for different incident angles, θ_i for TE and TM-modes, respectively whereas (c) highlights the absorption only at 350GHz as a function of incident angle.

values, respectively, with respect to the maximum total field in Fig. D.3a. As once can see, the field distribution is not circularly symmetric on the absorber plane. Therefore we evaluate the average electric field field values in E, D and H-planes separately, and then, calculate the average. Fig. D.3b shows the average of the field magnitude as a function of hole radius R and the way how it is evaluated.

Depending on the gap radius, one has to make a compromise between the absorbed uncontrolled power and the antenna aperture efficiency. To do so, we performed a parametric study as a function of R in the presence of hexagonally packed entire lens array when only the central lens is excited. The array can be seen from Fig. D.4.

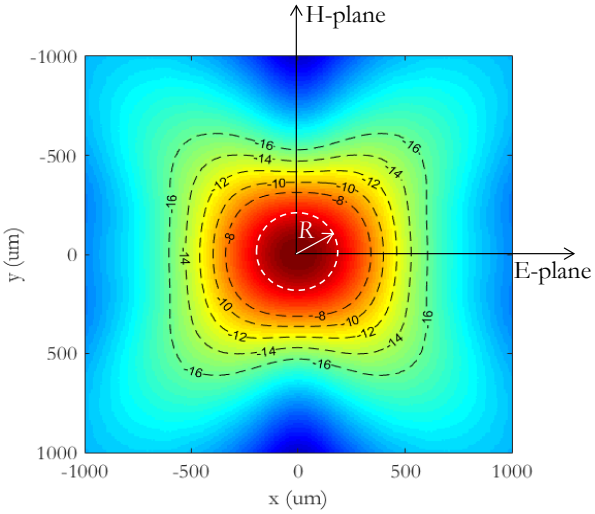

(a)

Normalized electric field (dB)				
R(um)	Ep	Hp	Dp	Average
350	-8.6	-9.6	-8.2	-8.65
400	-10.6	-11.7	-9.7	-10.42
450	-12.2	-13.7	-11.06	-12
500	-13.92	-15.3	-12	-13.3
550	-15.3	-17	-13	-14.575
600	-16.7	-18.6	-13.9	-15.775

$$Average = \frac{Ep + Hp + 2Dp}{4}$$

(b)

Figure D.3: 2D electric field distribution defined on top of silicon chip, at $z = 375\,\mu m$: (a) shows 2D field including $-8, -10, -12, -14$ and -16 dB contours whereas (b) shows the field magnitudes at E, H, D-planes and also in average for certain radii of R, starting from 350 µm*to*600 µm.

The aperture efficiency obtained from the CST simulations for various R values is reported in Figs. D.5. It is clear that the lower R is being used in the array, the lower aperture efficiency one gets. This, however, corresponds to better uncontrolled power absorption performance as shown in Fig. D.6a. Finding a compromise between these two, we ended up with using a gap radius of $R = 550$ µm in the design.

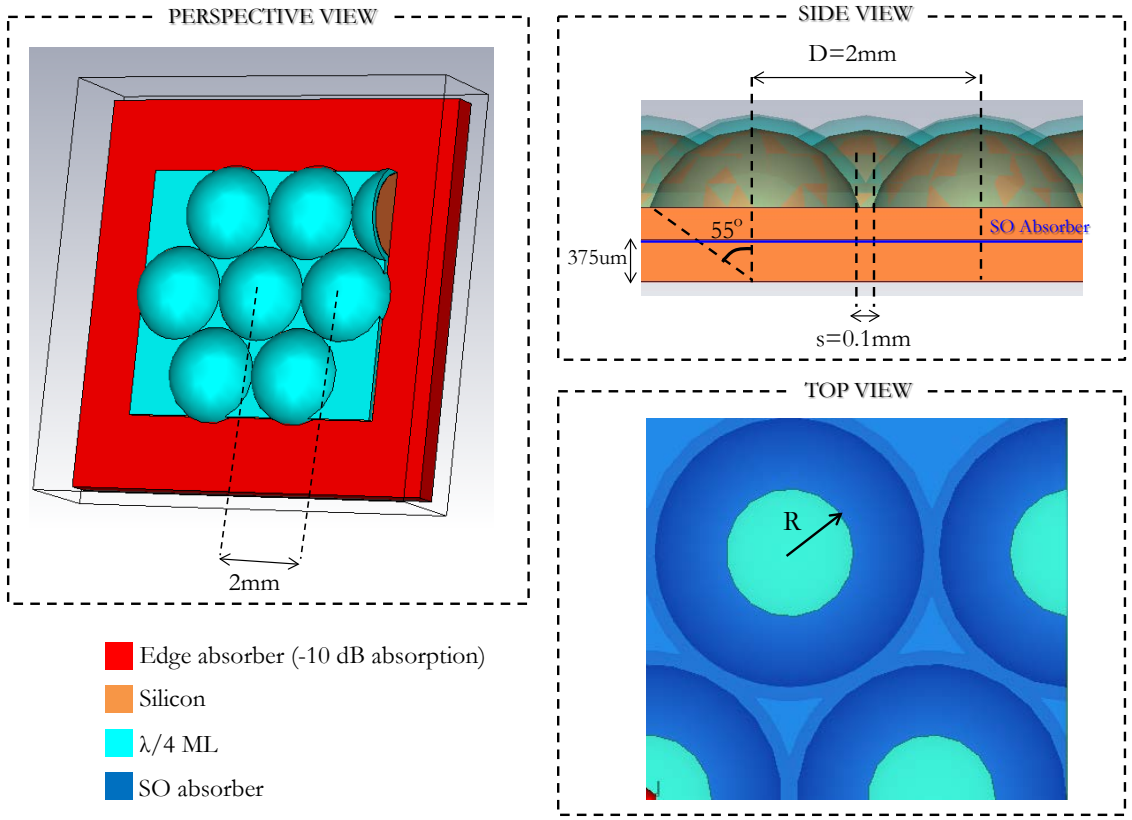

Figure D.4: Simulated hexagonal lens array with its design parameters seen from perspective, side and top views.

Aperture Efficiency @ 0.35 THz						
R(um)	**400**	**450**	**500**	**550**	**600**	**No SW abs**
Taper	0.9094	0.8948	0.9306	0.9611	0.9611	0.9435
Radiation	0.7444	0.7609	0.7640	0.7728	0.7843	0.796
Total	**0.6769**	**0.6808**	**0.7109**	**0.7427**	**0.7537**	**0.751**

Figure D.5: Aperture efficiency calculations for various absorber gap radii.

Power in SO absorber (P_{so}/P_{acc}) @ 0.35 THz	
R(um)	
400	17%
450	14.83%
500	14.14%
550	12.37%
600	10.67%

P_{so}: Absorbed power in the SO absorber

P_{acc}: Accepted power in port

(a)

Power in edge absorber @ 0.35 THz	
R(um)	
400	7.11%
450	7.34%
500	7.716%
550	8.12%
600	8.43%
No Absorber	15.62%

(b)

Figure D.6: Fractional absorbed power evaluated inside (a) the SO absorber, and (b) the edge absorber.

APPENDIX E

The Desgin of the Grooved Matching Layer

The lens antenna designs have been proposed for tightly spaced FPAs in the thesis typically use a conventional $\lambda/4$ ML made of Parylene material ($\epsilon_r \approx 2.62$). However, this is not the case for SAFARI and A-MKID #2 antennas due to the fabrication constraints. Therefore we will use an alternative ML design which is made of the same material as the lens (silicon) instead of Parylene ML and shaped in the form of grooves via laser machining. The idea is to achieve an effective permittivity that is close to the permittivity of $\lambda/4$ Parylene ML within an octave bandwidth (See Fig. E.1). In this Appendix, we will focus on the SAFARI scenario but the geometry can be extended to A-MKID design.

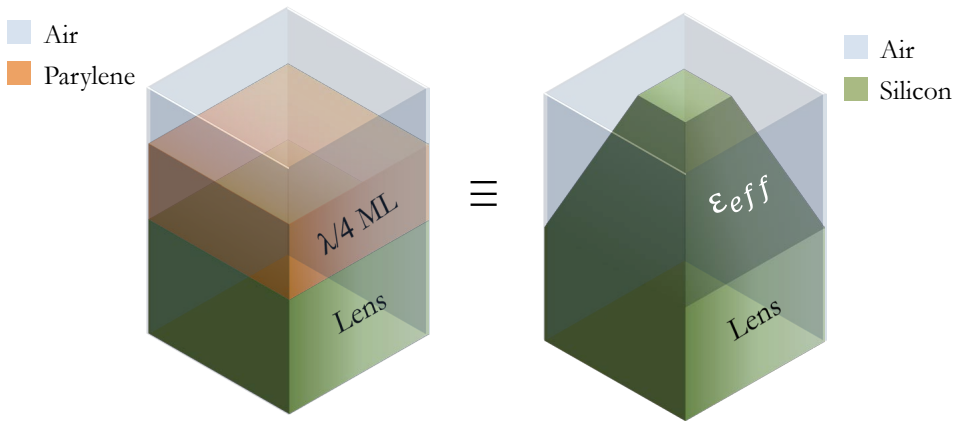

Figure E.1: Unit cell structure of a conventional $\lambda/4$ Parylene ML and an equivalent grooved silicon ML design.

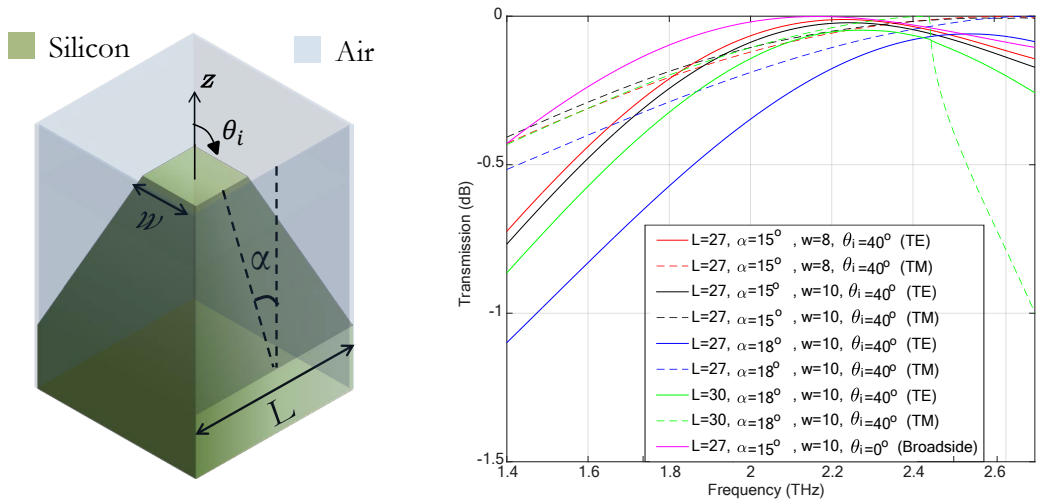

(a) (b)

Figure E.2: (a) The design parameters of a unit cell grooved silicon and (b) its transmission performance for various configurations.

The unit cell structure with its dimensions are highlighted in Fig. E.2a. A parametric study is performed to optimize the transmission characteristics of the unit cell structure by means of changing the groove period (L), the groove angle (α) and the groove width (w) as a function of the frequency within the proposed bandwidth. The results obtained from the parametric study are highlighted in Fig. E.2b. Considering the performance and the fabrication constraints, we chose $L = 27$ µm, $w = 10$ µm and $\alpha = 15^0$ as the optimum dimensions. The comparison of the transmission performance of the unit cell structure and the Parylene $\lambda/4$ ML within the SAFARI band can be seen from Fig. E.3. According to the figure, the grooved silicon unit cell has a quite similar performance to $\lambda/4$ Parylene ML design.

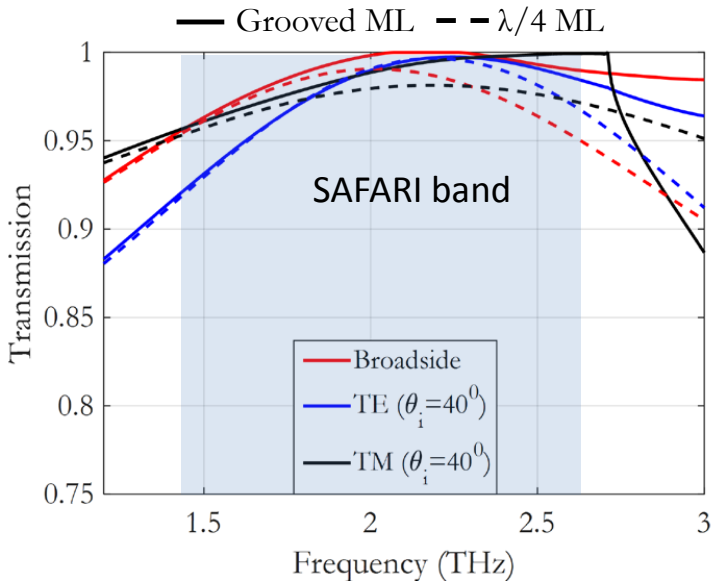

Figure E.3: Comparison of transmission performance for broadside and 40^0 oblique incidence (TE and TM) within the SAFARI band obtained by optimized unit cell silicon groove and $\lambda/4$ ML.

List of Figures

List of Tables

Bibliography

[1] A. Baryshev, J.J.A. Baselmans, A. Freni, G. Gerini, H. Hoevers, A. Iacono, and A. Neto, "Progress in antenna coupled kinetic inductance detectors," *IEEE Trans. THz Sci. Technol.*, vol. 1, no. 1, pp. 112–123, Sep. 2011.

[2] D.F. Filipovic, S.S. Gearhart, and G.M. Rebeiz, "Double-slot antennas on extended hemispherical and elliptical silicon dielectric lenses," *IEEE Trans. Microw. Theory Techn.*, vol. 41, no. 10, pp. 1738–1749, Oct. 1993.

[3] D. J. Burdette, J. Alverbro, Z. Zhang, P. Fay, Y. Ni, P. Potet, K. Sertel, G. Trichopoulos, K. Topalli, J. Volakis, and H. L. Mosbacker, "Development of an 80 x 64 pixel, broadband, real-time THz imager," *Proc. SPIE*, vol. 8023, pp. 80230F–80230F–12, doi:10.1117/12.884069, 2011.

[4] A.D. Semenov et al., "Terahertz performance of integrated lens antennas with a hot-electron bolometer," *IEEE Trans. Microw. Theory Tech.*, vol. 55, no. 2, pp. 239–247, Feb. 2007.

[5] "European comission 7th framework programme (fp7) [online].," Available:https://ec.europa.eu/research/fp7/indexen.cfm.

[6] "European research council starting grant [online].," Available: https://erc.europa.eu/funding-and-grants/funding-schemes/starting-grants.

[7] "Nwo international research incentives scheme vidi [online].," Available: http://www.nwo.nl/en/funding/our-funding-instruments/nwo/innovational-research-incentives-scheme/vidi/index.html.

[8] J. Glenn et al., "Current status of Bolocam: A large format millimeter-wave bolometer camera," *Proc. SPIE*, vol. 4855, doi:10.1117/12.459369, Feb. 2003.

[9] E. Kreysa et al., "Bolometer arrays for mm/sub-mm astronomy," 2002, vol. 616.

[10] A. Baryshev et al., "Large format antenna coupled microwave KID arrays for radioastronomy," in *The 39th International Conference on Infrared, Millimeter, and Terahertz Waves (IRMMW)*, Tuscon, AZ, USA, Sep. 2014.

[11] P. K. Day, H. G. LeDuc, Mazin, B. A., A. Vayonakis, and J. Zmuidzinas, "A broadband superconducting detector suitable for use in large arrays," *Nature*, vol. 425, no. 6960, pp. 817–821, Oct. 2003.

[12] B. A. Mazin, *Microwave kinetic inductance detectors*, Ph.D. thesis, California Institute of Technology, California, United States, 2004.

[13] P. J. de Visser et al., "The non-equilibrium response of a superconductor to pair-breaking radiation measured over a broad frequency band," *Applied Physics Letters*, vol. 106, no. 25, doi:10.1063/1.49230978 2015.

[14] R.M.J. Janssen, J.J.A Baselmans, Ferrari L. Endo, A., S.J.C. Yates, A.M. Baryshev, and T.M. Klapwijk, "Performance of hybrid NbTiN-Al microwave kinetic inductance detectors as direct detectors for sub-millimeter astronomy," *Proc. SPIE*, vol. 9153, DOI: 10.1117/12.2055537, Jul. 2014.

[15] R. Barens et al., "Niobium and tantalum high q resonators for photon detectors," *IEEE Trans. Appl. Supercond.*, vol. 17, no. 2, pp. 263–266, Jun. 2007.

[16] B. Beatriz, N. Llombart, A. Neto, and J. Bueno, "Development of lens-coupled LEKID detectors arrays for THz radiation," Mar. 2012, pp. 3264–3267.

[17] T. A. Milligan, *Modern Antenna Design*, John Wiley & Sons, Inc., Hoboken, New Jersey, second edition, 2015.

[18] A. Endo et al., "Development of DESHIMA: A redshift machine based on a superconducting on-chip filterbank," *Proc. SPIE*, vol. 8452, Aug. 2012.

[19] A. W. Blain et al., "Submillimeter galaxies," *Physics Reports*, vol. 369, no. 2, pp. 111–176, astro-ph/0406143, 2002.

[20] A. Neto, , et al., "Imaging speed of antenna coupled kinetic inductance detectors in the SAFARI/SPICA scenario," in *8th European Conference on Antennas and Propag.*, The Hague, Netherlands, Apr. 2014.

[21] P. Roelfsema et al., "The safari imaging spectrometer for the spica space observatory,," *Proc. SPIE.*, vol. 8842, pp. 112–123, DOI: 10.1117/12.927010, May 2012.

[22] O. Yurduseven, A. Cavallo, D. Neto, G. Carluccio, and M Albani, "Parametric analysis of extended hemispherical dielectric lenses fed by a broadband connected array of leaky-wave slots," *IET Microwaves, Antennas Propagation*, vol. 9, no. 7, pp. 611–617, 10.1049/iet-map.2014.0403, 2015.

[23] A. Neto, "UWB, non dispersive radiation from the planarly fed leaky lens antenna-part I: Theory and design," *IEEE Trans. Antennas Propag.*, vol. 58, no. 7, pp. 2238–2247, Jul. 2010.

[24] D. Pasqualini and S. Maci, "High frequency analysis of integrated dielectric lens antennas," *IEEE Trans. Antenn. Propag.*, vol. 52, no. 3, pp. 840–847, Mar. 2004.

[25] A. Boriskin et al., "Lens or resonator? electromagnetic behavior of an extended hemielliptic lens for a submillimeterwave receiver," *Microwave and Optical Technology Letters*, vol. 43, pp. 515–518, Dec. 2004.

[26] "The homepage of CST Microwave Studio [online]," Available: http://www.cst.com.

[27] "Esf research networking programme NEWFOCUS [online].," Available: http://www.esf-newfocus.org/activitiesgrants.html.

[28] P.H. Siegel, "Terahertz technology in biology and medicine," in *IEEE MTT-S International Microwave Symposium Digest*, Jun. 2004, vol. 3, pp. 1575–1578.

[29] "Core science requirements for the European Spica Instrument [online].," Available: http://sci.esa.int/science-e/www/object/index.cfm?fobjectid=42283.

[30] P.F. Goldsmith, C.-T. Hsieh, G.R. Huguenin, J. Kapitzky, and E.L. Moore, "Focal plane imaging systems for millimeter wavelengths," *IEEE Trans. Microw. Theory Techn.*, vol. 41, no. 10, pp. 1664–1675, 1993.

[31] N. Llombart and A. Neto, "THz time-domain sensing: The antenna dispersion problem and a possible solution," *IEEE Trans. THz Sci. Technol.*, vol. 2, no. 4, pp. 416–423, Jul. 2012.

[32] A. Neto, S. Monni, and F. Nennie, "Uwb, non dispersive radiation from the planarly fed leaky lens antenna-part II: Demonstrators and measurements," *IEEE Trans. Antennas Propag.*, vol. 58, no. 7, pp. 2248–2258, Jul. 2010.

[33] G.C. Trichopoulos, K. Sertel, and J.L. Volakis, "Slot spiral detector array for broadband THz imaging," in *IEEE Antennas and Propagation Society International Symposium (APSURSI)*, Toronto, Ontario, Canada, Jul. 2010, pp. 1–4.

[34] D. Cavallo and A. Neto, "A connected array of slots supporting broadband leaky waves," *IEEE Trans. Antennas Propag.*, vol. 61, no. 4, pp. 1986–1994, Apr. 2013.

[35] D.F. Filipovic, G.P. Gauthier, S. Raman, and G.M. Rebeiz, "Off-axis properties of silicon and quartz dielectric lens antennas," *IEEE Trans. Antennas Propag.*, vol. 45, no. 5, pp. 760–766, May 1997.

[36] Xidong W., G.V. Eleftheriades, and E. van Deventer, "Design and characterization of single and multiple beam mm-wave circularly polarized substrate lens antennas for wireless communications," in *IEEE Antennas and Propagation Society International Symposium*, Orlando, Florida, USA, Jul. 1999, vol. 4, pp. 2408–2411.

[37] G. Carluccio and M. Albani, "Efficient adaptive numerical integration algorithms for the evaluation of surface radiation integrals in the high-frequency regime," *Radio Sci.*, vol. 46, no. 5, pp. 760–766, Jun. doi:10.1029/2010RS004623, 2011.

[38] O. Yurduseven, D. Cavallo, and A. Neto, "Wideband dielectric lens antenna with stable radiation patterns fed by coherent array of connected leaky slots," *IEEE Trans. Antennas Propag.*, vol. 62, no. 4, pp. 1895–1902, Apr. 2014.

[39] C. Della Giovampaola and others., "Efficienct algorithm for the evaluation of the phyisical optics scattering by NURBS surfaces with relatively general boundary condition," *IEEE Trans. Antenn. Propag.*, vol. 61, no. 8, pp. 4194–4202, Aug. 2013.

[40] C. Giorgio and M. Albani, "Efficient adaptive numeral integration algorithms for the evaluation of the surface radiation integrals in the high-frequency regime," *Radio Science*, vol. 46, pp. RS0E04, DOI:10.1029/2010RS004623 2011.

[41] P. S. Kildal, "Synthesis of multireflector antennas by kinematic and dynamic ray tracing," *IEEE Trans. Antenn. Propag.*, vol. 38, no. 10, pp. 1587–1599, 1990.

[42] P. S. Kildal, "Analysis of numerically specified multireflector antennas by kinematic and dynamic ray tracing," *IEEE Trans. Antenn. Propag.*, vol. 38, no. 10, pp. 1600–1606, 1990.

[43] M.V. Ivashina, M.N.M. Kehn, P.-S. Kildal, and R. Maaskant, "Decoupling efficiency of a wideband vivaldi Focal Plane Array feeding a reflector antenna," *IEEE Trans. Antennas Propag.*, vol. 57, no. 2, pp. 373–382, Feb. 2009.

[44] R. Olsson, P.-S. Kildal, and S. Weinreb, "The eleven antenna: a compact low-profile decade bandwidth dual polarized feed for reflector antennas," *IEEE Trans. Antennas Propag.*, vol. 54, no. 2, pp. 368–375, Feb. 2006.

[45] A. Neto, J. Baselmans, A. Baryshev, S. Yates, and N. Llombart, "THz demonstration of the leaky lens antenna," in *7th European Conference on Antennas and Propagation (EuCAP)*, Gothenburg, Sweden, Apr. 2013, pp. 1734–1735.

[46] C.A. Fernandes, E.B. Lima, and J.R. Costa, "Broadband integrated lens for illuminating reflector antenna with constant aperture efficiency," *IEEE Trans. Antennas Propag.*, vol. 58, no. 12, pp. 3805–3813, Dec. 2010.

[47] R.C. Hansen, "Linear connected arrays [coupled dipole arrays]," *IEEE Antennas Wireless Propag. Lett.*, vol. 3, no. 1, pp. 154–156, Dec. 2004.

[48] A. Neto and J.J. Lee, "Ultrawide-band properties of long slot arrays," *IEEE Trans. Antennas Propag.*, vol. 54, no. 2, pp. 534–543, Feb. 2006.

[49] C. A. Balanis, *Antenna Theory: Analysis and Design (3rd Edition)*, John Wiley & Sons, Inc., New Jersey, USA, 2005.

[50] "The homepage of emerson & cuming microwave products [online]," Available: http://www.eccosorb.eu.

[51] E. Lima, J.R. Costa, M.G. Silveirinha, and C.A. Fernandes, "ILASH - software tool for the design of integrated lens antennas," in *IEEE Antennas and Propag. Society International Symposium*, San Diego, California, USA, Jul. 2008, pp. 1–4.

[52] Eduardo Lima, "Mechanical steerable lens for wireless communications," M.S. thesis, Instituto Superior Tecnico, Lisbon, Portugal, 2008.

[53] M. J. Griffin, J. Bock, and W. Gear, "Relative performance of filled and feedhorn-coupled focal-plane architectures," *Appl. Opt.*, vol. 41, pp. 6543–6554, 2002.

[54] R.M.J. Janssen, J.J.A Baselmans, Ferrari L. Endo, A., S.J.C. Yates, A.M. Baryshev, and T.M. Klapwijk, "High optical efficiency and photon noise limited sensitivity of

microwave kinetic inductance detectors using phase readout," *Appl. Phys. Lett.*, vol. 103, no. 20, DOI: 10.1063/1.4829657, Nov. 2013.

[55] J. Johansson, *Tapered slot antennas and focal plane imaging systems*, Ph.D. thesis, Chalmers University of Techonology, Gothenburg, Sweden, 1988.

[56] P. Focardi, R.M. William, and A. Neto, "Design guidelines for terahertz mixers and detectors," *IEEE Trans. Microw. Theory Tech.*, vol. 53, no. 5, pp. 1653–1661, May 2005.

[57] P. Focardi, A. Neto, and W.R. McGrath, "Coplanar-waveguide-based terahertz hot-electron-bolometer mixers-improved embedding circuit description," *IEEE Trans. Microw. Theory Tech.*, vol. 50, no. 10, pp. 2374–2383, Oct. 2002.

[58] S. L. van Berkel, A. Garufo, N. Llombart, and A. Neto, "A quasi-analytical tool for the characterization of transmission lines at high frequencies," *IEEE Antennas Propag. Mag.*, accepted for publication.

[59] A. Akgiray, S. Weinreb, W.A. Imbriale, and C. Beaudoin, "Circular quadruple-ridged flared horn achieving near-constant beamwidth over multioctave bandwidth: Design and measurements," *IEEE Trans. Antennas Propag.*, vol. 61, no. 3, pp. 1099–1108, Mar 2013.

[60] N. N. Tinh, A. V. Boriskin, L. Rolland, and R. Sauleau, "Shaped lens-like dome for uwb antennas with a gaussian-like radiation pattern," *IEEE Trans. Antennas and Propag.*, vol. 61, no. 4, pp. 1658–1664, Apr 2013.

[61] M. V. Ivashina, J. D. Bregman, J. G. B. de Vaate, L. Li, and A. J. Parfitt, "Experimental results for a focal plane array, synthesized with conjugate field method," in *International Symposium on Antennas and Propagation Society.*, Jun 2004, pp. 21–24.

[62] D.H. Schaubert, E.L. Kollberg, T. Korzeniowski, T. Thungren, Joakim Johansson, and K.S. Yngvesson, "Endfire tapered slot antennas on dielectric substrates," *IEEE Trans. Antennas Propag.*, vol. 33, no. 12, pp. 1392–1400, Dec 1985.

[63] J. Teniente, R. Gonzalo, and C. del Rio, "Ultra-wide band corrugated gaussian profiled horn antenna design," *IEEE Microw. Compon. Lett.*, vol. 12, no. 1, pp. 20–21, Jan. 2002.

[64] J. Nibarger et al., "An 84 pixel all-silicon corrugated feedhorn for CMB measurements," *Journal of Low Temperature Physics*, vol. 167, pp. 522–527, May. 2012.

[65] A. Hammar, Y. Karandikar, P. Forsberg, A. Emrich, and J. Stake, "A 340 GHz high gaussicity smooth spline horn antenna for the STEAMR instrument," in *IEEE Antennas and Propag. Society International Symposium (APSURSI)*, Memphis, TN, USA, Jul. 2014, pp. 649–650.

[66] C. Granet, Graeme L. James, R. Bolton, and G. Moorey, "A smooth-walled spline-profile horn as an alternative to the corrugated horn for wide band millimeter-wave applications," *IEEE Trans. Antennas Propag.*, vol. 52, no. 3, pp. 848–854, Mar. 2004.

[67] A. Iacono, T.J. Coenen, D.J. Bekers, A. Neto, and G. Gerini, "Trade-offs in multi-element receiving antennas with superconducting feed lines," in *4th European Conference on Antennas and Propagation (EuCAP)*, Barcelona, Spain, Apr. 2010, pp. 1–5.

[68] P. J. de Visser, J. J. A. Baselmans, J. Bueno, N. Llombart, and T. M. Klapwijk, "Fluctuations in the electron system of a superconductor exposed to a photon flux," *Nature Communications*, , no. 3130, DOI: 10.1038/ncomms4130, Feb. 2013.

[69] J. Costa and C. A. Fernandes, "Broadband slot feed for integrated lens antennas,," *IEEE Antennas Wireless Propag. Lett.*, vol. 6, pp. 396–400, Aug. 2007.

[70] J.M. Edwards, R. O'Brient, A.T. Lee, and G.M. Rebeiz, "Dual-polarized sinuous antennas on extended hemispherical silicon lenses," *IEEE Trans. Antennas Propag.*, vol. 60, no. 9, pp. 4082–4091, Sep. 2012.

[71] R. O'Brient et al., "A dual-polarized broadband planar antenna and channelizing filter bank for millimeter wavelengths," *Appl. Phys. Lett.*, vol. 102, no. 6, DOI: 10.1063/1.4791692, Feb. 2013.

[72] G. Alessandro, N. Llombart, and A. Neto, "Logarithmic spiral antenna on extended hemispherical lens antenna," *IEEE Trans. Antennas Propag.*, To be submitted.

[73] A. Neto, N. Llombart, J.J.A. Baselmans, A. Baryshev, and S.J.C. Yates, "Demonstration of the leaky lens antenna at submillimeter wavelengths," *IEEE Trans. Terahertz Sci. Technol.*, vol. 4, no. 1, pp. 26–32, Jan 2014.

[74] J.-C.S. Chieh, B. Dick, S. Loui, and J.D. Rockway, "Development of a Ku-band corrugated conical horn using 3-D print technology," *IEEE Antennas and Wireless Propag. Lett.*, vol. 13, pp. 201–204, Feb. 2014.

[75] P. J. Gibson, "The vivaldi aerial," Sep. 1979.

[76] "Datasheet provided by Farview Microwave [online]," Available: http://www.fairviewmicrowave.com/images/productPDF/SH190-20.pdf.

[77] A. W. Love, *Antenna Engineering Handbook*, McGraw-Hill, New York, USA, 1984.

[78] G. C. Trichopoulos, H. L. Mosbacker, D. Burdette, and K. Sertel, "Fluctuations in the electron system of a superconductor exposed to a photon flux," *IEEE Trans. Antennas Propag.*, vol. 61, no. 4, pp. 1733–1740, Apr. 2013.

[79] N. Llombart, O. Yurduseven, A. Neto, I. E. Lager, and J. Baselmans, "Dual polarised antenna for thz space applications: Design and optimization," in *44th European Microwave Conference (EuMC)*, Rome, Italy, Oct. 2014, pp. 100–103.

[80] A. A. Danylov and J. Waldman, "THz laboratory measurements of atmospheric absorption between 6% and 52% relative humidity," *Internal STL Report*, pp. 1–7, Sep. 2006.

[81] D. H. Hughes et al., "High-redshift star formation in the hubble deep field revealed by a submillimetre-wavelength survey," *Nature*, vol. 394, pp. 241–247, doi:10.1038/28328 1998.

[82] W. S. Holland et al., "SCUBA: A submillimeter camera operating on the James Clerk Maxwell Telescope," *Proc. SPIE*, vol. 3357, pp. 305–318, 10.1117/12.317366 1998.

[83] H. Umehata et al., "ALMA deep field in SSA22: A concentration of dusty starbursts in a z = 3.09 protocluster core," *The Astrophysical Journal Letters*, vol. 815, no. 1, 10.1088/2041-8205/815/1/L8, Dec. 2015.

List of Acronyms

ALMA	Atacama Large Millimeter/submillimeter Array
APEX	Atacama Pathfinder Experiment
BC	Boundary Conditions
BW	Bandwidth
CPW	Coplanar-waveguide
DESHIMA	Deep Spectroscopic High-Redshift Mapper
DSL	Double Shell Lens
EM	Electromagnetics
FIR	Far Infrared
FoV	Field of View
FW	Floquet Wave
FPA	Focal Plane Array
FTS	Fourier Transform Spectroscopy
GF	Green's Function
GO	Geometrical Optics
HDF	Hubble Deep Field
HF	High Frequency
HPBW	Half Power Beamwidth
ILASH	Integrated Lens Antenna Shaping Tool
IR	Infrared
ISM	Interstellar Medium
IST	Instituto Superior Tecnico
KID	Kinetic Inductance Detector
MIR	Middle Infrared
ML	Matching Layer
MS	Microstrip
NbTiN	Niobium Titanium Nitride

NEP	Noise Equivalent Power
NIR	Near Infrared
PEC	Perfect Electric Conductor
PWV	Precipitable Water
PO	Physical Optics
Rx	Reception
SMG	Sub-mm Wave Galaxy
SNR	Signal to Noise Ratio
SPICA	Space Infra-Red Telescope for Cosmology and Astrophysics
SRON	Netherlands Institute for Space Research
SSL	Single Shell Lens
TE	Transverse Electric
THz	Terahertz
TEM	Transverse ElectroMagnetic
TL	Transmission Line
TM	Transverse Magnetic
Tx	Transmission
TS	Terahertz Sensing
X-pol	Cross polarization

List of Publications

Journal Papers

J1. O. Yurduseven, N. Llombart and A. Neto, "A Dual-Polarized Leaky Lens Antenna for Wideband Focal Plane Arrays," *IEEE Trans. Antennas Propag.*, Accepted for publication.

J2. O. Yurduseven, and D. Cavallo, A. Neto, G. Carluccio and M. Albani "Parametric analysis of extended hemispherical dielectric lenses fed by a broadband connected array of leaky-wave slots," *IET Microw. Antennas Propag.*, vol. 9, no. 7, pp. 611-617, May. 2015.

J3. O. Yurduseven, D. Cavallo and A. Neto, "Wideband dielectric lens antenna with stable radiation patterns fed by coherent array of connected leaky slots," *IEEE Trans. Antennas Propag.*, vol. 62, no. 4, pp. 1895-1902, Apr. 2014.

Conference Proceedings

C1. O. Yurduseven, N. Llombart and A. Neto, "A Wideband Dual polarized Leaky Lens Antenna for Tightly Spaced FPAs," *IEEE Antennas and Propagation Society International Symposium (APSURSI 2016)*, Fajardo, Puerto Rico, Jul., 2016.

C2. A. Freni, N. Llombart, O. Yurduseven and A. Neto, "On the Use of Thevenin Circuits in Distributed Transmission lines and the Extension of the Methodology to the Problem of Antennas in Reception," *IEEE Antennas and Propagation Society International Symposium (APSURSI 2016)*, Fajardo, Puerto Rico, Jul., 2016.

C3. O. Yurduseven, N. Llombart and A. Neto, "A dual polarized antenna for wideband focal plane applications," *10th European Conference on Antennas and Propagation (EUCAP 2016)*, Davos, Switzerland, Apr., 2016.

C4. A. Neto, N. Llombart, O. Yurduseven and A. Neto, "On the use of Thevenin circuits in distributed transmission lines and its consequences for antennas in reception," *10th European Conference on Antennas and Propagation (EUCAP 2016)*, Davos, Switzerland, Apr., 2016.

C5. J. Baselmans, J. Bueno, O. Yurduseven, N. Llombart, S. Yates, A. Baryshev, A. Endo, D. Thoen and A. Neto, "Large format arrays of antenna coupled Kinetic Inductance Detectors for THz astronomy," *10th European Conference on Antennas and Propagation (EUCAP 2016)*, Davos, Switzerland, Apr., 2016 (Awarded with **"Best Paper on Electromagnetism and Antenna Theory")**.

C6. O. Yurduseven, N. Llombart, and A. Neto, "A dual polarized leaky lens antenna for wideband FPA applications," *In Joint Symposium URSI-Benelux, NARF, and IEEE AP-S Meeting on Smart Antennas and Propagation*, Enschede, The Netherlands, Dec., 2015.

C7. J. Bueno, O. Yurduseven, S. Yates, N. Llombart, M. Murugesan, A. Baryshev, A. Neto and J. Baselmans, "Photon noise limited performance over an octave of bandwidth of Kinetic Inductance Detectors for sub-mm astronomy," *36th ESA Antenna Workshop on Antennas and RF Systems for Space Science*, Noordwijk, The Netherlands, Oct, 2015.

C8. O. Yurduseven, N. Llombart, and A. Neto, "A dual polarized leaky lens antenna for wideband Focal Plane Arrays," *36th ESA Antenna Workshop on Antennas and RF*

Systems for Space Science, Noordwijk, The Netherlands, Oct, 2015.

C9. A. Neto, O. Yurduseven, N. Llombart and A. Freni, "On the antenna reception in the presence of generalized excitation," *IEEE Antennas and Propagation Society International Symposium (APSURSI 2015)*, Vancuover, Canada, Jul. 19-25, 2015.

C10. A. Neto, A. Baryshev, J. Bueno, J. Baselmans, N. Llombart, O. Yurduseven, S. Yates and V. Murugesan, "Photon noise limited performance over an octave of bandwidth of Kinetic Inductance Detectors for sub-millimeter astronomy," *16th International Workshop on low temperature detectors*, Grenoble, France, Jul., 2015.

C11. O. Yurduseven, J. R. Costa, C. A. Fernandes and A. Neto, "Frequency independent patterns from double shell lenses fed by leaky wave feeders," *9th European Conference on Antennas and Propagation (EUCAP 2015)*, Lisbon, Portugal, Apr. 12-17, 2015.

C12. A. Neto, O. Yurduseven, N. Llombart and A. Freni, "Antennas in reception," *9th European Conference on Antennas and Propagation (EUCAP 2015)*, Lisbon, Portugal, Apr. 12-17, 2015.

C13. O. Yurduseven, D. Cavallo and A. Neto, "Asymptotic evaluation of the radiation from small dielectric lenses fed by a single leaky-wave slot," *IEEE Antennas and Propagation Society International Symposium (APS 2014)*, Memphis, TN, USA, Jul., 2014.

C14. O. Yurduseven, D. Cavallo and A. Neto, "Investigation of the radiation characteristics of the leaky-lens antenna for small dielectric lenses," *8th European Conference on Antennas and Propagation (EUCAP 2014)*, The Hague, Netherlands, Apr. 6-11, 2014.

C15. N. Llombart, O. Yurduseven, A. Neto, I. E. Lager and J. Baselmans, "Dual polarised antenna for THz space applications: Design and optimization," *44th European Microwave Conference (EuMC 2014)*, pp. 100-103, Rome, Italy, Oct., 2014.

C16. N. Llombart, A. Neto, B. Blazquez, O. Yurduseven and A. Freni, "On the Optimization of the Imaging Speed in Broadband THz Focal Plane Arrays of Kinetic Inductance Detectors" *38th International Conference on Infrared, Millimeter and Terahertz Waves*, Mainz, Germany, Sep., 2013.

C17. A. Neto, N. Llombart, O. Yurduseven, B. Blazquez and A. Freni, "On the Use of Antenna Engineering Tools for the Optimization of the Focal Plane Sampling in

Direct Detection of Distributed Sources," *IEEE Antennas and Propagation Society International Symposium (APSURSI 2013)*, Orlando, FL, USA, Jul., 2013.

C18. D. Cavallo, O. Yurduseven, A. Neto, G. Carluccio and M. Albani, "Extended hemispherical lens fed by wideband arrays of connected leaky-wave slots," *IEEE Antennas and Propagation Society International Symposium (APSURSI 2013)*, Orlando, FL, USA, Jul., 2013.

C19. D. Cavallo, O. Yurduseven, A. Neto, G. Carluccio, and M. Albani, "Connected arrays of slots as feed of a dielectric lens," *Annual Netherlands Antenna Research Framework*, Enschede, The Netherlands, May., 2013.

C20. O. Yurduseven, D. Cavallo and A. Neto, "Dielectric lens fed by coherent connected-slot array as wideband reflector feed," *7th European Conference on Antennas and Propagation (EuCAP 2013)*, Gothenburg, Sweden, Apr., 2013. (Awarded with **"Best Student Paper Award"**)

Awards

A1. *"Best Paper on Electromagnetism and Antenna Theory"* at the 10th edition of European Conference on Antennas and Propagation (EUCAP), Davos, Switzerland (10-15 Apr. 2016), with the paper **C.5** listed in the conference publications.

A2. *"Best Student Paper Award"* at the 7th edition of European Conference on Antennas and Propagation (EUCAP), Gothenburg, Sweden (8-12 Apr. 2013), with the paper **C.20** listed in the conference publications.

About the Author

Ozan Yurduseven was born on June 27, 1987 in Istanbul, Turkey. He received his B.Sc. and M.Sc. degrees in Electronics and Communications Engineering from Yıldız Technical University, Istanbul, Turkey both with First-Class Honors Degree in 2009 and 2011, respectively. He worked as a research assistant in Electromagnetics Department at Ankara University from December 2010 to February 2012.

In February 2012, he started pursuing his Ph.D. degree in Electrical Engineering, Mathematics and Computer Science (EEMCS) department at Delft University of Technology, Delft, Netherlands. His Ph.D. subject was about the design of the wideband integrated lens antenna solutions for terahertz astronomy applications. This research has been carried out under the supervision of Prof. Dr. Andrea Neto as a promoter and Dr. Nuria Llombart as a copromoter. The work resulted in 3 journal publications and 20 conference papers. During his PhD research, he has been working at Instituto de Telecomunicações in Instituto Superior Técnico (IST), Lisbon, Portugal, as a visiting researcher, studying the dielectric lens antennas for THz imaging systems. His research interests include mm and sub-mm wave antenna design, dielectric lens antennas for THz imaging applications, numerical techniques in electromagnetics, radar cross section analysis, and metamaterials. He has authored and coauthored over 30 publications in peer-reviewed journals and conferences.

Mr. Yurduseven received the *"Best Student Paper Award"* at the 7th European Conference on Antennas and Propagation (EuCAP), Gothenburg, Sweden (8-12 Apr. 2013). He was also co-author of the work that was awarded with the *"Best Paper Award on Electromagnetism and Antenna Theory‘* at the 10th European Conference on Antennas and Propagation (EuCAP), Davos, Switzerland (10-15 Apr. 2016). He is a member of IEEE Antennas and Propagation Society (APS), The European Association on Antennas and

Propagation (EurAAP). He serves as a reviewer for IEEE Transactions on Antennas and Propagation, IEEE Antennas and Propagation Wireless Letters and IET Microwaves, Antennas and Propagation.